GAMMA HEATING IN THE MNR

A TIME-DEPENDENT DESCRIPTION OF IN-CORE GAMMA HEATING IN THE MCMASTER NUCLEAR REACTOR

By KURT STOLL, B.Eng., M.A.Sc.

A Thesis Submitted to the School of Graduate Studies in Partial Fulfilment of the Requirements for the Degree of Doctor of Philosophy

McMaster University DOCTOR OF PHILOSOPHY (2016) Hamilton, Ontario (Engineering Physics)

TITLE: A Time-Dependent Description of In-Core Gamma Heating in the McMaster Nuclear Reactor

AUTHOR: Kurt Jason Lorenz Stoll, B.Eng., M.A.Sc.

SUPERVISORS: Dr. John Luxat, Dr. Simon Day

NUMBER OF PAGES: xxi, 233

Abstract

Calculating or predicting the total in-core nuclear heating is a difficult tast. Full-core models can be constructed in a Monte Carlo code, such as MCNP6 or TRIPOLI4, and will allow an analyst to calculate the prompt-gamma heating at any given in-core location; however, such codes are generally unable to track the activated or fission-product isotopes and therefore the delayed-gamma sources can't be included in such a model.

Some analysts have coupled Monte Carlo transport codes to burnup codes in an effort to include delayed-gamma sources, but the solutions tend to be reactor specific, time-independent and a lot of work. New ideas are required to calculate the total time-dependent in-core nuclear heating.

Within this report, two new models have been derived: the nuclear heating equation, and the coupled neutron and nuclear heating point kinetics (NHPK) equations. These models can be used to calculate the time and position-dependent in-core heating. The nuclear heating equations are generalized expressions of the nuclear heating in a volume of interest, within an arbitrary geometry; these equations use Monte Carlo tallies as coefficients and treat the geometry's scalar neutron flux within as the independent variable. The NHPK model describes the nuclear heating in a volume of interest, within a critical assembly by coupling nuclear heating to the famous neutron point kinetics equations.

A SCK-CEN gamma thermometer (GT) was commissioned in a materials testing reactor (MTR), the McMaster Nuclear Reactor (MNR), to measure the dynamic in-core nuclear heating in two locations. The nuclear heating equation was used to calculate self-heating of the SCK-CEN GT by neutron capture reactions. This calculation used CapGam and IAEA PGAA prompt-gamma emission data; delayed-particle emission data from NuDat 2.6 was also employed. Analysis of the GT's signal resulted in a quantitative description of the dynamic delayed-gamma heating in MNR, and provided the coefficients for the NHPK model.

The NHPK model is capable of reproducing the measured time-dependent nuclear heating, and therefore should also be capable of predicting in-core nuclear heating as a function of reactor power.

Acknowledgements

> "There is no royal road to science, and only those who do not dread the fatiguing climb of its steep paths have a chance of gaining its luminous summits."
>
> — K.M.

Many people helped me along the steep paths, and they must be acknowledged here.

First and foremost, Dr. Simon Day spent more hours than anyone else answering my questions and reviewing drafts, probably by an order of magnitude. His subsequent requests for more information guided my work. As Dr. Day knows, I didn't always act on his advice but all the novel components of this thesis grew from his persistent questioning.

Dr. John Luxat provided advice and recommendations from the perspective of an applied scientist. Consciously or not, every nuclear engineer in Canada is influenced by the immense legacy of publicly funded research conducted by the historical NRC, AECL and Ontario Hydro. My awareness of and connection to this body of work came largely through Dr. Luxat. The completion of this work would not have been possible without his influence and support.

Dr. Adriaan Buijs and Dr. Benjamin Rouben of McMaster helped with the more difficult reactor physics concepts.

The McMaster Nuclear Reactor provided the facilities and materials required to achieve the experimental goals. Canadians are lucky to have this piece of infrastructure available to support research and produce medical isotopes. Thank you to Chris Heysel, Mike Butler, Andrea Armstrong, Rob Pasuta, Frank Labonte, Alice Pidruczny and the operators for accommodating the experimental campaign of this thesis.

SCK-CEN provided technical support for the gamma thermometer.

Clealand Berwick, Mike LaFontaine and Jim Garrett helped to construct a neutron detector.

Dr. Bignan, Dr. Vaglio-Gaudard and Dr. Guimbal at CEA Cadarache guided my work with AMMON and JHR while patiently tolerating my struggles with French and object-oriented programming. Christophe, Didier, Patrick, Jaques, Clément, Bernard, Patricia also contributed to this work.

My cohorts at McMaster and Cadarache provided much clarity. Thanks to Brad, Ken, Andrew, Dan, Azin, Adam, Matt, Justin, James, David, Alex, Mike, Jason, Fred, Mikołaj, Matthieu, Walid, Raquel, Sebastian, Małgorzata, Reijo.

And finally, thank you to my family and the rural community at home in Saskatchewan for placing me here.

Contents

1 Introduction **1**
1.1 Objective . . . 1
1.2 Motivation . . . 1

2 Background **3**
2.1 The basics of in-core gamma radiation . . . 3
2.2 Actinide fission . . . 4
2.2.1 Fission energy . . . 4
2.2.2 Prompt fission neutrons . . . 5
2.2.3 Delayed fission neutrons . . . 6
2.2.4 Prompt fission gammas . . . 7
2.2.5 Delayed fission gammas . . . 7
2.3 In-core neutronic processes . . . 10
2.3.1 Neutron transport . . . 10
2.3.2 Diffusion equation . . . 10
2.3.3 Burnup and isotope conversion . . . 11
2.4 Interaction of radiation with matter . . . 12
2.4.1 Energy conversion between radiation and internal energy . . . 12
2.4.2 Charged particle interactions with material . . . 12
2.4.3 KERMA, CEMA and absorbed dose . . . 13
2.4.4 Exposure . . . 13
2.5 Mechanisms of neutron-material interaction . . . 14
2.5.1 Neutron capture . . . 14
2.5.2 Neutron absorption reactions . . . 16
2.5.3 Elastic neutron scattering . . . 16
2.5.4 Inelastic neutron scattering . . . 16
2.6 Mechanisms of gamma-material interaction . . . 16
2.6.1 Rayleigh (coherent) scattering . . . 16
2.6.2 Photonuclear reactions . . . 17
2.6.3 The photoelectric effect . . . 17
2.6.4 The compton effect . . . 17
2.6.5 Pair production . . . 18
2.6.6 Symbolic representation of photon energy absorption . . . 18
2.6.7 Dependencies on gamma energy and atomic number . . . 20

3 Review of practices and literature **25**
3.1 Review of gamma measurement instruments . . . 25
3.1.1 Self-powered gamma detectors . . . 26
3.1.2 Thermoluminescent detectors . . . 26

3.1.3 Calorimeters and gamma thermometers . . . 27
3.1.4 Calorimeter/GT measurement of in-core, steady-state nuclear heating . . . 27
3.1.5 Calorimeter/GT measurement of in-core, time-dependent nuclear heating . . 29
3.2 The SCK-CEN GT . . . 29
3.2.1 GT use at Halden . . . 30
3.2.2 Use of the SCK-CEN GT in BR2 . . . 30
3.2.3 Use of the SCK-CEN GT at the CEA . . . 30
3.3 Common radiation transport software tools . . . 31
3.3.1 CINDER90 . . . 31
3.3.2 PEPIN2 . . . 31
3.3.3 ORIGEN-S . . . 31
3.3.4 TRIPOLI4 . . . 32
3.3.5 MCNP6 . . . 32
3.4 Energy deposition models in TRIPOLI4 and MCNP6 . . . 32
3.4.1 TRIPOLI4 DEPOSITED_ENERGY scores . . . 33
3.4.2 MCNP6 energy deposition tallies . . . 34
3.5 Calculations of gamma heating in low-power reactors . . . 35
3.5.1 The ADAPh program . . . 35
3.5.2 Amharrak's work following ADAPh . . . 44
3.5.3 The PERLE program . . . 45
3.5.4 The AMMON program . . . 45
3.5.5 Delayed gamma heating fraction in the CEA's low-power experiments . . . 52
3.5.6 Differences between low and high power reactor analysis . . . 52
3.6 Calculations of gamma heating in high-power reactors . . . 52
3.6.1 Gamma heating calculations of SRJH . . . 53
3.6.2 The CIRANO program . . . 53
3.6.3 Gamma heating calculations in OSIRIS . . . 54
3.7 Summary . . . 56

4 New models of time-dependent in-core gamma heating 57
4.1 The nuclear heating equation . . . 57
4.1.1 Considerations . . . 57
4.1.2 Generalized geometry . . . 58
4.1.3 Nuclear heating . . . 58
4.1.4 The mean transported energy . . . 59
4.1.5 External sources . . . 59
4.1.6 Heating by external sources . . . 60
4.1.7 Probability and yield . . . 60
4.1.8 Prompt sources . . . 61
4.1.9 Heating by prompt sources . . . 61
4.1.10 Delayed particle sources . . . 62
4.1.11 Heating by delayed sources . . . 63
4.1.12 The nuclear heating equation . . . 63
4.1.13 Using the heating equation . . . 64
4.2 The coupled neutron and photon point kinetics (PPK) model . . . 65
4.2.1 Review of the point reactor kinetics model . . . 65
4.2.2 Derivation of the two-particle point kinetics model . . . 68

5 Methodology of analysis 77
5.1 The McMaster Nuclear Reactor . . . 77
5.1.1 MNR Specifications . . . 77
5.1.2 The MNR power measurement and control . . . 79
5.1.3 Monitored MNR operating parameters . . . 80
5.2 The experimental use of the SCK-CEN GT . . . 80
5.2.1 Data logging . . . 80
5.2.2 Design of the experimental campaign . . . 80
5.2.3 Simplifying assumptions of analysis . . . 80
5.3 SCK-CEN GT signal processing steps . . . 82
5.4 MCNP6 modeling . . . 83
5.4.1 MCNP6 model of the MNR Reference Core (RC) . . . 83
5.4.2 MCNP6 model of the SCK-CEN GT . . . 85
5.5 Calibration of the SCK-CEN GT . . . 85
5.5.1 The steady-state GT heat transfer model . . . 85
5.5.2 Experimental dip test and steady-state calibration factor . . . 87
5.5.3 The GT's thermal response . . . 88
5.5.4 The transient calibration equation . . . 88
5.5.5 Solving the transient calibration equation . . . 90
5.5.6 Evaluating the transient calibration equation . . . 90
5.6 Self-heating of the SCK-CEN GT . . . 91
5.6.1 Application of the nuclear heating equation . . . 91
5.6.2 Mean transported energy . . . 92
5.6.3 Calculation of reaction rates with MCNP6 FM card . . . 93
5.6.4 Neutron capture - prompt radiation data . . . 94
5.6.5 Neutron capture - delayed radiation data . . . 104
5.7 Regression analysis of the corrected signal . . . 106

6 Measurements with the SCK-CEN GT in MNR and analysis 109
6.1 Experimental results . . . 109
6.1.1 Measurements in location 8F . . . 109
6.1.2 Measurements in location 2A . . . 114
6.2 Quantities calculated with the MCNP6 RC model . . . 117
6.2.1 Neutron and prompt photon flux . . . 117
6.2.2 Neutron reaction rates . . . 117
6.2.3 Neutron and prompt-gamma heating of the SCK-CEN GT . . . 124
6.3 MCNP6 analysis of gamma transport within the SCK-CEN GT . . . 124
6.4 Self-heating of the SCK-CEN GT . . . 124
6.5 The SCK-CEN GT-20 bias . . . 134
6.6 Results of analysis of the SCK-CEN GT-20 signal . . . 134
6.6.1 Coefficients obtained by regression analysis of GT data . . . 134
6.7 Discussion of the results . . . 137
6.7.1 Mechanism 1: differences between prompt and delayed gamma spectra . . . 137
6.7.2 Mechanism 2: dependency on control rod position changes . . . 142
6.7.3 The coupled neutron and nuclear heating point kinetics (NHPK) model . . . 142
6.7.4 Summary . . . 145

7 Summary, conclusions and recommendations for future work 151
7.1 Summary of motivation and analysis . . . 151
7.2 Summary of novelties . . . 152
7.3 Recommendations for future work . . . 152
7.4 Conclusions . . . 153

A The Monte Carlo method and associated uncertainties 155
A.1 Monte Carlo uncertainties . . . 155
A.2 Propagation of errors . . . 156

B Scaling of MCNP6 MNR reference core tallies 157

C Scaling of JHR TRIPOLI4 scores 159

D Spectral considerations 161
D.1 Normalization of spectra . . . 161
D.2 Energy bins . . . 161

E Gamma heating dependencies 165
E.1 The Jules Horowitz Reactor . . . 165
E.2 JHR specifications . . . 165
E.3 Methods of analysis . . . 167
E.3.1 Methods of calculation . . . 167
E.3.2 Labelling of JHR core components . . . 167
E.3.3 Start-up core configuration (zero burn-up) . . . 167
E.3.4 Start-up core configuration (equilibrium burn-up) . . . 168
E.3.5 Summary of TRIPOLI4 parameters . . . 168
E.3.6 Calculation of delayed gamma heating . . . 170
E.3.7 TRIPOLI4 biases . . . 170
E.3.8 Uncertainties . . . 171
E.4 Start-up core (no burn-up) calculations . . . 171
E.4.1 Nuclear heating in common materials . . . 171
E.4.2 Changes in spectra in the presence of C . . . 178
E.4.3 Gamma absorption spectra . . . 178
E.4.4 Dependency of heating on sample depth . . . 180
E.4.5 Dependency of heating on surrounding material . . . 191
E.4.6 Dependency of heating on control rod position . . . 196
E.5 Equilibrium core calculations . . . 199
E.5.1 Results . . . 199
E.6 Conclusions . . . 201
E.6.1 General observations . . . 201
E.6.2 Gamma heating in strong neutron absorbers . . . 201
E.6.3 Comparison of two and four-particle TRIPOLI4 calculations . . . 201
E.6.4 Further analysis . . . 201

F Thermocouples in the SCK-CEN GT 203
F.1 Thermocouples . . . 203
F.2 The SCK-CEN GT differential thermocouple . . . 204
F.2.1 Calculating the EMF generated by an ideal differential thermocouple . . . 205
F.2.2 CJC settings . . . 207
F.2.3 Conversion of GT data collected with "built-in" CJC setting . . . 207
F.2.4 Systematic error . . . 208

G GT signal processing **211**
G.1 Discrete fourier transform 211
G.2 Smoothing the raw GT signal 213
G.3 GT signal noise and error 217

H Curve fitting methodology **219**
H.1 Curve fitting with gnuplot 219
H.2 Statistical evaluation of fit 220
H.3 Determining the uncertainties of the fitting parameters 220
H.3.1 Tests of method 221
H.3.2 The problem of multiple sets of fit parameters 222

I Instrument rig design **225**

List of Figures

2.1 Normalized ^{235}U and ^{239}Pu prompt neutron energy distribution resulting from incident neutrons of 1.0×10^{-5}eV. Data was retrieved from the ENDF/B-VII.1 library MF=5 (energy distributions), MT=18 (particle induced fission) with the program Sigma (Herman 2014). 6

2.2 $\bar{\nu}_p(E')$ of ^{235}U and ^{239}Pu as a function of incident neutron of energy E. Data was retrieved from the ENDF/B-VII.1 library MF=1 (general information), MT=456 (average number of promt neutrons released per fission event) with the program Sigma (Herman 2014). 6

2.3 $\bar{\nu}_d(E)$ of ^{235}U as a function of incident neutron of energy E. Data was retrieved from the ENDF/B-VII.1 library MF=1 (general information), MT=455 (average number of delayed neutrons released per fission event) with the program Sigma (Herman 2014). 8

2.4 Normalized ^{235}U and ^{239}Pu prompt gamma energy distribution resulting from incident neutrons of 1.0×10^{-5}eV. Tabulated data was retrieved from the ENDF/B-VII.1 library MF=15 (energy distributions for photon production), MT=18 (particle induced fission) with the program Sigma (Herman 2014). 9

2.5 Illustration of the neutron capture, showing the resulting release of a prompt gamma, and later through decay, a delayed gamma (Glascock 1996). 15

2.6 The relative importances of the three major mechanisms of gamma-material interaction, as a function of Z and gamma energy (Evans 1955; 712). 21

2.7 Mass attenuation coefficients for water as a function of gamma energy (Evans 1955; 714) 22

2.8 Mass attenuation coefficients for lead as a function of gamma energy (Evans 1955; 716) 23

3.1 The CALMOS differential calorimeter (Carcreff *et al.* 2013; Fig1). 28

3.2 A GT design which uses gas to insulate a small section of the heated body. The associated temperature profile is shown above (Waring and Smith 1983; Fig.2). . . . 28

3.3 (L) Local linear power during a Xe transient as recorded by a string of Radcal GTs in a PWR; (R) Reactor power transient (top curve) and the corresponding GT signal showing slow growth from the delayed gamma component (Waring and Smith 1983). 29

3.4 Cutaway of GT (SCK-CEN 2009; Tab 1). 37

3.5 The EOLE core configuration BASALA-C/16Gd (Blanchet 2006; 104). 37

3.6 MINERVE driver zone showing the fuel, graphite reflector (Element Graphite) and test zone within the solid aluminium block (Massif MELODIE) (Blanchet 2006; 107). 38

3.7 The solid aluminium block (Massif MELODIE), central TLD irradiation location and fuel pins in the MINERVE experimental zone MELODY IV R1-UO2 (Blanchet 2006; 108). 38

3.8 The TRIPOLI4 calculated, prompt gamma spectra from the center of the MOX EOLE and UO_2 MINERVE cores (Blanchet 2006; 170). Note the 511 keV peak from positron annihilations. Photons below 100 keV were not counted. 40

3.9 Comparison between the prompt (from ENDF/B-VI) and delayed gamma spectra (calculated with PEPIN2 at equilibrium) for the EOLE reactor (Blanchet 2006; 180). 42
3.10 (L) The calculated prompt and delayed gamma doses; (R) prompt and delayed gamma doses normalized to the fission chamber's signal (Blanchet 2006). 42
3.11 The fission products which contribute the most delayed gamma dose during the constant 10 minute irradiation (L) and following shutdown (R); as calculated with PEPIN2 using the MOX fuel compositions (Blanchet 2006). 43
3.12 Comparison between the the ionization chamber signal (top) and calculated doses (which were normalized to the fission chamber signal) (Blanchet 2006; 204). 44
3.13 Cross-section of AMMON Reference configuration - plot made with the TRIPOLI model. The control rod is shown on the left, within the driver zone. 46
3.14 The solid aluminum central rod of the JHR (Vaglio-Gaudard *et al.* 2014). 47
3.15 Prompt photon production in several core materials (Vaglio-Gaudard *et al.* 2014). . 50
3.16 Delayed photon flux generated by ^{235}U fission at the center of the central JHR assembly in comparison to the prompt spectrum at the same location (Vaglio-Gaudard *et al.* 2014). 50
3.17 Nuclear heating scheme developed for the OSIRIS reactor (Malouch 2012; 5). 56

4.1 Arbitrary geometry V, described by discrete volumes d^3r, with an arbitrary volume of interest G. 59
4.2 The volume V describing a stylized reactor core made of plate fuel, with each fuel plate divided into discrete volumes. 64
4.3 (L) ORIGEN-S decay gamma source data and the resulting fit equation of the form (4.57), on a lin-lin plot, (R) and on a log-log plot. 74

5.1 (L) Profile cutaway view of fuel assembly showing cylindrical bottom end fitting; (C) top view of standard fuel assembly; (R) top view of control fuel assembly with guide tube for control rod. 78
5.2 (L) Six control fuel assemblies amongst standard assemblies in a core arrangement; (R) top of core view. 78
5.3 The MNR RC configuration (Day 2001). 95
5.4 A slice of the MCNP6 RC model showing the core's plan view. 96
5.5 (L) vertical slice of the MCNP6 RC model, showing the modelled SCK-CEN GT and instrument rig, (R) a slice of the SCK-CEN GT alone. 97
5.6 Cutaway showing GT inner body. 97
5.7 The plot made by the first four terms of equation (5.16) with fitting parameters A' and C' as defined by SCK-CEN of GT20, in lin-lin and semi-log format. 98
5.8 (L) and (C) Raw data from dip test on GT-20; (R) The region $15 \leq t \leq 50$ s which is linear on a semi-log plot and an exponential function of the form $T(t) = a \cdot e^{-b \cdot t}$ fit to the data. 98
5.9 GT inner body temperature profiles corresponding to various quantities of nuclear heating. 99
5.10 (L) Constant heating function and resulting ΔT temperature response; (R) associated temperature response of the entire GT inner body. 99
5.11 (L) Variable heating function and resulting ΔT temperature response; (R) associated temperature response of the entire GT inner body. 100
5.12 Comparison between methods used to obtain $Q(t)/\rho$ with constant (L) and variable heating (R). 100
5.13 Nulcear heating predicted by the calibration factor with and without the constants D and E. 101

5.14 The GT body, V, described by discrete volumes d^3r, heats the volume of interest, the GT's inner body, G. 102
5.15 The three GT material regions (shaded, not to scale), used to calculate the mean transported energy terms. 102
5.16 (L) form of function described by equation (5.41), (R) and by equation (5.42). . . . 106

6.1 GT data collected between Monday Oct. 19 to Friday Oct. 23 in 8F/G. 110
6.2 GT data from 8F/G showing the Tuesday Oct. 20 reactor operation. Time on bottom axis is relative to the start of data aquisition on 9:05 pm Monday Oct. 19. 111
6.3 GT data from 8F/G showing the Wednesday Oct. 21 reactor operation. Time on bottom axis is relative to the start of data aquisition on 9:05 pm Monday Oct. 19. . 111
6.4 GT data from 8F/G showing the Thursday Oct. 22 reactor operation. Time on bottom axis is relative to the start of data aquisition on 9:05 pm Monday Oct. 19. . 112
6.5 GT data from 8F/G showing the Friday Oct. 23 reactor operation. Time on bottom axis is relative to the start of data aquisition on 9:05 pm Monday Oct. 19. 112
6.6 GT data from Tuesday Oct. 20 and the fit curve. 113
6.7 GT data from Friday Oct. 23 and the fit curve. 113
6.8 GT data collected between Saturday Oct. 24 to Monday Nov. 9 in 2A/G. 114
6.9 GT data from 2A/G showing the Tuesday Nov. 3 reactor operation. Time on bottom axis is relative to the start of data aquisition on 10:53 pm Saturday Oct. 24. 115
6.10 GT data from 2A/G showing the Tuesday Nov. 5 reactor operation. Time on bottom axis is relative to the start of data aquisition on 10:53 pm Saturday Oct. 24. 115
6.11 GT data from Tuesday Nov. 3 and the fit curve. 116
6.12 GT data from Thursday Nov. 5 and the fit curve. 116
6.13 Neutron flux in the tallied volumes using the 50-group energy grid. 118
6.14 Photon flux in the tallied volumes using the 25-group energy grid. 118
6.15 MT-102 reaction tallies at from the MCNP6 RC MNR model using the FM card; 2A core midplane. 120
6.16 MT-103 reaction tallies at from the MCNP6 RC MNR model using the FM card; 2A core midplane. 120
6.17 MT-107 reaction tallies at from the MCNP6 RC MNR model using the FM card; 2A core midplane. 121
6.18 MT-16 reaction tallies at from the MCNP6 RC MNR model using the FM card; 2A core midplane. 121
6.19 MT-102 reaction tallies at from the MCNP6 RC MNR model using the FM card; 8F core midplane. 122
6.20 MT-103 reaction tallies at from the MCNP6 RC MNR model using the FM card; 8F core midplane. 122
6.21 MT-107 reaction tallies at from the MCNP6 RC MNR model using the FM card; 8F core midplane. 123
6.22 MT-16 reaction tallies at from the MCNP6 RC MNR model using the FM card; 8F core midplane. 123
6.23 Prompt gamma spectra from (n,γ) reactions in some GT materials. All horizontal axes are in unites of MeV 125
6.24 Prompt power of gammas released by MT-102 (n,γ) reactions in each isotope of the 304L material. 126
6.25 Prompt self-heating by gammas released by MT-102 (n,γ) reactions in each isotope of the 304L material. 127
6.26 Prompt self-heating by gammas released by MT-102 (n,γ) reactions in each isotope of the 316L material. 127

6.27 Prompt self-heating by gammas released by MT-102 (n,γ) reactions in each isotope of the alumina/TC materials. . . . 128
6.28 Total prompt self-heating of the SCK-CEN GT by gammas released by MT-102 (n,γ) reactions in each isotope of all materials. . . . 128
6.29 Delayed self-heating by gammas released by MT-102 (n,γ) reactions in each isotope of the 304L material. . . . 130
6.30 Delayed self-heating by gammas released by MT-102 (n,γ) reactions in each isotope of the 316L material. . . . 130
6.31 Delayed self-heating by gammas released by MT-102 (n,γ) reactions in each isotope of the alumina/TC materials. . . . 131
6.32 Delayed self-heating by gammas released by MT-102 (n,γ) reactions in each isotope of all materials. . . . 131
6.33 Delayed self-heating by charged particles released by MT-102 (n,γ) reactions in each isotope of 304L material. . . . 132
6.34 Delayed self-heating by charged particles released by MT-102 (n,γ) reactions in each isotope of 316L material. . . . 132
6.35 Delayed self-heating by charged particles released by MT-102 (n,γ) reactions in each isotope of alumina/TC materials. . . . 133
6.36 Delayed self-heating by gammas and charged particles released by MT-102 (n,γ) reactions in all isotopes in all SCK-CEN GT materials. . . . 133
6.37 Map of core 59Jiv. . . . 135
6.38 Calculated $Q_{\text{field}}(t)/\rho$ data sets used for curve fitting to determine the delayed-gamma heating constants. . . . 136
6.39 Prompt gamma spectrum emitted within 10^{-7} s after fission of ^{235}U (Keepin 1965; 66). 139
6.40 Delayed gamma spectra observed as a function of time after fission of ^{235}U (Keepin 1965; 132). . . . 140
6.41 The mass attenuation coefficients (solid line) and mass energy-absorption coefficients (dotted line) for Be and C (Hubbell and Seltzer 2014). . . . 141
6.42 Plot showing the magnitude of the mass energy-absorption coefficient of C relative to that of Be. . . . 141
6.43 Control rod positions on the days the GT data sets were collected. . . . 143
6.44 Control rod positions on the days the GT data sets were collected, relative to initial positions. . . . 143
6.45 Exponential function plotted using the Tuesday November 3 constants in Table 6.6. 146
6.46 Heating calculated by equations (6.5) using a constant neutron flux, duplicating the experimental data of Figure 6.45. . . . 146
6.47 A time-dependent data series of normalized $n(t)$. . . . 147
6.48 The nuclear heating predicted by the NHPK equations, corresponding to the changing neutron population of Figure 6.47. . . . 147
6.49 A time-dependent data series of normalized $n(t)$. . . . 148
6.50 The nuclear heating predicted by the NHPK equations, corresponding to the changing neutron population of Figure 6.49; using $\upsilon\Sigma = 1.0$. . . . 149
6.51 The nuclear heating predicted by the NHPK equations, corresponding to the changing neutron population of Figure 6.49; using $\upsilon\Sigma = 0.001$. . . . 149

E.1 The JHR core showing 37 cylindrical locations for either fuel assemblies or experimental devices (Blanchet 2006). . . . 166
E.2 The JHR reflector (Blanchet 2006). . . . 166
E.3 JHR core showing the component labels (TA 2011). The 34 fuel-element configuration shown has not been analyzed in this thesis. . . . 169

E.4 A horizontal section at the vertical mid-plane of the TRIPOLI4 model of the JHR start-up core. . . . 169
E.5 Startup core configuration (equilibrium burn-up) showing the burn-up (top number, in units of MW days per tonne) of each fuel assembly. . . . 170
E.6 (L) geometry placed at center of fuel assemblies EC101 and EC307, (R) geometry placed at the EC103 location. The material samples are centered about the core's vertical center. . . . 172
E.7 Nuclear heating calculated for neutrons and gammas in the mandrel of fuel assembly EC101. . . . 173
E.8 Neutron heating of sample within the mandrel of EC101 in both linear and logarithmic scales. . . . 173
E.9 Nuclear heating calculated for neutrons and gammas in non-fuelled location EC103. 174
E.10 Nuclear heating calculated for neutrons and gammas in the mandrel of fuel assembly EC307. . . . 174
E.11 Gamma heating calculated in the mandrel of fuel assembly EC101, EC103 and EC307. 175
E.12 Comparison between neutron spectra when cylinders (within the mandrel of fuel assembly EC101) are empty and filled with C. The geometry used is shown in Figure E.6. 179
E.13 Comparison between photon spectra when cylinders (within the mandrel of fuel assembly EC101) are empty and filled with C. The geometry used is shown in Figure E.6. 179
E.14 The geometry used to calculate the effect of environmental material changes on nuclear heating, and gamma absorption spectra in the sample cylinder. The material sample is centered about the core's vertical center. . . . 181
E.15 Energy deposition calculated spectrally at core location EC101. . . . 181
E.16 The multi-layered material samples: (L) geometry used at center of fuel assemblies EC101 and EC105, (R) geometry used in non-fuelled assembly location EC103. The material samples are centered about the core's vertical center. . . . 182
E.17 Nuclear heating within the layers of the C sample cylinder placed within the mandrel of fuel assembly EC101. . . . 182
E.18 Electron energy deposition within the layers of the C sample cylinder placed within the mandrel of fuel assembly EC101. . . . 183
E.19 Neutron energy deposition within the layers of the C sample cylinder placed within the mandrel of fuel assembly EC101. . . . 183
E.20 Electron flux through the outer surface of each C layer of the cylinder placed within the mandrel of fuel assembly EC101. . . . 184
E.21 Electron energy deposition within the layers of the Bi sample cylinder placed within the mandrel of fuel assembly EC105. . . . 184
E.22 Electron flux through the outer surface of each Bi layer of the cylinder placed within the mandrel of fuel assembly EC105. . . . 185
E.23 Electron energy deposition within the layers of the Bi sample cylinder placed within the aluminum cell of position EC103. . . . 185
E.24 Electron flux through the outer surface of each Bi layer of the cylinder cylinder placed within the aluminum cell of position EC103. . . . 186
E.25 Neutron spectra within the layers of the C cylinder within the mandrel of fuel assembly EC101. . . . 186
E.26 Neutron spectra within the layers of the Bi cylinder within the mandrel of fuel assembly EC105. . . . 187
E.27 Neutron spectra within the layers of the Bi cylinder within the aluminum cell of position EC103. . . . 187
E.28 Photon spectra within the layers of the C cylinder within the mandrel of fuel assembly EC101. . . . 188

E.29 Photon spectra within the layers of the Bi cylinder within the mandrel of fuel assembly EC105. . . . 188
E.30 Photon spectra within the layers of the Bi cylinder within the aluminum cell of position EC103. . . . 189
E.31 The mass attenuation coefficients (solid line) and mass energy-absorption coefficients (dotted line) for Al and Bi (Hubbell and Seltzer 2014). . . . 189
E.32 Electron heating of inner core of sample cylinder (shown in Figure E.14) as the environment changes, relative to electron energy deposition in the same volume when surrounded by a C environment. . . . 192
E.33 Electron heating of outer layer of sample cylinder (shown in Figure E.14) as the environment changes, relative to electron energy deposition in the same volume when surrounded by a C environment. . . . 192
E.34 Electronic inequality of high-density, high-Z material of region B, when region A is made of low-density, low-Z material. . . . 195
E.35 The geometry used to calculate the effect of control rod position changes on nuclear heating. The material samples are centered about the core's vertical center. . . . 196
E.36 Gamma heating profiles of the inner cores of the carbon samples located within assembly 101. . . . 197
E.37 Gamma heating profiles of the outer layers of the carbon samples located within assembly 101. . . . 197
E.38 Relative gamma heating profiles of the inner cores of the carbon samples located within assembly 101. . . . 198
E.39 Relative gamma heating profiles of the outer layers of the carbon samples located within assembly 101. . . . 198
E.40 Comparison between normalized neutron spectra of zero burn-up and equilibrium core at EC101. . . . 200
E.41 Comparison between normalized photon spectra of zero burn-up and equilibrium core at EC101. . . . 200

F.1 A simple single-junction thermocouple. . . . 204
F.2 The differential thermocouple used to measure the temperature difference between T_H and T_C of the SCK-CEN gamma thermometer. . . . 206
F.3 A differential thermocouple made with two typical thermocouples wired in series, with reversed polarity, which is effectively identical to the circuit shown in Figure F.2. . . . 206
F.4 Calculation of the systematic error introduced by use a regular K-type thermocouple polynomial to describe the voltage from the differential thermocouple contained within the SCK-CEN GT. . . . 208

G.1 Time domain signal of $y = 2\sin(2\pi 0.2t) + 0.5(2\pi 0.3t)$ + random noise and the corresponding amplitude spectrum. . . . 212
G.2 The raw GT signal and the corresponding amplitude spectrum. . . . 212
G.3 (L) signal smoothing of a step change in GT nuclear heating; (R) a detail of the step change "cliff edge." . . . 214
G.4 (L) signal smoothing of a step change in GT nuclear heating; (R) a detail of the step change "cliff edge." . . . 214
G.5 (L) signal smoothing of a step change in GT nuclear heating; (R) a detail of the step change "cliff edge." . . . 215
G.6 (L) signal smoothing of a step change in GT nuclear heating; (R) a detail of the step change "cliff edge." . . . 215
G.7 (L) signal smoothing of a step change in GT nuclear heating; (R) a detail of the step change "cliff edge." . . . 216

G.8 (L) signal smoothing of data from a typical MNR day; (R) a detail of the MNR start-up. 216

I.1 Production drawing of the intrument rig. 226

List of Tables

2.1 Emitted energies for fission of ^{235}U (Lamarsh and Baratta 2001; 88) 4

3.1 Estimates of percentages of gamma heating caused by delayed gammas. 52
3.2 Relative heating from all sources as calculated in different materials (Malouch 2012; 10). 56

5.1 Table showing only the three most probable gammas resulting from thermal neutron capture for the isotopes contained within the GT. 103
5.2 The energy per decay of each type of radiation emitted from most isotopes contained within the GT. 105

6.1 Neutron and photon scalar fluxes relative to the vertical center of 5C. Errors of all values are better than 1.7%. 117
6.2 Heating of the SCK-CEN inner-body, as calculated with the MCNP6 Reference Core model. 124
6.3 Scalar flux in the SCK-CEN inner-body, as calculated with the MCNP6 Reference Core model. 124
6.4 Mean transported energy terms for gamma radiation originating in the 3 material regions of the GT. 126
6.5 Details of the data sets used for regression analysis. 135
6.6 Results of regression analysis. 135

D.1 (L) 50 group neutron bin structure; (C) 8 group neutron bin structure; (R) 25 group photon bin structure. 163

E.1 S/M ratios for the sample cylinders of Figure E.6. 172
E.2 Calculated absolute gamma and neutron energy deposition within the sample cylinder placed within the mandrel of fuel assembly EC307 mandrel, at 70 MW. 175
E.3 Calculated absolute gamma and neutron energy deposition within the sample cylinder placed within the mandrel of fuel assembly EC101 mandrel, at 70 MW. 176
E.4 Calculated absolute gamma and neutron energy deposition within the sample cylinder placed within the aluminum cell at EC103 position, at 70 MW. 177
E.5 Comparison between photon KERMA and energy deposited by electrons, photons and positrons (prompt gammas only). 193
E.6 Positron and photon energy deposition compared to the energy deposited by electrons (prompt gammas only). 194

Chapter 1

Introduction

This chapter provides context for this work by summarizing the motivation to measure and describe the in-core delayed-gamma heating; the objectives of this work are also defined in this chapter. Chapter 2 outlines the prerequisite physics. Chapter 3 reviews the methods other researchers have used to measure and calculate in-core gamma heating; literature shows there is a lack of analytical methods available to describe the time-dependent heating. Chapter 4 proposes two new models for spatially and temporally describing in-core gamma heating: the nuclear heating equations and the coupled neutron-photon point kinetics equations. Chapter 5 describes the methods used to process the SCK-CEN GT signal obtained from measurements in MNR. Chapter 6 contains the experimental results, a discussion of the findings and the development of the coupled neutron and nuclear heating point kinetics equations. Chapter 7 summarizes the results and suggests new efforts for future research.

1.1 Objective

The objectives of this study are: 1) to measure the total time-dependent nuclear heating within a materials testing reactor (MTR) core, 2) isolate and describe the signal component caused by delayed gamma heating, 3) to develop a new time-dependent nuclear-heating model capable of predicting in-core nuclear heating and of reproducing the measured heating, as a function of neutron flux.

These objectives were defined because a literature review (summarized within this thesis) found no other works which have dedicated an experiment to measuring and describing the dynamics of the in-core nuclear heating. Experimental devices have incidentally recorded this time-dependent heating, but no description or models have been developed with these observations.

Therefore, a measurement and model of the total time-dependent heating within a MTR core are novel contributions to the field of nuclear engineering. The measurement will give others an understanding of the magnitude and dynamics of in-core nuclear heating to be expected in an MTR core, and the proposed model could be implemented in any reactor to predict the in-core nuclear heating, with the use of reactor-specific coefficients.

1.2 Motivation

Although the fraction of the total fission energy carried by gamma radiation is not large, gammas can induce as much as 90% of the local nuclear heating in non-fueled in-core components (Zisis *et al.* 2010; 837). But since gammas do not mediate the fission chain reaction as do neutrons nor carry a large fraction of the total fission energy, their presence has been considered to be of minor

consequence compared to neutrons. Unlike neutrons, physicists haven't developed the mature tools and methods required to predict the dynamics of in-core gamma populations or heating.

Radiation transport codes can be used to simulate the emission, transport and energy deposition of in-core photons but these codes still have large biases and uncertainties on heating calculations (Zisis *et al.* 2010; 837). Recent nuclear heating experiments in low-power critical assemblies suggest the nuclear data used in gamma-heating calculations are primarily to blame for systematic differences between calculated and measured gamma heating (Blanchet *et al.* 2008, Vaglio-Gaudard *et al.* 2014).

This lack of accuracy is a problem because some new reactor designs will induce large nuclear heating rates. This heating will cause in-core components to operate closer to their thermal limits; calculating the margins to thermal limits requires accurate design tools. Since the nuclear heating in many components is dominated by gamma heating the designers of new reactors such as France's Jules Horowitz reactor (JHR) are aiming to reduce the uncertainty of the gamma-heating calculations. The CEA and Areva have a goal of reducing the total nuclear-heating uncertainty to 5% (1σ) in the JHR experimental zones (Rimpault *et al.* 2012; 4).

Apart from the accuracy problem caused by erroneous or completely missing nuclear data, there is also a lack of simplified models capable of describing the dynamics of in-core gamma heating. Tracking the concentrations of the hundreds of in-core radioisotopes which birth delayed gammas and the transport of these emissions, in all regions of the core at once, is possible but not yet practical. As an approximation, the core's inventory of these radioisotopes could be assumed constant. This approximation may be acceptable for safety studies concerned with maximum heating rates, or for power reactors which operate for long periods at a constant power, but not when trying to determine the time-dependent behaviour of the delayed-gamma heating in a research reactor with a daily on-off schedule.

To help engineers predict the time-dependent behavior of the in-core energy deposition, this thesis aims to measure and describe the time-dependent in-core component of nuclear heating caused by delayed gammas and incorporate this description into a new time-dependent nuclear heating model. If this model is capable of predicting the total in-core gamma heating without tracking the radioisotope concentrations, it could be used to predict the in-core time-dependent nuclear heating.

Such a model might also be useful in the optimization of commercial MTR processes. The Szilard-Chalmers radiochemistry process is used to manufacture radioactive tracers for use in biochemical, medical or environmental studies; the products of this process are contaminated by the ionizing potential of gamma radiation (Vértes *et al.* 2003; 70). If those who manufacture tracers have detailed knowledge of the simultaneous in-core neutron and gamma fluxes, it would be possible to model and optimize the production of tracer materials (Armstrong 2013).

Chapter 2

Background

This chapter summarizes the physics which must be understood to discuss gamma transport and in-core nuclear heating. Not all topics reviewed in this chapter are used in the analysis contained in later chapters, but all have been included for the benefit of those new to the topic of gamma heating. This chapter begins with an introduction to gamma radiation and a discussion of how the fission energy is divided amongst the particles produced by fission. The chapter concludes with the mechanics of energy deposition in materials by neutrons and photons.

When discussing physics it is often useful to present empirical values which quantify the topical processes, thus some sections in this chapter present data retrieved from the ENDF/B-VII.1 nuclear data library. This library is compiled by the US Cross Section Evaluation Working Group (CSEWG) using evaluated data from decades of experiments (Chadwick *et al.* 2001). ENDF/B-VII.1 is a ubiquitous reference within the industry and is employed in later chapters in calculations.

2.1 The basics of in-core gamma radiation

Gamma radiation is the name given to electromagnetic radiation of the highest energy. The definition of gamma radiation varies between sources, and there appears to be no clear energy boundary between gamma radiation and lower-energy x rays. Some consider photons of wavelength shorter than 0.01 nm to be gamma radiation (Beiser 1995; 69). This implies gamma photons have an energy and frequency greater than:

$$E = \frac{hc}{\lambda} = \frac{(4.136 \times 10^{-15}\,\text{eV·s})(3.00 \times 10^{8}\,\frac{\text{m}}{\text{s}})}{1.00 \times 10^{-11}\,\text{m}} \approx 124\,\text{keV} \tag{2.1}$$

$$f = \frac{c}{\lambda} = \frac{3.00 \times 10^{8}\,\frac{\text{m}}{\text{s}}}{1.0 \times 10^{-11}\,\text{m}} = 3.0 \times 10^{19}\,\frac{1}{\text{s}} = 30\,\text{EHz}. \tag{2.2}$$

Others define each by their origin: x rays originate from atoms (or more specifically, the atom's electrons) and gamma rays from nuclei (Lamarsh and Baratta 2001; 18).

X rays are emitted when an atomic electron transitions from a higher to lower energy orbital. These photons have energies equal to the difference in binding energies between the initial and final shells (Knoll 2010; 14). Such transitions are usually not capable of producing photons of a very high energy since the energy difference between the ground state electron of the innermost orbital (which is the lowest energy and thus most tightly bound to the nucleus) and ionization is small.

Additionally, since every atom has a unique electron configuration, the photons emitted when the electrons de-excite are also unique, thus they are called characteristic x rays.

As electrons, nuclei also exist in quantized states of energy, called energy levels. The difference between quantized states is usually much larger in nuclei than between electron orbitals so the

photons released upon de-excitation are much more energetic; as do x rays, gamma rays result during de-excitation and are equal in energy to the difference between energy levels.

There are a number of phenomenon which can create high-energy electromagnetic radiation. The phenomena most relevant within a nuclear reactor core are:

Fission. Fission produces prompt fission gammas during the fission event, and delayed fission gammas through the decay of the fission products. Prompt fission gammas are discussed in section 2.2.4 and delayed gammas in section 2.2.5 as part of the review of the particles which result from actinide fission.

Neutron capture. Neutron capture reactions by nuclei produce prompt capture gammas at the time of capture, and delayed capture gammas through the decay of the product nucleus. These processes are discussed in section 2.5.1 as part of the review of neutron-material interactions, since neutron capture is one such interaction.

Annihilation. The positron emitted by β^+ decay or pair production will, upon losing its kinetic energy, combine with an electron in the surrounding material and annihilate. This process results in two oppositely-directed photons of 0.511 MeV (Knoll 2010; 12).

2.2 Actinide fission

Nuclear fission is usually induced in reactors when a single neutron is absorbed by a fissionable isotope. Fission occurs when the sum of the neutron's kinetic energy and its binding energy exceedes the fission energy barrier created by the nuclei's strong nuclear force (Knoll 2010; 9). The products of fission are energy and six particles: fission products, neutrons, electrons, positrons, neutrinos and photons.

The fission neutrons offer the potential to induce fission in other surrounding actinide nuclei, and may result in a fission chain reaction in a suitably-designed geometry; sustaining such a chain reaction is the main design requirement of all reactors.

This section reviews fission energy and the prompt and delayed fission particles. An awareness of all particles emitted by fission, and the energy they carry is required while studying nuclear heating. Some particles travel great distances and others are deposited very near their point of emission, thus allowing some fission particles to be discounted in the study of heating in materials distant from the reactor's fuel assemblies.

2.2.1 Fission energy

Form	Emitted Energy (MeV)
Fission fragments	168
Fission product decay	
β rays	8
gamma rays	7
neutrinos	12
Prompt gamma rays	7
Fission neutrons	5
TOTAL	207

Table 2.1: Emitted energies for fission of ^{235}U (Lamarsh and Baratta 2001; 88)

Table 2.1 presents the particles resulting from ^{235}U fission and their associated kinetic energies. The total energy released by fission is equal to the sum of these kinetic energies.

The energy released by a specific nuclear reaction is designated with the variable Q; $Q = 207$ MeV for fission of ^{235}U and the vast majority of this energy appears as fission product kinetic energy — about 168 MeV of the total 207 MeV released upon fission. Fission products have large electric charges and interact readily with the fuel material (Lamarsh and Baratta 2001; 89); consequently, they travel a very small distance within the reactor and the energy they carry is usually deposited entirely within the fuel material from which they originate (Hill and Luxat 2006; 39).

In contrast to fission products, β particles possess either a charge of only +e or -e and have a rest mass 1.8×10^3 times smaller than a resting proton, and thus travel further in any given material. However, even in very sparse material β particles still have a small mean path length; for example, 19.6 keV electrons travel an average of only 0.64 cm in 0 °C oxygen at 1 atm (Evans 1955; 612). This path length reduces even further with increases in material densities and with the number of protons per nuclei, Z. Thus, it is usually assumed the energies of β particles do not leave the fuel matrix from which they orginate (Hill and Luxat 2006).

Famously, neutrinos rarely interact with any material and thus their energy is not recoverable by the reactor.

Neutron and gamma radiation are quite capable of moving beyond the fuel matrix, the fuel cladding, into the surrounding coolant and all other materials within the reactor core. Thus, their energies account for all the nuclear heating of non-fuelled components within the reactor[1].

Of the fission energy which is possible to recover (207 - 12 = 195 MeV), the fraction of this energy neutrons and gammas carry is 5/195 = 0.026 and 14/195 = 0.072, respectively. Half of this gamma energy appears promptly, with the remainder appearing over a long duration following fission.

Although Table 2.1 is useful as a guide for this discussion, experiments show neither the total energy released per fission nor the energy of each component is constant, but are dependent upon the incident neutron energy E'. The total kinetic energy of each fission particle can be retrieved from ENDF/B-VII.1 in one of two formats within file MF=1 (general information), section MT=458 (components of energy release due to fission). In one format (when NPLY=0) the total energy of each component is described by a dedicated linear equation using coefficients stored in MF=1; the total fission energy is equal to the sum of the components. This format has shown to produce incorrect component energies but sum to the correct total energy (Herman and Trkov 2009; 46). Thus, a second format has been implemented (when NPLY≠0) which describes the energy of each component by a polynomial of degree NPLY.

Detailed energy spectra of the fission particles are stored in other sections of ENDF/B-VII.1 in file numbers MF=5 (energy distributions) and MF=15 (energy distributions for photon production); these spectra are referenced later in this section while discussing neutrons and photons. Note that when retrieving total fission energy from ENDF/B-VII.1 the authors recommend integrating the spectra (from MF=5 and MF=15) instead of using the energy totals contained in MF=1 (when NPLY=0); when NPLY≠0, differences are known to exist between the total energies listed in MF=1 and the integrated spectra (Herman and Trkov 2009; 47).

2.2.2 Prompt fission neutrons

Most fission neutrons are released within 10^{-14} seconds of fission and are thus called prompt neutrons; delayed neutrons make up the remainder and are less than 1% of the total number per fission. Delayed neutrons are released much later through decay of dozens of fission products (Duderstadt and Hamilton 1976; 61).

The prompt neutron energy distribution from ^{235}U and ^{239}Pu fission are shown in Figure 2.1 where the units result from the following multiplication (Herman and Trkov 2009; 111):

$$\frac{\mathrm{d}\sigma(E' \to E)}{\mathrm{d}E} = \bar{\nu}_p(E')\sigma(E')p(E' \to E) \tag{2.3}$$

[1]It must be remembered that non-fuelled components within the reactor are not only heated by neutrons and gammas, but also by conduction, convection and radiative heat ransfer from other in-core components.

where:

$\bar{\nu}_p(E')$ = average number of fission neutrons induced by a neutron of energy E', shown in Figure 2.2

$p(E' \rightarrow E)$ = normalized probability of obtaining a fission neutron of energy E from an incident neutron of energy E'

$\sigma(E')$ = microscopic cross section of fission (MT=18) from an incident neutron of energy E'.

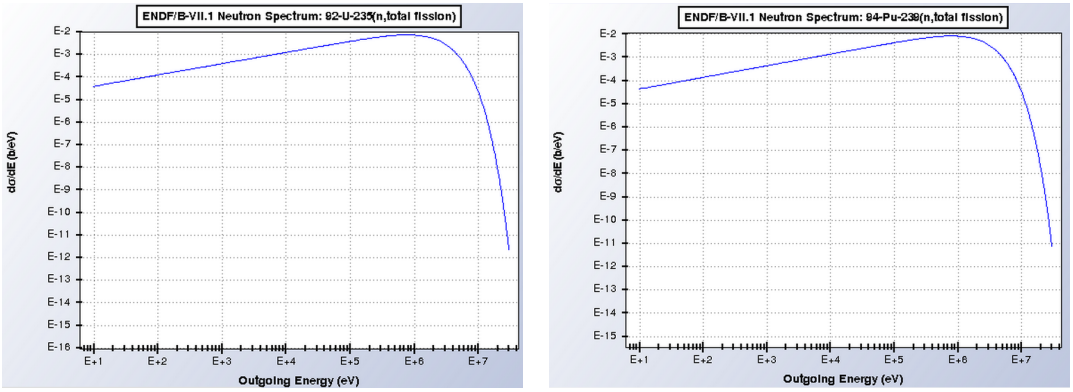

Figure 2.1: Normalized ^{235}U and ^{239}Pu prompt neutron energy distribution resulting from incident neutrons of 1.0×10^{-5}eV. Data was retrieved from the ENDF/B-VII.1 library MF=5 (energy distributions), MT=18 (particle induced fission) with the program Sigma (Herman 2014).

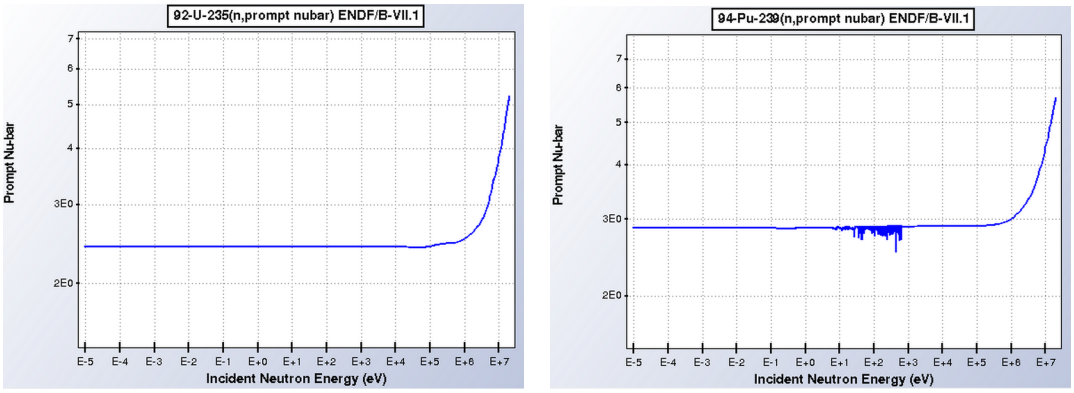

Figure 2.2: $\bar{\nu}_p(E')$ of ^{235}U and ^{239}Pu as a function of incident neutron of energy E. Data was retrieved from the ENDF/B-VII.1 library MF=1 (general information), MT=456 (average number of promt neutrons released per fission event) with the program Sigma (Herman 2014).

2.2.3 Delayed fission neutrons

The delayed birth of delayed neutrons make reactor power dynamics slow enough to be controllable (Duderstadt and Hamilton 1976; 79). Although most delayed neutrons result from fission product decay, some may be produced by photo-nuclear reactions.

The fission product isotopes at the beginning of a delayed-neutron-producing decay chain are called the neutron precursors. For analysis purposes, the net delayed neutron production is often

modeled as coming from the decay of six fictional fission product isotopes which are defined to decay simply with the emission of a single delayed neutron. In aggregate, these six isotopes have been found to closely describe the measured temporal yield of delayed neutrons when the associated decay constants and fission yields are carefully chosen. Because each fictional isotope describes a cluster of real neutrons, one says there are "six groups." The equation describing the delayed source $S_d(E',t)$ is assumed to be a summation of six exponential decay terms, corresponding to the six groups (Keepin *et al.* 1957; 6):

$$S_d(E',t) = \bar{\nu}(E') \left[\sum_{i=1}^{6} \beta_i(E') \mathrm{e}^{-\lambda_i(E')t} \right] \tag{2.4}$$

where:

$\bar{\nu}(E')$ = average number of neutrons (both prompt and delayed) released, per fission of a given actinide induced by a neutron of energy E'

$\beta_i(E')$ = fraction of all fission neutrons (both prompt and delayed) emitted per fission that appear from ith precursor group, $\beta_i(E') = \frac{\bar{\nu}_d^i(E')}{\bar{\nu}(E')}$

$\lambda_i(E')$ = decay constant of the ith precursor group (Duderstadt and Hamilton 1976; 63).

Figure 2.3 shows $\bar{\nu}_d(E')$ from the ENDF/B-VII.1 library for ^{235}U and ^{239}Pu. Notice $\bar{\nu}_d(E')$ is much lower at higher incident neutron energies for both isotopes. Also notice $\bar{\nu}_d(E')$ remains flat over 11 orders of magnitude before drastically changing at higher energies.

The numerical values for $\bar{\nu}(E')$, $\beta_i(E')$ and $\lambda_i(E')$ are not shown here but are contained in ENDF/B-VII.1 (MF=1, MT=455).

An energy distribution of neutrons from each delayed group is also included in ENDF/B-VII.1. Simple energy spectra are usually designated as $\chi(E)\mathrm{d}E$, equal to the average number of particles emitted with energy E within the energy bin of width $\mathrm{d}E$ (Duderstadt and Hamilton 1976; 61); $\chi(E)\mathrm{d}E$ is usually normalized. Access to an energy spectrum allows one to develop an energy-dependent description of the particle source, $S_d(E,E',t)$, where the E refers to delayed neutrons produced at energy E within the energy bin of width $\mathrm{d}E$, induced by a neutron of energy E' within the energy bin of width $\mathrm{d}E'$ (Bell and Glasstone 1970; 465):

$$S_d(E,E',t) = \sum_i \chi_i(E,E')\beta_i\lambda_i\bar{\nu}(E')\mathrm{e}^{-\lambda_i t} \tag{2.5}$$

where $\chi_i(E,E')$ is the normalized energy spectra of group i. The total $S(E,E',t)$ neutron source can then be written as:

$$S(E,E',t) = \chi_p(E,E')\left[1-\beta(E')\right]\bar{\nu}(E')\delta(t) + \sum_i \chi_i(E,E')\beta_i\lambda_i\bar{\nu}(E')\mathrm{e}^{-\lambda_i t} \tag{2.6}$$

where $\chi_p(E,E')$ is the normalized energy spectra of prompt neutrons, and $\delta(t)$ is the Kronecker delta.

2.2.4 Prompt fission gammas

The prompt gamma (sometimes called fission gamma) energy distribution of ^{235}U and ^{239}Pu fission are shown in Figure 2.4; according to ENDF/B-VII.1 the same spectra results for all incident neutron energies between 1.0×10^{-5}eV and 2.0×10^{7}eV.

2.2.5 Delayed fission gammas

As delayed fission neutrons, delayed fission gammas are birthed within the decay chains of the fission product isotopes. Fission products have a high probability of being neutron-rich and therefore tend

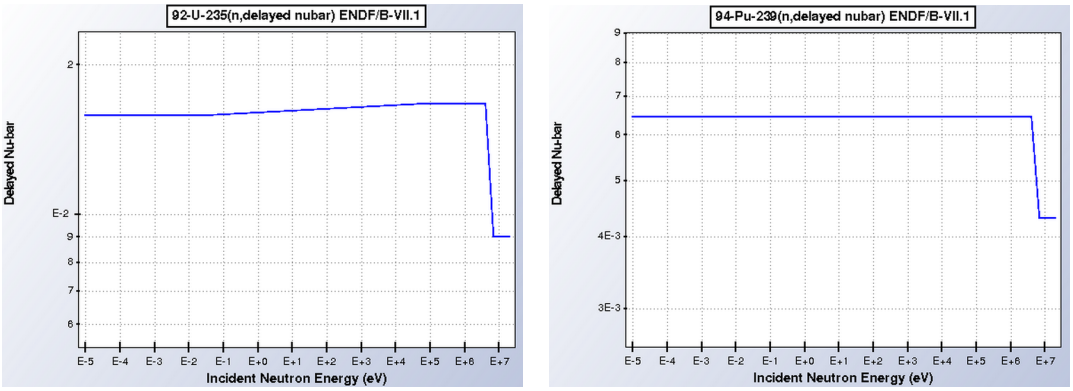

Figure 2.3: $\bar{\nu}_d(E)$ of ^{235}U as a function of incident neutron of energy E. Data was retrieved from the ENDF/B-VII.1 library MF=1 (general information), MT=455 (average number of delayed neutrons released per fission event) with the program Sigma (Herman 2014).

to convert a neutron into a proton; an electron (a β^- particle) and an anti-neutrino are then emitted in what is called β^- decay. Proton-rich isotopes can convert a proton into a neutron and then emit a positron, β^+, and a neutrino in β^+ decay (Lamarsh and Baratta 2001; 19). Following β^- or β^+ decay the daughter nuclei may remain in an excited energy level, which then promptly decays to a lower energy level by emitting a gamma ray, γ.

Each specific β decay is characterized by a fixed Q value. This value is normally presented in a data library assuming the decay transition is between ground states of both the parent and daughter nuclei; since the recoil energy of the nucleus is very small, Q is shared between the β particle, the neutrino and any gammas which may be emitted (Knoll 2010; 4). Although Q values are quantized, because of the energy sharing the β particle energy distribution is continuous rather than discrete; its maximum energy is equal to Q and is called the β endpoint energy. Since the neutrino energy is lost from a reactor completely, a conservative nuclear heating estimate would assume the β particle and gamma energy sum to Q; a conservative β-heating calculation would assume the β particle energy is equal to the endpoint energy, Q.

Since nuclides often have long lives prior to the β decay, relative to the time which passes before a gamma emission of the subsequent daughter nuclei, the emission of this γ radiation is effectively described by the β decay half-life of the parent nuclide.

Describing the intensity of all delayed fission gammas emitted over time by a volume of irradiated fissionable material requires knowing the time-dependent concentrations of many of the hundreds of fission products. Furthermore, some of these radionuclides move through a rather complicated cascade of multiple β decays and γ emissions, and each decay step may have multiple possible paths; all these processes must be considered in the description.

Delayed gamma data is contained within the ENDF/B-VII.1 library. The source of delayed gammas of energy E_γ within the energy bin of width dE, released at time t, after being released by a fission product induced by a neutron at energy E is denoted as $S_\gamma(E, E_\gamma, t)$. This source can be described in two formats from ENDF/B-VII.1: a) when LO=1, the decay photons are described discretely; and b) when LO=2, continuously (Herman and Trkov 2009; 48).

However, the ENDF/B-VII.1 authors recommend using a code such as CINDER or ORIGEN to obtain a detailed delayed-particle source description (Herman and Trkov 2009; 47); these codes are discussed further in this thesis.

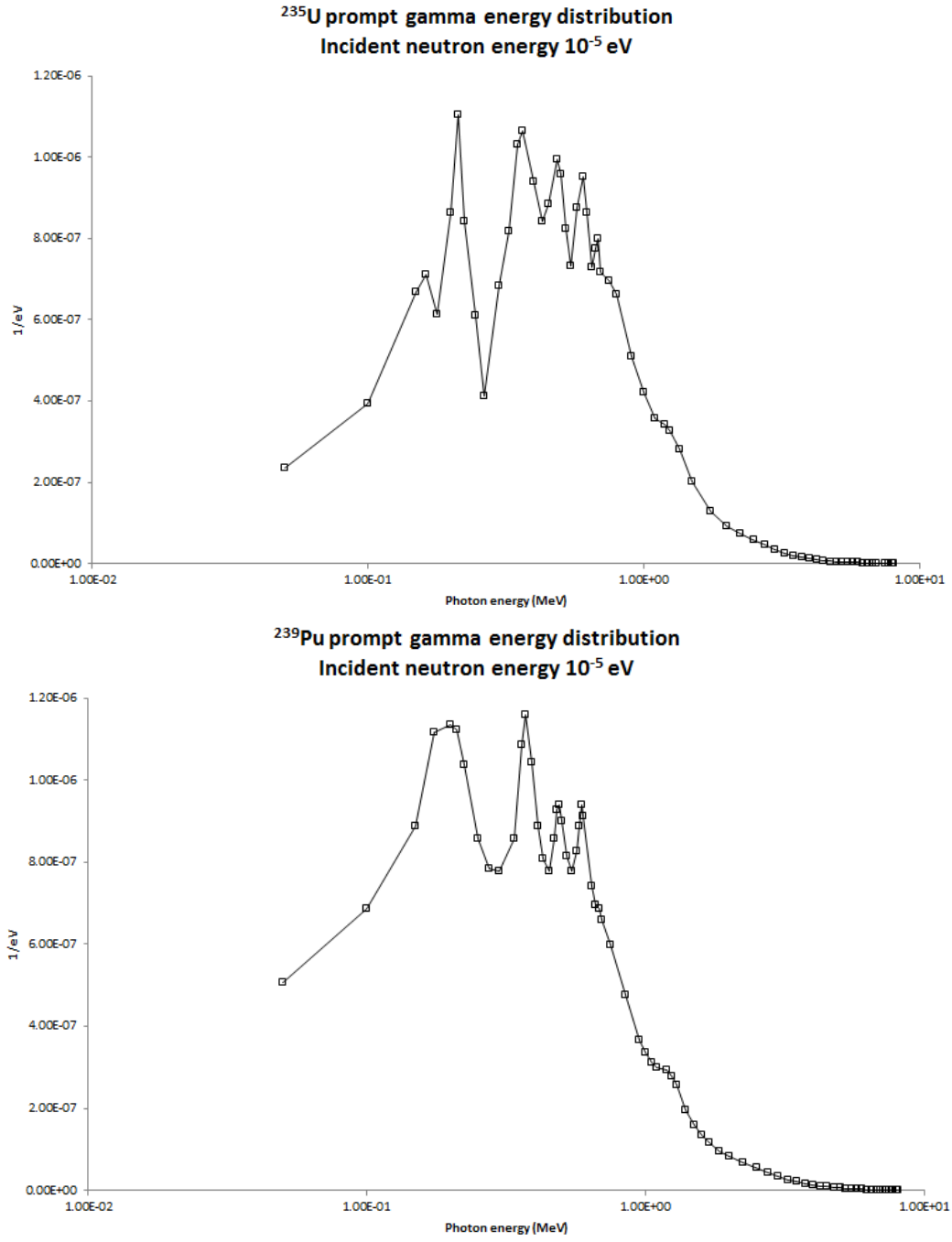

Figure 2.4: Normalized ^{235}U and ^{239}Pu prompt gamma energy distribution resulting from incident neutrons of 1.0×10^{-5}eV. Tabulated data was retrieved from the ENDF/B-VII.1 library MF=15 (energy distributions for photon production), MT=18 (particle induced fission) with the program Sigma (Herman 2014).

2.3 In-core neutronic processes

Since neutrons sustain the fission chain reaction and induce changes in material compositions through capture and fission, neutron physics must be considered before seriously looking at any problem in reactor physics. Even if one is motivated to determine only the in-core gamma flux, analysis must begin with neutrons because photon production is coupled to neutron absorption and neutron-induced fission. Only after the neutron population has been fully characterized can in-core gamma analysis begin.

This section reviews the physics and equations related to the neutron life-cycle: transport, diffusion and fuel burnup.

2.3.1 Neutron transport

Software codes which calculate the movement of neutrons through materials usually employ some approximation of the neutron transport equation. The equation is presented here but is derived completely in (Duderstadt and Hamilton 1976); derivation is accomplished by considering fission, absorption, scattering and leakage with the purpose of counting the number of neutrons within the energy bin $\mathrm{d}E$ about the energy E within the solid angle $\mathrm{d}\vec{\Omega}$ about the direction $\vec{\Omega}$ within a discrete volume d^3r about the position $\vec{r}$ at time t:

$$\frac{1}{\upsilon}\frac{\partial\varphi(\vec{r},E,\vec{\Omega},t)}{\partial t}+\vec{\Omega}\cdot\nabla\varphi(\vec{r},E,\vec{\Omega},t)+\Sigma_t(\vec{r},E)\varphi(\vec{r},E,\vec{\Omega},t)= \int_{4\pi}\mathrm{d}\vec{\Omega}'\int_0^\infty \mathrm{d}E'\Sigma_s(\vec{r};E'\to E,\vec{\Omega}'\to\vec{\Omega},E')\varphi(\vec{r},E',\vec{\Omega}',t)+ \frac{\chi(E)}{4\pi}\int_{4\pi}\mathrm{d}\vec{\Omega}'\int_0^\infty \mathrm{d}E'\nu(E')\Sigma_f(E')\varphi(\vec{r},E',\vec{\Omega}',t) \quad (2.7)$$

where:

$\varphi(\vec{r},E,\vec{\Omega},t)$ = angular neutron flux; dependent on the listed variables
$\nu(E')$ = average number of fission neutrons induced by a neutron of energy E'
$\chi(E)$ = fission spectrum energy distribution
$\Sigma_f(E')$ = macroscopic fission cross section
$\Sigma_t(\vec{r},E)$ = total macroscopic collision and absorption cross section
$\Sigma_s(\vec{r};E'\to E,\vec{\Omega}'\to\vec{\Omega},E')$ = macroscopic scattering cross section from $\mathrm{d}E'$, $\mathrm{d}\vec{\Omega}'$ to $\mathrm{d}E$, $\mathrm{d}\vec{\Omega}$.

2.3.2 Diffusion equation

Since only simplified versions of the neutron transport equation can be solved, even numerically, a number of dependent variables are eliminated and approximations made. First, the angular dependence is usually eliminated by integrating the equation over angle and expressing the equation in terms of scalar flux, defined as (Duderstadt and Hamilton 1976; 125):

$$\phi(\vec{r},E,t)=\int_{4\pi}\varphi(\vec{r},E,\vec{\Omega},t)\mathrm{d}\vec{\Omega}. \quad (2.8)$$

The scattering term of the transport equation is dependent upon two energies, E and E'. By assuming neutron scattering changes only the neutron direction the E' dependency is eliminated, and every term in the simplified equation is evaluated at a single energy E (Duderstadt and Hamilton 1976; 128); the explicit dependency on E' is thus eliminated to create the single-speed approximation to the transport equation.

The equation is made more tractable by approximating the current density term $J(\vec{r},E,t)$, which appears during angular integration, with Fick's law which is a simple gas diffusion model. The

resulting simplified equation is called the one-speed diffusion equation (Duderstadt and Hamilton 1976; 137):

$$\frac{1}{\upsilon}\frac{\partial\phi(\vec{r},t)}{\partial t} - \nabla\cdot D(\vec{r})\nabla\phi(\vec{r},t) + \Sigma_a(\vec{r})\phi(\vec{r},t) = \nu\Sigma_f(\vec{r})\phi(\vec{r},t) \tag{2.9}$$

where:
$D(\vec{r})$ = neutron diffusion coefficient
$\Sigma_a(\vec{r})$ = macroscopic absorption cross section.

When considering a simple homogeneous reactor or reactor segment, $D(\vec{r})$, $\Sigma_a(\vec{r})$ and $\Sigma_f(\vec{r})$ no longer depend on position and the equation simplifies further (Duderstadt and Hamilton 1976; 156):

$$\frac{1}{\upsilon}\frac{\partial\phi(\vec{r},t)}{\partial t} - D\nabla^2\phi(\vec{r},t) + \Sigma_a\phi(\vec{r},t) = \nu\Sigma_f\phi(\vec{r},t) \tag{2.10}$$

Applying this differential equation to simple reactor geometries provides many insights into the static and kinetic behaviours of reactors. Furthermore, the above single-speed equation can be applied to each energy group within an energy grid spanning the multiple orders of magnitude between fission-energy and thermal-energy neutrons. A series of coupled single-energy diffusion equations can be used to obtain a multi-energy description of $\phi(\vec{r},E,t)$ if each equation includes a term to account for inter-bin neutron scattering (Duderstadt and Hamilton 1976; 287).

2.3.3 Burnup and isotope conversion

Having an accurate description of the fuel composition is a prerequisite to many reactor physics calculations. But determining a subject composition is difficult because the concentration of each isotope is dependent on neutron flux and isotopic decay constants. The fission process burns the ^{235}U inventory and builds an inventory of fission products, many of which decay to other isotopes. Simultaneously, neutron capture reactions and the subsequent decay converts many isotopes into other species; most notably in uranium-fuelled reactors, neutron capture creates the entire ^{239}Pu inventory from ^{238}U. Thus a time-dependent description of the reactor's fuel composition must account for these processes. Descriptions must also consider the fact there are hundreds of direct fission product isotopes and some are simultaneously produced by the decay of other fission products, or by neutron capture reactions and subsequent decay.

The Bateman equations (or rate equations, as they are sometimes called) count these isotopes by summing all gain and loss terms for each isotope (Cacuci 2010; 1244):

$$\begin{aligned}\frac{\mathrm{d}N_i(t)}{\mathrm{d}t} = \sum_j \left[\int_0^\infty \gamma_{ij}(E,t)\sigma_j^f(E,t)\phi(E,t)\,\mathrm{d}E\right] N_j(t) + \\ \sigma_{i-1}^c(E,t)\phi(E,t)N_{i-1}(t) + \lambda_{i'}N_{i'}(t) - \\ \left\{\left[\int_0^\infty (\sigma_i^f(E,t)+\sigma_i^c(E,t))\phi(E,t)\,\mathrm{d}E\right] + \lambda_i\right\} N_i(t)\end{aligned} \tag{2.11}$$

where:
$\left[\int_0^\infty \gamma_{ij}(E,t)\sigma_j^f(E,t)\phi(E,t)\,\mathrm{d}E\right] N_j(t)$ = creation rate of isotope i due to fission of isotope j
$\sigma_{i-1}^c(E,t)\phi(E,t)N_{i-1}(t)$ = creation rate of isotope i from neutron capture in isotope i-1
$\lambda_{i'}N_{i'}(t)$ = creation rate of isotope i due to radioactive decay of isotope i'
$\left[\int_0^\infty (\sigma_i^f(E,t)+\sigma_i^c(E,t))\phi(E,t)\,\mathrm{d}E\right] N_i(t)$ = destruction rate of isotope i due to fission and radiative neutron capture
$\lambda_i N_i(t)$ = destruction rate by radioactive decay of isotope i.

When solving equation (2.11) for each isotope i, the neutron flux $\phi(E,t)$ is often assumed constant within discreet time steps.

2.4 Interaction of radiation with matter

The calculation of energy absorption is accomplished in two steps: first determining the energy carried by the incident radiation field, the intensity, and then determining the fraction of the incident energy which is deposited within the material, the dose. It is the dose, the absorbed energy, not the intensity of the radiation field, which heats the subject material and causes biological or material damage.

Calculating the energy deposited within a material by incident radiation is difficult because the primary radiation field may create secondary radiation. Energy deposition by both the primary and secondary radiation must be considered, and every particle species deposits energy in a different manner, requiring different models. The energy spectrum of the primary radiation field may also change as it is transported through the material.

To cover these topics thoroughly, this section discusses radiation energy conversion, exposure and dose; this review demonstrates the significance of charged particles in the energy deposition process.

2.4.1 Energy conversion between radiation and internal energy

The temperature of an object is dependent upon its internal energy. In the case of a gas, the internal energy is measured by the velocity of its free molecules. In the case of a liquid and a solid, the internal energy is measured by the frequency of the molecular vibrations. Increasing the rate of molecular vibration in a solid or liquid raises its temperature.

The alternating polarization of even very-low-energy non-ionizing photons can induce molecular rotation and vibration; high-energy non-ionizing photons can excite orbiting electrons to more energetic shells. The very-high-energy photons of ionizing radiation can fully remove an atomic electron, while giving the ionized electron great kinetic energy.

2.4.2 Charged particle interactions with material

Energetic charged particles induce great disturbances while moving through material by their colombic forces; their electric fields induce ionization, electronic excitation, vibration and molecular dissociation and result in an increase in the material's internal energy (Hurst and Turner 1970; 39).

Gamma rays are not charged, but incident gamma rays can produce electrons of great velocity. The kinetic energy of the electrons can carry the vast majority of the gamma ray's energy, which is then deposited in the surrounding material; most of an incident gamma ray's energy is deposited in the material by these secondary electrons. Therefore, uncharged particles such as photons and neutrons are refered to as indirectly-ionizing radiation because they first transfer kinetic energy to a charged particle before this energy is transferred to the surrounding material (Podgorsak 2005; 5). Radiation fields of charged particles are considered directly ionizing.

The average energy lost by a specific charged particle, in a specific material, per unit length, is defined by the stopping power $\mathrm{d}E/\mathrm{d}X$. Although some of this energy will be converted directly into heating energy, some may be converted to photons through radiative-loss processes: Bremsstrahlung, Cherenkov or annihilation (Podgorsak 2005; 49).

Bremsstrahlung radiation results when a charged particle (such as an electron) is accelerated. Energetic electrons decelerating within a material are often significant sources of Bremsstrahlung radiation, carrying energy from the particle's the kinetic energy. The energy spectrum of the Bremsstrahlung radiation produced by a monoenergetic electron beam impinging on a target is a continuum, with photon energies extending as high as the electron energy itself (Knoll 2010; 18).

Bremsstrahlung is important for electron energies above 10 MeV and therefore is not an important gamma source in reactors (Lüthi 1998; 18).

Cherenkov radiation also results from the deceleration of charged particles, specificially, charged particles which exceed the speed of light in the medium through which they are passing. Since the Cherenkov photon yield is so small this radiative-loss mechanism can also be neglected in the context of in-core gamma heating (Knoll 2010; 734).

Very-high-energy charged particles can create a chain reaction of several generations of secondary photons and charged particles, in what is called an electromagnetic shower by high-energy physicists. Although such chain reactions don't need to be considered by reactor physicists, the material volume of origin may not be where the secondary charged particles deposit their kinetic energy (Podgorsak 2005; 57). If electron transport is significant, this effect must be considered with either a radiation trasport code, or with a cavity correction factor (Podgorsak 2005; 61).

2.4.3 KERMA, CEMA and absorbed dose

Given the importance of charged particles in the process of gamma energy deposition into a material, it is important to quantify the amount of energy transferred from indirectly ionizing radiation to the kinetic energy of charged particles; the mean of this quantity is called the KERMA, Kinetic Energy Released per unit MAss. Similarly, for directly ionizing radiation, CEMA, Converted Energy per unit MAss, describes the kinetic energy lost from the primary directly ionizing radiation; CEMA doesn't include energy lost by secondary charged particles (Podgorsak 2005; 48).

Charged particles with kinetic energy, from either primary or secondary sources, tranfer some of their kinetic energy to the surrounding material, this energy is the absorbed dose when expressed per unit mass. Absorbed energy is distinguished from the energy converted to radiative losses. To illustrate, the conservation of energy can be used to describe the destination of the kinetic energy of an electron as it enters a volume of interest:

$$KE_{\text{incident}} = KE_{\text{exit}} + \text{ absorbed energy } + \text{ radiative loss energy } . \tag{2.12}$$

If a radiation beam of charged particles are incident on a volume, none of the charged particles leave the volume and there are no radiative losses, the absorbed energy is equal to the entire kinetic energy of all incident particles (Hurst and Turner 1970; 82).

The KERMA, CEMA and absorbed dose are all expressions of energy per unit mass (Podgorsak 2005; 48):

$$O = \frac{\mathrm{d}\bar{E}}{\mathrm{d}m} \qquad [O] = \frac{J}{\mathrm{kg}} = \mathrm{Gy} \quad \text{or} \quad \frac{\mathrm{MeV}}{\mathrm{kg}} \tag{2.13}$$

where O is either KERMA, CERMA or absorbed dose and $\bar{E}$ is the associated mean energy quantity.

Radiation physicists are most concerned with the absorbed dose. Absorbed energy is the energy which heats and induces material or biological damage; the local absorbed dose is the quantity one must calculate to determine the heating of each reactor component.

KERMA can be considered equal to absorbed dose under the conditions: a) electronic equilibrium, a consideration of geometry; and b) no radiative losses, which is often the case with low energy electrons (Podgorsak 2005; 58).

2.4.4 Exposure

To fully describe the energy contained within a primary radiation field, its itensity is required, which can be calculated if its scalar flux and energy spectra are known. However, since these parameters were difficult to obtain before the availability of radiation transport software, the intensity of gamma fields have historically been quantified by their ability to ionize air (Hurst and Turner 1970; 82). This quantity is termed exposure, X, and is equal to the total electric charge (of either sign) produced

when all the secondary electrons and positrons are stopped in a gas, per unit mass (Podgorsak 2005; 60).

$$X = \frac{\mathrm{d}\bar{Q}}{\mathrm{d}m}, \tag{2.14}$$

where Q is the total accumulated electric charge. The charge carrying ions are usually pairs of one negatively charged electron and its associated positively charged ionized atom.

Exposure, in units of C/kg can be converted to absorbed dose, in units of MeV/kg, conveniently because gases have been found to absorb, on average, the same amount of energy per ion pair produced, W (Hurst and Turner 1970; 74). Since the measurement of exposure is complete once the secondary particles have come to a stop, all kinetic energy is expended within the gas, exposure is a measurement of dose, and equal to KERMA when there are no radiative losses.

2.5 Mechanisms of neutron-material interaction

Neutrons do not interact with an atom's electron cloud but interact in many ways with nuclei; this section considers the reactions of greatest relevance to nuclear heating calculations (apart from fission which was previously discussed).

2.5.1 Neutron capture

Nuclei can absorb nucleon particles, such as neutrons and alpha particles. Such an absorption releases binding energy and results in an excited nuclear state as illustrated in Figure 2.5. The capture of a neutron by a stable isotope ${}^{A}_{Z}\mathrm{X}$ results in the excited nuclei ${}^{A+1}_{Z}\mathrm{X}^{*}$ which de-excites very quickly (promptly) by gamma emission; these prompt capture gammas can be as energetic as 9 MeV (Knoll 2010; 13).

The new isotope ${}^{A+1}_{Z}\mathrm{X}$ may be radioactive, with its decay rate described by half life λ. Gammas released in this manner are considered delayed in comparison to the appearance of the prompt gammas. The process of creating radioactive isotopes by neutron capture is called activation. Activation of reactor structural material, coolant and other stable in-core material nuclei must be considered as a significant source of both prompt and delayed gamma rays.

An equation describing the number of activated nuclei in a volume, $N_A(t)$, during constant neutron irradiation can be derived by starting with the following expression relating the rate of active nuclei created from target nuclei, $N_T\sigma\phi$, and the decay rate of the active nuclei, $\lambda N_A(t)$:

$$\frac{\mathrm{d}N_A(t)}{\mathrm{d}t} = N_T\sigma\phi - \lambda N_A(t) \tag{2.15}$$

where N_T is the number of target nuclei per unit volume and σ is the microscopic activation cross section. Notice this equation assumes N_T to be constant over time, not subject to burn-up, which is an acceptable approximation when $N_T >> \phi$. The equation also assumes the only mode of destruction of the activated isotope is through decay; in reality some active nuclei may have a large neutron absorption cross section, and thus may absorb another neutron and convert to another isotope.

Separation of variables provides the expression for $N_A(t)$:

$$\frac{\mathrm{d}N_A(t)}{N_T\sigma\phi - \lambda N_A(t)} = \mathrm{d}t \tag{2.16}$$

$$\int \frac{\mathrm{d}N_A(t)}{N_T\sigma\phi - \lambda N_A(t)} = \int \mathrm{d}t \tag{2.17}$$

$$\frac{-1}{\lambda}\ln\left|N_T\sigma\phi - \lambda N_A(t)\right| = t + C \tag{2.18}$$

$$\ln\left|N_T\sigma\phi - \lambda N_A(t)\right| = -\lambda t + C \tag{2.19}$$

$$\left|N_T\sigma\phi - \lambda N_A(t)\right| = \mathrm{e}^{-\lambda t + C} = \mathrm{e}^{C}\mathrm{e}^{-\lambda t} = D\mathrm{e}^{-\lambda t} \tag{2.20}$$

$$N_A(t) = \frac{1}{\lambda}\left[N_T\sigma_A\phi - D\mathrm{e}^{-\lambda t}\right]. \tag{2.21}$$

If the initial population of the active nuclei is $N_A(0) = 0$, $D = N_T\sigma\phi$, the equation becomes (Glascock 1996; 1):

$$N_A(t) = \frac{N_T\sigma\phi}{\lambda}\left[1 - \mathrm{e}^{-\lambda t}\right]. \tag{2.22}$$

Knowing the gamama yield per decay, Y, one can use equation (2.22) to describe the delayed gamma source resulting from this isotope at time t, S_A:

$$S_A(t) = \lambda Y N_A(t). \tag{2.23}$$

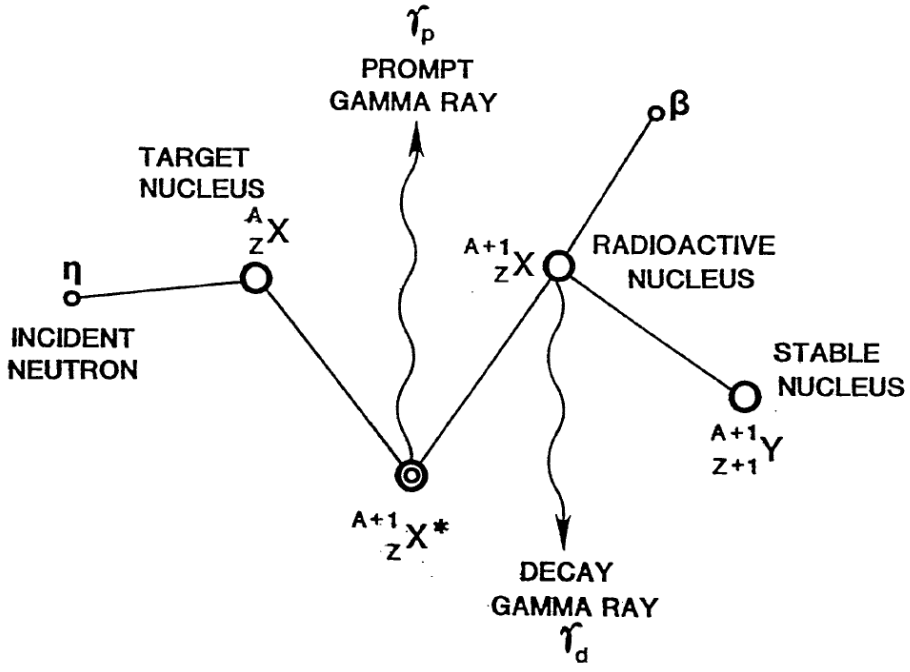

Figure 2.5: Illustration of the neutron capture, showing the resulting release of a prompt gamma, and later through decay, a delayed gamma (Glascock 1996).

2.5.2 Neutron absorption reactions

While neutron capture (n,γ) reactions are most probable at thermal energies, (n,α), (n,2n) and (n,p) reactions are also possible in the thermal energy range (Glascock 1996; 16).

2.5.3 Elastic neutron scattering

Since neutrons have no electric charge, they are capable of penetrating the electronic cloud of an atom and interacting with a nucleus. Elastic neutron-nucleus collisions (in which energy and momentum are conserved) transfer significant amounts of neutron energy to nuclei and are responsible for neutron thermalization.

In the centre of mass reference frame, the average recoil energy, $\bar{E}$, transferred to a nucleus of mass M by a neutron of mass m and energy E_o is (Hurst and Turner 1970; 64):

$$\bar{E} = \frac{2Mm}{(M+m)^2} E_o. \tag{2.24}$$

This equation shows much less energy is converted from the neutron if the collision involves heavier nuclei; which is why light elements are used as neutron moderators.

Neutrons are an indirectly ionizing particle since they impart no coulombic force in an electric field. Thus, no ionizations are induced by neutrons until the collision; the recoiling nucleus itself is the charged secondary radiation which transfers kinetic energy to the host material (Knoll 2010; 54).

2.5.4 Inelastic neutron scattering

Inelastic neutron scattering (n,n') takes place when the neutron is absorbed by the target nucleus, and then ejected again with a different energy. If the neutron is sufficiently energetic, the recoiling nucleus may be promoted to an excited state (Knoll 2010; 54). The nucleus then promptly decays with the emission of one or more inelastic gamma rays (Lamarsh and Baratta 2001; 53).

2.6 Mechanisms of gamma-material interaction

The different types of gamma-material interaction are reviewed here. There are three interactions of particular importance because they are the most probable and result in abrupt changes in the energy of the interacting photons, they are a) the photoelectric effect; b) the Compton effect; and c) pair production. These three interactions are usually the only interactions taken into account in nuclear engineering problems (Lamarsh and Baratta 2001; 90). In addition to being important processes in energy deposition, these interactions are also essential in the field of radiation instrumentation and detection since each generates free electrons; electrons are charge carriers and are used to ionize gas or build electrical potentials within various types of radiation detectors.

2.6.1 Rayleigh (coherent) scattering

Rayleigh scattering is actually a two part process whereby a very-low-energy photon is first absorbed and then re-emitted with a new direction and identical energy (Gilmore and Hemingway 1995; 24). Since this is an elastic interaction between the photon and atom, the atom involved in the interaction is neither ionized nor excited by the scattering event (Knoll 2010; 21). Since no energy is deposited by the photon, this reaction cannot be used in radiation detectors to generate a detector signal nor does it contribute to the heating of a material (Gilmore and Hemingway 1995; 24).

2.6.2 Photonuclear reactions

Sometimes photons can interact directly with an atomic nucleus. If a nucleus absorbs a high-energy gamma ray, photon-induced fission can occur or neutrons can be liberated (Duderstadt and Hamilton 1976). Generally though, photonuclear reactions are insignificant for photon energies below the binding energy of a neutron or proton (Evans 1955; 673). For most in-core gamma studies these reactions are discounted completely and are generally considered only when large numbers of photons above 5 MeV are present (Gilmore and Hemingway 1995; 24).

An important exception is the non-negligible ${}^{2}_{1}\mathrm{H}(\gamma, \mathrm{n})$ cross section. Given the large inventory of deuterium in heavy water reactors (such as CANDU), analysis of these reactors must consider this source of neutrons in criticality calculations. Another exception is ${}^{9}_{4}\mathrm{Be}(\gamma, \mathrm{n})$ which is used in many reactors as a neutron moderator or reflector. The thresholds for these reactions are 2.33 and 1.67 MeV, respectively (Bell and Glasstone 1970; 467).

2.6.3 The photoelectric effect

The photoelectric effect is the process where a photon interacts with a bound electron, resulting in a free electron and photon death (Harris 1999). The ejection of the electron from the atom is accomplished by a single photon. Each atom requires a different amount of energy to liberate (ionize) an electron, and this quantity is called the work function ϕ. The work function designates the energy required to remove the least strongly bound electron from a specific metal; other electrons on the same atom may require more energy to free, depending on their orbital shell.

In this process all the photon's energy is imparted upon the electron; the photon disappears and the electron is left with a kinetic energy equal to the difference between the photon's energy and the energy required to free the electron from its orbit. The maximum kinetic energy of an electron from isotope i is:

$$KE^{i}_{MAX} = hf - \phi^{i}, \tag{2.25}$$

where h is Planck's constant and f is the incident photon's frequency.

2.6.4 The compton effect

The Compton effect is the interaction of an photon with a free electron in which the photon survives but loses some of its energy (Harris 1999). While electrons bound to atoms aren't truly free, some are so weakly bound (relative to the energy of a gamma ray) they can be considered free. The collision conserves momentum and energy:

$$\text{x direction momentum} \qquad \frac{h}{\lambda} = \frac{h}{\lambda'}\cos\theta + \gamma_u m_e u \cos\phi \tag{2.26}$$

$$\text{y direction momentum} \qquad 0 = \frac{h}{\lambda'}\sin\theta - \gamma_u m_e u \sin\phi \tag{2.27}$$

$$\text{energy} \qquad h\frac{c}{\lambda} + m_e c^2 = h\frac{c}{\lambda'} + \gamma_u m_e c^2. \tag{2.28}$$

The above equations can be combined to show the difference in initial photon wavelength λ and post-collision photon wavelength λ':

$$\lambda' - \lambda = \frac{h}{m_e c}(1 - \cos\theta), \tag{2.29}$$

where θ is angle between the initial and resulting photon velocity vectors.

2.6.5 Pair production

Pair production is the transformation of a photon into an electron and positron pair (Harris 1999). This process cannot occur in a vacuum because the photon must electromagnetically interact with a near-by nucleus. Knowing mass and energy to be equivalent, the smallest energy photon capable of producing two charged particles of mass m_e can be determined:

$$2m_e c^2 = 1.62 \times 10^{-13}\text{J} \approx 1\,\text{MeV}. \tag{2.30}$$

A photon of greater-than-minimum energy which produces an electron and positron pair will give the particles a non-zero momentum (the particles produced with the above minimum energy photon will have zero velocity and thus zero momentum).

2.6.6 Symbolic representation of photon energy absorption

This section analytically presents the photon energy absorption processes discussed above, and illustrates the steps between radiation exposure and energy absorption. This symbolic representation is based upon the work found in (Turner 2008).

To begin, a standard nomenclature is established. The term fluence refers to number of particles (photons) per unit area and is designated as φ with units of:

$$[\varphi] = \frac{1}{\text{cm}^2}. \tag{2.31}$$

The fluence rate, or flux, is time dependent and is designated as:

$$\Phi = \frac{d\varphi}{dt} \qquad [\Phi] = \frac{1}{\text{cm}^2\text{s}}. \tag{2.32}$$

The energy fluence refers to energy per unit area and is designated as $[\psi] = \frac{\text{J}}{\text{cm}^2}$ or $= \frac{\text{MeV}}{\text{cm}^2}$. The time dependent energy fluence is often refered to as energy flux or intensity:

$$\Psi = \frac{d\psi}{dt} \qquad [\Psi] = \frac{\text{J}}{\text{cm}^2\text{s}} = \frac{\text{W}}{\text{cm}^2} \qquad or \qquad = \frac{\text{MeV}}{\text{cm}^2\text{s}}. \tag{2.33}$$

For photons, the energy fluence and intensity is related to the photon frequency f with:

$$\psi = \varphi hf \qquad and \qquad \Psi = \Phi hf. \tag{2.34}$$

For neutrons, macroscopic cross sections are noted as Σ. To distinguish between neutron and photon interaction, macroscopic cross section for photon reactions are noted as μ.

Just as the macroscopic cross section for neutron reactions, Σ, has units of cm^{-1}, so does μ. Photon attenuation and energy absorption reactions routinely use the mass attenuation coefficient $\frac{\mu}{\rho}$ which has units of cm^2g^{-1}.

The attenuation coefficient μ is the sum of contributions from all the photon/matter interactions, such as the photoelectric effect, Compton effect and pair production, τ, σ and κ, respectively:

$$\mu = \tau + \sigma + \kappa. \tag{2.35}$$

In an attempt to determine the energy a material of thickness x absorbs when bombarded with a photon beam of intensity Ψ_0, one might suggest using the attenuation coefficient μ to determine $e^{-\mu x}$, the fraction of photons in Ψ_0 which didn't interact with the material, and then say the rate of energy deposition in the material slab is equal to $\Psi_0(1 - e^{-\mu x})$. There is a problem with this idea though, namely that μ is only capable of describing the fraction of the original beam which has interacted though photoelectric effect, Compton scattering or pair production. μ does not describe the the amount of energy deposited. Upon interaction, the energy of any single photon may be

converted into different forms after the photon interacts with matter, and each of these possible energy paths must be considered separately.

Specifically, the three dominant mechanisms of photon-material interactions all produce charged particles with kinetic energy. These electrons may escape the material totally or emit Bremsstrahlung radiation, which may escape. Additionally, the atom which lost the electron may exist in an excited state following the interaction and may emit a flourescent photon or an Auger electron and both may escape from the material.

Electrons removed from their atomic orbit through the photoelectric effect have initial kinetic energies of $KE_0 = hf - \phi$. The vacant shell is filled by an electron originating in a higher energy orbit, resulting in a transition photon or Auger electron. If δ is the average energy produced in the form of fluorescence radiation, after the photoelectric ejection from orbit, then the fraction of initial photon energy transferred to both photoelectrons and Auger electrons is $\frac{hf-\delta}{hf} = 1-\frac{\delta}{hf}$. The transfer coefficient describing the photon energy which is transferred to electrons through the photoelectric effect is:

$$\frac{\tau_{tr}}{\rho} = \frac{\tau}{\rho}(1 - \frac{\delta}{hf}). \tag{2.36}$$

During Compton scattering, if the incident photons transfer their energy with a fractional average of $\frac{T_{avg}}{hf}$ into initial kinetic energy of Compton electrons, the mass energy-transfer coefficient is:

$$\frac{\sigma_{tr}}{\rho} = \frac{\sigma}{\rho}\frac{T_{avg}}{hf}. \tag{2.37}$$

Incident photons terminating through pair production will result in electrons with initial kinetic energies of $hf - 2m_ec^2$, where m_e is the mass of the electron/positron and $2m_ec^2$ is the rest energy of the pair. The mass energy-transfer coefficient for pair production is then:

$$\frac{\kappa_{tr}}{\rho} = \frac{\kappa}{\rho}(1 - \frac{2m_ec^2}{hf}). \tag{2.38}$$

Contributions from all the considered energy-transfer mechanisms results in a total energy-transfer coefficient - it expresses the total fraction of incident photon energy transferred into electron kinetic energy:

$$\frac{\mu_{tr}}{\rho} = \frac{\tau}{\rho}(1 - \frac{\delta}{hf}) + \frac{\sigma}{\rho}\frac{T_{avg}}{hf} + \frac{\kappa}{\rho}(1 - \frac{2m_ec^2}{hf}). \tag{2.39}$$

To account for the portion of initial electron kinetic energy subsequently emitted as Bremsstrahlung radiation, the factor g is designated as that fraction. It is assumed the remaining electron kinetic energies are deposited entirely within the material. The mass energy-absorption coefficient is then:

$$\frac{\mu_{en}}{\rho} = \frac{\mu_{tr}}{\rho}(1 - g). \tag{2.40}$$

During the derivation of $\frac{\mu_{en}}{\rho}$ the target slab material was assumed to be very thin so that multiple photon scattering could be considered negligible and that fluorescence and Bremsstrahlung photons could be assumed to escape totally from the slab. Also, it was assumed all the electron's energy not transmitted to fluorescence or Bremsstrahlung photons were deposited in the material. These assumptions must be considered anytime $\frac{\mu_{en}}{\rho}$ is applied.

The intensity of a photon beam transmitted through a slab of thickness x is:

$$\Psi = \Psi_0 e^{-\mu_{en}x}. \tag{2.41}$$

When $\mu_{en}x \ll 1$ the first two terms of a Taylor series approximation can be used to express the exponential as: $e^{-\mu_{en}x} = 1 - \mu_{en}x$. The difference in intensity between the initial photon beam and

the transmitted is then $\Psi_0 - \Psi = \Psi_0 \mu_{en} x$. If the slab area normal to the incident beam is A, the rate of energy absorption over the entire slab is $\Psi_0 \mu_{en} x A$. The total mass of the slab is $\rho A x$ and so the specific energy absorption rate, the dose rate, $\dot{D}$, is:

$$\dot{D} = \frac{\Psi_0 \mu_{en} x A}{\rho A x} = \Psi_0 \frac{\mu_{en}}{\rho}. \tag{2.42}$$

Similarily, the fraction of initial photon energy transferred into electronic kinetic energy is $1 - e^{-\mu_{tr} x}$, which is simplified with the Taylor series approximation:

$$1 - e^{-\mu_{tr} x} = 1 - (1 - \mu_{tr} x) = \mu_{tr} x. \tag{2.43}$$

The energy transferred to electrons over the entire slab is then $\Psi_0 \mu_{tr} x A$ and the specific rate transfer of energy to electrons is the KERMA rate:

$$\dot{K} = \frac{\Psi_0 - \mu_{tr} x A}{\rho A x} = \Psi_0 \frac{\mu_{tr}}{\rho}. \tag{2.44}$$

2.6.7 Dependencies on gamma energy and atomic number

To illustrate the probability of interactions of the three different gamma-material processes, Figure 2.6 shows the relative importances. It is obvious that at high energies, for all materials, pair production is the dominant mechanism in the creation of charged particles.

Continuing with the τ, σ and κ notation, Figures 2.7 and 2.8 give absolute values for mass energy absorption and total mass attenuation coefficients of water and lead, respectively. Note the high-Z lead generally has coefficient an order of magnitude greater than water.

These figures are used for illustrative purposes. Total (from all interactions) mass attenuation coefficients and mass energy absorption coefficients for use in calculations can be obtained from the US National Institute of Standards and Technology (NIST) for photons up to 100 MeV (Hubbell and Seltzer 2014).

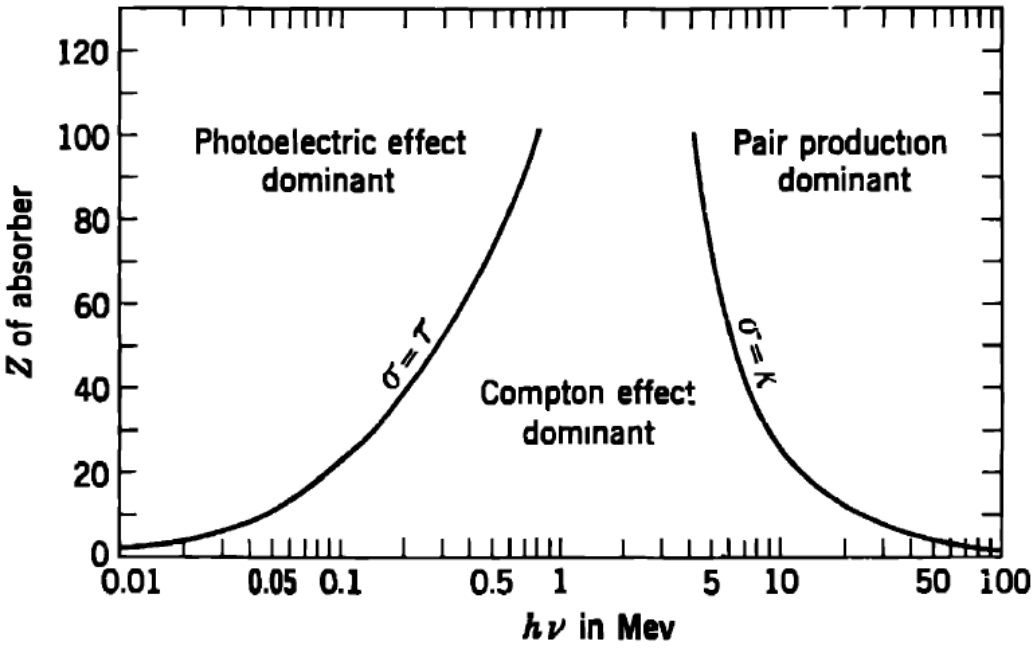

Figure 2.6: The relative importances of the three major mechanisms of gamma-material interaction, as a function of Z and gamma energy (Evans 1955; 712).

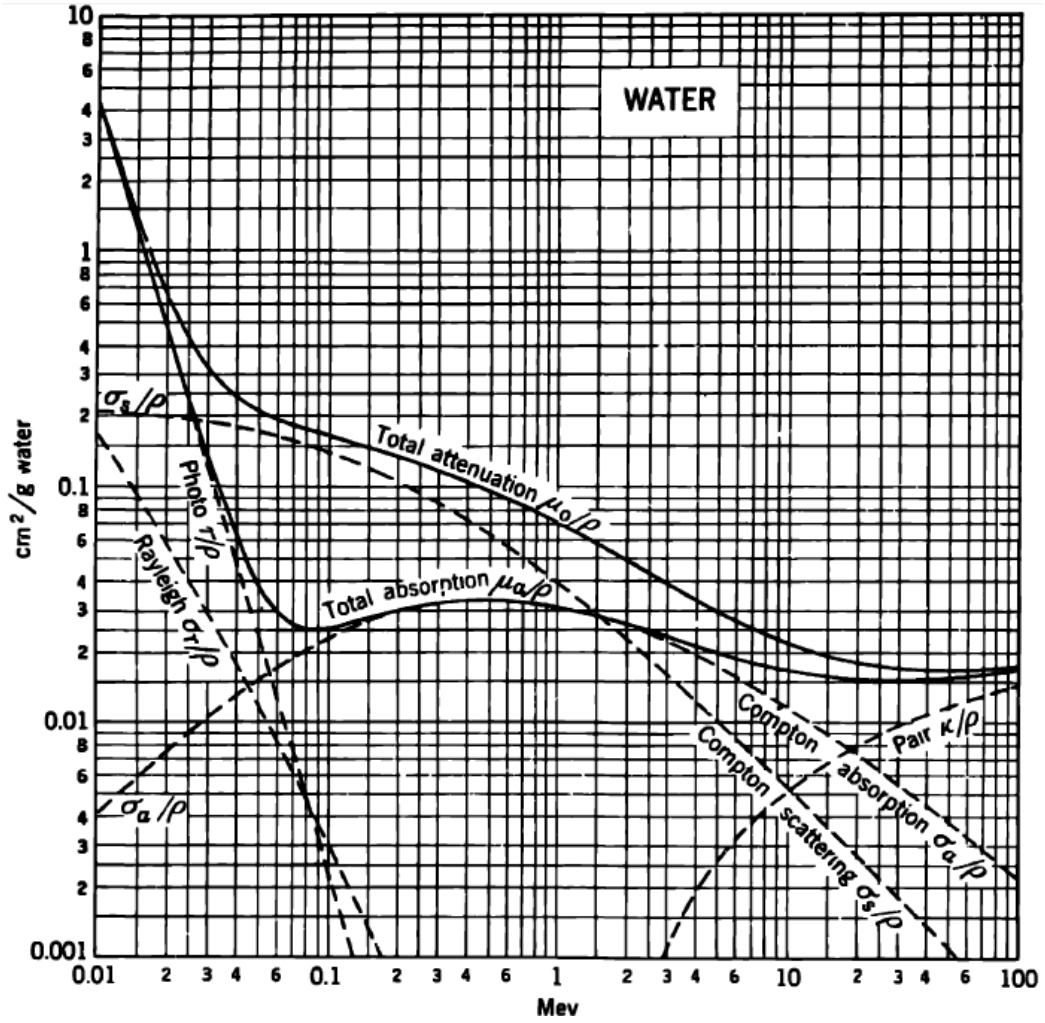

Figure 2.7: Mass attenuation coefficients for water as a function of gamma energy (Evans 1955; 714)

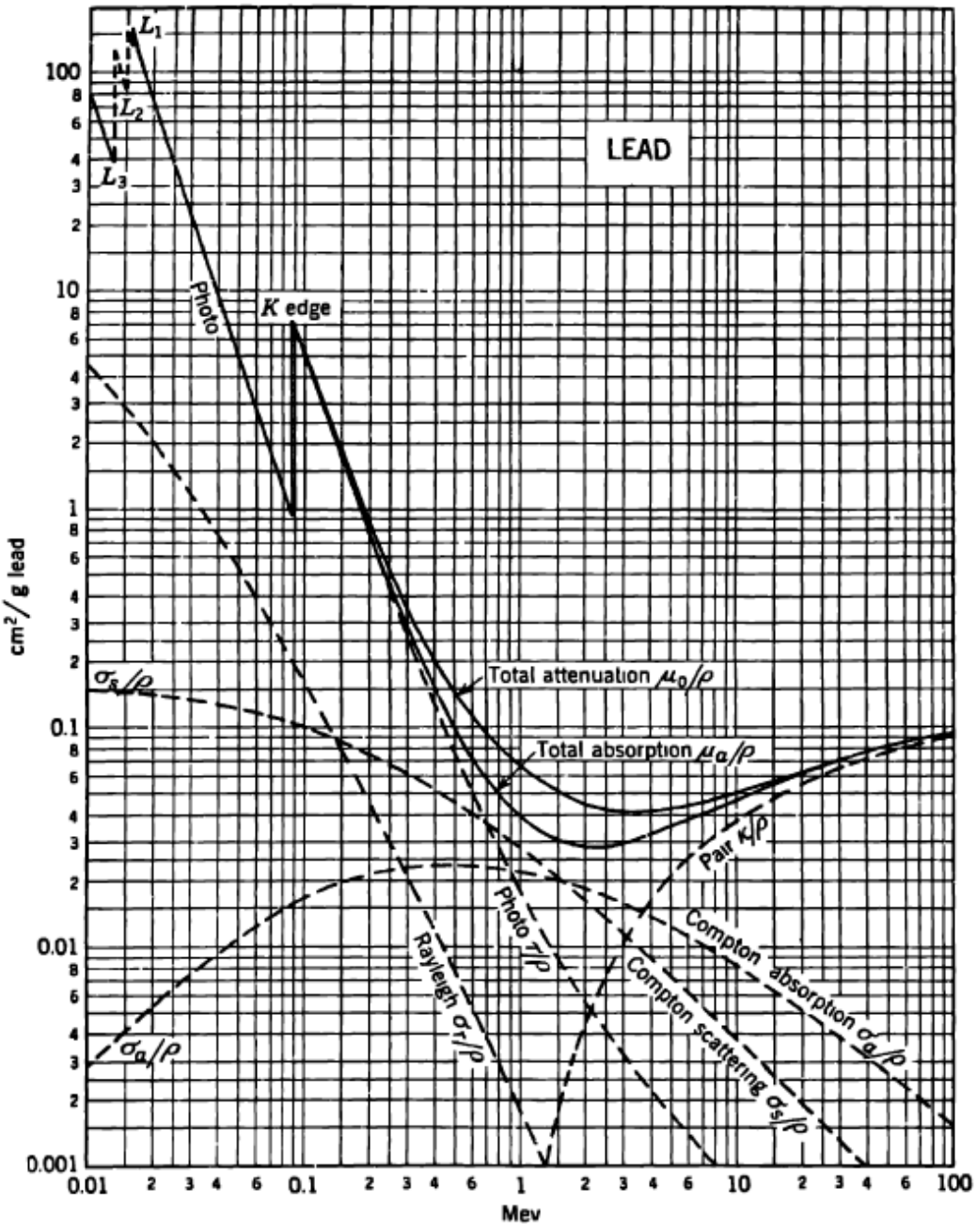

Figure 2.8: Mass attenuation coefficients for lead as a function of gamma energy (Evans 1955; 716)

Chapter 3

Review of practices and literature

This chapter reviews the most common instruments used for in-core gamma dosimetry, the gamma thermometer manufactured by SCK-CEN which has been commissioned in MNR as part of this study, the common software tools used to calculate in-core nuclear heating, and finally, the most relevant efforts of others which sought to calculate in-core gamma fluxes and nuclear heating in low and high-powered reactors.

A review of published calculations has revealed a large number of computational and experimental campaigns by French authors over the last decade. These works were motivated by the CEA's interest in: a) the Jules Horowitz Reactor (JHR) project; b) investigations regarding the conversion of fast spectrum reactors into plutonium burning configurations; c) the evaluation of radiation damage to PWR structural material; d) the design of generation IV reactors; and e) the materials challenges of plasma-facing components within the ITER program.

Many of the reviewed works were seeking to develop methods of calculating in-core gamma dosimetry. Although the calculated results were compared to TLD experimental results and this report makes no use of TLDs the calculational methods are still relevant to this report's goal of developing a new time-dependent nuclear heating model. By reviewing the experiences and methods of others we can see where further efforts could be focused to make new and novel contributions in the field.

Of all the experimental works reviewed, none have purposely measured the in-core delayed-gamma heating; nor has any work isolated this component of nuclear heating to describe its dynamic behavior. Of all the computational methods reviewed, none are able to describe gamma heating as a function of time in a high-power reactor; low-power reactor analyses have only calculated integrated delayed gamma doses, and high-power reactor analyses have only attempted to caclulate gamma heating at a single moment. Therefore, this thesis aims to measure and describe the time-dependent in-core component of nuclear heating caused by delayed gammas in a high-power MTR and incorporate this description into a new time-dependent model of the delayed-gamma heating.

The calculational methods of the CEA's AMMON program is reviewed within this chapter. The author of this thesis conducted some analysis on the AMMON program while in residence at CEA Cadarache and contributed to the content of (Vaglio-Gaudard *et al.* 2014).

3.1 Review of gamma measurement instruments

There are three instruments commonly used to experimentally determine in-core gamma fluxes or energy deposition: self-powered gamma detectors (SPGD), thermoluminescent detectors (TLD), calorimeters/gamma thermometers. This section considers each briefly.

3.1.1 Self-powered gamma detectors

Self-powered gamma detectors (SPGD) operate by collecting the electrons liberated by photon interactions within the SPGD emitter to induce a measurable current. The electrical current travels through a lead wire to allow the instrument to produce a real-time signal proportional to the gamma flux. SPGDs are often manufactured with diameters of 5 mm and lengths of 150 mm, making them suitable for in-core placement.

SPGDs are valuable for their sensitivity to doses lower than those of calorimeters and their very accurate relative measurements (Nieuwenhove and Vermeeren 2002; 827). However, these instruments are activated by neutron capture reactions in the emitter material; the subsequent decay results in decay betas which contribute to the SPGD signal, and decay gammas which produce secondary electrons which contribute to the signal. This process obscurs the signal and must be corrected for; the activation component of the signal can be minimized with a judicious choice of emitter material.

Absolute calibration of SPGDs must be achieved with a known gamma source, or a radiation transport simulation.

3.1.2 Thermoluminescent detectors

Thermoluminescence materials are doped crystals. The dopant atoms provide locations where excited electrons may become trapped for extended periods of time. When such a material is introducted into a radiation field, incident radiation excite electrons in the crystal structure and give them the energy required to move from the valence band into the trap sites. These excited electrons remain trapped in their excited state until phonons (created by heating the crystal) induce the electrons to fall back to lower energy levels; this results in the emission of luminescent photons with energy equal to the difference between excited and de-excited electron energy states. The measurement of absorbed dose depends upon the assumption the energy absorbed from the radiation field is correlated to the intensity of the light emitted (Amharrak *et al.* 2014; 58).

To determine this light intensity, following irradiation the crystals are heated in ovens which contain the required photomultiplier tubes and associated electronics required for counting.

TLDs are widely used for monitoring personnel dosimetry; they have also been used extensively to measure in-core radiation fields (Silva 1992, Santos *et al.* 2007, Torkzadeh *et al.* 2007, Herminghuysen and Blue 1994, Senn and Mixon 1971, Kim 1994, Ji *et al.* 1995, Blanchet *et al.* 2008, Lüthi *et al.* 2001, Yamaguchi *et al.* 1988, Tanaka and Sasamoto 1985, Batistoni *et al.* 2004, Lüthi 1998, Blanchet *et al.* 2005, Amharrak *et al.* 2011; 2010; 2012, Vaglio-Gaudard *et al.* 2014, Ravaux 2013).

The value of TLDs is their sensitivity to a large range of radiation fields, including fields which are too small to appreciably raise the temperature of the absorbing material - such a field precludes the use of a calorimeter. They are used to measure a total accumulated dose over time, thus the duration of exposure must be recorded to determine an average dose rate.

Users must ensure the TLD does not exhibit significant fading. Fading is the spontaneous de-excitation of the electrons and can be unacceptably large over long periods of time. Users must also be aware that some TLDs can lose their sensitivity with repeated use. Most importantly though, even slight changes between similiar TLD dosimeter materials can have large effects on the signal - even a group of TLDs originating from a common manufactured batch can display large variations in sensitivity (Blanchet 2006).

TLDs have a number of restrictions: a) since TLDs measure only accumulated dose and must be removed from the radiation field to extract a signal, they cannot be used for real-time measurement; b) they must be calibrated against a known radiation dose so that the intensity of the field under investigation is relative to the reference signal; c) employing TLDs in a mixed neutron and gamma radiation field requires determining the the neutron contribution to the TLD signal, if one is looking to measure only the gamma dose.

Optically stimulated thermoluminescence dosimeters (OSLD) are also available and function in the same manner as TLDs, except the trapped electrons are induced to recombine with electron holes with light rather than heat.

The works of (Amharrak *et al.* 2010; 2012, Ravaux 2013, Vaglio-Gaudard *et al.* 2014) are the most recent authors to use TLDs and OSLDs for the purpose of determining in-core gamma energy deposition.

3.1.3 Calorimeters and gamma thermometers

Calorimeters are bodies which have had their temperature profiles correlated with known rates of energy absorption. When a calorimeter is placed within an unknown radiation field the user can observe the resulting steady-state temperature and determine the rate of energy deposition. These instruments have been designed in many physical variations, but all measure energy deposition according to the temperature of the sample mass. (Silva 1992, Varvayanni *et al.* 2008, Senn and Mixon 1971, Bernnat and Siegel 1987, Reilly and Peters 1971, Lee *et al.* 2001, Carcreff *et al.* 2013, Fourmentel *et al.* 2013).

Calorimeters are usually calibrated by correlating the temperature of the calorimeter's mass to known quantities of power deposited by an electric current (Joule heating). If heating the sample mass is not possible, one must resort to developing an analytical or numerical heat-transfer model of the sample mass to correlate temperature to energy deposition.

The advantage of calorimeters is their ability to provide an absolute measurement of nuclear heating while in-core (Van Nieuwenhove, R. 1996; App.Pg.3). However, calorimeters can be large in size and are often designed for only steady-state measurements. Furthermore, large calorimeter sample masses have long thermal responses and can be incapable of real-time measurement of dynamic radiation fields.

Gamma thermometers (GT) are simply small calorimeters designed specifically for use in gamma fields. Their small size provides a relatively-quick thermal response and a nearly real-time measurement of nuclear heating of in-core spaces without greatly perturbing the radiation field.

Calorimeters and GTs are non-adiabatic; heat is deposited within the body and conducts along a designed path to the ultimate heat sink, which is usually the reactor coolant. The instrument's signal is one or more temperature measurement of the body.

The most recent calorimeter designed specifically to measure the in-core heating was the CEA's calorimeter commissioned in the 70 MW MTR OSIRIS reactor as part of the CALMOS program. This differential calorimeter consists of two components as shown in Figure 3.1: the sample and reference cells. The top sample cell contains graphite in the head, the bottom reference cell contains only N gas in the cell head. The calorimeter is installed in-core and measures nuclear heating at vertical positions in a two-step process. First, the sample cell obtains thermal equilibrium at the desired vertical location and the user determines the temperature difference between the sample head and its aluminum base; second, both cells are raised and the reference cell moves into the measurement location and the temperature difference between the reference head and base are recorded. The energy deposition in the graphite is determined after observing the difference in heating between the sample and reference cells (Carcreff *et al.* 2013).

Figure 3.2 shows the longitudinal cross section of a common cylindrical GT design with arrows showing the direction of the thermal gradient; the middle of the GT will have a small thermal gradient in the radial direction because of the insulating gas gap on the outer radius.

3.1.4 Calorimeter/GT measurement of in-core, steady-state nuclear heating

Investigators have demonstrated the ability to measure in-core static nuclear heating with calorimeters (Silva 1992, Santos *et al.* 2007).

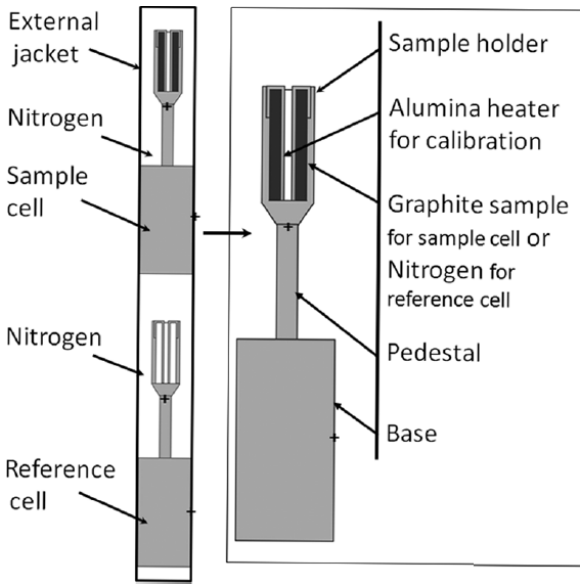

Figure 3.1: The CALMOS differential calorimeter (Carcreff *et al.* 2013; Fig1).

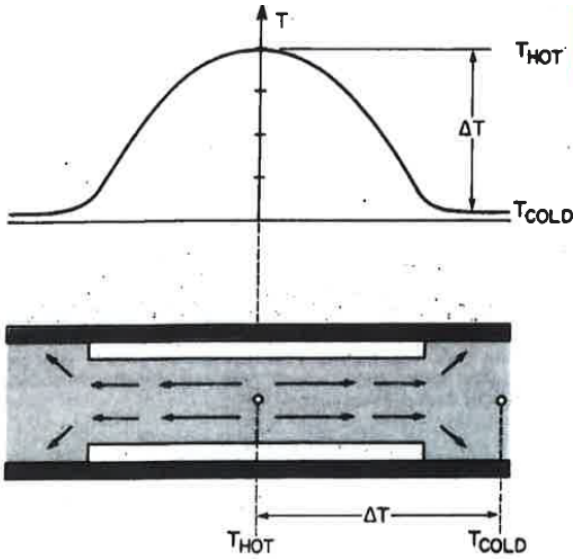

Figure 3.2: A GT design which uses gas to insulate a small section of the heated body. The associated temperature profile is shown above (Waring and Smith 1983; Fig.2).

GTs have also been used for this purpose; their most common application is in power reactors to map the in-core power distribution. GTs may even be better suited to this task than neutron-based instruments since the gamma fields have less spatial variation than the thermal neutron flux (Johnson and Burns 1981, Bernnat and Siegel 1987).

3.1.5 Calorimeter/GT measurement of in-core, time-dependent nuclear heating

GTs have proven successful at measuring dynamic behaviours, such as fluid level and void measurements (Johnson and Burns 1981, Tosi *et al.* 1995) and for estimating the moderator temperature coefficient of reactivity (Demaziere *et al.* 2003). When used to monitor reactor power, GTs have recorded reactor power transients over minutes and hours (Haaland *et al.* 1991). Even fuel burnup over weeks (Haaland *et al.* 1991) and incremental increases of research reactor power (Kizhakkekara *et al.* 1998) have been recorded by GTs. Strings of vertically-placed GTs installed in PWR power reactors were even able to detect the spatial evolution of a Xe transient, as shown in Figure 3.3 (L).

In other work, as Figure 3.3 (R) shows, a GT signal proved sensitive to the delayed gammas; heating of the GT continued to increase after the reactor had reached a constant fission rate. The delayed gammas were also observed heating the GT post-shutdown (Waring and Smith 1983). No subsequent quantitative description of the dynamics of the delayed gamma heating were published despite the author's acknowledgement of this phenomenon.

The author of this thesis is unaware of any study which specifically sought to measure the delayed component of nuclear heating in a power or MTR-type core. Some researchers have specifically noted the existance of the delayed gamma heating component in a GT signal, but since they were interested in determining the fission rate this time-dependent component of the GT signal was considered problematic, rather than worthy of dedicated examination.

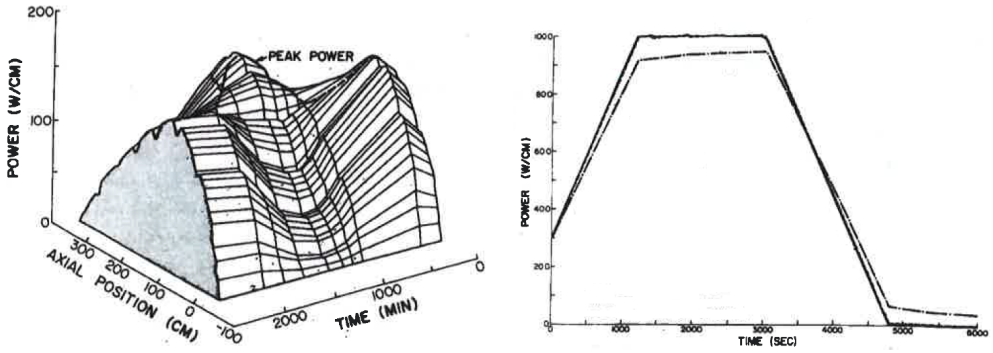

Figure 3.3: (L) Local linear power during a Xe transient as recorded by a string of Radcal GTs in a PWR; (R) Reactor power transient (top curve) and the corresponding GT signal showing slow growth from the delayed gamma component (Waring and Smith 1983).

3.2 The SCK-CEN GT

To measure the nuclear heating within MNR a GT has been commissioned in the McMaster Nuclear Reactor; details of this work are supplied in later chapters. This GT was manufactured by the SCK-CEN and was designed with small dimensions such that it can be placed within a MTR core.

Figure 3.4 shows a section view, displaying the inner body contained within the GT's outer body. The inner body of the GT is the "active" component of the GT; it is heated by radiation and the

temperature of its tip is measured. The inner and outer body are both made of AISI 304 stainless steel and the gap between them is filled with Ar gas (SCK-CEN 2009).

The temperature of the inner body is measured with a differential thermocouple. The hot junction is embedded within the tip of the GT inner body, while the cold junction is embedded within the metal-sheathed signal lead, a few centimeters from the GT body. Appendix F describes the operation of this differential thermocouple in detail.

3.2.1 GT use at Halden

The design of the SCK-CEN GT is based upon the design developed by staff at the OECD/NEA Halden Reactor Project, for their boiling water test reactor in Halden, Norway. GTs have been fabricated and used at the Halden reactor since the 1960s for power monitoring, liquid level monitoring and for comparison to GTs from other manufacturers (Aarrestad 1993; 8).

At Halden, gamma thermometers were once used for fuel channel power measurement - a task which is now accomplished with SPNDs (Van Nieuwenhove, R. 1996; 2). The GT's were (and the SPNDs are now) calibrated to the channel power by assuming the channel power is equal to the power deposited within the channel coolant (as determined by measuring the temperature increase of the coolant through the channel). However, since gamma radiation from surrounding fuel channels heats the structures within the measured fuel channel, the channel's fuel power can be sytematically high; Halden now uses the GTs to correct these measurements during the calibration of the SPNDs, by measuring the absolute gamma energy deposition.

Halden calibrates their GTs directly from the instrument's time constant which is determined by heating the GT's inner body to a high, uniform temperature and then observing its cooling decay. To heat the GT, usually an electrical current is sent through the thermocouple to heat the inner body (Joule heating); this method can be used at anytime, even when the GT is inside the reactor (Liu 1994; 4). Section 5.5 discusses the theory behind this method in detail.

3.2.2 Use of the SCK-CEN GT in BR2

Halden developed miniaturized GTs with an outer length of approximately 50 mm, and this is the design SCK-CEN based their GT design upon for use in the SCK-CEN BR2 reactor. The Halden GT design could not be used because of BR2's much higher nuclear heating values ($\approx$15 W/g compared to $\approx$1 W/g in Halden) (Van Nieuwenhove, R. 1996; 2); BR2 is a 100 MW PWR with a Be and H_2O moderator.

SCK-CEN use the GT in the BR2 reactor to determine absolute nuclear heating; the GTs are used to measure gamma heating in fuel channels for predicting thermal heating of in-core irradiation devices.

3.2.3 Use of the SCK-CEN GT at the CEA

The SCK-CEN gamma thermometers are used by multiple research reactor operators but the CEA is the only institution which has published results or analysis of the instrument.

The CEA made comparisons between the responses of a SCK-CEN GT and a CEA differential calorimeter within the OSIRIS reactor. This work was part of the effort to develop instruments for the measurement of experimental conditions (nuclear heating and neutron flux) within the JHR. The goal of this work was to determine which instrument is best suited for use in the JHR (Fourmentel *et al.* 2013; 328).

The differential calorimeter was of the same two-cell design as was used in the CALMOS project with the exception that the size had been changed to increase the instrument's sensitivity. This increased sensitivity was required since all measurements were conducted outside the OSIRIS core where the nuclear heating was expected to be lower than in-core, around 2 W/g (Fourmentel *et al.* 2013; 330).

Four experimental locations (beside the core) were chosen for the irradiation of both instruments. Each location had a different expected ratio of neutron to photon heating. All irradiations were conducted at steady reactor power of 68 MW (Fourmentel *et al.* 2013; 331). The differential calorimeter measured the nuclear heating at 3 vertical positions in each experimental location; the GT measured the heating at the same 3 locations, plus 1 other. An ionization chamber and a SPGD were irradiated simultaneously to measure the total photon flux; wires were irradiated to measure the total neutron flux (Fourmentel *et al.* 2013; 332).

The irradiations showed the SCK-CEN GT consistently predicted greater heating than the calorimeter. The authors speculated this is a result of the inner body being made of stainless steel, which has a larger Z than the calorimeter's graphite sample (Fourmentel *et al.* 2013; 333).

Simple 2D (slab) models of the calorimeter and GT were made in MCNP5 using neutron and gamma spectra specific to the experimental locations, as calculated by a TRIPOLI4 model of the OSIRIS reactor. The predictions of the MCNP5 models were correlated with experiments but predicted heating about 20% higher than was measured by the calorimeter and 30% higher than was measured by the GT; this difference was attributed to the crude MCNP5 modeling and uncertainties in the ionization chamber signal which was used to define the gamma source in the model (Fourmentel *et al.* 2013; 334).

The authors concluded the GT‘s size is convenient but noted its 10% (a priori) absolute uncertainty is not small enough for the standards of the JHR (Fourmentel *et al.* 2013; 334).

3.3 Common radiation transport software tools

Practically all radiation transport calculations are conducted with at least one software tool; the most commonly used software packages are briefly reviewed in this section. Most of these tools have been employed by the authors reviewed within this chapter to calculate the transporation of gamma radiation and energy deposition.

3.3.1 CINDER90

CINDER90 is a transmutation nuclide inventory code originally developed for accelerator applications (ORNL 2012). It can be used as a burnup code in reactor analysis since it tracks the buildup of fission products. It also tracks the production of activated material. CINDER90 contains a library of 63 energy groups for 3400 nuclides between Z=1 and Z=103.

CINDER90 contains a script called GAMMA_SOURCE which prepares decay gamma source descriptions for subsequent MCNPX calculations.

3.3.2 PEPIN2

PEPIN2 is the point depletion module of the CEA's burnup code DARWIN and is available through the Nuclear Energy Agency (NEA) and is capable of calculating concentrations, activities, gamma ray spectra and residual heat from fission product decay (OECD-NEA 2012).

3.3.3 ORIGEN-S

ORIGEN-S is the point depletion module of the SCALE (Standardized Computer Analyses for Licensing Evaluation) modular code system (ORNL 2011a). ORIGEN-S is based directly upon the now-unsupported, but still relevant, ORIGEN2.2 which solves the decay chain equations. Both ORIGEN-S and ORIGEN2.2 contain libraries which can be used to determine concentrations, activities, gamma ray spectra and residual heat from fission product decay. ORIGEN-S comes with one-group cross-section libraries for PWRs, BWRs, LMFBRs and CANDUs — which is required for conducting the depletion calculation; the user can also define a custom one-group library.

3.3.4 TRIPOLI4

TRIPOLI4 is a Monte Carlo program maintained by the CEA. TRIPOLI4 is capable of transporting neutrons, photons, electrons and positrons and features a variety of score options treating criticality, reaction rate, current, flux and energy deposition. TRIPOLI4 uses continuous-energy libraries and evaluates the properties in a point-wise manner (i.e. it determines cross sections for each particle and nuclei interaction individually, on a case-by-case basis, as opposed to properties averaged over energy groups) (Diop *et al.* 2006).

Users of TRIPOLI4 can construct 3D geometries within the program with either predefined shapes or custom volumes defined with user-defined surfaces. TRIPOLI4 can then use this geometry to conduct shielding, criticality, core physics or instrumentation calculations. The code is capable of running in parallel on multiple processors, so it is of use to large applications — such as the simulation of radiation transport within an entire core.

3.3.5 MCNP6

The MCNP code series developed by the Los Alamos National Laboratory (LANL) is one of the world's most utilized radiation transport codes (Goorley *et al.* 2012; 305). Its validated capabilities, ample documentation and large number of users, make it a dependable analysis tool.

MCNP6, as is TRIPOLI4, is a continuous-energy (i.e. no energy groupings of cross-sections or flux) Monte Carlo program (Pelowitz 2013). MCNP6 has all the capabilities of TRIPOLI4, plus extensive statistical tally checks, biasing techniques and an interactive geometry and tally plotter.

The difference between MCNP6 and the previous version MCNP5 is more than just an update, it includes all the features of what used to be a completely separate Monte Carlo package, MCNPX. This gives MCNP6 a number of capabilities which make it useful for scientists who work with more than neutrons; it is capable of modeling the transport of 34 particle species and 2205 heavy ions over a much larger energy range than MCNP (up to 1 TeV particles) (LANL 2012).

MCNP6 has two input cards which may evolve into valuable tools for the study of in-core gammas, BURN and particularly ACT. Neither were available in MCNP5, but their implementation in MCNP6 restricts their use to small problems, unfortunately.

BURN is the burnup/depletion feature which uses CINDER90 data in KCODE criticality simulations only. This feature is of great value in the determination of fuel element inventories, and thus the delayed gamma source, but the use of this feature requires great computational time.

ACT permits MCNP6 users to include the delayed particles which result from activation or fission. Delayed gamma emission spectra data can be described in two ways: multigroup and line data, both are based on ENDF/B-VI evaluations (Durkee *et al.* 2012; 7). The multigroup library is available in a 25 group format for 3400 radionuclides, and is considered more comprehensive than the line data. The atom densities of activated or fission-product nuclides are calculated with the isotopic transmutation code CINDER90 (Durkee *et al.* 2012; 10).

However, ACT has a number of limitations. ACT can be used only in defined-source simulations (Pelowitz 2013; 3-81), and CINDER90 data, which is retrieved during ACT calculations, cannot be used to describe delayed particles with multi-processors. Thus employing the ACT card in a full core model, in criticality mode, to calculate the heating resulting from delayed particles is unfortunately not possible. Most importantly, the delayed particles are integrated over 1.0×10^{10} seconds, thus preventing MCNP6 from giving a time-dependent description of the source radionuclides, or of the resulting delayed particles.

3.4 Energy deposition models in TRIPOLI4 and MCNP6

Of the literature reviewed, the two most common Monte Carlo codes employed in gamma heating studies are TRIPOLI4 and MCNP6. Therefore it is important to understand how these codes

calculate energy deposition.

3.4.1 TRIPOLI4 DEPOSITED_ENERGY scores

The content of this section is a summary of the reference (CEA 2016) and shows the TRIPOLI4 energy deposition scores are based on KERMA theory.

KERMA is an important quantity because charged particles (fission products, electrons and positrons) deposit their kinetic energy very close to where they originate, relative to gamma rays. Thus it is often assumed the local energy deposited by neutrons or photons is equal to the neutron or photon KERMA, respectively.

However, the amount of kinetic energy attributed to the secondary charged particles changes drastically depending upon the number of particles TRIPOLI4 is tracking; the following discussion explains this in detail.

Two-particle TRIPOLI4 transport

In the case of two-particle transport (coupled neutrons-photons) in TRIPOLI4, the neutron DEPOSITED_ENERGY score calculates heating (energy deposition) values equal to the neutron KERMA within the volume of interest, and the photon DEPOSITED_ENERGY score calculates values equal to the photon KERMA.

The neutron or photon heating scores can be expressed with KERMA factors $k_{i,j}(E)$ which have units of $\mathrm{eV} \cdot \mathrm{cm}^2$:

$$H(E) = \sum_i \sum_j N_i \cdot k_{i,j}(E) \cdot \phi(E), \tag{3.1}$$

where i is the index of elements, j of reactions and N_i is the atomic concentration.

KERMA factors are calculated by the energy balance method. Knowing that the total energy available for any reaction j of element i is the sum of the incident particle energy E and the binding energy released $Q^{\mathrm{eff}}_{i,j}$ during the reaction, the total kinetic energy of all resulting particles is known:

$$E + Q^{\mathrm{eff}}_{i,j} = \sum_c \bar{E}^c_{i,j}(E) + \bar{E}^{\gamma}_{i,j}(E) + \bar{E}^{\mathrm{n}}_{i,j}(E), \tag{3.2}$$

where $\bar{E}^{\gamma}_{i,j}(E)$ and $\bar{E}^{\mathrm{n}}_{i,j}(E)$ are the average kinetic energies of gammas and neutrons which may result from the reaction.

The sum of average kinetic energies of each type c of charged particles can be calculated with the following equation:

$$\sum_c \bar{E}^c_{i,j}(E) = E + Q^{\mathrm{eff}}_{i,j} - \bar{E}^{\gamma}_{i,j}(E) - \bar{E}^{\mathrm{n}}_{i,j}(E). \tag{3.3}$$

The KERMA factors are equal to this sum of kinetic energy of charged particles, times the microscopic cross-section corresponding to that reaction in that isotope:

$$k_{i,j}(E) = \bar{E}^c_{i,j}(E) \cdot \sigma_{i,j}(E). \tag{3.4}$$

The value $Q^{\mathrm{eff}}_{i,j}$ is taken directly from nuclear data libraries for simple reactions such as neutron absorption. However, for more complex reactions such as fission, the total energy given in the libraries $Q^{\mathrm{total}}_{i,j}$ must have various quantities subtracted because these quantities are not considered by the TRIPOLI4 code:

$$Q^{\mathrm{eff}}_{i,j} = Q^{\mathrm{total}}_{i,j} - \bar{E}^{\nu}_{i,j}(E) - \bar{E}^{\gamma\mathrm{D}}_{i,j}(E) - \bar{E}^{\beta\mathrm{D}}_{i,j}(E). \tag{3.5}$$

Where $\bar{E}^{\nu}_{i,j}(E)$ is the average kinetic energy of neutrinos, $\bar{E}^{\gamma \mathrm{D}}_{i,j}(E)$ is the average kinetic energy of delayed gammas, and $\bar{E}^{\beta \mathrm{D}}_{i,j}(E)$ is the average kinetic energy of delayed beta particles.

Single-particle TRIPOLI4 transport

In the case of single-particle transport (neutron-only transport) photons are not tracked and the photon energy which would be carried away by photons in the case of coupled neutrons-photons is assumed to be deposited at the site of neutron-material interaction. The term $\bar{E}^{\gamma}_{i,j}(E)$ is not subtracted from the total available energy $E + Q^{\mathrm{eff}}_{i,j}$:

$$\sum_{c} \bar{E}^{c}_{i,j}(E) = E + Q^{\mathrm{eff}}_{i,j} - \bar{E}^{\mathrm{n}}_{i,j}(E). \tag{3.6}$$

Thus the neutron KERMA is much larger in single single-particle transport than in two-particle transport.

Four-particle TRIPOLI4 transport

Reference (CEA 2016) does not explicitly discuss the implementation of DEPOSITED_ENERGY scores with four-particle (coupled neutrons-photons-electrons-positrons) transport in TRIPOLI4. However, since electrons and positrons are transported the calculated energy deposited by photons will be much less than the photon KERMA.

3.4.2 MCNP6 energy deposition tallies

MCNP6 has two energy deposition tallies: F6 and F7 tallies. F7 tallies are fission energy tallies only and simplistically treat the photons by assuming them to be deposited at the point of fission; this simplification precludes their use in gamma heating analysis requiring transport. F6 tallies are total energy deposition tallies and transport photons in an analogous manner. The heating quanitity H_t calculated by an F6 tally over a volume V is (X-5 Monte Carlo Team 2008; 2-88):

$$H_t = \frac{\rho_a}{m} \int dE \int dt \int dV \int d\Omega \sigma_t(E) H(E) \psi(\vec{r}, \hat{\Omega}, E, t) \tag{3.7}$$

where:
H_t = energy deposition in a cell volume V in units of $\frac{\mathrm{MeV}}{\mathrm{g}}$
ρ_a = atom density in units of $\frac{\mathrm{atoms}}{\mathrm{barns \cdot cm}}$
m = volume mass in units of g
$\sigma_t(E)$ = microscopic total cross section in units of barns
$H(E)$ = heating number in units of $\frac{\mathrm{MeV}}{\mathrm{collision}}$
$\psi(\vec{r}, \hat{\Omega}, E, t)$ = flux in units of particles per cm^2 per shake per MeV per steradian.

The heating number $H(E)$ for neutrons is:

$$H(E) = E - \sum_{i} p_i(E)[\bar{E}_{i,out}(E) - Q_i + \bar{E}_{i,\gamma}(E)] \tag{3.8}$$

where:
$p_i(E) = \frac{\sigma_i(E)}{\sigma_T(E)}$ = probability of reaction i at neutron energy E
$\bar{E}_{i,out}(E)$ = average exiting neutron energy for reaction i at neutron incident energy E
Q_i = Q value of reaction i
$\bar{E}_{i,\gamma}(E)$ = average exiting gamma energy for reaction i at neutron incident energy E.

The heating number $H(E)$ for photons is calculated while assuming all energy transferred to electrons is assumed to be deposited locally:

$$H(E) = E - \sum_{i=1}^{3} p_i(E)[\bar{E}_{i,out}(E)] \tag{3.9}$$

where:

$i = 1$ is Compton scattering with form factors
$i = 2$ is pair production; $\bar{E}_{i,out}(E) = 2m_e c^2 = 1.62 \times 10^{-13}\text{J} \approx 1\text{MeV}$
$i = 3$ is photoelectric absorption; $\bar{E}_{i,out}(E) = 0$
$p_i(E)$ = probability of reaction i at gamma incident energy E
$\bar{E}_{i,out}(E)$ = average exiting gamma energy for reaction i at neutron incident energy E.

Running a MODE P E simulation in MCNP will track electrons and photons individually.

3.5 Calculations of gamma heating in low-power reactors

This section reviews the methods others have developed to calculate the gamma heating within the core of low-power reactors. By reviewing these methods the existing nuclear and gamma heating models are discovered as are opportunities for improved modeling techniques.

In support of the JHR project the CEA has conducted a number of experimental campaigns to measure the gamma heating within low-power critical assemblies: a) the ADAPh program; b) Amharrak's further analysis of ADAPh; c) the PERLE program, and; d) the AMMON program. Following measurement (all programs used TLDs) gamma heating within the same geometries was calculated for the purpose of comparison to experimental data; these methods of calculation are reviewed. Despite the fact these programs have been conducted in low power reactors with TLDs, instead of in MTRs, these programs are reviewed because they are the most extensive known efforts to calculate in-core gamma heating.

3.5.1 The ADAPh program

ADAPh was an experimental program designed to measure integral gamma doses within two low-power, pool-type reactors at CEA Cadarache: EOLE and MINERVE. ADAPh is a French acronym for Amelioration des Donnees de bAse Photonique - Improvement of Basic Photonics Data. The primary goal of the program was to use TLD measurements to determine the accuracy of the HORUS3D/P calculational scheme and the uncertainties in photonic heating originating from the nuclear data.

Prior to commencing ADAPh, the cumulative uncertainties on gamma heating calculations were estimated to be 30% (2 σ) as a result of nuclear data uncertainties (Blanchet *et al.* 2008; 732). ADAPh was meant to help reduce these large uncertainties and to validate procedures for the in-core use of thermoluminescent detectors, in anticipation of the then-planned AMMON experimental program (Cacuci 2010; 2070).

Experimentally, the ADAPh program used thermoluminescent dosimetry to measure the in-core heating of the EOLE core, which was loaded with MOX fuel, in early 2004 and also within the UO_2-fuelled MINERVE reactor in early 2005 (Blanchet 2006; 110). TRIPOLI and MCNP were used to calculate gamma energy deposition in the TLD of these experiments. Summaries of the comparisons between the EOLE experimental results and the calculated values are outlined in a 2005 paper (Blanchet *et al.* 2005). A 2008 paper summarizes the MINERVE experimental and calculated values (Blanchet *et al.* 2008). Blanchet's PhD thesis (which is written in French) contains the full narration of the entire ADAPh program (Blanchet 2006).

The ADAPh work is important because its experimental and calculation methodology has served as a basis for others working at CEA Cadarache on the JHR project; specifically, the PERLE and AMMON gamma heating investigations at CEA Cadarache have both built upon the Blanchet methodology, with improvements.

The ADAPh experimental configurations of EOLE and MINERVE

The EOLE core is a critical facility, where the fuel is assembled within a cylindrical light-water tank 1 m in diameter and 1 m in height at 20 °C (Blanchet 2006; 103). The assembly is made critical by adding fuel elements and further controlled by a single control rod.

During the ADAPh experimental campaign the EOLE core was loaded with MOX fuel. The specific EOLE configuration was BASALA-C/16Gd, which had 16 fuel pins containing Gadolinium in each of the 81 fuel pin assemblies. BASALA was a joint Japanese/French experimental program which supported investigations into MOX-fuelled boiling water reactor analysis (Blanchet 2006; 103). Figure 3.5 shows a cross section of the BASALA-C/16Gd configuration of EOLE. There were three grid locations where the TLD were inserted into the EOLE core (labelled "Position des tubes guides pour l'irradiation des TLD" in Figure 3.5). Two fission chambers were used to monitor core power (their positions are labelled "Position des chambres a fission" in Figure 3.5).

The MINERVE reactor has an HEU driver zone with plate-type fuel surrounded by a graphite reflector at the bottom of a 3 m deep light-water pool. The central experimental zone is inside the driver zone and can be configured as required. During the ADAPh TLD irradiations, the experimental zone was filled with an aluminum block containing 776 UO_2 fuel pins, enriched to 3% ^{235}U (Blanchet *et al.* 2008; 734). This test zone was configured for another test program, MELODY IV, and was designated core assembly R1-UO2. Figure 3.6 shows a cross section of the MINERVE driver zone and Figure 3.7 shows the MINERVE experimental zone.

A miniaturized fission chamber was present in one of the peripheral core locations during the irradiations to monitor reactor power, and a microinization chamber was used to measure the in-core fluxes (Blanchet *et al.* 2008; 735).

In-core cavity correction factors

Blanchet didn't have access to sufficient computing resources to run a whole-core TRIPOLI4 simulation which transported neutrons, γ, e^+ and e^- in a coupled manner to calculate absorbed photon energy. To work around this problem, the calculation of TLD deposited energy was split into two steps.

The first step used the TRIPOLI4 full-core model to calculate both the gamma spectrum and exposure at the TLD in-core locations, from both prompt and delayed sources; these processes are explained later in detail.

The second step predicted the absorbed TLD dose by multiplying the total TLD exposure by an in-core cavity correction factor, based upon the Burlin cavity theory (Blanchet 2006; 157). This cavity correction factor is the ratio between two calculated terms, $ED^{reactor}/K\gamma_{air}^{reactor}$, where $ED^{reactor}$ is the TLD deposited energy (in units of Gy), and $K\gamma_{air}^{reactor}$ the TLD exposure at the in-core location (KERMA air, measured in units of Gy). The superscript "reactor" was used to distinguish these values from a similar correction factor used for TLD calibration.

$ED^{reactor}$ was obtained by calculating the energy deposited in the TLD by γ, e^+ and e^- in a MCNP model of the TLD and its immediate environment (Blanchet *et al.* 2008; 738). The MCNP model consisted of a sphere of 6 cm radius with the TLDs at its centre. An inward-pointing gamma source was defined isotropically on the inside of the sphere surface. This gamma source spectra was calculated using the full-core TRIPOLI4 model.

Rather than calculate a cavity correction factor specific to each TLD and each exposure, cavity correction factors were calculated for each TLD type with a typical exposure $K\gamma_{air}^{reactor}$ (Blanchet *et al.* 2008; Table 3).

The radius of the MCNP model sphere was carefully selected with a parametric study to optimize between the need to have each TLD within the Lucoflex containers exposed equally (which improves with sphere radius) and the Monte Carlo uncertainty (which decreases with increases in sphere radius) (Blanchet 2006; 161).

Figure 3.4: Cutaway of GT (SCK-CEN 2009; Tab 1).

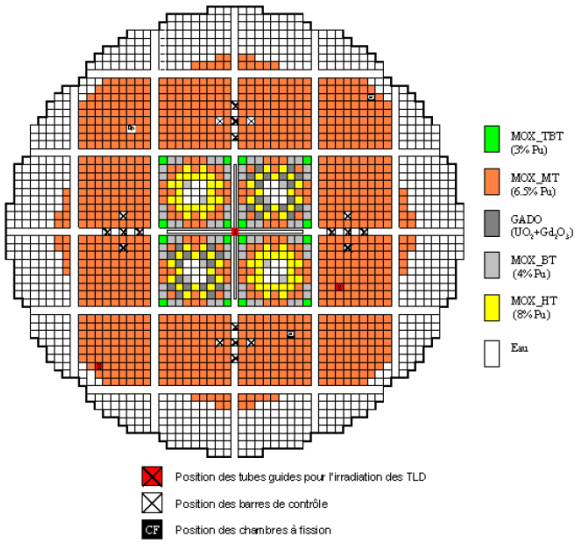

Figure 3.5: The EOLE core configuration BASALA-C/16Gd (Blanchet 2006; 104).

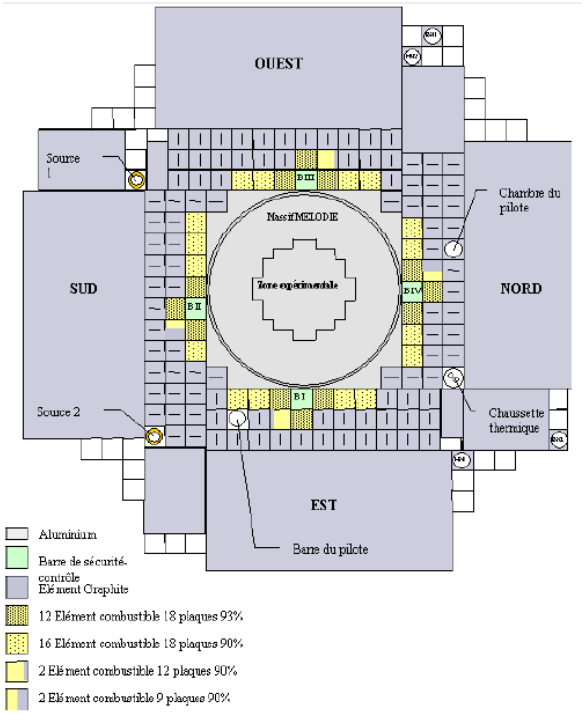

Figure 3.6: MINERVE driver zone showing the fuel, graphite reflector (Element Graphite) and test zone within the solid aluminium block (Massif MELODIE) (Blanchet 2006; 107).

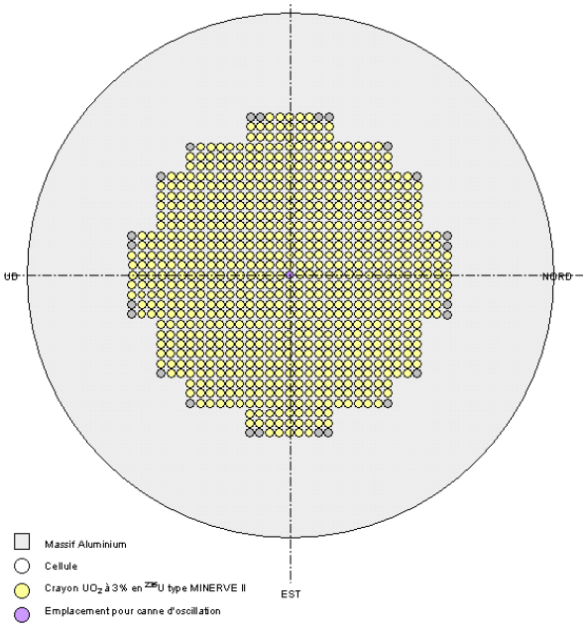

Figure 3.7: The solid aluminium block (Massif MELODIE), central TLD irradiation location and fuel pins in the MINERVE experimental zone MELODY IV R1-UO2 (Blanchet 2006; 108).

Simplified core model

Full core calculations are computationally expensive, so homogenized materials of each reactor core were used to determine the mean free path of a 1 MeV photon (the average prompt photon energy). This mean free path was then taken into account to define a small TRIPOLI model of the fuel geometry with reflective surrounding surfaces, which was thought to be representative of the cores, with respect to photons. These simplified models were used to conduct parametric studies - such as sensitivity analyses and to determine the relative contributions of different isotopes or neutron reactions to the gamma total dose (Blanchet 2006; 166).

Calculation of total dose

The formula used to calculate the total absorbed TLD dose was (Blanchet *et al.* 2008; 736):

$$D_{\mathrm{tot,calc}} = \frac{Tf_{\mathrm{exp}}}{Tf_{\mathrm{calc}}} \left[(K\gamma_{\mathrm{air}}^{\mathrm{P}} + K\gamma_{\mathrm{air}}^{\mathrm{D}}) \cdot \left(\frac{ED^{\mathrm{reac}}}{K\gamma_{\mathrm{air}}^{\mathrm{reac}}} \frac{K\gamma_{\mathrm{air}}^{\mathrm{calib}}}{ED^{\mathrm{calib}}} \right) + D_{\mathrm{n}} \right], \tag{3.10}$$

where D_n is the TLD neutron dose calculated with TRIPOLI4, and adjusted with energy-dependent factors which account for the sensitivities of the TLD to neutrons; the prompt and delayed gamma exposures at the TLD locations are $(K\gamma_{\mathrm{air}}^{\mathrm{P}})$ and $(K\gamma_{\mathrm{air}}^{\mathrm{D}})$, respectively; $\frac{Tf_{\mathrm{exp}}}{Tf_{\mathrm{calc}}}$ the power normalization factor; $\frac{ED^{\mathrm{reac}}}{K\gamma_{\mathrm{air}}^{\mathrm{reac}}}$ the calibration cavity correction factor.

Thus the TLD energy deposition was not calculated directly, only the exposure, which was then translated into absorbed TLD energy with the cavity correction factor.

Calculating prompt gamma dose

To calculate the prompt gamma dose, a full-core model was constructed in TRIPOLI4 using the ENDF/B-VI/R4 library. The code was used in CRITICALITY mode to transport neutron-γ in a coupled manner, with fuel compositions having zero burnup (Blanchet 2006; 168). During such a simulation, all neutron sources (including delayed) are included, as are gammas from prompt fission, neutron capture and inelastic neutron scattering (Blanchet *et al.* 2008; 736). This TRIPOLI4 model calculated both the gamma spectrum and the exposure (in units of Kerma of air) at the location of the TLD, $K\gamma_{air}^{P}$ (Blanchet 2006; 161).

The exposure was calculated using track length estimate tallies (this is the DEPOSITED_ENERGY score in TRIPOLI, which is equivalent to the F6 tally in MCNP).

A photon cutoff energy of 100 keV was used in both EOLE and MINERVE to save on processing time; Figure 9.10 of Blanchet's thesis shows that the contribution from <100 keV gammas is negligible, and thus this energy cutoff is acceptable (Blanchet 2006; 169).

Figure 3.8 shows the resulting spectra at central TLD locations; it was determined that the prompt gamma spectrum was not spatially-dependent, only that the intensity of the spectrum decreased with proximity to the core periphery (Blanchet 2006; 169).

The model of the MOX EOLE core determined that neutrons and gammas from ^{239}Pu, ^{240}Pu, ^{241}Pu, ^{235}U and ^{238}U provide 95% of the prompt gamma heating and 47% of the prompt gamma heating was the result of fission gammas from these isotopes (Blanchet *et al.* 2005; 5). In the UO_2 MINERVE model 81.5% of prompt gamma heating was attributed to ^{235}U and ^{238}U and fission provided 49% of prompt gamma heating (Blanchet *et al.* 2008). The average prompt gamma energy was determined to be 1.2 MeV in both reactor cores.

Calculating delayed gamma dose

Blanchet assumed the fission product inventory created prior to the TLD irradiation to be negligible; thus the associated delayed gamma dose was assumed negligible.

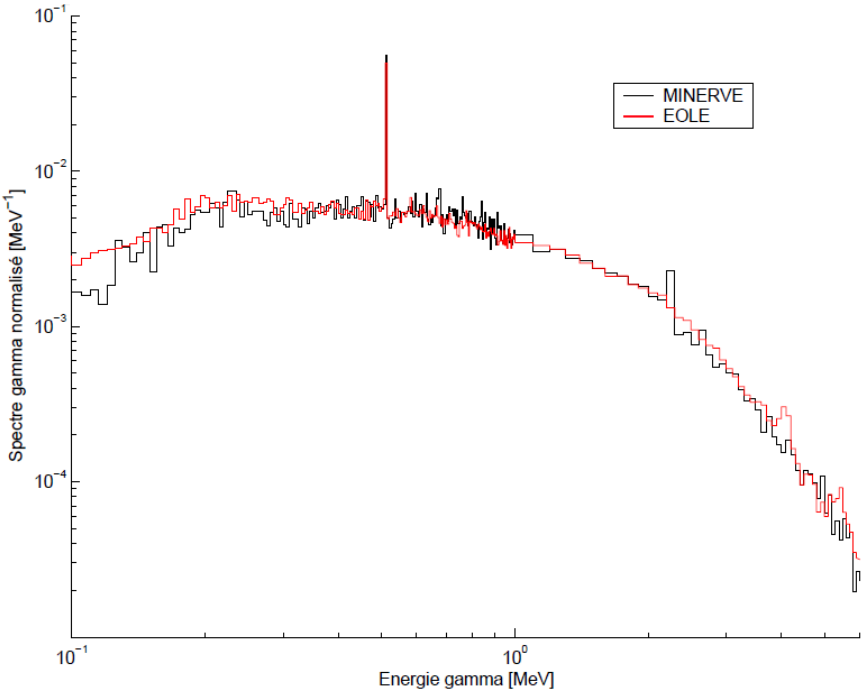

Figure 3.8: The TRIPOLI4 calculated, prompt gamma spectra from the center of the MOX EOLE and UO_2 MINERVE cores (Blanchet 2006; 170). Note the 511 keV peak from positron annihilations. Photons below 100 keV were not counted.

TRIPOLI4 does not inventory fission products nor consider the gammas which result from the decay of fission products. A mult-step process was employed to link TRIPOLI4 and PEPIN2 in a way which calculated the delayed gamma dose resulting from the fission products produced only during the TLD irradiation.

First, a model of TRIPOLI4 was used to calculate the neutron flux in each fuel pin. It was assumed that the neutron flux distribution within the reactor remained identical to the TRIPOLI4 results, varying only in magnitude, proportional to reactor power. The fission chamber signal recorded during the TLD irradiation was modelled by many discreet steps of constant power. The neutron flux at each power level was then passed to PEPIN2, with the initial fuel composition, to calculate the delayed gamma source term at each time point of the discritized grid, in each fuel element of the simplified core model (Blanchet 2006; 178,193). Analytically, the decay gamma intensity in each fuel segment is expressed as (Blanchet *et al.* 2008; 737):

$$D(E_\gamma, t) = \sum_{i}^{allFP} \lambda_i N^i(t) \bar{E}^i_\gamma d^i(E_\gamma), \tag{3.11}$$

where:

$D(E_\gamma, t)$ = the delayed gamma source of energy $\bar{E}^i_\gamma$ at time t for all isotopes i
$N^i(t)$ = the time-dependent fission product inventory of each fission product i
λ_i = the fission product decay constant from JEF2
$\bar{E}^i_\gamma$ = the average gamma ray energy within $\mathrm{d}^i(E_\gamma)$
$\mathrm{d}^i(E_\gamma)$ = normalized delayed gamma ray spectrum of nuclide i per decay from JEF2.

The delayed gamma source terms of each fuel pin was distributed within the simplified core TRIPOLI4 model. Instead of defining the delayed gamma source in each fuel pin at each discretized time segment and calculating the TLD exposure from delayed gammas at each time point, a single delayed gamma source was developed by weighting the source terms by the time-integrated neutron flux (Blanchet 2006; Fig.9.18). Thus TRIPOLI4 calculated the integrated TLD exposure in a single defined-source photon transport calculation.

This method of defining delayed photon sources in each fuel pin of a TRIPOLI4 photon transport calculation was validated by defining the prompt ^{239}Pu spectra from ENDF/B-VI within each fuel pin of a TRIPOLI4 photon transport model, normalized to the power, and comparing the results to a full TRIPOLI4 neutron-gamma coupled model which allowed only the production of prompt ^{239}Pu gammas - the difference was only 0.88% (Blanchet 2006; 178).

The delayed gamma and the prompt gamma spectrum are compared in Figure 3.9. The average prompt gamma energy of ^{239}Pu and ^{235}U, as described by ENDF/B-VI, was calculated to be 0.87 MeV and 0.94 MeV, respectively; the mean delayed gamma of the same isotopes was 1.3 MeV and 1.57 MeV, as calculated at equilibrium using PEPIN2 with JEF2 (Blanchet 2006; 178).

The calculated delayed gamma fraction of the total gamma dose was found to be 29% in the case of the 15 W, 10 minute irradiation in EOLE and 24.4% for the 10 W, 20 minute irradiation in MINERVE; at equilibrium the delayed gamma contribution was calculated to be 32.2% in EOLE and 29% in MINERVE (Blanchet 2006; 195). Additionally, it was observed that both prompt and delayed spectrum shapes are similar after attenuation through the core, thus Blanchet proposed that a simple approximation to total gamma exposure would be increasing the intensity of the prompt gamma ray spectrum by the delayed gamma portion of the total gamma dose (Blanchet *et al.* 2008; 737). This method has been adoped by analysts within Service du RJH (SRJH) to account for the delayed gamma dose, however they have assumed the delayed gamma dose is 30% of total (a number given by Blanchet in (Blanchet *et al.* 2008; 737) but not explicitly in his thesis) and scale the prompt gamma dose by 1/0.7 ; section 3.6.1 discusses this process further.

Blanchet also used the simplified core model to investigate the delayed gamma source. The delayed sources were calculated for each fuel pin in the model, at each time point, using PEPIN2. The prompt and delayed gamma exposure rates calculated over the approach to full power, the constant

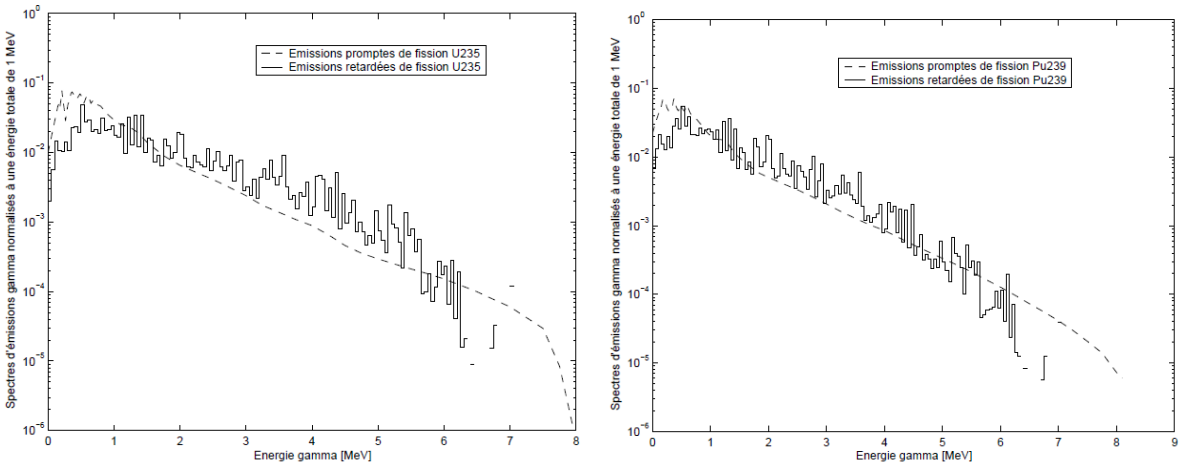

Figure 3.9: Comparison between the prompt (from ENDF/B-VI) and delayed gamma spectra (calculated with PEPIN2 at equilibrium) for the EOLE reactor (Blanchet 2006; 180).

10 minute irradiation and shutdown are shown for each discretized time point in Figure 3.10(L). Figure 3.10(R) shows the same calculated values, summed and normalized to the raw fission chamber signal obtained during the TLD irradiation.

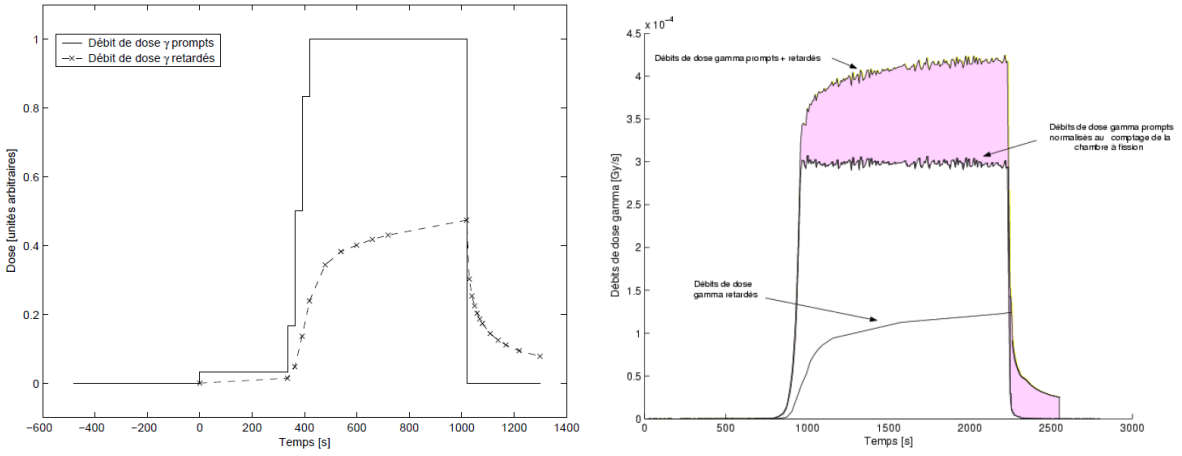

Figure 3.10: (L) The calculated prompt and delayed gamma doses; (R) prompt and delayed gamma doses normalized to the fission chamber's signal (Blanchet 2006).

Figure 3.11(L) shows the fission products which contribute the most to the TLD dose over the constant 10 minute irradiation, normalized to the maximum dose rate experienced just before shutdown; Figure 3.11(R) shows the most significant fission products after shutdown.

Comparisons between experimental and calculated dose

After correcting the TLD signal for the energy deposited by neutrons, Blanchet found the total calculated gamma energy dose compares to MINERVE experimental values with an average ratio of $\frac{C}{E} = 0.72 \pm 15\%(2\sigma)$. The EOLE ratio was $\frac{C}{E} = 0.75 \pm 15\%(2\sigma)$ (Blanchet *et al.* 2005; 740).

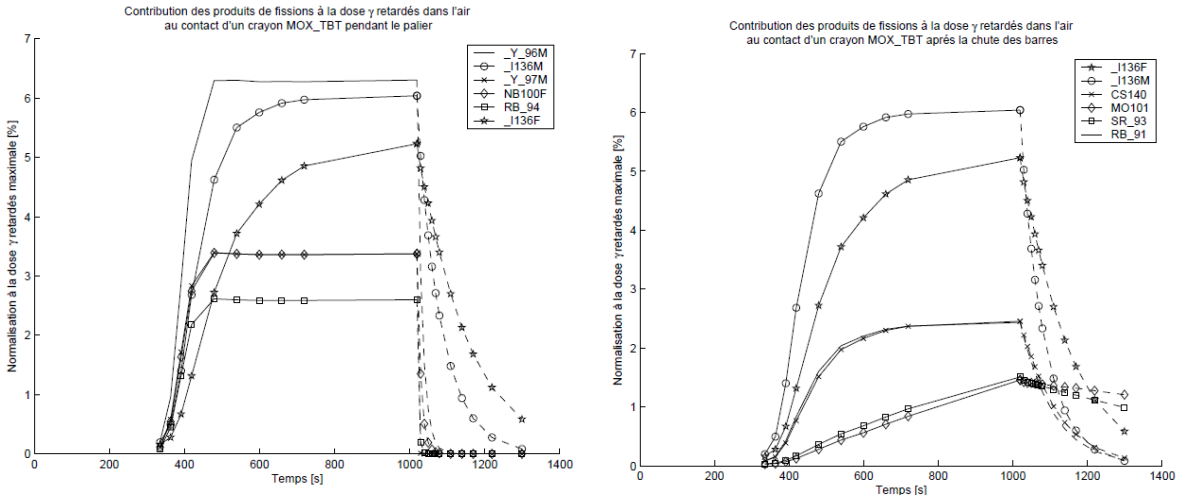

Figure 3.11: The fission products which contribute the most delayed gamma dose during the constant 10 minute irradiation (L) and following shutdown (R); as calculated with PEPIN2 using the MOX fuel compositions (Blanchet 2006).

Blanchet speculated the systematic bias was a result of errors in the nuclear data libraries JEF2 and ENDFB-VI; specifically "...a lack of gamma ray emission data (Blanchet *et al.* 2008; 740)." Specifically addressing the methods used to model the delayed gamma dose, Blanchet commented "...the only biases imaginable would be by uncertainties or missing radioactive decay data" in the JEF2 library used by PEPIN2 (Blanchet 2006; 193).

Dose comparisons between ionization chamber and calculation

During the TLD irradiation in MINERVE, the signal from a miniature in-core ionization chamber was also recorded. These intruments respond to both neutron and gamma flux, so the signal interpretation requires a calibration factor for both particles. Large uncertainties existed on the neutron calibration factor, thus the signal was not useful for measuring absolute gamma doses while MINERVE was near full power. The signal was considered valuable after shutdown when the dose from delayed neutrons was considered negligible, allowing for a measurement of the delayed gamma exposure (Blanchet 2006; 204).

Figure 3.12 shows the ionization chamber signal during the TLD irradiation in comparision to calculated exposures. The integrated measured delayed gamma component compared to the integrated calculated value with a fraction of $\frac{C}{E} = 0.88 \pm 11\%$ $(2\sigma)(Blanchet et\ al.\ 2008; 740)$.

Summary of ADAPh calculational method

The general features of the scheme employed by Blanchet to calculate in-core gamma energy deposition are as follows:

- the empirical data used for comparison to calculations were collected in a low power reactor
- the entire core geometry was constructed within a Monte Carlo model
- two Monte Carlo simulation steps were used to determine gamma exposure at the in-core location of interest: i) one criticality calculation to determine the prompt gamma exposure using coupled neutrons-gammas, ii) one defined source gamma transport calculation to determine the delayed gamma exposure

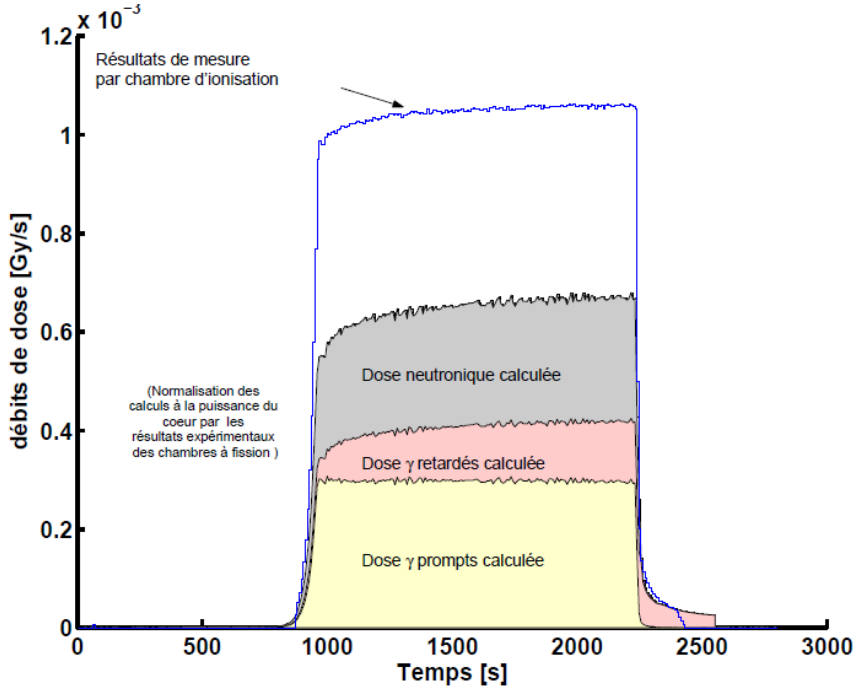

Figure 3.12: Comparison between the the ionization chamber signal (top) and calculated doses (which were normalized to the fission chamber signal) (Blanchet 2006; 204).

- the dose from decay of legacy fission products (fission products created prior to TLD irradiation) were subtracted from the measured dose and not considered at all in the calculation of dose; only the dose resulting from the decay of fission products created during the dosimeter irradiation were considered by calculations

- integrated delayed gamma source terms were calculated for each fuel element with a point-depletion code; the entire absorbed delayed gamma exposure was then calculated with a defined-source TRIPOLI4 gamma-transport calculation

- the calculated gamma exposure from all sources, was converted into absorbed energy using a calculated cavity correction factor

3.5.2 Amharrak's work following ADAPh

Since the ADAPh program showed an underprediction of the gamma heating calculations (with respect to the MINERVE in-core TLD measurements) by $\approx 25\% \pm 15\%(2\sigma)$ various efforts were made to reduce this systemic bias by both Blanchet and Amharrak. Blanchet attributed the C/E bias mostly to deficiencies in the nuclear data and employed a Bayesian method of adjusting nuclear data to search for improvements (Blanchet *et al.* 2008). Amharrak focused on the ADAPh TLD experimental process and looked to reduce the TLD experimental uncertainties (Amharrak *et al.* 2012; 2).

Amharrak conducted TLD and OSLD measurements on the same MINERVE core configuration (R1-UO2) as the ADAPh program; however, many changes were made to the TLD measurement and calibration procedures to reduce experimental variance. Amharrak's work was conducted in anticipation of the AMMON experimental program, which was to follow as the next comprehensive

JHR test program at Cadarache (Amharrak *et al.* 2012; 12). As a result, the AMMON experiment fully implemented the TLD measurement and calibration techniques developed by Amharrak et al.

Comparisons between experimental and calculated dose

Amharrak utilized the same methods of calculation as Blanchet for both the prompt and delayed gamma doses (Amharrak *et al.* 2012; 2) and calculated the delayed gamma component to be 32% of the total absorbed gamma dose (Amharrak *et al.* 2011; 5) (Amharrak *et al.* 2012; 8).

The efforts expended to increase the experimental repeatability resulted in an improvement between calculated and experimental values: $\frac{C}{E} = 1.05 \pm 5.3\%(2\sigma)$ for the TLDs and $\frac{C}{E} = 0.96 \pm 7.0\%(2\sigma)$ for the OSLDs (Amharrak *et al.* 2011; 8); the bias was thought to be a result of the TLD and OSLD neutron corrections and "...all the uncertainties related to calculations of cavity corrections (Amharrak *et al.* 2011; 9)."

3.5.3 The PERLE program

The PERLE (Programme dEtude de Réflecteur Lourd dans EOLE Heavy Reflector in EOLE Study Program) was an experimental program designed to validate the analytical tools of Areva's EPR. The neutronic characteristics of the EPR's heavy steel reflector were investigated (Cacuci 2010; 2074). Simultaneously, the gamma heating within the modelled reflector was measured with TLDs and the results were compared to calculated gamma heating values.

In the course of analysis of the PERLE program, Ravaux developed a method of calculation which was an evolution from the ADAPh methods. Specifically, the use of an in-core cavity correction factor was abandoned for the use of a single full-core TRIPOLI4 calculation which directly calculated the energy deposited within the TLDs (Ravaux 2013). This method was subsequently used by the AMMON program, and is fully described in the following section.

The results Ravaux obtained were $\frac{C-E}{E} = 1 \pm 12\%(2\sigma)$ within the steel reflector. Larger uncertianties of $\frac{C-E}{E} = -2 \pm 24\%(2\sigma)$ resulted near water channels of the steel reflector where it was surprisingly observed that heating increased by 15% (Amharrak *et al.* 2014; 62).

3.5.4 The AMMON program

Although the ADAPh and PERLE experimental programs aided in the development of neutronic and gamma heating analytical methods, these experimental programs didn't conduct measurements in the presence of unique JHR characteristics, such as a high moderator to fuel volume ratio or 27% ^{235}U fuel. The AMMON experimental program was designed specifically to provide JHR-relevant experimental data by employing JHR fuel assemblies. AMMON was therefore expected to serve as a valuable emperical reference for the JHR design (Klein *et al.* 2009; 2). Additionally, AMMON experimental values will aid in the verification and validation of the calculational scheme of HORUS3D (Blanchet *et al.* 2005; 10).

Experimental measurements commenced in 2011 in the EOLE facility (at CEA Cadarache) and ran until the end of 2012. Analysis of the experimental results and comparisons with calculated data will validate the calculational tools and build confidence in the validity of the claims of the JHR safety report.

The AMMON experimental program was composed of a number of different EOLE core configurations. While no two configurations were the same, the general arrangement for all configurations was as follows: a driver zone made of hundreds of UO_2 PWR fuel pins (3.7% ^{235}U enrichment) surrounding a solid aluminum hexagonal test section, which contained seven holes to accomodate JHR fuel assemblies, or other components.

The driver and experimental zones each had dedicated, temperature regulated, light-water coolant circuits. This allowed for the addition of boron to the experimental zone, if required, and gave the

ability to determine the reactivity dependency on coolant water temperature for each zone (Blanchet *et al.* 2005; 4).

The lattice pitch of the UO_2 pins was designed to produce the same neutron spectrum as the experimental zone (Blanchet *et al.* 2005; 3).

The AMMON reference configuration

The reference configuration (AMMON-Ref) was the first AMMON configuration assembled in the EOLE reactor. It consisted of a solid aluminum hexagonal block with holes to receive seven JHR fuel assemblies and six 3.1 cm diameter aluminium spacers. These structures formed the experimental zone. Surrounding the experimental zone was the driver zone made of 623 UO_2 fuel pins, 80 cm long. These pins were clad in Zircaloy-4 with a stainless steel overcladding. 20 safety shutdown rods were positioned above the core during operation, and their empty guide tubes were also in the driver zone. A cross-section of the configuration's vertical mid-plane is shown in Figure 3.13.

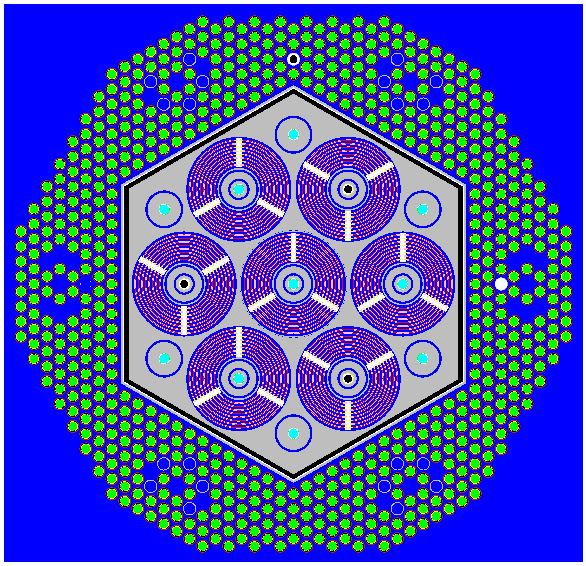

Figure 3.13: Cross-section of AMMON Reference configuration - plot made with the TRIPOLI model. The control rod is shown on the left, within the driver zone.

The AMMON program used the experimental and calibration methods published by Amharrak. During the dosimeter irradiation in AMMON-Ref, two fillers and two JHR assemblies were all loaded with 5 stacked aluminum pillboxes each. Each pillbox contained a PTL717, TLD400 and OSLD. The pillboxes were stacked such that they centered about the reactor's vertical midplane. Figure 3.14 shows the central aluminum rod which was removed from two assemblies in the AMMON-Ref configuration to accomodate five stacked dosimeter pillboxes.

The EOLE reactor was held at a full power of 10 W for 10 minutes, following a relatively quick approach to power. The reactor was then made subcritical, the dosimeters were removed and their responses recorded. To account for the dose received during the approach to 10 W, another set of dosimeters were identically placed and irradiated through only the approach to power - the resulting dosimeter signals were subtracted from the signal of the fully irradiated dosimeters.

A set of TLD's were also placed in the core a few hours prior to the full power irradiation to measure the background dose from the decay of legacy fission products; these measurements predicted the gamma heating from these sources to be equal to 3% of the dose measured during the full power irradiation (Vaglio-Gaudard *et al.* 2014; 577).

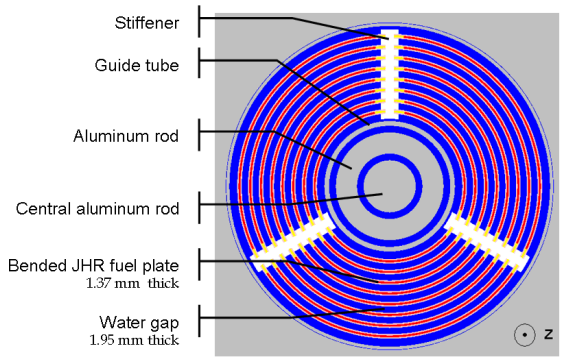

Figure 3.14: The solid aluminum central rod of the JHR (Vaglio-Gaudard *et al.* 2014).

AMMON analysis

CEA staff has published the results of a few important AMMON-Ref analyses: one on neutronic parameters and another on nuclear heating.

The first publication details how the TRIPOLI4.7 code and JEFF3.1.1 European library were used to construct a neutronic model of AMMON-Ref to calculate k and the core's power distribution (Vaglio-Gaudard *et al.* 2012). The resulting comparisons between the calculated and measured reactivity showed a difference between the two of C-E=376 $\pm$ 290(1σ)pcm and calculation of the power distribution of the JHR assemblies was within 1.1% of reality.

The second publication details the analytical methods the CEA employed to calculate gamma heating in the AMMON-Ref core and a comparison to experimental values (Vaglio-Gaudard *et al.* 2014). The calculational methods employed were influenced greatly by the analytical experiences of the other CEA experimental programs, ADAPh and PERL. TRIPOLI4.8.1 and JEFF3.1.1 were used to construct a model of the entire AMMON-Ref core. Every component of both the driver and experimental zone was faithfully described in TRIPOLI, including the very thin layers (1 mm) of the OSLD material. Each fuel plate and fuel pin, was modelled in axial segments to allow for the scoring of volumetric fission rates. In total, tens of thousands of volumes were described in the TRIPOLI model.

Using this TRIPOLI4.8.1 core model, two runs of TRIPOLI were required to calculate the prompt and delayed gamma energy deposition. For each simualtion, the CEA utilized their substantial computational resources to process billions of histories in each case to reduce statistical uncertainties to acceptable magnitudes. Each step is described in detail below.

Calculating prompt gamma dose

To calculate the prompt gamma dose resulting from fission and neutron capture a TRIPOLI4.8.1 simulation in CRITICALITY mode tracked four particles (neutrons, photons, electrons and positrons) in a coupled manner while scoring the energy deposition within the TLD and OSLD volumes with DEPOSITED_ENERGY scores for each particle. Additionally, the fission rate in each axial segment of each fuel pin and plate was scored for later use in the delayed gamma dose calculation. During this simulation neutrons were the primary sampled particles - the other particles appear in the TRIPOLI model in such simulations as the result of neutron interactions with materials.

Tracking four types of particles, in such a complicated geometry, over so many cycles is a huge computational task. To reduce this burden, electron and positron transport was restricted in all volumes to particles with energies above 2 MeV, except those which immediately surrounded the TLD/OSLD dosimeters. The closer volumes were thought to be more relevant to energy deposition

within the TLD/OSLDs, compared to more distant volumes, because the expected distance of travel of electrons and positrons is usually small. In the close volumes, e^- and e^+ were tracked over a full energy range of 25 keV and 20 MeV. The 2 MeV restrictive limit was thought to be a reasonable simplification because low-energy charged particles typically travel very small distances.

Neutrons between $1{\times}10^{-11}$ and 20 MeV and photons between 1 kev and 20 MeV were transported in the entire geometry.

The size of the volumes surrounding the dosimeters (where the full spectrum of charged particle transport was permitted) was carefully defined. Making these volumes too small would underestimate the energy deposited within the dosimeters, and making them too large would increase the processing burden. A volume of 1.5 cm on all sides of the TLD/OSLDs was permitted for the full spectrum transportation; as a check on the validity of using 1.5 cm, the Katz and Penfold formula predicts 2 MeV electrons would have a maximum range of 0.4 cm in aluminum (Vaglio-Gaudard *et al.* 2014; 578).

All scores were normalized to the EOLE reactor power, using the experimental fluxes measured with Au and Ni foils which were irradiated during the AMMON-Ref experiment.

Accounting for Al activation

As is discussed in the next section, a number of simplifying assumptions were made before determining the delayed gamma sources. One of these assumptions, is the discounting of gammas from neutron activation products - with the exception of Al. ^{27}Al (the only naturally occurring isotope of the reactor's structural Al material) is present in large quantities within the AMMON-Ref core and furthermore the half life of ^{28}Al is 2.241 minutes, which makes it non-negligible compared to the experimental duration.

To account for ^{28}Al decay, the ^{27}Al JEFF3.1.1 evaluation file was modified to promptly emit the 1.78 MeV photon upon neutron radiative capture (Vaglio-Gaudard *et al.* 2014; 581). This change allowed the gammas produced neutron capture of ^{27}Al to be incorporated into the prompt gamma TRIPOLI4 calculation.

Calculating delayed gamma dose

PEPIN-2 and the JEFF2.2 library were used to describe the delayed gamma spectrum which results from the decay of fission products. This photon spectrum was then used to define a delayed photon source in each of the fuel plates and pins during a TRIPOLI4.8.1 simulation in SHIELDING mode. This TRIPOLI4 calculation tracked three particles (photons, electrons and positrons) in a coupled manner while scoring the energy deposition within the TLD and OSLD volumes with DEPOSITED_ENERGY scores for each particle.

For simplicity, the authors assumed all fissions were ^{235}U; this was thought to be a reasonable approximation because TRIPOLI predicted only 0.7% of the fissions to be from ^{238}U. Additionally, the following simplifying assumptions were thought to be reasonable since the EOLE power was so low that neutron flux reached only $\approx 10^9$ n/cm^2/s (Vaglio-Gaudard *et al.* 2014; 580):

1. the fission product inventory prior to commencement of the TLD/OSLD irradiation was nil
2. the plutonium inventory was considered non-existant at all times
3. neutron activation was considered negligible (with the exception of ^{28}Al which is discussed in the previous section)
4. the burnup of fission products was neglected.

The third assumption refers to the longer lived activation products, which may decay by emitting a gamma - the much more important prompt gamma emissions resulting from neutron capture were taken into account in the first TRIPOLI4 simulation of the prompt gamma sources.

PEPIN-2 describes the photon emissions in 94 energy groups and has the ability to calculate the fission product gamma emission spectrum at any given time following a single ^{235}U fission. The dosimeters remained within the core for 15 minutes, 10 of these were full power core operation and the remaining 5 was the time required for experimentalists to remove the dosimeters from the core following shutdown. PEPIN-2 was used to calculate an average delayed gamma spectrum over these 15 minutes.

The PEPIN-2 output defined the gamma source function $S_\gamma(g,t)$ resulting from the fission of a single ^{235}U atom, equal to the average number of gammas emitted from each energy group g at each time step t, where $t = 0$s is the time of fission, for all g and t; the source terms are unitless.

One fission was assumed to occur per second over a 10 minute duration (the time the reactor was at full-power during TLD irradiation) and the resulting $S_\gamma(g,t)$ functions were summed for each of the 94 energy groups at each t in the interval $0 \leq t \leq 15$ minutes (the total in-core duration of the TLDs). The superimposed sources were scaled by the fission rate to obtain the total gamma source for each g and t. A spectra was defined as an isotropic fixed photon source in each of the axial fuel plate and pin segments, normalized to the relative fission rates scored in each of these segments in the first TRIPOLI calculation.

Within the fuel pins and plates, the delayed gamma source was defined uniformly radially for simplicity, which contrasts to reality which likely shows a greater fission rate at outer radii compared to the inner fuel volumes. This was thought to be an acceptable approximation.

As discussed in the introduction of this section, a TRIPOLI4.8.1 simulation was run in SHIELDING mode with three coupled particles, using the same energy boundaries and e^-, e^+ restricted volumes as used in the prompt gamma TRIPOLI simulation; the energy deposition scores were normalized to the EOLE reactor power using the same Au and Ni foils as were used in the prompt gamma simulation.

Results of calculations

No numerical variance reduction techniques were used in the TRIPOLI simulations, but the AMMON-Ref core symmetry was leveraged to reduce the Monte Carlo uncertainties. Within the TRIPOLI model, pillboxes were placed within the peripheral JHR fuel assemblies which are identical, by symmetry, to the one which actually contained the dosimeters during the experiment; this effectively increased the number of scoring particle histories which passed through the small volumes of interest, and thus reduced the statistical uncertainties; for the same purpose and by the same justification, dosimeters were added to all six fillers within the TRIPOLI model.

The stack of 5 pillboxes had a small overall height in comparison to the active core height of 60 cm, and the neutron flux is essentially constant over the pillbox stack. Therefore the dose of each dosimeter type was assumed to be equal to the average value of the 5 dosimeters, for both the experiment and calculation.

Figure 3.15 shows the prompt photon production in several core materials. The peak at 511 keV is the result of e^- and e^+ annihilation and the others result from neutron inelastic scattering or capture in specific core materials (Vaglio-Gaudard *et al.* 2014; 4). Figure 3.16 shows the prompt and delayed gamma spectra within the central JHR assembly are predicted by the TRIPOLI calculations to be quite similar. In this calculation, 25% of the total photon absorbed dose is thought to be from delayed gammas (Vaglio-Gaudard *et al.* 2014; 580); it must be remembered that this does not include the dose from fission products which were in the reactor prior to the TLD irradiation, which was measured to be 3% of the total dose (see section 3.6.1).

The calculated prompt energy deposition predicted 60% of the prompt gamma dose was from fission photons, about 33% from radiative neutron capture and 7% from inelastic neutron scatter.

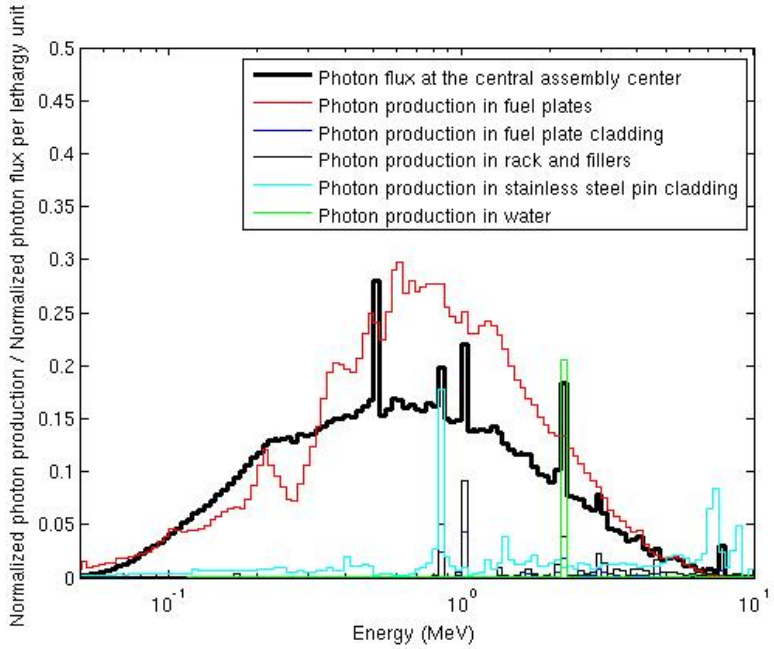

Figure 3.15: Prompt photon production in several core materials (Vaglio-Gaudard *et al.* 2014).

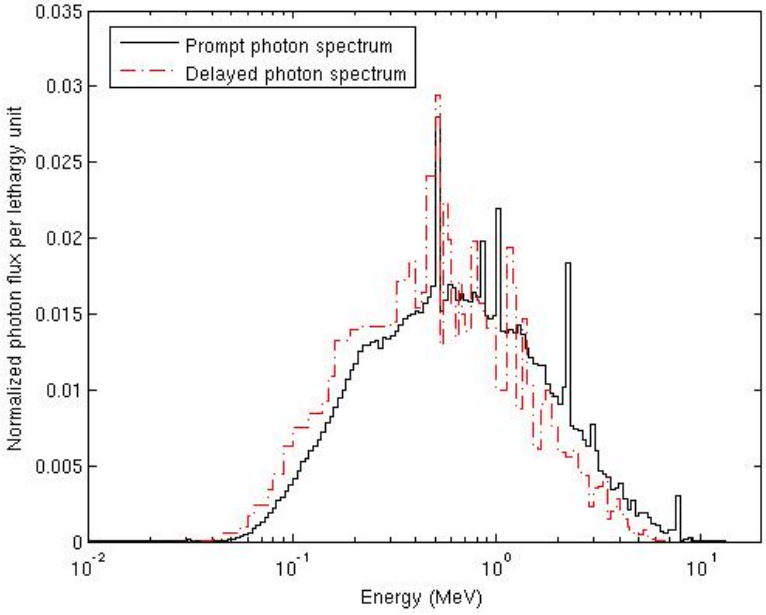

Figure 3.16: Delayed photon flux generated by ^{235}U fission at the center of the central JHR assembly in comparison to the prompt spectrum at the same location (Vaglio-Gaudard *et al.* 2014).

Comparisons between experimental and calculated dose

In comparision to the experimental doses, the calculated doses were smaller; the average (C-E)/E value of all dosimeter placements within the AMMON-Ref core was $-8\pm4.5\%$. The authors speculate the deviation results from underestimation of the JEFF3.1.1 prompt photon emission and/or ^{27}Al neutron interaction cross sections - the calculations have shown to be very sensitive to ^{27}Al reaction data.

The authors of the analysis suspected the underestimation of gamma heating to be the result of "...underestimation of the global energy released by delayed photons," and "...the missing photon spectra," of the prompt photon emission data in JEFF3.1.1 (Vaglio-Gaudard *et al.* 2014; 582).

Summary

The methods used to calculate the AMMON-Ref gamma energy deposition generally follows that employed by Ravaux and Bernard in the interpretation of the PERLE experiment (Ravaux 2013). The prominent feature of this method is the calculation of both the prompt and delayed gamma doses by dedicated Monte Carlo simulations of the entire core (one Monte Carlo calculation for prompt and another for delayed) while energy deposition scores are tabulated on each of the dosimeter volumes.

This method contrasts to that employed by Blanchet and Amharrak (the ADAPh method), which requires a "two-step" process where a full-core Monte Carlo simulation only determines the gamma spectrum at the dosimeters' in-core location. This spectrum is then used to define a fixed source for a second, Monte Carlo simulation of only the dosimeters and the immediate surroundings to calculate the absorbed dose (Blanchet 2006, Amharrak *et al.* 2012).

Although the AMMON-Ref method requires far more computational resources, it faithfully modelled the entire experimental geometry which accounts for the heterogeneous geometry surrounding the dosimeters and eliminates the need to calculate an in-core "cavity correction factor" (which is required in the ADAPh method when calculating energy deposition in dosimeters).

To summarize, the salient features of the AMMON-Ref calculations are:

- the entire core geometry is constructed within a Monte Carlo code
- one Monte Carlo simulation determines k and transports n, p, e^-, e^+ in a coupled manner to calculate the prompt gamma energy deposition
- one Monte Carlo simulation using a defined delayed gamma source in each fuel volume transports p, e^-, e^+ in a coupled manner to calculate the delayed gamma deposition
- the dose from decay of legacy fission products was subtracted from the measured dose and not considered at all in the calculation of dose; the dose from the pre-test fission product inventory was measured in a dedicated TLD/OSLD experiment and subtracted from the dosimeter signal accumulated over the full-power test
- a point depletion code is used to determine an average delayed gamma spectrum prepresentative of the time of dosimeter irradiation
- transport of e^- and e^+ restricted to volumes of most importance to save on processing
- ^{235}U was assumed to be the only fissioning actinide
- gammas from neutron activation are considered negligible for all isotopes except ^{27}Al
- decay energy from α and β radiation assumed to have been deposited locally
- the burnup of fission products considered negligible.

3.5.5 Delayed gamma heating fraction in the CEA's low-power experiments

It is interesting to note the differing estimates of the fraction of total gamma heating attributable to the delayed gammas. The following table gives a summary:

Program/P.I. Fuel	Reactor Percentage
ADAPh ^{235}U	MINERVE 24.4%
ADAPh MOX	EOLE 29%
Amharrak ^{235}U	MINERVE 32%
AMMON ^{235}U	EOLE 25%

Table 3.1: Estimates of percentages of gamma heating caused by delayed gammas.

All these values were calculated using methods summarized in previous sections. The variance of these values in Table 3.1 are a result of the differences in the following parameters:

- the in-core residency time of the dosimeter
- the time the reactors were at full power
- the dominant fissioning isotope
- the reactor construction and composition.

3.5.6 Differences between low and high power reactor analysis

The methods used to calculate gamma heating in the ADAPh, PERLE and AMMON programs may not be applicable to material-testing or power-generating reactors for the following reasons:

- full power in each experiment was very low, resulting in low neutron fluxes; these low fluxes induce relatively small amounts of activation and fission product neutron absorption
- the experiments operated at full power for short periods, preventing fission product inventories from building or reaching equilibrium; Blanchet estimated the delayed gamma contribution would have been 32.2% in EOLE and 29% in MINERVE at equilibrium (Blanchet 2006; 195)
- all calculations of delayed gamma dosimetry are integrated, with no method to easily calculate the delayed gamma flux or dose.

3.6 Calculations of gamma heating in high-power reactors

This section reviews the methods others have used to calculate the gamma heating within the core of high-power reactors.

3.6.1 Gamma heating calculations of SRJH

The division SRJH (Service Réacteur Jules Horowitz) is the administrative branch of the CEA responsible for the operation of the JHR. SRJH also conducts physics analysis and is responsible for the design of in-core experimental devices. These tasks frequently require the calculation of gamma heating within various in-core components; the results of such calculations are often used with heat transfer codes to predict the temperatures of the components under investigation.

The methods used by SRJH to calculate gamma energy deposition are based upon the methods used in the analysis of the PERLE and AMMON programs and the results of the Blanchet and Amharrak investigations. As in PERLE and AMMON, a complete 3D core and reflector TRIPOLI4 model is used with coupled neutrons and gammas to calculate the prompt gamma energy deposition in objects of interest.

Known biases, uncertainties and delayed gammas are included by scaling the prompt dose term according to the findings of CEA experimental programs. As discussed previously, between the TLDs and OLSDs, the worst comparision of calculation to experiment by Amharrak was $\frac{C}{E} = 0.96 \pm 7.0\%(2\sigma)$. The ADAPh evaluation estimated the delayed gamma component to be 30% of the total gamma heating in one estimate and SRJH has assumed this to be an appropriate estimate of the delayed gamma dose in RJH, at all locations, within the equilibrium core. The prompt gamma dose D_p is scaled to estimate the total gamma heating as (CEA 2016):

$$D_p = \frac{D_p}{0.7} * 1.04 \pm 7.0\%(2\sigma). \tag{3.12}$$

Once the the AMMON analysis is completed, this formula will likely be updated with the resulting bias and uncertainty.

This is clearly a simplistic method, although it may be conservative and be valuable for safety analysis.

3.6.2 The CIRANO program

Lüthi developed a calculational algorithm for determining gamma heating in fast reactors and implemented the scheme in the ERANOS (European Reactor Analysis Optimized System) code package (Lüthi *et al.* 2001). This method was intended for use in the analysis of gamma heating in plutonium burning reactors (possibly a redesigned Superphoenix core), and to replace the VASCO-1 method which lacked certain basic data and which had a deficient calculational algorithm. Lüthi compared his new calculational method against experimental data obtained from the CIRANO critical assembly, which was designed to examine plutonium burning physics.

The developed methodology has multiple steps. First, the S_N transport code BISTRO (from the ERANOS code package) is used to calculated $\Phi_{i,g}$, the 33 group neutron flux, over each spatial mesh i and neutron energy group g. Then the neutron flux is used to calculate the gamma source term S_{i,g_γ}, where g_γ is the gamma energy group index. The gamma flux Φ_{i,g_γ} can then be calculated in each spatial mesh with BISTRO, while treating each S_{i,g_γ} as a fixed external source. The gamma heating is then calculated in each mesh.

The gamma source term is determined once $\Phi_{i,g}$ is known with the following equations:

$$S_{i,g_\gamma} = \sum_g \sum_e \sum_X \Phi_{i,g} \cdot N_{i,e} \cdot \sigma_{i,e,X,g} \cdot Q_{\gamma,e,X,g} \cdot \chi_{e,X}(g \to g_\gamma) \tag{3.13}$$

where $N_{i,e}$ is the atomic density of isotope e, $\sigma_{i,e,X,g}$ is the effective (self-shielded) microscopic cross section for isotope e, reaction type X and neutron energy group g. $Q_{\gamma,e,X,g}$ is the average total energy emitted by an interaction of type X of a neutron in group g with isotope e. $\chi_{e,X}(g \to g_\gamma)$ is the gamma emission spectrum for the corresponding reaction which, by definition, needs to satisfy:

$$\sum_{g_\gamma} \chi_{e,X}(g \to g_\gamma) \cdot \bar{E}_{g_\gamma} = 1. \tag{3.14}$$

The gamma heating is simply calculated:

$$H_{\gamma,i} = \sum_{g_\gamma} \sum_{e} \Phi_{i,g_\gamma} \cdot N_{i,e} \cdot K_{\gamma,e,g_\gamma} \tag{3.15}$$

where K_{γ,e,g_γ} is what Lüthi calls the gamma KERMA (units of eV $\cdot$ barn) for isotope e.
The neutron heating is similarily calculated:

$$H_{n,i} = \sum_{g} \sum_{e} \sum X\Phi_{i,g} \cdot N_{i,e} \cdot \sigma_{i,e,X,g} \cdot k_{n,e,X,g} \tag{3.16}$$

where $k_{n,e,X,g}$ is what Lüthi calls reduced neutron KERMA in neutron reaction type X. Reduced neutron KERMA has units of eV and is simply related to K_γ by the following relation (Lüthi 1998):

$$K_{\gamma,i,e,g_\gamma} = \sum_{X} \sigma_{i,e,X,g_\gamma} \cdot k_{n,e,X,g_\gamma}. \tag{3.17}$$

The above equations demonstrate the dependency of Lüthi's method upon a variety of nuclear data. Lüthi completed a significant amount of work to compile the required nuclear data from ENDF sources: ENDF/B, JEFF and JENDL libraries. The data was compiled and processed with NJOY into an appropriate format for calculations.

As a simplifying assumption, this calculational method assumes the fission product's decay rate to be equal to rate of production. This eliminated the burden of making the fission product inventory time-dependent, in exchange for what Lüthi estimated was a minor error (Lüthi 1998).

This calculational method was compared against the CIRANO experiment at CEA's MASURCA facility which was dedicated to investigating plutonium burning cores (Lüthi 1998). TLDs were used to measure the absolute gamma heating rates in both the PuO_2/UO_2 fueled cores and steel/sodium reflector regions. The calculation values underpredicted the experimental values by 10% in the core region and 12% in the reflector region. Lüthi attributed the discrepency to low energies of the fission gammas and low capture cross sections, in the nuclear data (Lüthi *et al.* 2001).

3.6.3 Gamma heating calculations in OSIRIS

OSIRIS is a 70 MW light water, open-pool MTR at CEA Saclay which uses 20% enriched plate-type silicide fuel, arranged on a 7x8 grid (CEA 2013). The core contains 6 control elements, 7 beryllium reflectors and 5 experimental elements.

Two publications have outlined two different methods for calculating gamma heating in OSIRIS. In 2001 Lee outlined a method which used a full-core TRIPOLI4 model to calculate the gamma heating in an irradiation facility adjacent to the core, and compared the results against calorimetric measurements (Lee *et al.* 2001). Another 2012 article by Malouch uses the same methods (Malouch 2012). The later work uses a geometrically complete TRIPOLI4 model, with the newest version of the software employing energy deposition scores.

Lee et al. 2001

Lee was motivated by the poor results of a previously-used method. The former method used the diffusion code DAIXY to calculate neutron flux and the gamma-ray production source from neutron capture; the point-kernal code MERCURE-5 then calculated the gamma transport and the gamma heating in a geometry of interest. This method produced acceptable results unless large irradiation targets were placed in the irradiation facility - large targets tend to distort the neutron flux in

a manner diffusion codes can't predict. Additonally, the point-kernal method is not condusive to modelling complex irradiation facility geometries. The new gamma heating methodology was used as an analysis tool to evaluate the possible need for additional cooling of the irradiation facility.

Lee's method used a full TRIPOLI4 model of the reactor core and adjacent irradiation facility; only reactor components thought to be irrelevant were omitted. The diffusion code DAIXY calculated a "power map" of the historical core, which was then employed by the TRIPOLI-4 model; presumably, TRIPOLI4 was not operated in CRITICITY mode but instead the power map was used in TRIPOLI-4 (Lee *et al.* 2001; 149). Greater geometrical core details of regions close to the experimental facility were considered by DAIXY. TRIPOLI-4 was then run in coupled neutron-gamma mode to calculate the neutron and gamma fluxes in the calorimeter cells. The KERMA factors of graphite were used to determine deposited energy from the calculated fluxes; these factors were developed with the Argonne National Lab code MACK-IV and ENDF/B libraries.

200 MeV and 2.432 neutrons per fission were used to scale the TRIPOLI4 scores to 65 MWth; power was assumed to be constant.

Some simplifying assumptions made include: a) assuming fresh fuel compositions; and b) neglecting Ni and Hf absorber materials in some fuel components.

DARWIN was used to generate a gamma spectra and intensity resulting from fission product decay, assuming 90,000 MWd/t burnup; presumably, this also assumed constant power.

The calculated energy deposition scores were compared to differential calorimeter data; the calculated values tended to be 25% lower than the corresponding measured data. While it is not possible to determine the cause of the systematic difference by reading the published paper, at least some of it may be a result of the method not including the delayed gammas which result from activation of core material. Lee et al. observed the delayed fission gammas were softer than the prompt fission and capture gammas, and as a result were easier to shield.

Today Lee's method may be considered outdated since a diffusion code is no longer required to determine a "power map" and TRIPOLI4 and MCNP6 both now have energy-deposition scores/tallies, eliminating the need for MACK-IV to calculate the KERMA factors.

Malouch 2012

With the goal of determining the heating of in-core experimental devices a two-step full core TRIPOLI4.7 model was developed, shown schematically in Figure 3.17; a TRIPOLI4 criticality calculation with coupled neutrons-gammas accounted for prompt-gammas resulting from neutron reactions, and another defined-gamma-source calculation to transport the delayed fission gammas.

The TRIPOLI4 model was geometrically complete, without simplifications. The fuel material descriptions were developed with burn-up calculations using the APOLLO-2 lattice code, and a OSIRIS-specific diffusion code with ENDF-3.1.1. The resulting fuel composition corresponds to a single moment in the reactor fuel cycle. PEPIN-2 then provided delayed gamma spectra and intensity for this moment in time. Gamma cross sections from EPDL-97 were used within TRIPOLI4 for photon transport and energy deposition.

The calculated energy deposition scores were compared to differential calorimeter data; the calculated values ranged between 15 and 25% lower than the measured data, depending on the vertical core position. Malouch considered this comparison acceptable for proof of concept.

Notice that although PEPIN-2 was used to specifically determine the delayed fission gamma sources, the reference doesn't give specific details of how these sources were calculated; presumably, like the prompt gammas, the delayed fission gamma sources were described for one moment in reactor time. There is also no indication of if or how delayed activation gammas may have been included in the scheme.

Malouch provided Table 3.2 showing the fraction of total nuclear heating resulting from prompt gammas and neutrons, as calculated by the critical simulation, and the delayed gammas, as calculated with the fixed-source simulation.

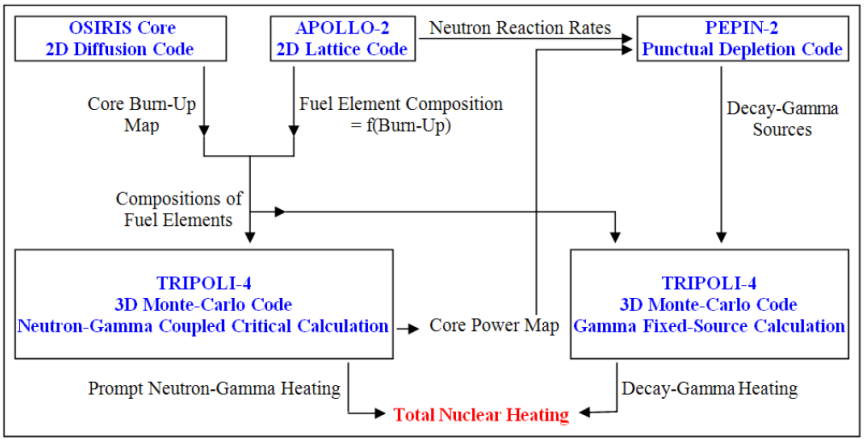

Figure 3.17: Nuclear heating scheme developed for the OSIRIS reactor (Malouch 2012; 5).

Material	Gamma heating Critical simulation	Neutron Heating Critical simulation	Gamma Heating Fixed-source simulation	Total
Graphite	62%	17%	21%	100%
Aluminum	73%	4%	23%	100%
Iron	76%	1%	23%	100%
Zirconium	74%	1%	25%	100%
Tungsten	78%	0%	22%	100%

Table 3.2: Relative heating from all sources as calculated in different materials (Malouch 2012; 10).

3.7 Summary

Of all the calculational methods reviewed, none are able to describe gamma heating as a function of time in a high-power reactor; low-power reactor analyses have only calculated integrated delayed gamma doses, and high-power reactor analyses have only attempted to caclulate gamma heating at a single moment. Therefore, to help engineers predict the time-dependent behavior of the in-core energy deposition, this thesis aims to measure and describe the time-dependent in-core component of nuclear heating caused by delayed gammas and incorporate this description into a new time-dependent nuclear-heating model.

Chapter 4

New models of time-dependent in-core gamma heating

A literature review has shown mature Monte Carlo codes are capable of calculating in-core prompt-gamma heating. However, the in-core delayed gamma heating cannot easily be calculated with TRIPOLI4 or MCNP6 because fission products and activated isotopes are not tracked. Efforts to couple burnup codes to Monte Carlo codes have been documented but remain difficult to implement and the schemes are often reactor-specific. MCNP6 does have the capability to track active isotopes, but is not yet implemented in a way which allows the modeling of a full reactor core. Even when Monte Carlo codes become capable of modeling these processes in an entire core, the computational processing will be great and modeling the entire reactor's geometry will still require great effort. New ideas are now required to describe the total time-dependent in-core photon heating in a simpler manner.

This chapter proposes two new methods to describe time and position-dependent in-core prompt and delayed gamma heating. The first is a generalized equation called the nuclear heating equation, describing the time-dependent nuclear heating in a volume of interest, within an arbitrary geometry. Such an equation is valuable to symbolically represent the relevant physical processes and abstract them from any specific geometry, reaction or material; similar to the way the neutron transport equation represents and formalizes neutron transport. The second is an extension of the neutron point-kinetics equations to include the gamma population in a coupling of the neutron and gamma populations.

Although the proposed nuclear heating equation is thought to be a valuable method to employ in simple geometries, the coupled neutron-gamma point-kinetics equations should be an easier method to apply to complex critical geometries such as reactor cores.

4.1 The nuclear heating equation

4.1.1 Considerations

As reviewed in previous chapters, the physical quantities and processes relevant to in-core nuclear heating are:

1. the intensity of all incident radiation
2. the rate of nuclear reactions induced by all radiation
3. the intensity of all prompt radiation resulting from nuclear reactions

4. the intensity of all delayed radiation resulting from nuclear reactions
5. the transport of all radiation through the geometry of interest
6. the conversion of radiation into other species during transport
7. the power deposited, by all radiation types, in the volume of interest.

Monte Carlo radiation transport codes, such as MCNP6 and TRIPOLI4, are capable of modelling all the above mechanisms when combined with the capabilities of other codes.

MCNP6 is capable of modelling all the above processes alone in a single run, except the intensity of all delayed radiation. Although MCNP6's ACT card does have the capability to describe a time-integrated description of heating resulting from delayed radiation, an integration is fundamentally incapable of describing time-dependent gamma heating. The ACT card also does not work with the KCODE mode, which is the prefered mode for almost all studies of critical assemblies.

Given the great capacity of MCNP6 and TRIPOLI4, the nuclear heating equation derived in this chapter specifically considers these codes and employs variables which they are capable of calculating.

The nuclear heating equation has been derived useing the variable notation of Duderstadt when possible (Duderstadt and Hamilton 1976).

4.1.2 Generalized geometry

As a physical basis for the equation, consider a collection of arbitrary geometries as shown in Figure 4.1, collectively refered to as V, divided into differential volumes d^3r. The geometry V can be a multiplying medium, or not, and can be either irradiated by an external source of neutrons and/or gammas, or contain a neutron and/or gamma source, or both.

The nuclear heating equation is meant to describe the nuclear heating, $H_G(\vec{r}_G, t)$ (in units of MeV/s), within a target volume G at position $\vec{r}_G$ and time, t; the target volume is shown as a cylinder in Figure 4.1.

4.1.3 Nuclear heating

The total nuclear heating at position $\vec{r}_G$ is simply equal to a sum of heating caused by all external (ES) and internal (IS) radiation sources. This simple formulation is complicated by the fact that internal radiation sources, which result from internal nuclear reactions, are comprised of prompt (P) and delayed(D) particles:

$$H(\vec{r}_G, t) = H_{\mathrm{ES}}(\vec{r}_G, t) + H_{\mathrm{IS}}(\vec{r}_G, t) \tag{4.1}$$

$$H(\vec{r}_G, t) = H_{\mathrm{ES}}(\vec{r}_G, t) + H_{\mathrm{P}}(\vec{r}_G, t) + H_{\mathrm{D}}(\vec{r}_G, t) \tag{4.2}$$

Monte Carlo codes (MCNP6 and TRIPOLI4) can calculate the position-dependent scalar neutron flux $\phi(\vec{r}, E, t)$ for most geometries and sources; therefore $\phi(\vec{r}, E, t)$ is treated as the independent variable in the derivation of the nuclear heating equation. This allows all radiation source terms to be written as a function of $\phi(\vec{r}, E, t)$, which is convenient in reactor physics since essentially all energy and radiation come from neutron-induced nuclear reactions.

$\phi(\vec{r}, E, t)$ is usually calculated by Monte Carlo codes while assuming long-term physical changes such as burn-up are insignificant, and these codes emit delayed neutrons at the same time as prompt neutrons (X-5 Monte Carlo Team 2008; 2-52). Therefore, calculated values of $\phi(\vec{r}, E, t)$ consider both prompt and delayed neutrons and these values are time dependent in direct proportion to the reactor power $P(t)$ in the case of a critical geometry, or the external neutron source $S(t)$ in the case of a sub-critical geometry.

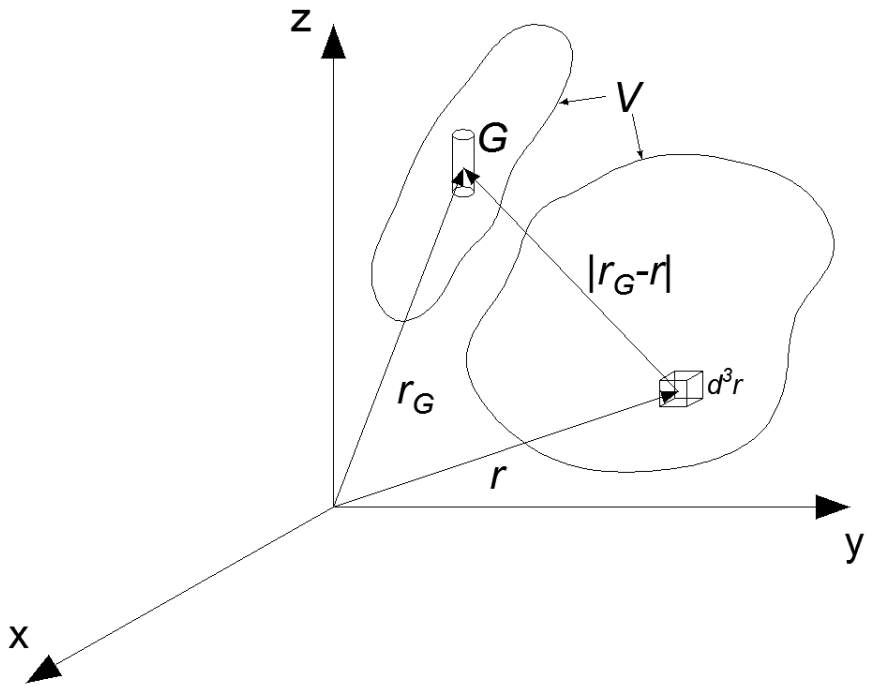

Figure 4.1: Arbitrary geometry V, described by discrete volumes d^3r, with an arbitrary volume of interest G.

4.1.4 The mean transported energy

Consider a quantity called (in this report) the mean transported energy.

The heating of volume G as a result of radiation of energy E' being emitted by the differential volume d^3r, depends on the ability of each emission to travel along the path $|\vec{r}_G - \vec{r}|$ shown in Figure 4.1. Radiation transport is a stochastic process, so even in the case of a source emitting directly towards G, each emission from d^3r will follow a different path and only some emissions will arrive at volume G. The mean transported energy is defined as the average energy deposited in G by an emission of energy E' after being emitted by d^3r.

Since the mean transported energy is dependent upon the physical properties (such as the geometry and materials along the path $|\vec{r}_G - \vec{r}|$) and the properties of the emitted particle (such as the particle species and particle energy E'), the mean transported energy is noted as $E(|\vec{r}_G - \vec{r}|, E')$; it is also dependent upon the directional biasing of the emitted particles, but this is not explicitly noted since all emissions considered in this thesis are isotropic.

The variable $E(|\vec{r}_G - \vec{r}|, E')$ is not written with explicit notation specifying the species of the associated particle, even though it is species-dependent.

4.1.5 External sources

In reactor physics, external sources usually emit neutrons and are often made of Be and an alpha-emitter. Refer to the entire source volume as W (not shown in Figure 4.1) and assume its per-unit-volume source $S_W(\vec{r}, E', t)$ to be a known quantity, in units of $1/\mathrm{cm}^3\mathrm{s}$; the source of volume d^3r is then $S(\vec{r}, E', t) = S_W(\vec{r}, E', t)\mathrm{d}^3r$.

The power[1] emitted (in units of MeV/s) by the source is simply the energy of the emitted particle,

[1]The term "intensity" is often used to describe the power of a radiation source but "intensity" is usually expressed

E', multiplied by the total source strength:

$$P_{\mathrm{ES}}(\vec{r}, E', t) = E' S(\vec{r}, E', t) = E' S_W(\vec{r}, E', t)\mathrm{d}^3 r. \tag{4.3}$$

4.1.6 Heating by external sources

The expression of $P_{\mathrm{ES}}(\vec{r}, E', t)$ can be converted into an expression of the heating of volume G by the external source, by replacing the energy of the emitted particle, E', with the mean transported energy:

$$H_{\mathrm{ES}}(\vec{r}_G, \vec{r}, E', t) = E(|\vec{r}_G - \vec{r}|, E') S_W(\vec{r}, E', t)\mathrm{d}^3 r. \tag{4.4}$$

Assuming the source has a continuous energy spectrum, the total energy deposited within G at time t is then:

$$H_{\mathrm{ES}}(\vec{r}_G, \vec{r}, t) = \int_{E'} E(|\vec{r}_G - \vec{r}|, E') S_W(\vec{r}, E', t)\mathrm{d}E'\mathrm{d}^3 r. \tag{4.5}$$

and integrating over all $\mathrm{d}^3 r$ volumes in W finishes the expression:

$$H_{\mathrm{ES}}(\vec{r}_G, t) = \int_W \int_{E'} E(|\vec{r}_G - \vec{r}|, E') S_W(\vec{r}, E', t)\mathrm{d}E'\mathrm{d}^3 r. \tag{4.6}$$

4.1.7 Probability and yield

This section summarizes the concepts of probability and yield within the context of radiation production by nuclear reactions. The notation used in this section is employed in the nuclear heating equation.

For any given reaction rate F the particle source can be written as $S(E') = \phi\Sigma py$ with the following units:

$S(E')$	$=$	ϕ	Σ	p	y	
$\frac{\text{particles}}{\text{cm}^3\text{s}}$	$=$	$\frac{\text{neutron}}{\text{cm}^2\text{s}}$	$\frac{1}{\text{cm}}$	$\frac{\text{emission}}{\text{reaction}}$	$\frac{\text{particles}}{\text{emission}}$	(implicit units)
$\frac{1}{\text{cm}^3\text{s}}$	$=$	$\frac{1}{\text{cm}^2\text{s}}$	$\frac{1}{\text{cm}}$	unitless	unitless	(explicit units)

where:
$S(E')$ = the source of prompt particles of energy E'
p = probability of an emission per reaction
y = average yield of prompt particles of energy E' per emission
$F = \phi\Sigma$ = reaction rate; units $1/\text{cm}^3\text{s}$
$Y = py$ = average yield of prompt particles of energy E' per nuclear reaction.

For most nuclei, when considering particles specifically of energy E', only a single particle is released following certain nuclear reactions meaning $y = 1$ and $Y = p$. Since many nuclear data libraries present p, p is used in the nuclear heating equation in place of Y.

in units of energy per unit time per unit area (Turner 2008); the term "power" is used here because the quantity being considered is in units of energy per unit time.

4.1.8 Prompt sources

Particle sources from within V are easily represented symbolically if we recognize that in reactor physics, all internal-source particles and the energy they carry result from nuclear reactions induced by neutrons, either directly or indirectly. So any expression describing particle sources must be based upon neutron-induced reaction rates.

For a single particle of energy E' promptly emitted following nuclear reaction r, the source of prompt radiations resulting from isotope i within the differential volume d^3r is:

$$S^i_{r\mathrm{P}}(\vec{r}, E', t) = p^i_{r\mathrm{P}}\Sigma^i_r(\vec{r})\phi(\vec{r}, t)\mathrm{d}^3r \tag{4.7}$$

where:

$S^i_{r\mathrm{P}}(\vec{r}, E', t)$ = rate of prompt radiations of energy E' emitted by reaction r at time t; in units of 1/s

$\Sigma^i_r(\vec{r})$ = average macroscopic r cross section over the volume of interest; 1/cm

$\phi(\vec{r}, t)$ = average scalar neutron flux over the volume of interest at time t; 1/cm^{2}s.

The term $p^i_{r\mathrm{P}}$ is the probability of emitting a prompt particle of energy E' from isotope i per reaction r, and is unitless.

The prompt power released by reaction r by target isotope i can be determined if the energy of the promptly emitted particle, $E'^i_{r\mathrm{P}}$ (in units of MeV), is known:

$$P^i_{r\mathrm{P}}(\vec{r}, E', t) = E'^i_{r\mathrm{P}}S^i_r(\vec{r}, E', t) \tag{4.8}$$

$$P^i_{r\mathrm{P}}(\vec{r}, E', t) = E'^i_{r\mathrm{P}}p^i_{r\mathrm{P}}\Sigma^i_r(\vec{r})\phi(\vec{r}, t)\mathrm{d}^3r \tag{4.9}$$

It is known that each isotope i may emit multiple particles per reaction r, each with a specific energy and probability of emission, so the product $E'^i_{r\mathrm{P}}p^i_{r\mathrm{P}}$ should be replaced with a discrete sum $\sum_e({}^eE'^i_{r\mathrm{P}})({}^ep^i_{r\mathrm{P}})$ over each e prompt particle which may be released; this sum is also equal to the average energy yield (in units of MeV) per reaction r:

$$P^i_{r\mathrm{P}}(\vec{r}, t) = \sum_e({}^eE'^i_{r\mathrm{P}})({}^ep^i_{r\mathrm{P}})\Sigma^i_r(\vec{r})\phi(\vec{r}, t)\mathrm{d}^3r = \Sigma^i_r(\vec{r})\phi(\vec{r}, t)\sum_e({}^eE'^i_{r\mathrm{P}})({}^ep^i_{r\mathrm{P}})\mathrm{d}^3r \tag{4.10}$$

where:

${}^eE'^i_{r\mathrm{P}}$ = energy of prompt particle e; MeV

${}^ep^i_{r\mathrm{P}}$ = probability of emitting a particle of energy ${}^eE'$ from isotope i, per reaction; unitless.

4.1.9 Heating by prompt sources

The heating of volume G by the prompt particles emitted by isotope i induced by reaction r from the differential volume d^3r is obtained by replacing the energy of the emitted particle, ${}^eE'^i_{r\mathrm{P}}$ with the mean transported energy:

$$H^i_{r\mathrm{P}}(\vec{r}_G, \vec{r}, t) = \Sigma^i_r(\vec{r})\phi(\vec{r}, t)\sum_e({}^eE(|\vec{r}_G - \vec{r}|, E'))({}^ep^i_{r\mathrm{P}})\mathrm{d}^3r. \tag{4.11}$$

The same reaction in all other isotopes also contribute:

$$H_{r\mathrm{P}}(\vec{r}_G, \vec{r}, t) = \phi(\vec{r}, t)\sum_i\Sigma^i_r(\vec{r})\sum_e({}^eE(|\vec{r}_G - \vec{r}|, E'))({}^ep^i_{r\mathrm{P}})\mathrm{d}^3r, \tag{4.12}$$

as do prompt radiation resulting from all other nuclear reactions:

$$H_{\mathrm{P}}(\vec{r}_G, \vec{r}, t) = \phi(\vec{r}, t)\sum_r\sum_i\Sigma^i_r(\vec{r})\sum_e({}^eE(|\vec{r}_G - \vec{r}|, E'))({}^ep^i_{r\mathrm{P}})\mathrm{d}^3r. \tag{4.13}$$

Finally, all reactions and all isotopes, from all d^3r volumes in V sum to provide an expression of $H_{\mathrm{P}}(\vec{r}_G, t)$:

$$H_{\mathrm{P}}(\vec{r}_G, t) = \int_V \phi(\vec{r}, t) \sum_r \sum_i \Sigma_r^i(\vec{r}) \sum_e ({}^eE(|\vec{r}_G - \vec{r}|, E'))({}^ep_{r\mathrm{P}}^i)\mathrm{d}^3r. \tag{4.14}$$

4.1.10 Delayed particle sources

Following nuclear reaction r in the volume d^3r by isotope i and the emission of one or more prompt particles, isotope i may be converted into the isotope or fragment j; this nuclear reaction is often noted as $i(\mathrm{n}, g)j$, where g is the particle emitted following the reaction induced by the neutron n. Isotope j may be radioactive and emit a delayed particle during decay which may contribute to nuclear heating of G.

To describe the resulting delayed source it is important to know $N^j(\vec{r}, t)$, the atomic concentration of j, since the source is proportional to the product $\lambda^j N^j(\vec{r}, t)$, where λ^j is j's decay constant. The Bateman equations will have to be employed to express $N^j(\vec{r}, t)$ as a rate of change:

$$\frac{\mathrm{d}N^j(\vec{r}, t)}{\mathrm{d}t} = \sum_r \sum_i p_{rj}^i \sigma_r^i(\vec{r})\phi(\vec{r}, t)N^i(\vec{r}, t) + \sum_i p_j^i \lambda^i N^i(\vec{r}, t) - \sum_r \sigma_r^j(\vec{r})\phi(\vec{r}, t)N^j(\vec{r}, t) - \lambda^j N^j(\vec{r}, t) \tag{4.15}$$

where:
j = index of all radioactive isotopes
i = index of all stable and radioactive isotopes, except the specific j under consideration
p_{rj}^i = probability of producing isotope j by nuclear reaction r in isotope i; unitless
$\sum_r \sum_i p_{rj}^i \sigma_r^i(\vec{r})\phi(\vec{r}, t)N^i(\vec{r}, t)\mathrm{d}^3r$ = production rate of j by all reactions in all isotopes in volume d^3r; in units of 1/s
p_j^i = probability of isotope i decaying into isotope j
$\sum_i p_j^i \lambda^i N^i(\vec{r}, t)\mathrm{d}^3r$ = production rate of j by decay of all other isotopes in volume d^3r
$\sum_r \sigma_r^j(\vec{r})\phi(\vec{r}, t)N^j(\vec{r}, t)\mathrm{d}^3r$ = destruction rate of j by all reactions
$\lambda^j N^j(\vec{r}, t)$ = destruction rate of j by decay.

In the development of the nuclear heating equation a very general expression is desired, which would allow $\phi(\vec{r}, t)$ to vary arbitrarily with time. Thus $\phi(\vec{r}, t)$ can't be expressed as a fixed function of t, such as $\phi(\vec{r}, t) = t^2$, but as a set of data. Analytical methods cannot then be used to resolve the differential equation (4.15) into a universal expression for $N^j(\vec{r}, t)$, the nuclear heating equation will have to be coupled with the differential equation and will be solvable only with numerical techniques.

Assuming equation (4.15) has been solved for $N^j(\vec{r}, t)$, the delayed source of particles of energy E' from isotope j within the differential volume d^3r can be defined as:

$$S_{r\mathrm{D}}^j(\vec{r}_G, \vec{r}, E', t) = p^j \lambda^j N^j(\vec{r}, t)\mathrm{d}^3r \tag{4.16}$$

where p^j is the probability of a particle emission per decay.

The emitted power (in units of MeV/s) is obtained, as with the prompt source, with the discrete sum $\sum_e ({}^eE_{r\mathrm{D}}'^j)({}^ep_{r\mathrm{D}}^j)$ over each e delayed particle which may be released per decay:

$$P_{r\mathrm{D}}^j(\vec{r}_G, \vec{r}, t) = \sum_e ({}^eE_{r\mathrm{D}}'^j)({}^ep_{r\mathrm{D}}^j)\lambda^j N^j(\vec{r}, t)\mathrm{d}^3r. \tag{4.17}$$

4.1.11 Heating by delayed sources

Using the mean transported energy again, the heating of volume G by delayed particles emitted by isotope j induced by reaction r from the differential volume d^3r is:

$$H^j_{r\mathrm{D}}(\vec{r}_G,\vec{r},t)=\sum_e({}^eE(|\vec{r}_G-\vec{r}|,E'))({}^ep^j_{r\mathrm{D}})\lambda^jN^j(\vec{r},t)\mathrm{d}^3r. \tag{4.18}$$

When including the other radioactive isotopes in d^3r the equation becomes:

$$H_{r\mathrm{D}}(\vec{r}_G,\vec{r},t)=\sum_j\lambda^jN^j(\vec{r},t)\sum_e({}^eE(|\vec{r}_G-\vec{r}|,E'))({}^ep^j_{r\mathrm{D}})\mathrm{d}^3r \tag{4.19}$$

Integrating over all differential volumes d^3r in V gives an expression for total delayed nuclear heating:

$$H_{r\mathrm{D}}(\vec{r}_G,t)=\int_V\sum_j\lambda^jN^j(\vec{r},t)\sum_e({}^eE(|\vec{r}_G-\vec{r}|,E'))({}^ep^j_{r\mathrm{D}})\mathrm{d}^3r. \tag{4.20}$$

4.1.12 The nuclear heating equation

The whole equation is then completed by placing equations (4.6), (4.14) and (4.20) in equation (4.2):

$$\begin{aligned}H(\vec{r}_G,t)&=\int_W\int_{E'}E(|\vec{r}_G-\vec{r}|,E')S_W(\vec{r},E',t)\mathrm{d}E'\mathrm{d}^3r+\int_V\phi(\vec{r},t)\sum_r\sum_i\Sigma^i_r(\vec{r})\sum_e({}^eE(|\vec{r}_G-\vec{r}|,E'))({}^ep^i_{r\mathrm{P}})\mathrm{d}^3r\\&+\int_V\sum_j\lambda^jN^j(\vec{r},t)\sum_e({}^eE(|\vec{r}_G-\vec{r}|,E'))({}^ep^j_{r\mathrm{D}})\mathrm{d}^3r\end{aligned} \tag{4.21}$$

$$\frac{\mathrm{d}N^j(\vec{r},t)}{\mathrm{d}t}=\sum_r\sum_i p^i_{rj}\sigma^i_r(\vec{r})\phi(\vec{r},t)N^i(\vec{r},t)+\sum_i p^i_j\lambda^iN^i(\vec{r},t)-\sum_r\sigma^j_r(\vec{r})\phi(\vec{r},t)N^j(\vec{r},t)-\lambda^jN^j(\vec{r},t)$$

$$\vdots$$

one instance of the ODE for each j

For convenience, the variables are defined again here:
t = time
j = index of all radioactive isotopes
i = index of all stable and radioactive isotopes, except the specific j under consideration
e = index of (prompt or delayed) particle released following reaction r
E' = energy of the particle emitted following a reaction
$\vec{r}$ = position vector of the differential volume d^3r
$\vec{r}_G$ = position vector of target volume G
ϕ = scalar flux of incident particles
$N(\vec{r},t)$ = atomic concentration at position $\vec{r}$ at time t
λ = decay constant
$\Sigma^i_r(\vec{r})$ = average macroscopic r cross section over volume d^3r
$E(|\vec{r}_G-\vec{r}|,E')$ = mean transported energy
${}^ep^i_{r\mathrm{P}}$ = probability of emitting prompt (P) particle e of energy E' from isotope i per reaction r
p^i_{rj} = probability of producing isotope j by nuclear reaction r in isotope i; unitless
p^i_j = probability of isotope i decaying into isotope j.

Notice equation (4.21) has no sub or super-script variable to index the incident particle species considered. In this thesis, equation (4.21) will be applied in the context of incident neutrons, with

ϕ representing scalar neutron flux and Σ representing the neutron macroscopic cross section, but another instance of equation (4.21) could consider protons, or neutrinos or muons. The user simply must decide which incident particles are relevant.

4.1.13 Using the heating equation

Although equation (4.21) may appear intractable, it is only a symbolic representation of multiple quantities which are easily understood. Furthermore, it has been derived specifically with the capabilities of Monte Carlo codes such as MCNP6 and TRIPOLI4 in mind.

Calculating the mean transported energy

The mean transported energy $E(|\vec{r}_G - \vec{r}|, E')$ is a quantity which can be calculated by Monte Carlo codes. Each $E(|\vec{r}_G - \vec{r}|, E')$ term is equal to the MCNP6 (or TRIPOLI4) energy deposition tally/score over the volume G obtained from a model of V with a source of E' particles emitted by d^3r. In MCNP6 the tally can be multiplied by the mass of G to convert the MCNP6 tally units of MeV/g to units of MeV. Explicitly, $E(|\vec{r}_G - \vec{r}|, E')$ has units of energy; implicitly, all energy deposition tallies/scores calculated by MCNP6/TRIPOLI4 have units of energy per source particle.

These Monte Carlo energy deposition tallies/scores are defined as the mean energy deposition of a sample group of particles (X-5 Monte Carlo Team 2008; 2-109). This quantity is universally used to obtain a predicted heating of volume G, by multiplying by the tally/score by the rate of emitted source particles in the physical system. The same quantity is used in this thesis to represent the average energy deposited by a single particle; since this quantity is used in an unusual way in a new equation it is described with a new label, mean transported energy, within this thesis.

Note that $E(|\vec{r}_G - \vec{r}|, E')$, as calculated by MCNP6 and TRIPOLI4, differs depending upon the number of particle species being transported in the Monte Carlo model; for example, the calculated energy deposition by photons is greater when electrons and positrons are not transported. The user must decide which species must be transported, depending on the application.

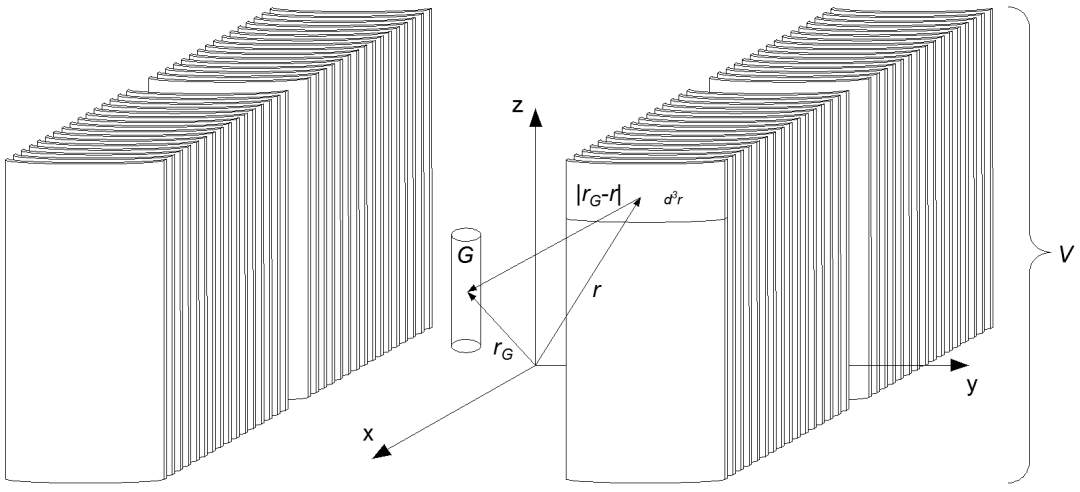

Figure 4.2: The volume V describing a stylized reactor core made of plate fuel, with each fuel plate divided into discrete volumes.

Energy binning

Calculating many ${}^{e}E(|\vec{r}_G - \vec{r}|, E')$ terms for each $\vec{r}$ and E' could easily become a large task for a complex geometry with many source gammas. To simplify the process it is proposed the source gammas be binned into the 25 energy bin structure presented in Appendix D.2. This will limit the number of $E(|\vec{r}_G - \vec{r}|, E'_g)$ terms for each $\vec{r}$ to 25 and should accurately represent the gamma sources.

While using the energy binning method, instead of calculating ${}^{e}E(|\vec{r}_G - \vec{r}|, E')$ terms for each e emission ${}^{k}E(|\vec{r}_G - \vec{r}|, E')$ is calculated for each energy bin; the bins are indexed by k. Calculating ${}^{k}E(|\vec{r}_G - \vec{r}|, E')$ with a Monte Carlo code requires defining a gamma source within $\vec{r}$ which samples energy E' uniformly between the energy boundaries of bin k.

In a solution of the nuclear heating equation employing the energy binning method, the probability of obtaining a gamma from energy bin k is:

$$ {}^{k}p = \sum_{e} ({}^{e}p) \tag{4.22}$$

where the summation considers only those emissions with ${}^{e}E'$ between the energy bin boundaries of bin k.

No optimization of the bin boundary locations has been conducted apart from the considerations discussed in Appendix D.1. Any optimization would be dependent upon geometry.

The nuclear heating equation applied to a reactor core

The nuclear heating equation could be used to describe the heating in a single volume G when V is an entire reactor core, as is stylistically presented in Figure 4.2. Each fuel plate could be sectioned axially (and/or radially) into volumes d^3r where $\phi(t)$ is assumed spatially constant; this proposal would require the calculation of $n \cdot p \cdot k \cdot g$ $E(|\vec{r}_G - \vec{r}|, E')$ terms, where n is the number of d^3r volumes, p the number of fuel plates, k the number of gamma energy groups and g the number of $\vec{r}_G$ locations under investigation. More volumes would be required if the coolant, structural members or control devices are deemed significant sources of gammas. This is a burden left to sophisticated programmers.

4.2 The coupled neutron and photon point kinetics (PPK) model

Although the proposed nuclear heating equation is thought to be a thorough representation of time-dependent nuclear heating, an easier method to employ in complex critical geometries is sought.

Considering the success of the neutronic point kinetics equations and the current difficulty associated with calculating the delayed gamma flux, this section proposes extending the neutron point kinetics equations to include photons.

To begin the derivation of the two-particle point kinetics model, the rate production of all gamma sources are written symbolically. These rates are then summed to produce a time-dependent description of the total gamma population in the core.

4.2.1 Review of the point reactor kinetics model

The point reactor kinetics model is derived from the one-speed diffusion equation and is employed often to describe the time behaviour of neutrons in a reactor. The diffusion equation for a homogeneous discrete volume d^3r is (Duderstadt and Hamilton 1976; 156):

$$ \frac{1}{\upsilon}\frac{\partial\phi(\vec{r},t)}{\partial t} - D\nabla^2\phi(\vec{r},t) + \Sigma_{\mathrm{a}}\phi(\vec{r},t) = \nu\Sigma_{\mathrm{f}}\phi(\vec{r},t). \tag{4.23}$$

The definition of $\phi(\vec{r},t)$ must be clear. $\phi(\vec{r},E,t)$ is the scalar flux of neutrons at energy E, it is defined as neutron density $N(E)$ in the discrete volume d^3r at position $\vec{r}$, multiplied by the neutron velocity $\upsilon(E)$ (Duderstadt and Hamilton 1976; 106). The scalar flux $\phi(\vec{r},t)$ in the one-speed diffusion equation is equal to the sum of the scalar flux of all neutrons at all energies in the discrete volume d^3r at position $\vec{r}$ at time t (Duderstadt and Hamilton 1976; 109):

$$\phi(\vec{r},t) = \int_0^\infty \phi(\vec{r},E,t)\mathrm{d}E. \tag{4.24}$$

The constants in equation (4.23), neutron velocity, υ, neutron diffusion coefficient, D, macroscopic absorption cross section, Σ_a and macroscopic fission cross section, Σ_f, are flux-weighted averages over each discrete volume d^3r, which are then volume-weighted over the entire reactor volume V (Duderstadt and Hamilton 1976; 290):

$$O = \frac{1}{\int_V \mathrm{d}^3r} \int_V \frac{\int_0^\infty O(\vec{r},E)\phi(\vec{r},E,t)\mathrm{d}E}{\int_0^\infty \phi(\vec{r},E,t)\mathrm{d}E}\mathrm{d}^3r \tag{4.25}$$

where $O(\vec{r},E)$ is an energy and position dependent variable such as $\upsilon(\vec{r},E)$, $D(\vec{r},E)$, $\Sigma_\mathrm{a}(\vec{r},E)$, $\Sigma_\mathrm{f}(\vec{r},E)$. Equation (4.23) assumes these variables are constant with time.

Equation (4.23) is often applied to a slab, infinite in two dimensions, to produce simplistic but informative solutions. However, to solve the equation through separation of variables the scalar flux must be a product of two independent functions, one spatial and one temporal (Duderstadt and Hamilton 1976; 199):

$$\phi(x,t) = \psi(x)T(t) \tag{4.26}$$

The separated differential equation of the spatial function $\psi(x)$ is a homogeneous second order linear equation with constant coefficients (Zill and Cullen 2000; 119); the slab's boundary conditions force $\psi(x)$ to zero at specific values of x and result in an infinite number of solutions for $\psi(x)$ (Zill and Cullen 2000; 103). The separated differential equation of the temporal function $T(t)$ is a homogeneous linear first order equation; $T(t)$ is thus an exponential function, which also has an infinite number of solutions, with one corresponding to each solution of $\psi(x)$ (Duderstadt and Hamilton 1976; 200). Because equation (4.23) is homogeneous, the general solution of $\phi(x,t)$ can be expressed as a superposition of all solutions (Zill and Cullen 2000; 105):

$$\phi(x,t) = \sum_{j(odd)}^{\infty} \psi_j(x)T_j(t) \tag{4.27}$$

For $t > 0$ in a critical slab with $k = 1$ all terms above $j = 1$ decay away leaving only one solution, $\phi(x,t) = \psi_1(x)T_1(t)$. When $k = 1$ the neutron flux is independent of time and $\phi(x,t) = \psi_1(x)$; thus the flux shape of a critical reactor is described by a single solution $\psi_1(x)$, called the fundamental mode or the shape factor.

A full description of the neutron flux with time must include the delayed neutrons. The source term of equation (4.23) is updated with delayed terms and coupled to a set of six differential equations describing the rate of change of atomic concentration of the nth precursor group, C_n (Duderstadt and Hamilton 1976; 238):

$$\frac{1}{\upsilon}\frac{\partial\phi(\vec{r},t)}{\partial t} - D\nabla^2\phi(\vec{r},t) + \Sigma_{\mathrm{a}}\phi(\vec{r},t) = (1-\beta)\nu\Sigma_{\mathrm{f}}\phi(\vec{r},t) + \sum_{n=1}^{6}\lambda_n C_n(\vec{r},t) \tag{4.28}$$

$$\frac{\partial C_n(\vec{r},t)}{\partial t} = -\lambda_n C_n(\vec{r},t) + \beta_n\nu\Sigma_{\mathrm{f}}\phi(\vec{r},t) \qquad n = 1,2...6.$$

Notice the right hand side of this equation, the neutron sources, isn't an energy-dependent description but is a description of the energy-integrated (i.e. total) neutron source.

The C_n terms are concentrations of fictitious isotopes which are defined to decay simply with the emission of a single delayed neutron. The half lives λ_n and fission yields β_n of each isotope are obtained with the regression method of Keepin (Keepin *et al.* 1957); these constants represent "grouped" isotopes which produce an equivalent number of delayed neutrons as the hundreds of real fission products which emit delayed neutrons.

Since the higher order modes decay very quickly given D, Σ_a and physical size of most reactors, the higher order spatial modes, $j > 1$, can be ignored; this makes equation (4.27) much simpler (Duderstadt and Hamilton 1976; 235). The scalar flux and concentrations C_n are then each defined as the product of two independent functions. They are written here using the common notation for the temporal function $n(t)$ (Duderstadt and Hamilton 1976; 238):

$$\phi(\vec{r},t) = \upsilon n(t)\psi_1(\vec{r}) \tag{4.29}$$

$$C_n(\vec{r},t) = C_n(t)\psi_1(\vec{r}). \tag{4.30}$$

The neutron point kinetic equations can then be derived from equation (4.28) using separation of variables (Duderstadt and Hamilton 1976; 239):

$$\frac{\mathrm{d}n(t)}{\mathrm{d}t} = \left[\frac{\rho(t)-\beta}{\Lambda}\right]n(t) + \sum_{n=1}^{6}\lambda_n C_n(t) \tag{4.31}$$

$$\frac{\mathrm{d}C_n(t)}{\mathrm{d}t} = \frac{\beta_n}{\Lambda}n(t) - \lambda_n C_n(t) \qquad n = 1,2...6$$

where the reactivity $\rho(t)$ is defined as:

$$\rho(t) = \frac{k(t)-1}{k(t)}, \tag{4.32}$$

$\Lambda = l/k$ is the mean generation time between birth of neutron and subsequent absorption inducing fission and l is the mean neutron lifetime.

Since $\psi_1(\vec{r})$ is normalized as (Duderstadt and Hamilton 1976; 236):

$$\int_V \psi_1(\vec{r})d^3r = 1, \tag{4.33}$$

it has units of:

$$[\psi_1(\vec{r})] = \frac{1}{\mathrm{cm}^3}. \tag{4.34}$$

The quantity $n(t)$ is unitless and represents the total number of neutrons in the reactor at time t (Duderstadt and Hamilton 1976; 236). The function $n(t)$ can be thought of as an amplitude factor and $\psi_1(\vec{r})$ as the neutron population's shape factor. Similarly the neutron precursor concentration

$C_n(t)$ is unitless and represents the total number of fictitious precursor atoms in the reactor at time t.

Within the context of the point kinetics equations the variable $n(t)$ is rarely used to represent an absolute value since it can be arbitrarily normalized (Duderstadt and Hamilton 1976; 236). For example, the fission power (or any other quantity proportional to a reaction rate) at $\vec{r}$ is calculated as:

$$\begin{array}{lcccccc} P(\vec{r},t) & = & E & \Sigma(\vec{r}) & \phi(\vec{r},t) & & \\ P(\vec{r},t) & = & E & \Sigma(\vec{r}) & \upsilon & n(t) & \psi(\vec{r}) \\ \frac{\mathrm{W}}{\mathrm{cm}^3} & = & \mathrm{J} & \frac{1}{\mathrm{cm}} & \frac{\mathrm{cm}}{\mathrm{s}} & & \frac{1}{\mathrm{cm}^3} \end{array}$$

where E is the energy released per fission. When calculating the fission power released over the entire core:

$$\begin{array}{lcccccc} P(t) & = & E & \Sigma & \int_V \phi(\vec{r},t)\mathrm{d}^3r & & \\ P(t) & = & E & \Sigma & \int_V \upsilon n(t)\psi(\vec{r})\mathrm{d}^3r & & \\ P(t) & = & E & \Sigma & \upsilon & n(t) & \int_V \psi(\vec{r})\mathrm{d}^3r \\ P(t) & = & E & \Sigma & \upsilon & n(t) & 1 \\ W & = & \mathrm{J} & \frac{1}{\mathrm{cm}} & \frac{\mathrm{cm}}{\mathrm{s}} & & \end{array}$$

Because $P(\vec{r},t)$, $P(t)$ and all other reaction-rate-dependent quantities vary directly with $n(t)$, $n(t)$ can be expressed relative to any convenient reference value n_{ref} as $n(t)/n_{\mathrm{ref}}$ while conserving the required units. Furthermore, $n(t)/n_{\mathrm{ref}}$ can be cited as "reactor power" since power relative to some reference power P_{ref} varies directly with $n(t)/n_{\mathrm{ref}}$.

For clarity, in this thesis the absolute neutron population is always expressed as $n(t)$, and the relative population as $n(t)/n_{\mathrm{ref}}$.

In summary, equations (4.31) track the relative population of neutrons and neutron precursors within the entire reactor, without regard for where they exist within the core.

4.2.2 Derivation of the two-particle point kinetics model

Initial assumptions of the two-particle point kinetics model

Using the neutron point kinetics equations as an example, the derivation of the two-particle point kinetics equations can begin by making the following fundamental assumptions:

1. $g(t)$ **is the total population of gamma rays in the reactor.** $g(t)$ includes gammas of all energies, in all volumes, produced by all reactions and all decays, from all isotopes in the entire core. This definition is analogous to the definition of $n(t)$ in equation (4.31).

2. **Delayed gammas can be modeled as resulting from fictitious precursor isotopes, which always decay with the emission of a single gamma.** These isotopes are indexed by g, and their concentrations are noted as $C_g(t)$. This assumption is analogous to Keepin's modeling of the delayed neutron precursor isotopes.

3. **The spatial distribution of the gamma flux is time-independent and expressed as $\kappa(\vec{r})$.** This variable is similar to the neutron spatial flux $\psi_1(\vec{r})$ as expressed in equation (4.29).

If, as neutrons in equation (4.29), the reactor's time-dependent total gamma population $g(t)$ and the gamma precursor isotope concentrations $C_g(t)$ are assumed independent of the gamma spatial distribution $\kappa(\vec{r})$:

$$\Phi(\vec{r},t) = \upsilon_\gamma g(t)\kappa(\vec{r}) \tag{4.35}$$

$$C_g(\vec{r},t) = C_g(t)\kappa(\vec{r}). \tag{4.36}$$

Derivation of the two-particle point kinetics model can now proceed by considering all gamma sources in an effort to develop expressions for $g(t)$ and $C_g(t)$.

Prompt gammas from fission

To write an expression for the rate of prompt fission (FP) gammas generated in the entire reactor, S_{FP}, assume the prompt gamma spectra is described by an energy grid with K energy bins (indexed by k) as discussed in section 4.1.13. If M is the total number of fissionable isotopes (indexed by m), ${}^k p^m_{\mathrm{FP}}$ is the average number of gamma rays produced in energy bin k when isotope m is fissioned by a neutron. Similar to equation (4.22), ${}^k p^m_{\mathrm{FP}}$ is calculated as:

$${}^k p^m_{\mathrm{FP}} = \sum_e ({}^e p^m_{\mathrm{FP}}), \tag{4.37}$$

where ${}^e p^m_{\mathrm{FP}}$ is the probability of emitting a single gamma e of energy E'. The summation considers only those emissions with ${}^e E'$ between the energy bin boundaries of bin k. If the ${}^k p^m_{\mathrm{FP}}$ terms are known to be dependent upon the incident neutron energy E, these values will have to be averaged over the core. The total prompt fission yield of gammas is then:

$$p^m_{\mathrm{FP}} = \sum_k^K ({}^k p^m_{\mathrm{FP}}). \tag{4.38}$$

The fission rate of isotope m in differential volume $\mathrm{d}r^3$ is:

$$\begin{aligned} F^m_{\mathrm{F}}(\vec{r}) &= \left[\Sigma^m_{\mathrm{F}}(\vec{r})\right]\left[\phi(\vec{r})\right] = \left[\frac{\int_0^\infty \Sigma^m_{\mathrm{F}}(\vec{r},E)\phi(\vec{r},E)\mathrm{d}E}{\int_0^\infty \phi(\vec{r},E)\mathrm{d}E}\right]\left[\int_0^\infty \phi(\vec{r},E)\mathrm{d}E\right] \\ &= \int_0^\infty \Sigma^m_{\mathrm{F}}(\vec{r},E)\phi(\vec{r},E)\mathrm{d}E \end{aligned}$$

where:

$$\left[F^m_{\mathrm{F}}(\vec{r})\right] = \frac{1}{\mathrm{cm}^3\mathrm{s}}. \tag{4.39}$$

Knowing equation (4.38), the prompt fission gamma source from isotope m in differential volume $\mathrm{d}r^3$ is then:

$$S^m_{\mathrm{FP}}(\vec{r}) = p^m_{\mathrm{FP}} F^m_{\mathrm{F}}(\vec{r}) = p^m_{\mathrm{FP}} \int_0^\infty \Sigma^m_{\mathrm{F}}(\vec{r},E)\phi(\vec{r},E)\mathrm{d}E \qquad \left[S^m_{\mathrm{FP}}(\vec{r})\right] = \frac{1}{\mathrm{cm}^3\mathrm{s}} \tag{4.40}$$

and the total source from m in all differential volumes $\mathrm{d}r^3$ in the entire core volume V is:

$$S^m_{\mathrm{FP}} = \int_V S^m_{\mathrm{FP}}(\vec{r})\mathrm{d}r^3 = p^m_{\mathrm{FP}} \int_V \int_0^\infty \Sigma^m_{\mathrm{F}}(\vec{r},E)\phi(\vec{r},E)\mathrm{d}E\mathrm{d}r^3 \qquad [S^m_{\mathrm{FP}}] = \frac{1}{\mathrm{s}} \tag{4.41}$$

Repeating the same summation for each of the M fissionable isotopes gives an expression for the total prompt fission source S_{FP}:

$$S_{\mathrm{FP}} = \sum_{m=1}^{M} p^m_{\mathrm{FP}} \int_V \int_0^\infty \Sigma^m_{\mathrm{F}}(\vec{r},E)\phi(\vec{r},E)\mathrm{d}E\mathrm{d}r^3. \tag{4.42}$$

Alternatively, the total fission prompt gammas resulting from isotope m can be calculated by multiplying the core averaged macroscopic cross section Σ^m_{F} by the total core scalar flux $\phi = \upsilon n(t)$ where υ is the core averaged neutron velocity and $n(t)$ is the total number of neutrons in the reactor at time t:

$$n(t) = \int_V n(\vec{r},t)\mathrm{d}r^3 \qquad [n(\vec{r},t)] = \frac{1}{\mathrm{cm}^3} \qquad [n(t)] = \text{unitless scalar}, \tag{4.43}$$

$$S^m_{\mathrm{FP}} = p^m_{\mathrm{FP}}\Sigma^m_{\mathrm{F}}\upsilon n(t). \tag{4.44}$$

The total source term S_{FP} is then written as:

$$S_{\mathrm{FP}} = \sum_{m=1}^{M} p^m_{\mathrm{FP}}\Sigma^m_{\mathrm{F}}\upsilon n(t). \tag{4.45}$$

Notice this derivation of an expression for S_{FP} assumed the material properties and flux are independent of time.

Delayed gammas from fisson

The absolute fission yield of the fictitious precursor isotope g created by a fission of isotope m, is denoted here as ${}^g p^m_{\mathrm{FD}}$ where delayed fission is indicated by FD. Adopting the method of Keepin, the equation describing the number of delayed gammas being produced at time t following fission of a single atom of isotope m is written as the summation of G exponential decay terms, corresponding to the G fictitious isotopes (Keepin *et al.* 1957; 6):

$$p^m_{\mathrm{FD}}(t) = \sum_{g=1}^{G} {}^g p^m_{\mathrm{FD}} \cdot \mathrm{e}^{-({}^g\lambda^m_{\mathrm{FD}})(t)} \tag{4.46}$$

where precursor isotope g decays at a rate described by ${}^g\lambda^m_{\mathrm{FD}}$. Notice ${}^g p^m_{\mathrm{FD}}$ and $p^m_{\mathrm{FD}}(t)$ are assumed not to depend on the incident neutron energy. Nor do these variables describe the energy of the gammas emitted; $p^m_{\mathrm{FD}}(t)$ describes the total number of gamma rays at all energies from m.

The time-dependent concentration of precursor isotope g, resulting from fission of isotope m, in differential volume $\mathrm{d}r^3$, at time t, is defined as ${}^g C^m_{\mathrm{FD}}(\vec{r},t)$; integrating this variable over the entire core volume V gives the total in-core concentration ${}^g C^m_{\mathrm{FD}}(t)$ at time t:

$${}^g C^m_{\mathrm{FD}}(t) = \int_V {}^g C^m_{\mathrm{FD}}(\vec{r},t)\mathrm{d}r^3 \qquad [{}^g C^m_{\mathrm{FD}}(\vec{r},t)] = \frac{1}{\mathrm{cm}^3} \qquad [{}^g C^m_{\mathrm{FD}}(t)] = \text{unitless scalar}. \tag{4.47}$$

The rate of change in this concentration at time t, in differential volume $\mathrm{d}r^3$, is a balance between production from fission and loss by decay:

$$\frac{\mathrm{d}^g C^m_{\mathrm{FD}}(\vec{r},t)}{\mathrm{d}t} = {}^g p^m_{\mathrm{FD}} \Sigma^m_{\mathrm{F}}(\vec{r}) \upsilon(\vec{r}) n(\vec{r},t) - {}^g \lambda^m_{\mathrm{FD}} {}^g C^m_{\mathrm{FD}}(\vec{r},t) \tag{4.48}$$

$$\vdots$$

$$M \cdot G \text{ instances of this equation}$$

Assuming each of the M fissioning isotopes can have its delayed gammas described by G precursor groups, there are $M \cdot G$ instances of this equation. The same equations can be applied to the entire core volume by using the core-averaged macroscopic cross section Σ^m_{f}, core-averaged neutron velocity υ and $n(t)$, the total number of neutrons in the reactor at time t:

$$\frac{\mathrm{d}^g C^m_{\mathrm{FD}}(t)}{\mathrm{d}t} = {}^g p^m_{\mathrm{FD}} \Sigma^m_{\mathrm{F}} \upsilon n(t) - {}^g \lambda^m_{\mathrm{FD}} {}^g C^m_{\mathrm{FD}}(t) \tag{4.49}$$

$$\vdots$$

$$M \cdot G \text{ instances of this equation.}$$

Notice equation (4.49) assumes the isotope g does not absorb neutrons, and thus the only loss of concentration is by decay.

Solving for ${}^g C^m_{\mathrm{FD}}(\vec{r},t)$ allows one to calculate the total delayed fission gamma source at time t, in differential volume $\mathrm{d}r^3$:

$\mathrm{S}_{\mathrm{FD}}(\vec{r},t) = \sum_{m=1}^{M} \sum_{g=1}^{G} {}^g \lambda^m_{\mathrm{FD}} {}^g C^m_{\mathrm{FD}}(\vec{r},t), (4.49)$

where the decay yield of each isotope is 1, by definition. The total delayed fission gamma source in the entire reactor volume V is then:

$$\begin{aligned} S_{\mathrm{FD}}(t) &= \int_V \sum_{m=1}^{M} \sum_{g=1}^{G} {}^g \lambda^m_{\mathrm{FD}} {}^g C^m_{\mathrm{FD}}(\vec{r},t) \mathrm{d}r^3 \\ &= \sum_{m=1}^{M} \sum_{g=1}^{G} {}^g \lambda^m_{\mathrm{FD}} \int_V {}^g C^m_{\mathrm{FD}}(\vec{r},t) \mathrm{d}r^3 \\ S_{\mathrm{FD}}(t) &= \sum_{m=1}^{M} \sum_{g=1}^{G} {}^g \lambda^m_{\mathrm{FD}} {}^g C^m_{\mathrm{FD}}(t). \end{aligned} \tag{4.50}$$

Prompt gammas from neutron capture

Not all isotopes within the reactor will capture neutrons in significant quantities. For the L isotopes which do, assume p^l_{CP} is the absolute number of prompt capture (CP) gamma rays emitted by isotope l. The source of these gammas over the entire core volume V is similar to the prompt fission gamma source equation (4.45):

$$S_{\mathrm{CP}} = \sum_{l=1}^{L} p^l_{\mathrm{CP}} \Sigma^l_{\mathrm{C}} \upsilon n(t). \tag{4.51}$$

Delayed gammas from neutron capture

The L neutron capture isotopes are likely to emit decay gammas. In the case of a single gamma emission, the decay rate will be described by a decay constant λ^l_{CD} and p^l_{CD} capture delayed gammas are emitted. For isotopes with complicated decay schemes, the dominant decay constant and cumulative gamma yield are used here as an approximation.

The rate of change in the activated isotope's concentration at time t, in differential volume $\mathrm{d}r^3$, $C^l_{\mathrm{CD}}(\vec{r},t)$, is a balance between production from fission and loss by decay:

$$\begin{aligned}\frac{\mathrm{d}C^l_{\mathrm{CD}}(\vec{r},t)}{\mathrm{d}t} &= p^l_{\mathrm{CD}}\Sigma^l_{\mathrm{C}}(\vec{r})\upsilon n(\vec{r},t) - \lambda^l_{\mathrm{CD}}C^l_{\mathrm{CD}}(\vec{r},t) \\ &\vdots \\ &L \text{ instances of this equation.}\end{aligned} \tag{4.52}$$

Using the core-averaged macroscopic cross section Σ^l_{cap}, core-averaged neutron velocity υ and $n(t)$, the total number of neutrons in the reactor at time t, equations expressing $C^l_{\mathrm{CD}}(\vec{r},t)$ over the entire reactor volume V are:

$$\begin{aligned}\frac{\mathrm{d}C^l_{\mathrm{CD}}(t)}{\mathrm{d}t} &= p^l_{\mathrm{CD}}\Sigma^l_{\mathrm{C}}\upsilon n(t) - \lambda^l_{\mathrm{CD}}C^l_{\mathrm{CD}}(t) \\ &\vdots \\ &L \text{ instances of this equation.}\end{aligned} \tag{4.53}$$

The total delayed capture gamma source in the entire reactor volume V is:

$$\begin{aligned}S_{\mathrm{CD}}(t) &= \int_V \sum_{l=1}^{L} \lambda^l_{\mathrm{CD}}C^l_{\mathrm{CD}}(\vec{r},t)\mathrm{d}r^3 \\ &= \sum_{l=1}^{L} \lambda^l_{\mathrm{CD}} \int_V C^l_{\mathrm{CD}}(\vec{r},t)\mathrm{d}r^3 \\ S_{\mathrm{CD}}(t) &= \sum_{l=1}^{L} \lambda^l_{\mathrm{CD}}C^l_{\mathrm{CD}}(t).\end{aligned} \tag{4.54}$$

It is assumed the activated isotopes do not capture another neutron after their formation.

Gamma leakage and absorption

So far only gamma sources which contribute positively to $g(t)$ have been considered. The rate gammas are lost either through leakage from the core geometry or by absorption is expressed here by assuming the loss rate is simply proportional to $g(t)$, where the factor of proportionality is defined as L_c with units of 1/s:

$$\text{loss rate} = L_c g(t). \tag{4.55}$$

The coupled neutron-gamma point kinetics equations

The neutronic point-kinetics equations (4.31) can be extended to include coupled differential equations describing $g(t)$ by including equations (4.45), (4.49), (4.50), (4.51), (4.54) and (4.55):

$$
\begin{aligned}
\frac{\mathrm{d}n(t)}{\mathrm{d}t} &= \left[\frac{\rho(t)-\beta}{\Lambda}\right] n(t) + \sum_{n=1}^{6} \lambda_n C_n(t) \qquad (4.56)\\
\frac{\mathrm{d}C_n(t)}{\mathrm{d}t} &= \frac{\beta_n}{\Lambda} n(t) - \lambda_n C_n(t) \qquad n = 1, 2...6.\\
\frac{\mathrm{d}g(t)}{\mathrm{d}t} &= \sum_{m=1}^{M} p_{\mathrm{FP}}^{m} \Sigma_{\mathrm{F}}^{m} \upsilon n(t) + \sum_{m=1}^{M}\sum_{g=1}^{G} {}^{g}\lambda_{\mathrm{FD}}^{m}\, {}^{g}C_{\mathrm{FD}}^{m}(t) + \sum_{l=1}^{L} p_{\mathrm{CP}}^{l} \Sigma_{\mathrm{C}}^{l} \upsilon n(t)\\
&\qquad + \sum_{l=1}^{L} \lambda_{\mathrm{CD}}^{l} C_{\mathrm{CD}}^{l}(t) - L_c g(t)\\
\frac{\mathrm{d}\,{}^{g}C_{\mathrm{FD}}^{m}(t)}{\mathrm{d}t} &= {}^{g}p_{\mathrm{FD}}^{m} \Sigma_{\mathrm{F}}^{m} \upsilon n(t) - {}^{g}\lambda_{\mathrm{FD}}^{m}\, {}^{g}C_{\mathrm{FD}}^{m}(t)\\
&\vdots\\
M &\cdot\ G \text{ instances of this equation}\\
\frac{\mathrm{d}C_{\mathrm{CD}}^{l}(t)}{\mathrm{d}t} &= p_{\mathrm{CD}}^{l} \Sigma_{\mathrm{C}}^{l} \upsilon n(t) - \lambda_{\mathrm{CD}}^{l} C_{\mathrm{CD}}^{l}(t)\\
&\vdots\\
L &\quad \text{instances of this equation}
\end{aligned}
$$

where:

$n(t)$ = total number of neutrons in the core at time t; unitless
$g(t)$ = total number of gamma rays in the core at time t; unitless
L = number of neutron capture isotopes, indexed by l
M = number of fissionable isotopes, indexed by m
υ = core-averaged neutron speed; cm/s
Σ_{F}^{m} = core-averaged macroscopic fission cross section of isotope m; 1/cm
Σ_{C}^{l} = core-averaged macroscopic capture cross section of isotope l; 1/cm
p_{FP}^{m} = prompt gamma yield from fission of isotope m; unitless
p_{CP}^{l} = absolute number of prompt capture gammas emitted by isotope l per reaction; unitless
${}^{g}p_{\mathrm{FD}}^{m}$ = absolute number of delayed gammas emitted by a fission of isotope m; unitless
p_{CD}^{l} = absolute number of delayed gammas emitted by activated isotope l per reaction; unitless
${}^{g}C_{\mathrm{FD}}^{m}(t)$ = number of fictitious precursor atoms of isotope g, created by fission of m, in entire core; unitless
$C_{\mathrm{CD}}^{l}(t)$ = number of activated atoms of isotope l in entire core; unitless
${}^{g}\lambda_{\mathrm{FD}}^{m}$ = decay constant of fictitious precursor isotope g, created by fission of m; 1/s
$\lambda_{\mathrm{CD}}^{l}$ = decay constant of activated isotope l; 1/s
L_c = loss rate coefficient.

Obtaining decay constants and yields - at the source

As shown in previous sections, the method of Keepin can be used to describe the delayed gamma emissions in a grouped manner. Probably the easiest way to obtain this delayed gamma emission source data is from the depletion module of Scale 6.1, ORIGEN-S (ORNL 2011b).

As predicted by ORIGEN-S, the total number of gammas emitted per second from a 0.3 mg ^{235}U sample following a very short irradiation is plotted in Figure 4.3. Using Keepin's grouping method, the following equation can be fit to the data to obtain the yields A_i and decay constants λ_i of the Q precursor groups.

A comprehensive investigation of this method is left for others to complete.

$$f(t) = \sum_{q=0}^{Q} A_i \cdot \mathrm{e}^{-\lambda_i \cdot t} \tag{4.57}$$

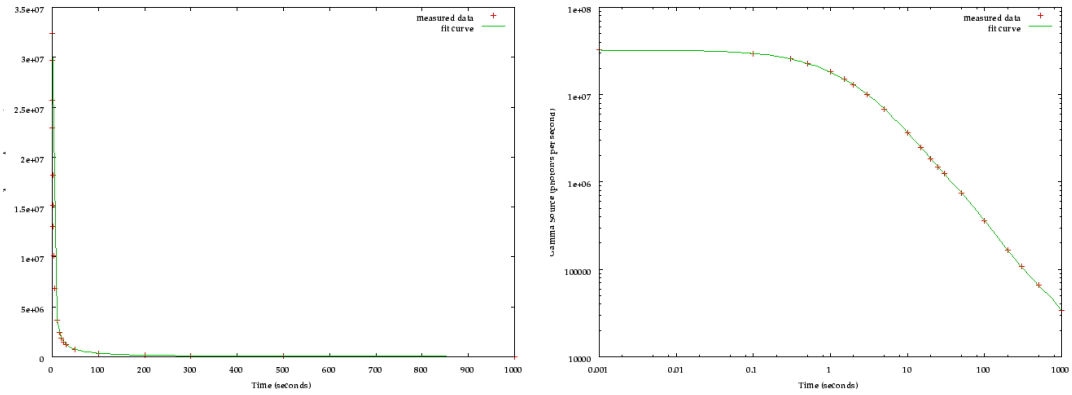

Figure 4.3: (L) ORIGEN-S decay gamma source data and the resulting fit equation of the form (4.57), on a lin-lin plot, (R) and on a log-log plot.

Obtaining decay constants and yields - at the point of absorption

Rather than describing the delayed yields and decay constants of grouped gammas for each isotope, as described in the previous section, it might be possible to experimentally measure the relative gamma population $g(t)/g_{\mathrm{ref}}$ with a calorimeter. Such a measurement would describe, at once, the net delayed gamma dynamics from all fissionable and neutron-capture isotopes in a specific reactor.

By equation (4.35) the $g(t)$ measured at one location would apply to all other $\vec{r}$.

Instead of considering each fissionable isotope and each neutron-capturing isotope seperately, as in equation (4.56), a calorimeter can be used to develop a much simpler version of the two-particle point kinetics model.

The position and time-dependent photon heating of an in-core object G can be calculated if the local gamma flux, $\Phi(\vec{r}_G, t)$, and the effective mass energy-absorption coefficient, $\mu_{\mathrm{effective}}(G, E_{\mathrm{avg}})/\rho$, are known:

$$H(\vec{r}_G, G, t) = \frac{\mu_{\mathrm{effective}}(G, E^{\mathrm{avg}})}{\rho} E^{\mathrm{avg}}(\vec{r}_G)\Phi(\vec{r}_G, t) \tag{4.58}$$

$$H(\vec{r}_G, G, t) = \frac{\mu_{\mathrm{effective}}(G, E^{\mathrm{avg}})}{\rho} E^{\mathrm{avg}}(\vec{r}_G)\upsilon_\gamma g(t)\kappa(\vec{r}) \tag{4.59}$$

where $E^{\mathrm{avg}}(\vec{r}_G)$ is the average photon energy at $\vec{r}_G$, $\mu_{\mathrm{effective}}(G, E^{\mathrm{avg}})/\rho$ has units of $1/\mathrm{cm}\cdot\mathrm{cm}^3/\mathrm{g}$ and equation (4.35) was used to define $\Phi(\vec{r}_G, t)$. An "effective" μ is required because section E.4.1 showed the actual quantity of deposited energy is dependent upon the geometry of G since self-shielding of the target G can be significant; including G as an independent variable in $\mu_{\mathrm{effective}}(G, E^{\mathrm{avg}})$ means "μ

is dependent upon both the geometry and Z of G." Ignore the problem of obtaining $E^{\text{avg}}(\vec{r}_G, t)$ and $\mu_{\text{effective}}(G, E^{\text{avg}})/\rho$ since the above equation is not meant to be practical and is simply illustrative.

If a data series of $H(\vec{r}_G, G, t)$ were experimentally obtained with an in-core calorimeter, a reference heating value $H_{\text{ref}}(\vec{r}_G, G)$ associated with a reference gamma population g_{ref} could be used to obtain a relative time-dependent description of $g(t)$:

$$\frac{H(\vec{r}_G, G, t)}{H_{\text{ref}}(\vec{r}_G, G)} = \frac{\frac{\mu_{\text{effective}}(G, E^{\text{avg}})}{\rho}}{\frac{\mu_{\text{effective}}(G, E^{\text{avg}})}{\rho}} \frac{E^{\text{avg}}(\vec{r}_G)}{E^{\text{avg}}(\vec{r}_G)} \frac{\upsilon_\gamma}{\upsilon_\gamma} \frac{g(t)}{g_{\text{ref}}} \frac{\kappa(\vec{r})}{\kappa(\vec{r})} = \frac{g(t)}{g_{\text{ref}}}. \tag{4.60}$$

Thus by equation (4.60), an in-core dynamic measurement using a calorimeter provides an expression of both $H(\vec{r}_G, G, t)$ and $g(t)$. If the measurement is designed appropriately, Keepin's grouping and regression analysis can be used with the empirical data to describe the dynamic behavior of the delayed gammas, resulting in grouped gamma yields and decay constants.

Once these group constants have been determined they can be used with a version of the coupled point-kinetics equations to determine $g(t)$ for any $n(t)$, and by equation (4.60) also determine $H(\vec{r}_G, G, t)$. These constants allow the point-kinetics equations to be rewritten "top-down" instead of writing the equations by summing the gamma production rates from all isotopes and reactions in a "bottom-up" manner as in equations (4.56); this eliminates the need to obtain the variables ${}^g p^m_{\text{FD}}$, p^l_{CD}, ${}^g \lambda^m_{\text{FD}}$, Σ^m_{F}, Σ^l_{C} and λ^l_{CD} for each M, L and G:

$$\begin{aligned}
\frac{1}{n_{\text{ref}}} \frac{\mathrm{d}n(t)}{\mathrm{d}t} &= \left[\frac{\rho(t) - \beta}{\Lambda}\right] \frac{n(t)}{n_{\text{ref}}} + \sum_{n=1}^{6} \lambda_n C_n(t) \\
\frac{\mathrm{d}C_n(t)}{\mathrm{d}t} &= \frac{\beta_n}{\Lambda} \frac{n(t)}{n_{\text{ref}}} - \lambda_n C_n(t) \qquad n = 1, 2...6. \\
\frac{1}{g_{\text{ref}}} \frac{\mathrm{d}g(t)}{\mathrm{d}t} &= p_{\text{P}} \upsilon \Sigma \frac{n(t)}{n_{\text{ref}}} - L_c \frac{g(t)}{g_{\text{ref}}} + \sum_{g=1}^{G} \lambda_g C_g(t) \\
\frac{\mathrm{d}C_g(t)}{\mathrm{d}t} &= p_g \upsilon \Sigma \frac{n(t)}{n_{\text{ref}}} - \lambda_g C_g(t) \\
&\vdots \\
&G \text{ instances of this equation.}
\end{aligned} \tag{4.61}$$

where:
$\frac{n(t)}{n_{\text{ref}}}$ = relative number of neutrons in the core at time t; unitless
n_{ref} = reference number of neutrons in the core; unitless
$\frac{g(t)}{g_{\text{ref}}}$ = relative number of gammas in the core at time t; unitless
p_{P} = core-averaged prompt gamma yield per neutron reaction, for all relevant reactions and isotopes
p_g = probability of creating one delayed gamma precursor $C_g(t)$
g_{ref} = reference number of gammas in the core; unitless
λ_g = decay constant of the delayed group gamma group g; 1/s
$C_g(t)$ = gamma precursor population in entire core; unitless
υ = core-averaged neutron speed; cm/s
Σ = core-averaged macroscopic cross section, for all relevant gamma-producing reactions and isotopes; 1/cm
G = the number of precursor groups which are required to accurately describe the total delayed fission and capture gammas
L_c = loss rate coefficient.

Solving equation (4.61) for $g(t)/g_{\text{ref}}$ would then allow $H(\vec{r}_G, G, t)$ to be known for all $n(t)$ at any $\vec{r}_G$, provided $H_{\text{ref}}(\vec{r}_G, G)$ was measured or calculated for some object G.

The product $p_{\text{P}}\upsilon\Sigma n(t)/n_{\text{ref}}$ represents the prompt gamma production rate, normalized to n_{ref}. The product $p_g\upsilon\Sigma n(t)/n_{\text{ref}}$ represents the delayed gamma precursor production rate, of group g, normalized to n_{ref}.

The absolute value of $g(t)$ can't be obtained because $E^{\text{avg}}(\vec{r}_G)$ and $\mu_{\text{effective}}(G, E_{\text{avg}})/\rho$ in equation (4.59) are unknown.

There is a potential problem with using a calorimeter to infer information about $g(t)/g_{\text{ref}}$: the measured heating $H(\vec{r}_G, G, t)$ is material dependent. Some calorimeter material (object G) may have a very small $\mu(Z, E)/\rho$ at some gamma energies E. Despite this possibility, the method still has validity since such hard-to-absorb gammas may also not be consequential in other common materials and therefore be inconsequential. This underestimation could be amplified by constructing a calorimeter of a material known to be a poor gamma absorber, this is unlikely to happen though since the very purpose of a calorimeter is to absorb radiation.

It is also possible a calorimeter made of material Z_1 and another of Z_2 would predict different magnitudes of $g(t)$, as caused by the relative values of $\mu(Z, E)/\rho$ over a range of E. This possibility will need to be considered further.

Chapter 5

Methodology of analysis

The previous chapter proposed the grouping method of Keepin be applied to a calorimeter's signal to obtain a grouped description of the delayed gamma population. It should be possible to obtain such a signal from the SCK-CEN GT in MNR.

This chapter describes the methods employed in this thesis to process the SCK-CEN GT signal to obtain the grouped delayed gamma group yields and decay constants of equation (4.61). The subsequent chapter contains the results of this analysis and makes frequent references to specific sections in this chapter.

5.1 The McMaster Nuclear Reactor

The McMaster Nuclear Reactor (MNR) is an open-pool, materials testing reactor (MTR-type) on the McMaster University campus and operates on an intermittent 16 hr/day, 5-6 days per week schedule, where reactor power usually varies between 2.0 and 3.0 MW. The reactor serves as an educational and research platform for the university but also conducts a variety of commercial applications, notably the production of the medical isotope ^{125}I, neutron radiography and neutron activation analysis.

As most research reactors, MNR is used for in-core sample irradiation, so there is a desire to characterize the gamma flux to predict the nuclear heating of both in-core samples and in-core ^{125}I production equipment. As discussed previously, isotope production techniques would benefit from this knowledge.

Gamma heating is relevant from a safety perspective when considering increasing MNR operating power to increase isotope production rates. Increasing reactor power to 5 MW would require thorough examinations of nuclear heating rates. The temperature of the ^{125}I rigs have been measured in the past and are known to react strongly to increases in reactor power (Avelar 2013).

5.1.1 MNR Specifications

MNR was designed by AMF Atomics (Canada) Ltd. and first went critical in 1959 after being granted its first operating license by the Atomic Energy Control Board (AECB). Since then it has been granted successive operating licences by the old AECB, and its successor the now-named Canadian Nuclear Safety Commission (CNSC).

MNR operated at 1 MW until 1964 when it increased to 2 MW. During the extended shutdown of Chalk River's NRU in the early 1970s, MNR was used for ^{99}Mo production and operated at 5 MW (McMaster Nuclear Reactor 2002; Sec.01). Currently MNR operates at 3 MW Monday through Friday, sixteen hours a day, with two eight-hour shifts of operation (McMaster Nuclear Reactor 2002; Sec.01).

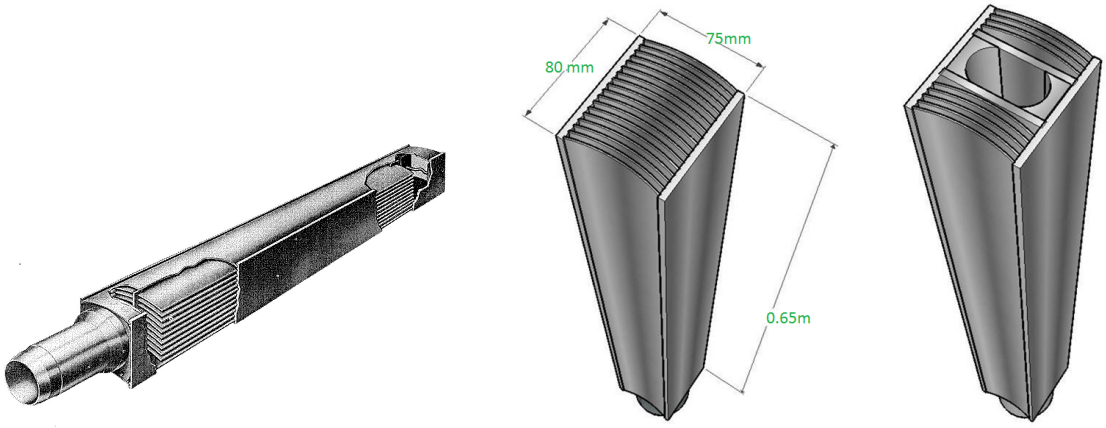

Figure 5.1: (L) Profile cutaway view of fuel assembly showing cylindrical bottom end fitting; (C) top view of standard fuel assembly; (R) top view of control fuel assembly with guide tube for control rod.

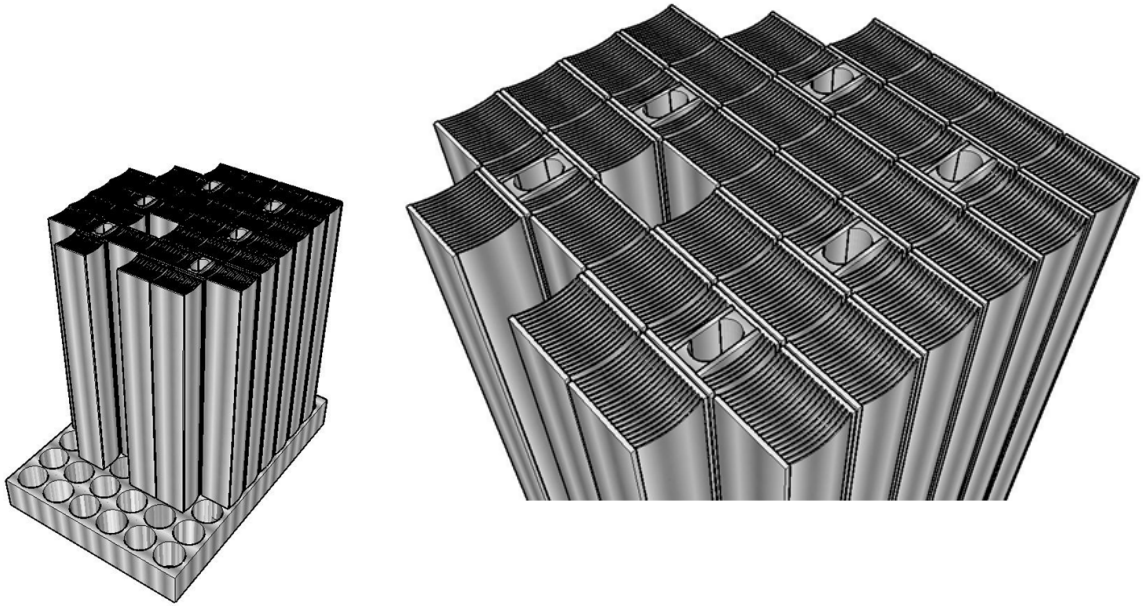

Figure 5.2: (L) Six control fuel assemblies amongst standard assemblies in a core arrangement; (R) top of core view.

The reactor has a pool-type configuration, meaning the core is submerged in a pool of demineralized light water. The core is built by assembling with the MTR fuel on the grid plate. The MTR fuel elements are shown stylistically in Figure 5.1. The fuel elements stand vertically when assembled in the core on the 9x6 grid plate — see Figure 5.2. The core is assembled by placing the bottom end fittings of the fuel assemblies into one of the 54 holes in the rectangular grid plate. The grid plate holes accept either fuel elements or other core components such as the graphite reflector blocks; the unused holes are plugged to prevent flowing pool water (during forced-convection cooling) from bypassing the coolant channels.

As with many other MTR-type reactors, MNR was designed to operate with 93% ^{235}U (highly

enriched uranium - HEU). It has since been converted to 20% LEU fuel.

The fuel elements currently used in MNR contain eighteen plates (Figure 5.1 (C)), the inner sixteen plates contain uranium fuel; the outer two plates are made of only aluminum and are referred to as dummy plates. The control fuel elements (Figure 5.1 (R)) have the same outer dimensions as a standard element but also have an allowance for the penetration of a neutron absorbing control rod. All nine of the plates in a control element contain fuel.

Each fuel plate is fabricated by sandwiching the uranium-aluminum fuel meat between two thin aluminum cladding plates. The fuel meat is 0.51 mm thick and composed of the uranium/silicon molecule U_3Si_2 bound in an aluminum matrix (McMaster Nuclear Reactor 2002; Table 5-3). The aluminum cladding is 0.38 mm thick, and the total fuel plate width is 1.27 mm. The coolant channel between the plates is nominally 3 mm wide. Each fuel plate is slightly curved to control the direction of thermal expansion. Each LEU standard fuel assembly contains 225 g of ^{235}U.

MNR is controlled by six metallic neutron absorber rods which protrude into the control elements from above the core. The vertical positions of all six control rods are set by electric linear actuators. Five rods are the manually controlled shim/safety rods (SSR). These are made of Cd-In-Ag and are used for coarse power adjustment and for rapid gravity-drop safety insertions. The sixth rod is a stainless steel regulating rod, whose position is actively adjusted by the control system.

During refueling, a small number of fresh fuel elements are exchanged for end-of-life elements. As fuel elements reach their end-of-life they are removed and the remaining assemblies are shuffled to obtain optimum burnup and to satisfy operational requirements. The core arrangement and number of components may change during a fuel change. The manipulation of the fuel assemblies and other core components is done manually with a long tool which allows the operator to reach the core from a bridge spanning the reactor pool, directly above the core.

Under high power conditions (>100 kW) the pool water is forced through coolant channels between the fuel plates. The coolant enters through the top of each fuel element and exits through the bottom of the cylindrical bottom end fitting (BEF) (shown on the left in Figure 5.1). Under low power operating conditions, regulations allow the core to be cooled by natural convection. Under natural convection flow, the buoyancy induced flow draws pool water up through the coolant channels inside and exits the top of each fuel element.

5.1.2 The MNR power measurement and control

This section provides a short summary of MNR's control system. These systems must be understood to interpret the SCK-CEN GT's signal since activities in the control room have an effect on the signal.

At normal operating powers, measurement of MNR thermal power is always determined by measuring the coolant's temperature rise across the core:

$$P_{\mathrm{TH}} = \dot{m} c_P (T_{\mathrm{out}} - T_{\mathrm{in}}), \tag{5.1}$$

where the initial coolant temperature T_{in} is the temperature of the pool water just above the core, and the core outlet temperature T_{out} is measured below the pool and downstream of the core. The core power, determined with this method, is formally measured and recorded in the control room at regular intervals. When approaching the nominal reactor power each day, this is the method used to determine when nominal power has been reached.

Throughout an operating day where the desired neutron flux is constant, the regulating rod automatically adjusts in height to maintain k close to unity. However, because the reactor only operates 16 hours per day, Xe transients proceed throughout each day and require the addition or subtraction of large amounts of reactivity. Therefore, throughout an operating day the regulating rod must move significantly to compensate for the changes in Xe concentration. Licensing guidelines dictate the regulating rod is allowed to operate only between the positions of 20 and 80% withdrawn from the core, so as the rod moves to compensate for Xe changes these boundaries are reached and the reactor operators must manually shim with the shim/safety rod bank to allow the regulating rod

to return to acceptable bounds. This shimming occurs multiple times per day and the shim/safety rod positions are formally measured and recorded in the control room at regular intervals.

On operating days where the desired neutron flux is constant, the thermal power increases as a result of the inventory buildup and decay of active isotopes. As the thermal power increases from the nominal power, reactor operators adjust the reactor's power demand, which momentarily moves the regulating rod enough to decrease k significantly enough to reduce the prompt fission power. This process moves the reactor's thermal power back to its nominal value.

The neutron population in the core is recorded by ion chambers adjacent to the core. There are multiple chambers and multiple associated control and safety channels. The channel of interest to the experimentalist is the Lin N channel which presents a signal proportional to the neutron flux; an automated ink pen and a long roll of chart paper record the Lin N signal in the control room.

5.1.3 Monitored MNR operating parameters

After all SCK-CEN GT experiments the control room records of nominal power, shim/safety rod positions and Lin N chart are reviewed.

Unfortunately, no calibration analysis has been conducted on the Lin N channel to allow for a conversion between any given deviation on the Lin N signal and a corresponding change in reactor power, but it's paper chart is still a useful record of shimming and power demand changes.

5.2 The experimental use of the SCK-CEN GT

The SCK-CEN GT-20 has been mounted on an instrument rig designed and fabricated specifically to accomodate the GT; an engineering drawing of this rig is shown in Figure I.1. This rig allows the GT to be placed within any of the graphite assemblies, the Be assembly, or the central irradiation facility.

5.2.1 Data logging

A LabVIEW program written by Frank Labonte (a MNR staff member) logs the GT signal after it travels through the signal chain of: 1) instrument lead, 2) coaxial cable connected to the instrument lead above the core, 3) National Instruments 9211 thermocouple input module on the DAQ computer placed adjacent to the reactor pool. The LabVIEW program presents the GT signal on a customized GUI.

All data was aquired on a frequency of 1 Hz.

5.2.2 Design of the experimental campaign

The SCK-CEN GT is employed in this work to measure the total nuclear heating in MNR over time. Further processing of the GT signal will result in a description of the nuclear heating component caused by delayed gammas.

Repeated measurements at various core locations will show the delayed-gamma heating does, or does not, have the same dynamics in all regions of the core. These measurements will test the validity of equation (4.35).

5.2.3 Simplifying assumptions of analysis

Throughout the experimental procedure, the following assumptions are made which reduce the burden of analysis to manageable levels:

1. **Large changes in coolant water temperature near the GT do not progress quickly.** This is a safe assumption since the source of all water passing through the core and over the GT is the large-volume reactor pool. The instrument rig has also been designed to allow water to freely circulate around the GT, likely eliminating the possibility of nuclear heating causing a localized volume of hot water.

2. **Small, quick changes in coolant water temperature near the GT do not affect the GT signal trend.** It is possible the local coolant temperature changes quickly, with a small magnitude of change. The GT's differential thermocouple can compensate for slow changes in temperature, but even small coolant temperature changes which progress over a time comparable to, or shorter than, the GT's thermal response of $\tau_0 = 18.4 \pm 0.2$ s will affect the GT signal. However, since this study is concerned with measuring the changes in nuclear heating which take hours, small rapid changes in coolant temperature will simply contribute to the GT signal noise.

3. **Changes in fuel composition have no effect on the photon transport within the core.** See section E.5 for a comparison between the prompt gammas in cores with and without significant fission products. Although this analysis was conducted on another reactor core, the same fundamental physics apply.

4. **The small power perturbations caused by small control rod changes, power demand changes or position changes of irradiated in-core objects have a neglibible effect on the long-duration trend sought in the GT signal.** Throughout an operating day, MNR's shim/safety rods are moved significantly (manually) to compensate for the reactivity changes caused by changes in concentration of strongly-absorbing fission products. The regulating rod's position changes often to compensate for small changes in reactivity (automatically) and to increase or decrease reactor power (manually). The analysis in this thesis acknowledges these changes induce small changes in reactor power, the nuclear heating of the GT, and thus the GT signal, but assumes that small changes in reactor power do not obscure the longer underlying trend within the GT signal caused by the delayed-gamma heating. Any large change in these variables will obscure the trend and thus collecting GT data while relatively few reactor changes are occurring is best.

5. **The large shim/safety rod position changes made throughout a normal operating day have a neglibible effect on the long-duration delayed-gamma heating trend sought in the GT signal.** Throughout an operating day, the large movements of these rods are made in bank with many incremental steps to compensate for the reactivity changes caused by changes in concentration of strongly-absorbing fission products. The previous point addressed the small temporary power changes induced at the moment of each incremental movement is made, but it is also possible the global gamma flux distribution changes throughout the day as the rod position changes greatly, as the reactor power remains constant. These large rod position changes are known to affect the core's global neutron flux distribution (Day 2002; 17). The in-core gamma flux is known to be more uniformly distributed through the core than the neutron flux and JHR analysis showed limited changes to prompt gamma heating with changes in control rod position - see section E.4.6. This assumption is made knowing it may not be true, but will be reviewed in later analysis for further consideration.

6. **The large regulating rod position changes made throughout a normal operating day have a neglibible effect on the long-duration delayed-gamma heating trend sought in the GT signal.** The single regulating rod cannot affect the neutron or gamma flux distribution to the same magnitude as the shim/safety rods; if the shim/safety rods are negligible, so is the regulating rod.

5.3 SCK-CEN GT signal processing steps

This section summarizes the steps which have been executed to obtain useful data from the SCK-CEN GT signal. This sequential summary brings together all the steps discussed in this chapter and a few others:

1. Collect the raw GT signal during a measurement. This signal is $\Delta T = T_H - T_C$ as measured by the differential thermocouple as detailed in section 5.5.
2. Subtract the GT's off-zero bias from the raw signal.
3. Correct the GT signal to account for T_C. This correction is required because the DAQ isn't programmed to correctly interpret a differential thermocouple signal; the correction is detailed in section F.2.4.
4. Plot and inspect the data; select sections for further analysis. Not all collected data is interesting or of acceptable quality.
5. Break the selected sections out for further analysis.
6. Smooth the selected data. Smoothing reduces the variability of the data to improve the curve fitting results and to make visual inspection of the curve fit easier. The smoothing methods used are detailed in section G.2.
7. Calculate a preliminary estimate of the data error. This estimate is the propagated result of: 1) the RMS error of each data section relative to the smoothed value $S(t_i)$ at each time t_i, and 2) the standard deviation of the off-zero bias. This error estimate systematically under-estimates the data noise because the smoothed time series itself contains noise; this error estimate is used only in the following step to evaluate the quality of fit.
8. Curve fit to the smoothed data to obtain the assumed true value of ΔT at each time t. Gnuplot is used to fit a function with the methods discussed in section H. The fit equations are of the form of (5.41) and (5.42), with coefficients in units of °C instead of W/g.
9. Calculate the standard deviation σ of the ΔT data. This value is the propagated result of the following uncertainties: 1) the RMS error, as discussed in section G.3, relative to the true value of ΔT as defined by the fit curve, and 2) the standard deviation of the off-zero bias.
10. Calculate the total nuclear heating $Q_{\text{total}}(t)/\rho$ with the true value of ΔT. The nuclear heating is calculated using equation (5.26); this equation also compensates for the GT's thermal lag. The error σ is propagated through equation (5.26), as is the uncertainty of A' and C'.
11. Calculate the GT self-heating using the methods detailed in section 5.6. The self-heating errors are equal to the propagated Monte Carlo neutron reaction rates and reactor power uncertainty.
12. Subtract the prompt and delayed GT self-heating from $Q_{\text{total}}(t)/\rho$. The prompt and delayed self-heating errors are propagated to calculate the error of $Q_{\text{total}}(t)/\rho$.
13. Subtract the neutron heating from $Q_{\text{total}}(t)/\rho$. The energy deposited by neutrons is calculated using the methods detailed in section 5.4.1. The relatively small neutron heating error is not propagated.
14. Curve fit to the $Q_{\text{field}}(t)/\rho$ time series. Gnuplot is used to fit a function, with the methods discussed in section H. The fit equations are of the form of (5.41) and (5.42).
15. Calculate the uncertainty of the fit parameters. Gnuplot cannot calculate these uncertainties, so equation (H.4) is used instead.

5.4 MCNP6 modeling

MCNP6 has been employed as a tool multiple times in the analysis of the GT. It has been used to:

- calculate the neutron and prompt gamma flux in the SCK-CEN GT in multiple MNR core locations
- calculate the neutron and prompt gamma energy deposition in the SCK-CEN GT in multiple core locations
- calculate the neutron reaction rates in the GT materials
- examine the transport of gamma rays within the GT.

All calculations with MCNP6 employed version 6.1.0; this iteration was released in May 2013 and is the first merger of the previously independent codes MCNP5 and MCNPX (Pelowitz 2013; 1-1).

This section summarizes how MCNP6 was used.

5.4.1 MCNP6 model of the MNR Reference Core (RC)

The number of standard fuel assemblies within the MNR core is not constant; they can be added or removed during refueling, as required by reactor operations. To avoid the need to conduct safety analysis on each core arrangement, a configuration called the Reference Core (RC) has been developed which conservatively envelopes actual MNR core configurations (Day 2001; 15). This conservatism has allowed the RC to serve as a representative core for analysis within the MNR Safety Analysis Report (SAR) which supports the reactor's current operating license

Figure 5.3 presents the RC configuration and the percentage of burnup assumed in each fuel assembly. The RC uses the same number of control assemblies and control rods as every MNR core arrangement. The location, or even presence, of the central irradiation facility (CIF) changes in real MNR core configurations.

Since the RC has already been accepted as an MNR analytical model, it has also been adopted within this thesis for analysis.

Prior to this present study, MNR staff made a full-core MCNP5 model of the of this RC configuration. The MCNP5 model of the RC is a near-faithful 3D representation of all structural, fuel, control, beamlines, moderator and coolant geometries. One geometrical simplification was implemented in this model: the representation of the curved fuel plates with non-curved plates. This approximation was estimated to have little physical significance and the rest of the model is a correct representation of the core geometry.

The MNCP5 RC model has been run in MCNP6 for calculations within this thesis and updated as detailed in following sections. A plot from MCNP6 showing a horizontal slice of the full core model is shown in Figure 5.4.

It is assumed that calculations with the MCNP6 RC model are a close approximation of actual core configurations.

RC data libraries

The RC model was originally developed with MCNP5 and thus used material descriptions from the following libraries (Team 2008; App.G):

- ENDF/B-VI.8 (library named "actia" in MCNP5)
- ENDF/B-VI.6:X (library named "endf66a" in MCNP5)

- ENDF/B-VI.1 (library named "endf60" in MCNP5)
- ENDF/B-V.0 (library named "kidman" in MCNP5).

These have been updated to the latest continuous-energy neutron cross-section libraries, and in all cases this is the ENDF71x MCNP6 library which is based on the ENDF/B-VII.1 data library (Pelowitz 2013; App.G). The following are exceptions:

- C is described elementally as it is in ENDF71x
- ^{18}O atoms are added to ^{17}O atoms because ^{18}O isn't included in ENDF71x
- the moderator/coolant in the RC model uses only ^{16}O (not ^{17}O or ^{18}O)

The ENDF71x evaluation at 293.6 K has been selected in all isotopes, which is the closest available evaluation temperature to the actual material temperature in MNR.

Thermal neutron scattering libraries have been assigned to some low-Z core materials which are present in large quantitites: H in the moderator water, graphite, Be. The continuous secondary energy data library endf70sab was selected and is also based on ENDF/B-VII.0 data.

Most elements were already described isotopically in the original MCNP5 RC model. Those which weren't (Mg, Si, Ar, Ca, Ti, V, In) have been updated to full isotopic descriptions in the MCNP6 RC model.

Physics specifications of the model

The MCNP6 RC model has been run with KCODE as a criticality calculation, as opposed to a defined-source calcuation. All KCODE calculations have been in MODE N P, resulting in neutrons and photons being transported in a fully coupled manner. As discussed previously, in KCODE calculations MCNP6 includes prompt gammas only.

In all cases the energy cutoff of photons has been specified to be 1 keV; not tracking these inconsequential gammas reduces the processing burden. The 1 keV value is used to match the work reviewed in Chapter 3 and the analysis in section E.3.

By default MCNP6 uses a neutron energy cutoff of 0 MeV and a photon energy cutoff of 1.0×10^{-6} MeV unless the CUT card is specified (Pelowitz 2013; Table 2-2); the inconsistent MCNP6 manual claims on another page the default photon cutoff is 1 keV (Pelowitz 2013; 3-85). To be sure, the CUT card for photons was used to specify the 1 keV demarcation. The default 0 MeV neutron cutoff was used in all cases.

Since electrons and positrons are so important to the production of photons and the deposition and transport of photon energy their absence in a MODE N P calculation must be addressed.

Electrons and positrons are not transported in MODE N P. However, when MCNP6 is run in MODE N P Bremsstrahlung photons are generated with the thick-target approximation (Pelowitz 2013; 1-12); this approximation generates electrons but assumes they are locally stopped and the generated Bremsstrahlung photons are assumed to continue in the direction of the parent electron (Team 2008; 2-57).

Modelling the SCK-CEN GT in MNR

The full SCK-CEN GT geometry and instrument rig has been added to the MCNP6 MNR RC model. The model is a complete geometrical representation of the GT, with full material description. Each part of the GT was described as per the drawing supplied by SCK-CEN (SCK-CEN 2009; Tab 1). The only geometrical simplification made was the combining of the two thermocouple wires into a a homogeneous, representative material; these wires are only 0.2 mm in diameter and the material of these two wires were mixed with the surrounding alumina insulation (diameter of 0.34

mm). Material descriptions for all GT materials were based upon the assays supplied by SCK-CEN (SCK-CEN 2009).

Figure 5.5 (L) shows the GT and instrument rig in the MCNP6 RC model. This GT and rig geometry can be placed anywhere within the MCNP6 RC model.

Quantitities calculated with the MCNP6 RC model

The MCNP6 RC model containing the full SCK-CEN GT and instrument rig geometry has been used to calculate the following quantities:

1. neutron energy deposition in the GT inner body, at various GT locations; using F6 tallies discussed in section 3.4.2
2. prompt photon energy deposition in the GT inner body, at various GT locations; using F6 tallies.

The MCNP6 RC model without the full SCK-CEN GT and instrument rig geometry has been used to calculate the neutron reaction rate in all GT materials; this process is discussed fully in section 5.6.3. The same simulation was used to calculate the neutron and prompt gamma flux in potential GT core locations with F4 volume-averaged tallies.

The tallies from all calculations were scaled with, C, the reactor power scaling factor discussed in section B.

5.4.2 MCNP6 model of the SCK-CEN GT

MCNP6 has also been used for a detailed study on the transport of gamma radiation within the SCK-CEN GT. The geometry of this model consists of just the SCK-CEN GT; Figure 5.5 (R) shows this geometry. A detailed description of how this model was used is included in section 5.6.2.

5.5 Calibration of the SCK-CEN GT

Following fabrication, SCK-CEN calibrates each GT with a dip test. This process results in a multiplicative calibration factor which allows the user to convert the GT signal, which is a measurement of temperature difference between two junctions (in units of °C) into a nuclear heating value Q (in units of W/g). This calibration factor is valid for steady-state nuclear heating conditions.

This section summarizes the derivation of the steady-state calibration factor and derives a new calibration equation which is applicable to transient heating conditions.

5.5.1 The steady-state GT heat transfer model

The steady-state temperature profile of the GT inner body can be modeled as a solid cylinder (see Figure 5.6), with volumetric heat generation and axial and radial heat conduction. The axial conduction is assumed to be towards the inner-body base as the inner-body tip is assumed to be perfectly insulated. Radial heat conduction is assumed to move through the gas gap, from the inner body, through all three mechanisms of heat transfer: conduction, convection and radiation. The resulting differential equation is (Van Nieuwenhove, R. 1996; App.B,Eq.1):

$$\frac{\mathrm{d}^2T}{\mathrm{d}x^2} - A \cdot T = -B \tag{5.2}$$

where the axial position, x, measured along the inner body is defined on the range $0 \leq x \leq L$ from the base to tip,

$A = \frac{2 \cdot k_e}{a \cdot k_b}$, [A]=1/m^2
$B = \frac{2 \cdot k_e}{a \cdot k_b} \cdot T_b + \frac{Q}{k_b}$, [B]=K/m^2
$C = \frac{c_v \cdot \rho}{k_b}$, [C]=s/m^2
a=the radius of the inner body, $[a]$ =cm
T_b =the temperature of the inner-body base $\approx$ pool water temperature
ρ =the density of the inner body, $[\rho]$ =g/cm^3
Q =the volumetric heating, $[Q]$ = W/cm^3
k_b =thermal conductivity of the inner body, $[k_b]$ = W/(cm $\cdot$ K)
c_v =specific heat of inner body, $[c_v]$ = J/(g $\cdot$ K).

The variable k_e is the effective conduction coefficient $[k_e]$ = W/(cm^2 $\cdot$ K) of the gas gap, which accounts for all three mechanisms of heat transfer.

The boundary conditions $\mathrm{d}T/\mathrm{d}x = 0$ (at $x = L$) and $T = T_b$ (at $x = 0$) are used to solve for the solution of equation (5.2) (Van Nieuwenhove, R. 1996; App.B,Eq.7):

$$T(x) = \frac{Q}{A \cdot k_b} \cdot \left(1 - \frac{\cosh(\sqrt{A} \cdot (L - x))}{\cosh(\sqrt{A} \cdot L)}\right) + T_b. \tag{5.3}$$

At $x = L$ (the approximate location of the hot junction):

$$T(L) = \frac{Q}{A \cdot k_b} \cdot \left(1 - \frac{1}{\cosh(\sqrt{A} \cdot L)}\right) + T_b \tag{5.4}$$

so the difference in hot and cold junction temperatures, $\Delta T = T(L) - T_b$, can be related to the volumetric heating Q with (Van Nieuwenhove, R. 1996; App.A,Eq.27):

$$\frac{Q}{\Delta T} = \frac{A \cdot k_b}{\left(1 - \frac{1}{\cosh(\sqrt{A} \cdot L)}\right)}. \tag{5.5}$$

Equation (5.5) has units of,

$$\left[\frac{Q}{\Delta T}\right] = \frac{\mathrm{W}}{\mathrm{cm}^3 \cdot \mathrm{K}}, \tag{5.6}$$

and can be expressed in the more convenient units of W/g using the definition of C:

$$C = \frac{c_v \cdot \rho}{k_b} \tag{5.7}$$

$$k_b = \frac{c_v \cdot \rho}{C} \tag{5.8}$$

$$\frac{Q}{\Delta T} = \frac{A \cdot k_b}{1 - \frac{1}{\cosh(\sqrt{A} \cdot L)}} \tag{5.9}$$

$$\frac{Q}{\Delta T \cdot \rho} = \frac{A \cdot c_v}{C \cdot \left\{1 - \frac{1}{\cosh(\sqrt{A} \cdot L)}\right\}}, \tag{5.10}$$

and can be simplified further using the following equations (SCK-CEN 2009; Tab 7):

$$A' = A \cdot L^2 \tag{5.11}$$

$$C' = C \cdot L^2 \tag{5.12}$$

$$\frac{Q}{\Delta T \cdot \rho} = \frac{A' \cdot c_v}{C' \cdot \left\{1 - \frac{1}{\cosh(\sqrt{A'})}\right\}}. \tag{5.13}$$

Equation (5.13) is the steady-state calibration factor; the GT user can multiply this factor by the temperature difference between the hot and cold junctions, as predicted by the differential thermocouple, and obtain the model's predicted heating value in units of W/g.

However k_e and thus A' are unknown and the heat-transfer model itself is only an approximation of reality. For example, the temperature at the base of the GT inner body is actually higher than T_b (the pool water temperature) since nuclear heating is also present in the body. To account for the unknown k_e and compensate for approximations in the model, the constants A' and C' are adjusted to make the calibration factor correspond to experimental data using techniques described in the following section.

5.5.2 Experimental dip test and steady-state calibration factor

SCK-CEN uses a two-step dip of the GT (hot-to-cold) to determine the unknown constants A' and C' in the steady-state calibration factor (equation (5.13)) and the GT's dominant thermal time constant.

The GT is placed in boiling water or oven to bring the entire GT (inner and outer body) to approximately 100 °C. The GT is then quickly removed from the boiling water and placed into an ice bath. The thermocouple's output is recorded while the inner and outer bodies cool to approximately 0 °C.

The GT inner body temperature $T(x,t)$ can be modelled similar to equation (5.2), without volumetric heat generation as (Van Nieuwenhove, R. 1996; App.A,Eq.1):

$$\frac{\mathrm{d}^2T}{\mathrm{d}x^2} - A \cdot T = -B + C \cdot \frac{\mathrm{d}T}{\mathrm{d}t}. \tag{5.14}$$

where all variables are the same as equation (5.2) except $B = \frac{2 \cdot k_e}{a \cdot k_b} \cdot T_b$ because $Q = 0$.

Assuming a uniform initial temperature of $T(x,t) = T_i$ for all x and $t < 0$, and $\mathrm{d}T/\mathrm{d}x = 0$ at $x = L$ for all t and $T(0,t) = 0$ for $t > 0$, the temperature of the inner-body tip ($x = L$) is (Van Nieuwenhove, R. 1996; App.A,Eq.10):

$$T(L,t) = \sum_{n=0}^{\infty} \frac{4 \cdot T_i}{\pi} \cdot \frac{1}{2n+1} \cdot (-1)^n \cdot \mathrm{EXP}\left(-1 \cdot \frac{\left[\frac{(2n+1)\pi}{2L}\right]^2 + A}{C} \cdot t\right), \tag{5.15}$$

and substituting in the equations for A' and C' gives (SCK-CEN 2009; Tab 7):

$$T(L,t) = \sum_{n=0}^{\infty} \frac{4 \cdot T_i}{\pi} \cdot \frac{1}{2n+1} \cdot (-1)^n \cdot \mathrm{EXP}\left(-1 \cdot \frac{\left[\frac{(2n+1)\pi}{2}\right]^2 + A'}{C'} \cdot t\right). \tag{5.16}$$

This equation is fit to the experimental GT dip-test experimental data. Using only the first four terms ($n = 3$) of the infite sum is thought to be an acceptable approximation (SCK-CEN 2009; Tab 7). SCK-CEN uses A' and C' as the curve fitting parameters; A' is unknown because k_e is unknown, and C' is treated as an unknown because the effective values of c_v, ρ and k_b are unknown since the GT inner body is not a uniform cylinder but a 304L cylinder with a thermocouple in its center.

Following a dip test, the SCK-CEN found the 4-term-version of equation (5.16) fit the GT cooling data of GT-20 best when $A' = 1.24 \pm 0.03$, $C' = 68.0 \pm 0.5$ s when $T_i = 99.2 \pm 0.08$ °C (SCK-CEN 2009); Figure 5.7 plots equation (5.16) using the fit parameters A' and C'.

Note that the domain of the plotted function in Figure 5.7 is $1 \leq t \leq 200$ because the function does not equal the correct $T_i = 99.2\,^{\circ}\mathrm{C}$ at $t = 0$.

The resulting steady-state calibration factor of GT-20 is calculated using equation (5.13) and the experimentally-determined values of A' and C' (SCK-CEN 2009; Tab 7):

$$\frac{\Delta T \cdot \rho}{Q} = 44.7 \pm 4.5 \frac{^{\circ}\mathrm{C}}{\mathrm{W/g}}. \tag{5.17}$$

5.5.3 The GT's thermal response

The time constant of the GT response is an important parameter in describing the response of the GT. Fitting a four term version of equation (5.16) to the dip test data results in four time constants. The first of the four dominates the description of the temperature decay, especially at later stages of cooling (Van Nieuwenhove, R. 1996; App.A,Pg.7). It is so dominant, the time constant of the GT can be described by the first exponential term only. This time constant, which corresponds to n=0, is expressed as:

$$\tau_0 = \frac{C'}{(\frac{\pi}{2})^2 + A'}. \tag{5.18}$$

Using the values of A' and C' determined by SCK-CEN and equation (5.18), the dominant time constant of GT-20 is $\tau_0 = 18.4 \pm 0.2$ s (SCK-CEN 2009; Tab 7).

The dominant time constant τ_0 can also be determined by plotting the GT dip-test temperature decay on a semi-log plot, the time constant is determined by the slope (Liu 1994; 4). The semi-log plot of Figure 5.7 shows the dominant time constant is visible on the domain $t > 10$ s where the plot appears linear. The slope of this linear curve has been confirmed by both hand calculations and curve fitting (a single exponential term) to agree with $\tau_0 = 18.4 \pm 0.2$ s.

As a check, another dip test of GT-20 was conducted at McMaster from boiling water to an ice water. The raw GT signal is plotted in Figure 5.8.

An exponential function of the form $T(t) = a\mathrm{e}^{-b \cdot t}$ was fit with gnuplot to the data between $15 \leq t \leq 50$ s where the semi-log plot is linear (Williams and Kelley 2015). The resulting time constant is $\tau_0 = 20$ s which confirms the order of magnitude of τ_0 calculated by SCK-CEN; the $\tau_0 = 18.4 \pm 0.2$ s value calculated by SCK-CEN is assumed to be the correct value.

5.5.4 The transient calibration equation

The previous sections demonstrated how the thermal time constant in water, and the steady-state calibration factor of GT-20 was determined. This section focuses on the development of an equation applicable to non-steady-state conditions; this equation is an expression of the time-dependent heating, $Q(t)$.

In conditions where the internal thermal resistance of a body is small relative to the resistance of heat moving into the environment, the lumped-heat-capacitance method is used to describe the time-dependent temperature response, $T(t)$, of an object as it changes from an initial temperature of T_0 to a new temperature of T_∞ according to the form (Kreith and Bohn 2001; 118):

$$\frac{T(t) - T_\infty}{T_0 - T_\infty} = \mathrm{e}^{-\frac{1}{\tau}t}. \tag{5.19}$$

Using this model, the minimum time required for the GT-20 to reach 99.9% of a specific T_∞ is $\ln(0.001) * (-18.4\mathrm{s}) = 127$ s; similarly, the same amount of time is required to reach a new steady-state, associated with a new Q. Thus, 127 s is considered the time required for the GT to fully respond to a specific quantity of heating.

However, knowing τ and the steady-state calibration factor is of little use for a GT signal which is continuously changing. For example, imagine a simple step change of the heating function $Q(t)$ from Q_1 to Q_2 at time t_{step}. Assume a steady initial GT signal corresponding to Q_1; one would be required to wait between t_{step} and $t_{step} + 127$ s to employ the steady-state calibration factor to determine Q_2 from the then-steady GT signal. Furthermore, if $Q(t)$ itself were continuously changing so would the GT signal, and by definition the GT would never reach conditions where the steady-state calibration factor were valid. Additionally, the in-core nuclear heating $Q(t)$ is known to be continuously variable.

To develop an expression for $Q(t)$, refer to equation (5.2) and (5.14). Notice the only difference between the two is the presence of the time-derivative term $T(t, x)$, and the definition of the constant B. The constant's definition changes between equations because Q (itself assumed a constant) is assumed to be $Q = 0$ in equation (5.14). When combined, these equations contain all the information required to describe the time-dependent nuclear heating $Q(t)$:

$$\begin{aligned}
\frac{\mathrm{d}^2T(x,t)}{\mathrm{d}x^2} \; - \; A \cdot T(x,t) &= -B + C \cdot \frac{\mathrm{d}T(x,t)}{\mathrm{d}t} \\
\frac{\mathrm{d}^2T(x,t)}{\mathrm{d}x^2} \; + \; \left(\frac{2k_e}{ak_b}\right) T(x,t) &= \left(-\frac{2k_e}{ak_b}T_b - \frac{Q(t)}{k_b}\right) + \left(\frac{c_v\rho}{k_b}\right) \frac{\mathrm{d}T(x,t)}{\mathrm{d}t},
\end{aligned} \tag{5.20}$$

which is rearranged to solve for $Q(t)$:

$$\frac{Q(t)}{k_b} = -\frac{2k_e}{ak_b}T_b + \frac{2k_e}{ak_b}T(x,t) + \frac{c_v\rho}{k_b}\frac{\mathrm{d}T(x,t)}{\mathrm{d}t} - \frac{\mathrm{d}^2T(x,t)}{\mathrm{d}x^2} \tag{5.21}$$

$$Q(t) = -\frac{2k_e}{a}T_b + \frac{2k_e}{a}T(x,t) + c_v\rho\frac{\mathrm{d}T(x,t)}{\mathrm{d}t} - k_b\frac{\mathrm{d}^2T(x,t)}{\mathrm{d}x^2} \tag{5.22}$$

$$Q(t) = \frac{2k_e}{a}\left(T(x,t) - T_b\right) + c_v\rho\frac{\mathrm{d}T(x,t)}{\mathrm{d}t} - k_b\frac{\mathrm{d}^2T(x,t)}{\mathrm{d}x^2}. \tag{5.23}$$

This equation can be expressed in terms of the emperical parameters A' and C':

$$\frac{A'}{C'} = \frac{A}{C} = \frac{2k_e}{ak_b}\frac{k_b}{c_v\rho} = \frac{2k_e}{ac_v\rho} \tag{5.24}$$

$$k_e = \frac{A'}{C'}\frac{ac_v\rho}{2}, \tag{5.25}$$

and can express $Q(t)$ in the convenient units of W/g by dividing by ρ:

$$\frac{Q(t)}{\rho} = \frac{A'}{C'}c_v\left(T(x,t) - T_b\right) + c_v\frac{\mathrm{d}T(x,t)}{\mathrm{d}t} - \frac{k_b}{\rho}\frac{\mathrm{d}^2T(x,t)}{\mathrm{d}x^2},$$

which is evaluated at the hot junction axial position x_{T_H} and expressed with two modifying constants D and E:

$$\frac{Q(t)}{\rho} = \left(\frac{A'}{C'}c_v\left(T(x_{T_H},t) - T_b\right) + c_v\frac{\mathrm{d}T(x_{T_H},t)}{\mathrm{d}t} - \frac{k_b}{\rho}\frac{\mathrm{d}^2T(x_{T_H},t)}{\mathrm{d}x^2}D\right)/E. \tag{5.26}$$

Throughout this thesis this equation is refered to as the transient calibration equation.

5.5.5 Solving the transient calibration equation

Equation (5.26) is solved for $Q(t)$ ρ, at each experimental GT signal datum.

The first derivative in equation (5.26) can be calculated with the finite difference approximation (Cheney and Kincaid 1999; 173):

$$\frac{\mathrm{d}T(x_{T_H},t)}{\mathrm{d}t} = \frac{1}{2\Delta t}[T(x_{T_H},t+\Delta t) - T(x_{T_H},t-\Delta t)], \tag{5.27}$$

where Δt is the time step of the experimental GT data. This rate of change refers to the hot junction temperature $T(x_{T_H},t)$, and is equal to the rate of change of the GT signal $\Delta T = T(x_{T_H},t) - T_b$ when T_b is constant.

The second derivative in equation (5.26) at x_{T_H} is calculated with the finite difference approximation (Cheney and Kincaid 1999; 180):

$$\frac{\mathrm{d}^2T(x_{T_H},t)}{\mathrm{d}x^2} = \frac{1}{h^2}[T(x_{T_H}+h,t) - 2T(x_{T_H},t) + T(x_{T_H}-h,t)], \tag{5.28}$$

where h is the distance between axial nodes on the GT inner body where $T(x,t)$ is defined. Notice $\mathrm{d}^2T(x_{T_H},t)/\mathrm{d}x^2$ is always 0 at $x = L$. Thus, when solving equation (5.26) the hot junction possition cannot be assumed to be $x = L$, its position at x_{T_H} must be determined with a best estimate.

Calculating $\mathrm{d}^2T(x_{T_H},t)/\mathrm{d}x^2$ with the above equation requires knowing the axial temperature distribution at each time t. The steady-state axial temperature profile of the GT's inner body for three Q values is plotted in Figure 5.9, as calculated by equation (5.3). Notice the first and second derivative with respect to x changes for each Q at any given x.

At each experimental GT signal datum t an estimate of nuclear heating Q_{estimate} was made using the rearranged steady-state equation (5.3):

$$Q_{\text{estimate}} = \frac{(T(x_{T_H},t) - T_b)A \cdot k_b}{\left(1 - \frac{\cosh(\sqrt{A}\cdot(L - x_{T_H}))}{\cosh(\sqrt{A}\cdot L)}\right)}, \tag{5.29}$$

this estimate is then used in equation (5.3) to describe the approximated axial temperature profile at time t:

$$T(x) = \frac{Q_{\text{estimate}}}{A \cdot k_b} \cdot \left(1 - \frac{\cosh(\sqrt{A}\cdot(L-x))}{\cosh(\sqrt{A}\cdot L)}\right) + T_b. \tag{5.30}$$

Within this thesis 100 nodes ($h = 0.015$ cm) are used to describe the axial profile and T_b is used as a boundary condition.

The use of equation (5.29) introduces a systematic error into equation (5.26). It was found that including a modifying constant of $D = 1.25$ corrects $\mathrm{d}^2T(x_{T_H},t)/\mathrm{d}x^2$ and increases the dynamic response of equation (5.26); $E = 1.1645$ is required to correct for the error introduced by D.

5.5.6 Evaluating the transient calibration equation

The transient calibration equation (5.26) can be confirmed against equation (5.17) in steady-state conditions since both should predict the same nuclear heating Q for any given $\Delta T = T_H - T_C$. Assuming the following physical constants:

$L = 1.5$ cm
$A' = 1.24 \pm 0.03$
$C' = 68.0 \pm 0.5$ s
$c_v = 0.5$ J/(g $\cdot$ K)
$\rho = 8.0$ g/cm^3
$x_{T_H} = 1.38 \pm 0.01$ cm,

where unspecified uncertainties are assumed to be zero. The value of x_{T_H} was measured from an engineering drawing of the SCK-CEN GT and the associated uncertainty is the smallest division of the instrument.

Since the specific values of A' and C' were established experimentally and they are also defined as functions of material properties, A' and C' are defining effective material properties. Using the definition of C', throughout this thesis k_b is defined as:

$$k_b = \frac{c_v \rho L^2}{C'} = 0.132\,\mathrm{W/(cm \cdot K)}. \tag{5.31}$$

Assuming $\Delta T = T_H - T_C = 10.0\,^{\circ}\mathrm{C}$ equation (5.26) is solved for Q/ρ using the methods outlined in section 5.5.5, resulting in $Q/\rho = 0.22$ W/g, identical to the prediction of equation (5.17).

Equation (5.26) can also be confirmed against equation (5.20) in transient conditions. Equation (5.20) is solved using the PDEPE PDE solver in MATLAB for a variety of $Q(t)$ functions (The MathWorks 2004). Figure 5.10 (L) shows the constant heating function $Q(t)$ and resulting ΔT response predicted by equation (5.20) when initial conditions are $Q(t) = 0$ W/cm^3 and $\Delta T = 0$; Figure 5.10 (R) shows the temperature response of the entire inner body length (relative to the constant base temperature).

Figure 5.11 (L) and (R) show the same repsonses to a variable $Q(t)$.

The merit of equation (5.26) is obvious when viewing the $Q(t)/\rho$ predicted in comparison with that predicted by equation (5.17), as in Figure 5.12 for constant (L) and variable heating (R).

Figure 5.13 shows the effects of the constants D and E in equation (5.26); without these corrective constants the dynamic response of equation (5.26) is worse, as a result of the $\mathrm{d}^2T(x_{T_H}, t)/\mathrm{d}x^2$ term being underpredicted by the steady-state approximation technique discusses in the previous section.

5.6 Self-heating of the SCK-CEN GT

The purpose of using the GT as a dosimeter is to determine the nuclear heating caused by the background in-core radiation field. Energy released by the GT material itself, such as by nuclear reactions with non-zero Q values, can contribute to heating of the GT. This self-heating must be estimated to be subtracted from the GT signal to obtain an estimate of the heating induced by the background in-core radiation field. This study of GT self-heating seeks to determine the energy absorbed by the GT inner body, after it has been released by the GT material itself as a result of nuclear reactions in the GT material.

Glascock's Tables for Neutron Activation Analysis implies (n,γ), (n,α), (n,2n) and (n,p) reactions are common during the neutron irradiation of most materials (Glascock 1996). Fission (n,f) reactions and photo-nuclear reactions are known to be insignificant at in-core neutron and photon energies. Therefore only (n,γ), (n,α), (n,2n) and (n,p) reactions were considered in this self-heating study.

5.6.1 Application of the nuclear heating equation

Determining the GT self-heating is a simple application for the nuclear heating equation, where the entire GT geometry is considered instead of the arbitraty geometry V shown in Figure 4.1. The volume of interest, G, in this application is the GT inner body as shown in Figure 5.14.

When seeking to calculate the GT self-heating, the nuclear heating equation (4.21) can be simplified for the following reasons:

- the heating by external sources are not to be considered, only the heating by radiation emitted after nuclear reactions within the GT material
- GT dimensions are small so $\phi(\vec{r}, t)$ is assumed to be uniform over $\vec{r}$ within V; $\phi(\vec{r}, t)$ is also assumed to be constant with time, thus $\phi(\vec{r}, t) = \phi$

- initial inventory of all activation products are assumed null, $N^j(\vec{r},0)=0$
- since ϕ is not position-dependent the d^3r volumes can be divided according to the GT material volumes; there are 3 material volumes indexed by mat, the 304L, 316L and alumina/TC volumes
- for gamma emissions, 75 ${}^kE(|\vec{r}_G-\vec{r}|,E')$ terms are required for the 3 material volumes (indexed by mat) and 25 energy groups (indexed by k)
- reaction rate index r considers only the (n,γ), (n,α), (n,2n) and (n,p) reactions; noted as C, ALPHA, 2n, and p.

Since ϕ is assumed constant and $N^j(\vec{r},0)=0$, the ODE in equation (4.21) can be eliminated and replaced with an expression for $N^j(\vec{r},t)$ from section 2.5.1; the delayed source and heating resulting from isotope j can be rewritten as:

$$N^j(\vec{r},t) = \frac{N^i(\vec{r})\sigma_r^i(\vec{r})\phi(\vec{r})}{\lambda^j}\left[1-\mathrm{e}^{-\lambda^j t}\right] \tag{5.32}$$

$$S^j_{r\mathrm{D}}(\vec{r},E',t) = p^j\lambda^j N^j(\vec{r},t)\mathrm{d}^3r \tag{5.33}$$

$$S^j_{r\mathrm{D}}(\vec{r},E',t) = p^j N^i(\vec{r})\sigma^i_{r(\vec{r})}\phi\left[1-\mathrm{e}^{-\lambda^j t}\right]\mathrm{d}^3r \tag{5.34}$$

$$H^j_{r\mathrm{D}}(\vec{r},t) = \Sigma^i_r(\vec{r})\phi(\vec{r})\left[1-\mathrm{e}^{-\lambda^j t}\right]\sum_e({}^eE(|\vec{r}_G-\vec{r}|,E'))({}^ep^j_{r\mathrm{D}})\mathrm{d}^3r. \tag{5.35}$$

Implementing the above simplifications results in a much simpler nuclear heating equation. The simplified equation is written here, considering only the gamma emissions which result from (n,γ) reactions:

$$H(\vec{r}_G,t)=\phi\sum_{mat}^{3}V_{mat}\sum_i\Sigma^i_{\mathrm{C}}(\vec{r})\sum_k({}^kE(|\vec{r}_G-\vec{r}|,E'))({}^kp^i_{\mathrm{CP}})+$$
$$\phi\sum_{mat}^{3}V_{mat}\sum_{ji}\Sigma^i_{\mathrm{C}}(\vec{r})\left[1-\mathrm{e}^{-\lambda^j t}\right]\sum_k({}^kE(|\vec{r}_G-\vec{r}|,E'))({}^kp^j_{\mathrm{CD}}), \tag{5.36}$$

where CP indicates prompt capture and CD delayed capture; the index ij indicates both i and j change together, since j is the isotope created by (n,γ) reaction in i. Similar equations can be derived for the other reactions and emission species.

5.6.2 Mean transported energy

Figure 5.15 shows the 3 GT material volumes considered in self-heating calculations: the 304L, 316L and alumina/TC volumes. These volumes are considered seperately as sources of self-heating radiation.

The very small inner diameter of the 316L TC sheath wire, the TC and alumina materials have been combined into a single material description using the correct total number of atomic populations.

The mean transported energy terms are required for each material volume. For gammas, 25 mean transported energy terms are required for each material volume, corresponding to the 25 group photon energy bin structure presented in section D.2. Thus 75 dedicated MCNP6 photon-transport calculations have been completed, one for each transported energy term.

The MCNP6 model of the GT body was surrounded by a 10 cm-radius sphere filled with water (ρ=0.9984 g/cm^3) to model gamma reflection. A thorough model of reflection would include the

entire MNR core but reflection is also dependent upon the GT's in-core location; the water sphere is thought to be a fair universal approximation.

For each ${}^{k}E(|\vec{r}_G - \vec{r}|, E')$ term, a defined gamma source term sampled the point of origin uniformly within the material region, and uniformly within the energy bin. In each calculation, MCNP6 was run in mode p with F6 energy deposition tallies averaged over the GT's inner-body volumes (labeled as G in Figure 5.15).

Neutron interactions with the Ar gas have been assumed insignificant. The GT lead wire beyond the body was not included in the geometry.

Since ϕ was assumed not to be position-dependent, the flux within each of the 3 material volumes were not calculated separately.

Charged particles are assumed to be deposited within their volume of origin, so $E(|\vec{r}_G - \vec{r}|, E')$ terms are assumed to be zero for d^3r volumes outside G and equal to E' within G. Thus only charged particles emitted by volume G were considered.

5.6.3 Calculation of reaction rates with MCNP6 FM card

The reaction rates $\phi\Sigma_r^i(\vec{r})$ of (n,γ), (n,p), (n,α) and (n,2n) for each isotope i contained within the GT have been obtained using the MCNP6 MNR Reference Core model.

The reaction rates were calculated using the MCNP6 FM tally multiplier card which multiplies the neutron flux tally by the microscopic cross section of the specified reaction rate. The ENDF/B reaction labels used in the FM card are MT=102 for (n,γ), MT=103 for (n,p), MT=107 for (n,α) and MT=16 for (n,2n). The FM product is calculated over the specified volume in the following form (Pelowitz 2013; 3-204):

$$FM_{\text{product}} = \int_E \varphi(E)R(E)\mathrm{d}E, \tag{5.37}$$

where $\varphi(E)$ is energy dependent neutron fluence averaged over the specified volume, in units of n/cm^2, and $R(E)$ the energy-dependent operator (in this case equal to each reactions's microscopic cross-section) in units of barns, thus FM_{product} is unitless if $R(E)$ are expressed in units of cm^2.

As all other MCNP6 tallies, FM_{product} is implicitly "per starting particle" and must be scaled to the reactor power with a factor C which has units 1/s and which represents the number of fission neutrons created per second (X-5 Monte Carlo Team 2008; 2-81); scaling the Reference Core tallies and calculating C is discussed in section B. Since $R(E)$ represents only the microscopic cross-section, the atomic concentration N_i must also be included in the expression of reaction rate:

$$\Sigma_r^i(\vec{r})\phi = N_i C \left(\frac{1\times10^{-24}\mathrm{cm}^2}{1\text{ barn}}\right)\int_E \varphi(E)R(E)\mathrm{d}E. \tag{5.38}$$

Reaction rate units are 1/cm^{3}s.

The MCNP6 ENDF71x library was selected for all GT isotopes except for ^{18}O which is not contained in the ENDF71x library; this is an acceptable approximation since this isn't an abundant isotope.

The GT geometry and materials were not present within the MCNP6 Reference Core model during the calculation of the neutron flux and associated FM tallies. These quantities were volumetrically-averaged over cylindrical environments at appropriate GT locations. The diameters of the volumes were equal to the water material at the locations being considered, 3.3274 cm, and equal in height to the GT, 5.7 cm. It was assumed the volume-averaged neutron flux is equal to that which would exist inside the GT. The advantage of this method is not being required to describe the full GT geometry; the disadvantage is the reaction rates are "infinitely diluted" and the neutron spectra does not include the very small changes which occur within an irradiated GT geometry; section E.4.4 discusses the dependency of neutron spectra on geometry depth.

5.6.4 Neutron capture - prompt radiation data

Within the self-heating calculations it was assumed neutron capture by isotope i, described as ${}^{A}_{Z}\mathrm{X}$, creates the isotope j, described as ${}^{A+1}_{Z}\mathrm{X}$.

The radiation energies released by isotope i upon neutron capture and the associated fractional probability are available from the CapGam library of thermal neutron capture gamma rays (National Nuclear Data Center 2015). CapGam shows many prompt gammas may be realeased, for example 349 gammas are listed for ^{59}Co by CapGam.

The majority of the prompt-gamma data for isotopes contained within the GT material have been retrieved from CapGam. The 3 most probable gammas for each isotope contained within the GT are given in Table 5.1 along with $I_{\max}$ which is CapGam's variable indicating the probability of the most probable gamma; the probability of all other gammas are expressed relative to $I_{\max}$.

Prompt-gamma data for some isotopes are incomplete in CapGam; this missing data was retrieved from the IAEA Database of Prompt Gamma Rays from Slow Neutron Capture for Elemental Analysis and is highlighted in Table 5.1 (IAEA 2015). The IAEA reference does not present the emission probability of specific prompt gammas as CapGam, instead it presents the "partial elemental capture cross section" which is defined as (IAEA 2007; Pg.5):

$$\sigma_{\gamma}^{Z}(E_{\gamma}) = \theta \cdot P(E_{\gamma}) \cdot \sigma_{O} \tag{5.39}$$

where:

$P(E_{\gamma})$ is the probability of producing a gamma ray of energy E_{γ} (IAEA 2007; Pg.6)

σ_O = the 2200 m/s neutron capture cross section; unitless

θ = the isotopic abundance; unitless.

The above equation can then be reorganized to obtain:

$$P(E_{\gamma}) = \frac{\sigma_{\gamma}^{Z}(E_{\gamma})}{\theta \cdot \sigma_{O}}, \tag{5.40}$$

using σ_O and θ as provided by the IAEA database (IAEA 2015); this method has been confirmed by calculating $P(E_{\gamma})$ for a number of isotopes for which this probability is already provided by CapGam.

Notice that the individual emissions are not exclusive, sometimes multiple gammas are emitted; in most cases this leads to the total sum of each fractional probability being greater than unity, which is unnerving when used to dealing with exclusive events whose probabilities sum to unity.

Note the following regarding data retrieved from the IAEA reference:

1. ^{90}Zr, ^{10}B, ^{100}Cd: probabilities per particle are much greater than 100% - which implies multiple photons of the same energy are released per neutron absorption. These isotopes have not been included in any calculations.

2. ^{94}Zr: the three most probable gammas as listed in CapGam do not match the energies given in IAEA data, nor are they presented with associated probabilities, thus the IAEA gamma energies and associated probabilities are used.

Since only elemental carbon is included in the ENDF library, ^{12}C and ^{13}C data are combined with a weighting factor equal to their natural isotopic abundance.

In total, 6578 prompt gammas have been included.

Uncertainties associated with gamma data have not been considered. By using CapGam and the IAEA PGAA it is assumed neutron capture reactions are dominated by thermal captures — which was confirmed by the MCNP6 FM calculations.

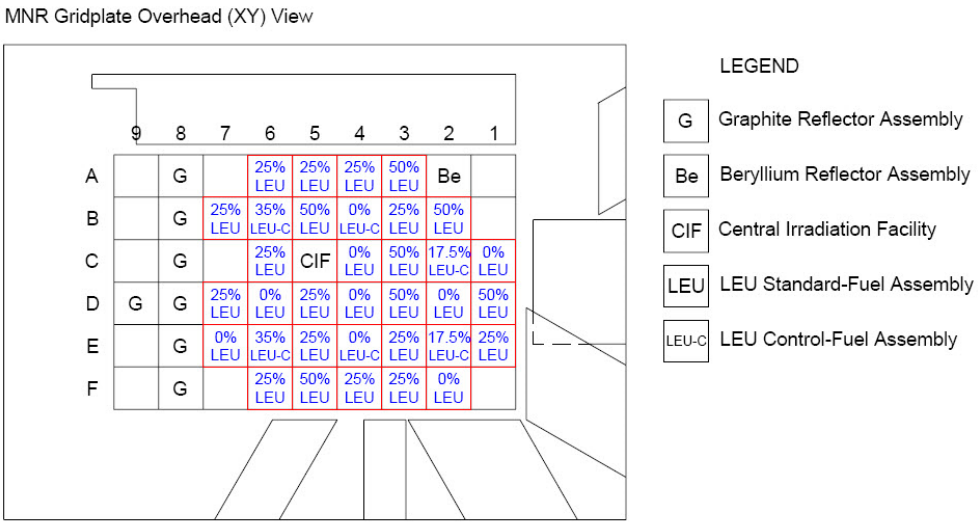

Figure 5.3: The MNR RC configuration (Day 2001).

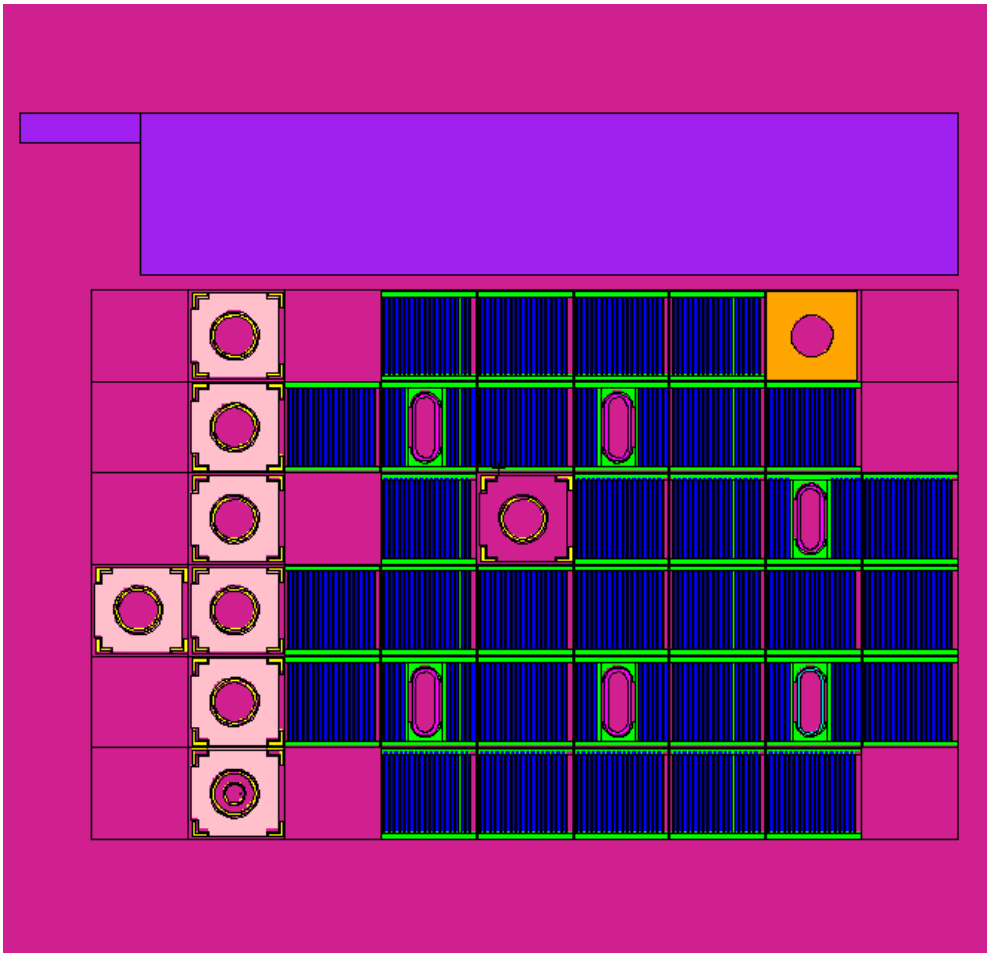

Figure 5.4: A slice of the MCNP6 RC model showing the core's plan view.

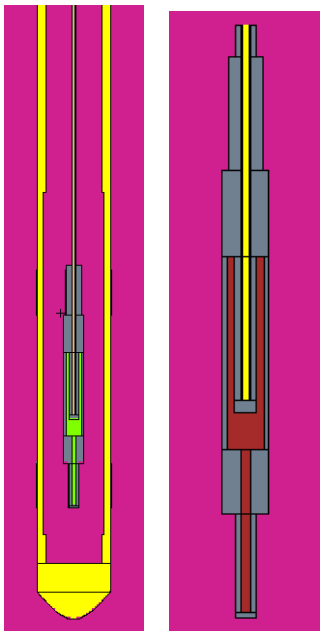

Figure 5.5: (L) vertical slice of the MCNP6 RC model, showing the modelled SCK-CEN GT and instrument rig, (R) a slice of the SCK-CEN GT alone.

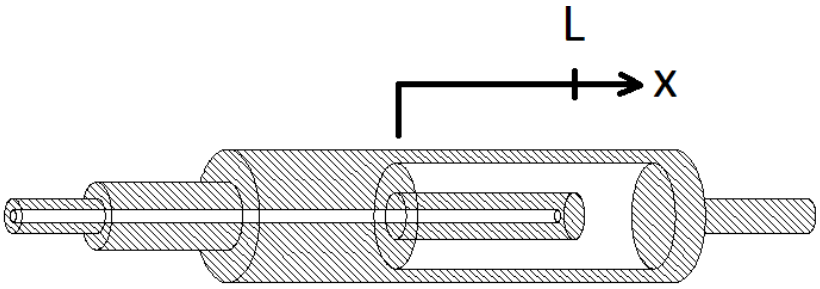

Figure 5.6: Cutaway showing GT inner body.

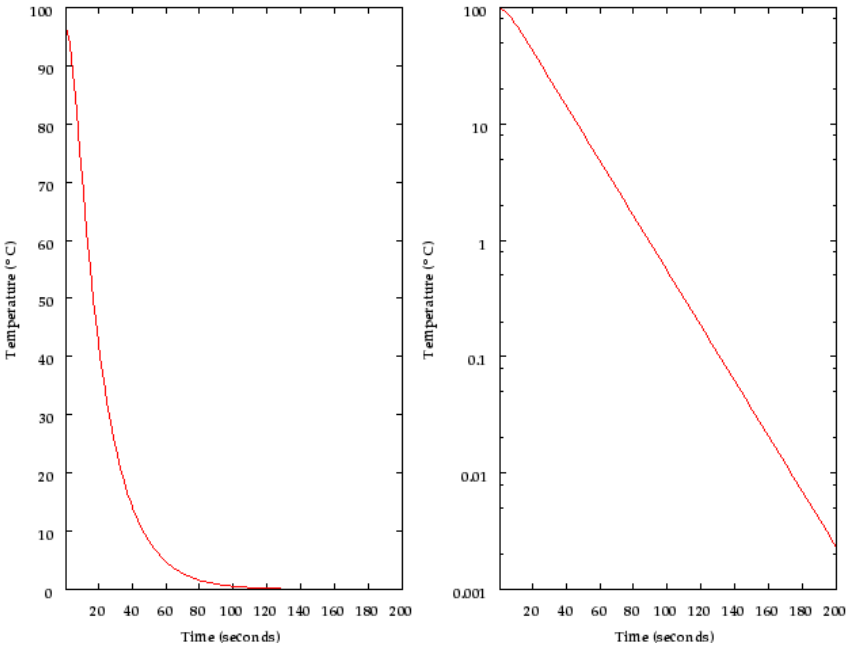

Figure 5.7: The plot made by the first four terms of equation (5.16) with fitting parameters A' and C' as defined by SCK-CEN of GT20, in lin-lin and semi-log format.

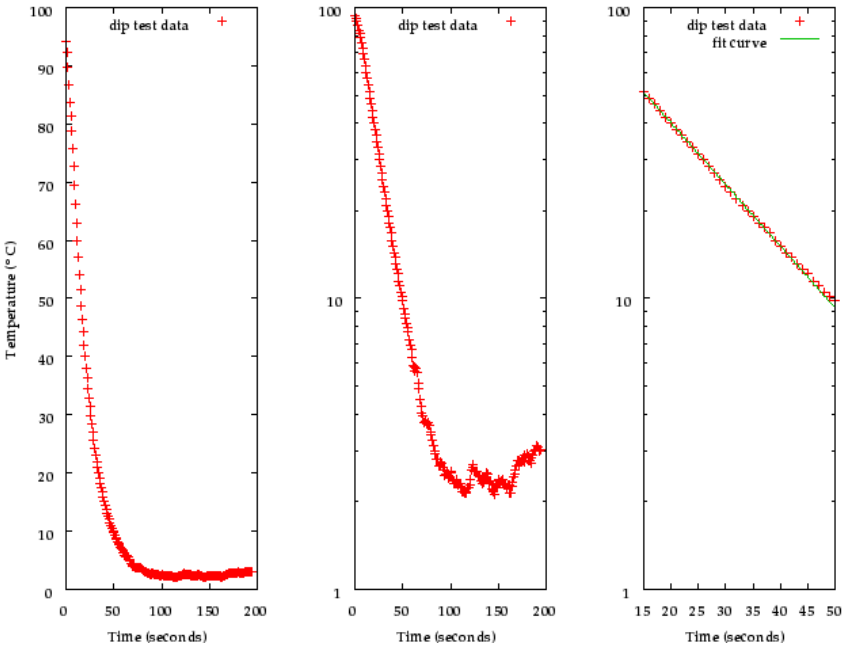

Figure 5.8: (L) and (C) Raw data from dip test on GT-20; (R) The region $15 \leq t \leq 50$ s which is linear on a semi-log plot and an exponential function of the form $T(t) = a \cdot e^{-b \cdot t}$ fit to the data.

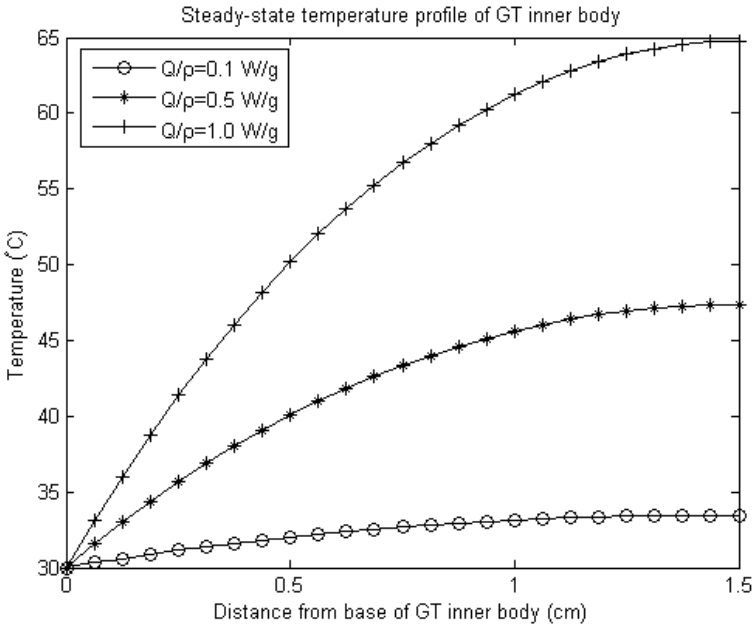

Figure 5.9: GT inner body temperature profiles corresponding to various quantities of nuclear heating.

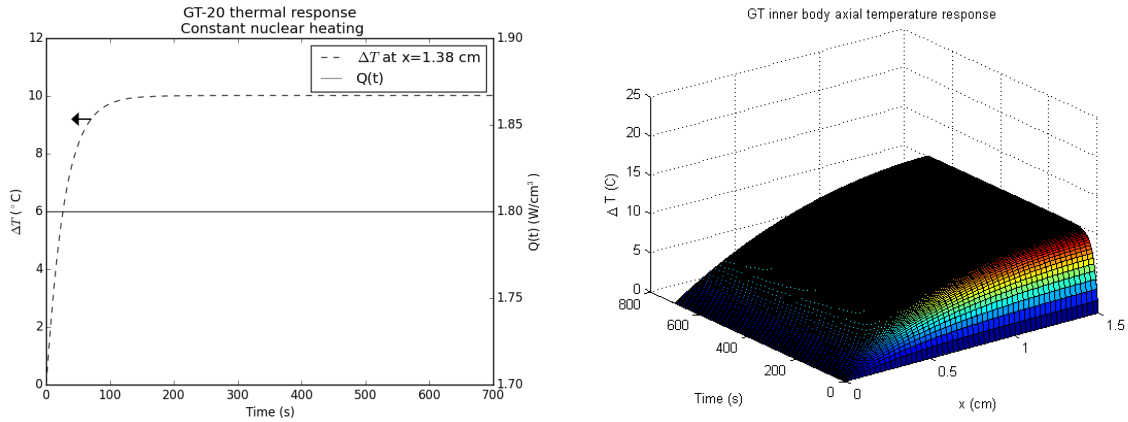

Figure 5.10: (L) Constant heating function and resulting ΔT temperature response; (R) associated temperature response of the entire GT inner body.

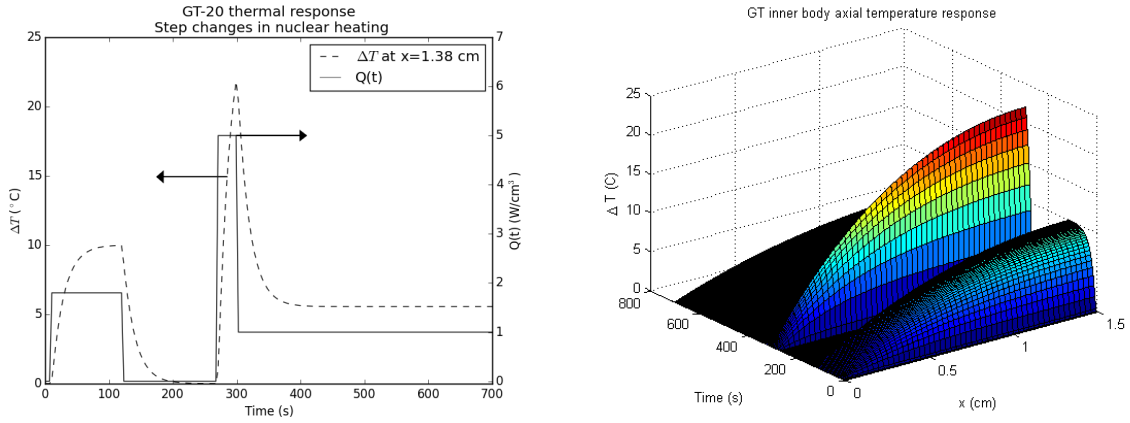

Figure 5.11: (L) Variable heating function and resulting ΔT temperature response; (R) associated temperature response of the entire GT inner body.

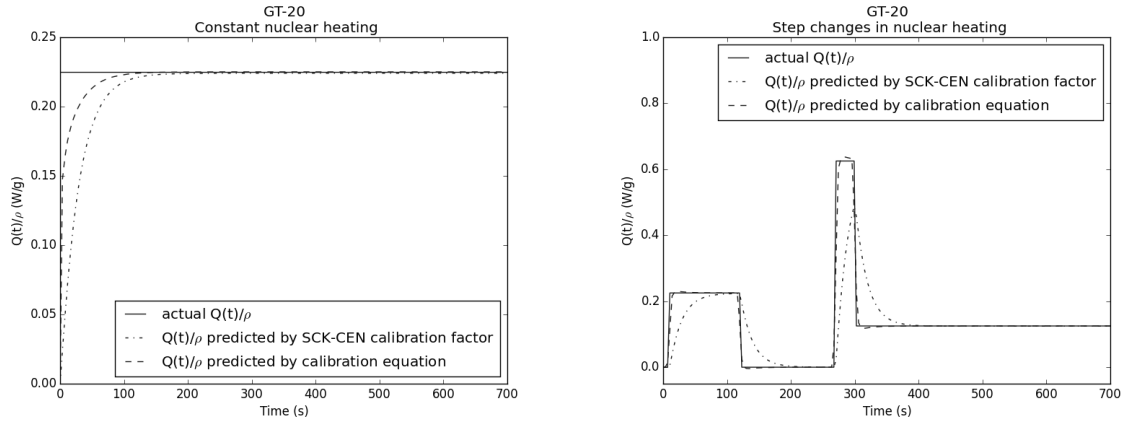

Figure 5.12: Comparison between methods used to obtain $Q(t)/\rho$ with constant (L) and variable heating (R).

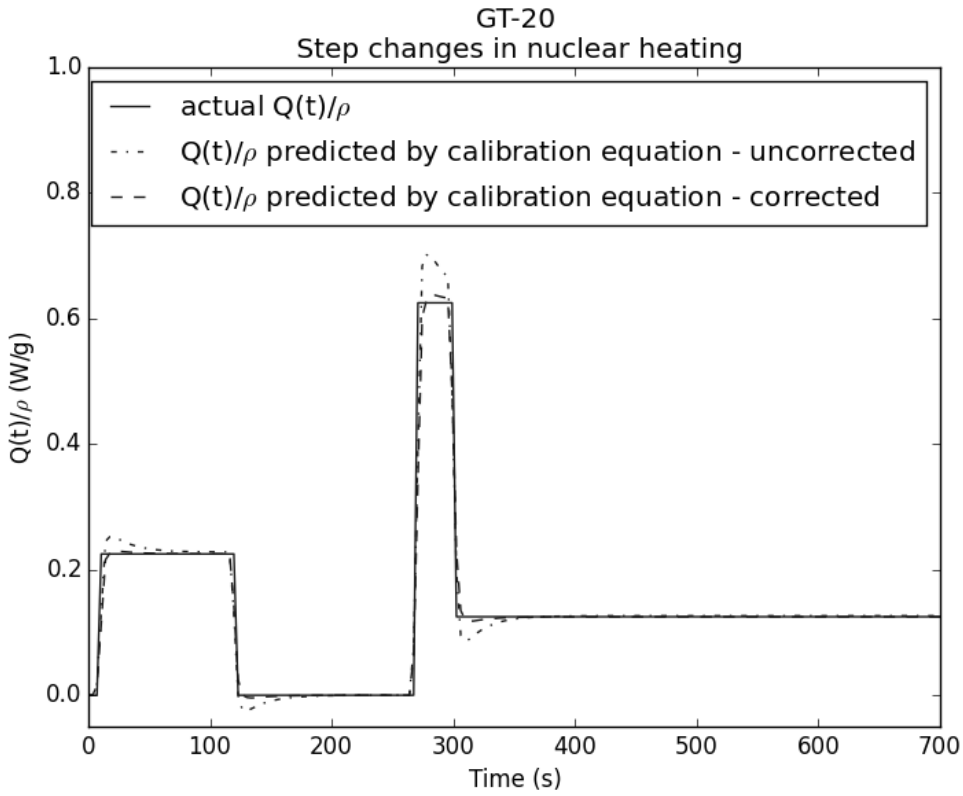

Figure 5.13: Nulcear heating predicted by the calibration factor with and without the constants D and E.

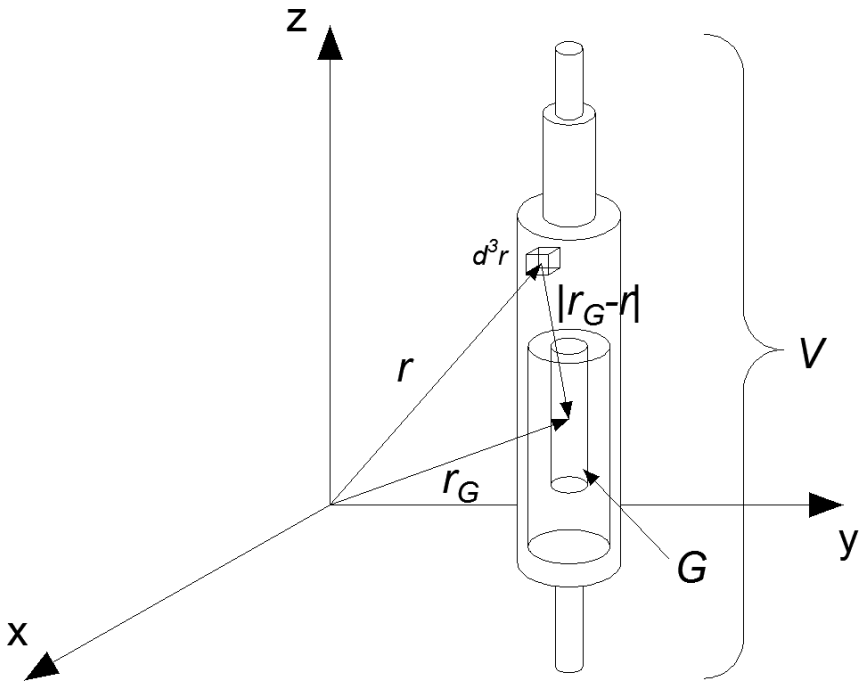

Figure 5.14: The GT body, V, described by discrete volumes d^3r, heats the volume of interest, the GT's inner body, G.

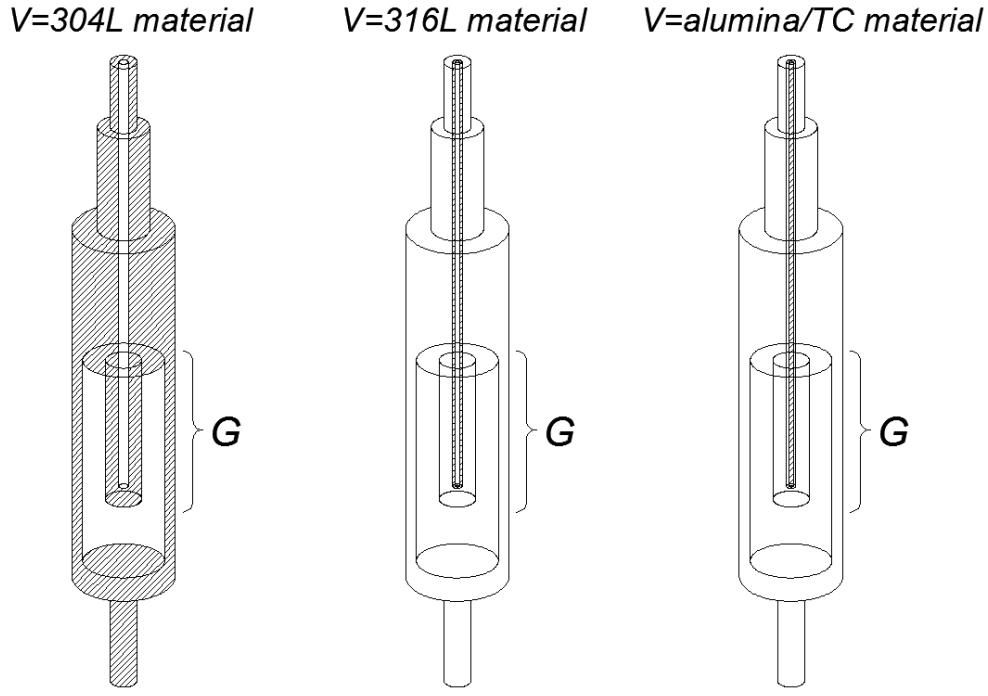

Figure 5.15: The three GT material regions (shaded, not to scale), used to calculate the mean transported energy terms.

GT Material Prompt Neutron Capture Gammas 3 Most Probable Gammas			
	keV	I/Imax (%)	Imax (%)
Ni-58	8998.6	100.0	50.6
	8533.7	47.8	
	464.9	54.1	
Ni-60	7819.6	100.0	52.8
	283.0	65.7	
	7536.6	57.0	
Ni-61	1172.8	100.0	76.0
	875.6	18.8	
	2301.4	13.7	
Ni-62	6838.2	100.0	86.0
	5837.0	7.6	
	155.5	8.1	
Ni-64	6034.8	100.0	67.0
	5787.8	26.4	
	310.2	32.8	
Cr-50	749.0	100.0	84.8
	28.0	43.8	
	8512.2	37.5	
Cr-52	7938.6	100.0	66.6
	2320.9	32.9	
	5618.2	32.3	
Cr-53	834.9	100.0	79.8
	8884.8	55.7	
	9718.8	18.5	
Cr-54	6246.4	100.0	65.8
	6004.4	24.1	
	241.9	39.8	
Fe-54	9297.8	100.0	56.8
	412.0	28.8	
	8886.4	18.6	
Fe-56	7631.2	100.0	29.0
	7645.6	86.2	
	6018.4	34.1	
Fe-57	810.5	100.0	66.0
	863.6	27.4	
	1674.2	20.9	
Fe-58	287.0	100.0	59.0
	727.4	34.2	
	6293.6	79.7	

GT Material Prompt Neutron Capture Gammas 3 Most Probable Gammas			
	keV	I/Imax (%)	Imax (%)
Si-28	3539.0	100.0	70.6
	4934.0	93.3	
	2092.9	27.7	
Si-29	2235.2	100.0	45.6
	3864.9	65.4	
	6743.2	67.4	
Si-30	752.2	100.0	88.3
	2780.6	76.0	
	3054.3	77.1	
Cu-63	7916.3	100.0	33.1
	7638.0	48.9	
	278.2	72.5	
Cu-65	186.0	100.0	36.5
	385.8	46.3	
	465.2	54.4	
C-12	3090.0	100.0	100.0
	4945.3	67.5	
	1860.0	57.0	
C-13	8174.0	100.0	84.0
	6092.4	19.4	
	1586.9	10.1	
Mn-55	26.6	100.0	18.0
	7057.8	61.1	
	7243.8	68.3	
P-31	512.7	100.0	47.2
	636.7	42.4	
	78.1	73.2	
S-32	841.0	100.0	65.5
	2379.6	65.7	
	5420.5	91.6	
S-33	2127.5	100.0	70.0
	1788.8	24.8	
	1176.7	23.6	
S-34	4637.9	100.0	53.0
	2347.7	96.2	
	1572.3	61.1	
S-36	646.2	100.0	93.5
	3657.3	74.9	
	1991.6	25.1	

GT Material Prompt Neutron Capture Gammas 3 Most Probable Gammas			
	keV	I/Imax (%)	Imax (%)
Co-59	58.9	100.0	1.1
	229.7	31.6	
	277.1	29.1	
Al-27	30.6	100.0	27.9
	7724.0	96.1	
	3033.9	31.5	
Na-23	472.2	100.0	90.4
	91.0	49.3	
	869.2	22.6	
Ca-40	1942.6	100.0	88.5
	2001.6	21.4	
	6420.7	49.2	
Ca-42	5886.0	100.0	53.0
	372.7	71.7	
	2046.3	71.7	
Ca-43	1156.9	100.0	97.0
	1126.0	55.8	
	1074.1	11.5	
Ca-44	174.2	100.0	91.3
	1725.7	57.1	
	5515.0	70.5	
Ca-46	2013.6	100.0	100.0
	861.7	12.4	
	5262.1	75.5	
Ca-48	5146.2	100.0	75.0
	2023.2	33.3	
	3123.4	33.3	
Mg-24	585.1	100.0	74.8
	2828.2	75.8	
	3916.9	99.5	
Mg-25	1808.7	100.0	93.0
	1129.6	49.5	
	3831.5	23.4	
Mg-26	2881.7	100.0	66.1
	3561.3	91.8	
	1615.3	25.8	
Zr-90	1204.7	100.0	742.0
	1466.3	86.3	
	2041.7	44.4	

GT Material Prompt Neutron Capture Gammas 3 Most Probable Gammas			
	keV	I/Imax (%)	Imax (%)
Zr-91	334.5	100.0	89.8
	561.0	22.5	
	1405.2	23.2	
Zr-92	266.8	100.0	20.4
	2190.1	48.5	
	1425.0	31.9	
Zr-94	1198.3	100.0	48.4
	1054.8	88.1	
	1892.9	80.1	
Zr-96	1102.7	100.0	420.0
	5574.9	9.8	
	160.9	0.5	
B-10	477.6	100.0	719600.0
	7006.8	0.0	
	4444.0	0.0	
B-11			
Cd-106			
Cd-108			
Cd-110	245.3	100.0	11940.0
	342.2	36.5	
	171.3	20.8	
Cd-111	617.5	100.0	94.4
	851.2	7.6	
	798.1	6.1	
Cd-112			
Cd-113	558.5	100.0	74.4
	651.3	18.9	
	805.9	6.9	
Cd-114			

GT Material Prompt Neutron Capture Gammas 3 Most Probable Gammas			
	keV	I/Imax (%)	Imax (%)
Cd-116			
O-16	870.7	100.0	100.0
	1087.9	82.0	
	2184.5	82.0	
O-17	1982.0	100.0	13.7
	3588.0	37.8	
	822.0	28.9	
O-18	197.1	100.0	96.0
	1356.8	53.1	
	1444.1	2.7	
Mo-92	943.8	100.0	65.0
	7125.2	73.9	
	1492.3	56.9	
Mo-94	204.2	100.0	843.0
	2222.5	42.7	
	7163.9	23.0	
Mo-95	778.3	100.0	62.0
	850.0	21.5	
	847.7	17.1	
Mo-96	481.0	100.0	60.8
	720.5	52.4	
	679.6	24.3	
Mo-97	787.4	100.0	67.0
	722.7	30.7	
	6624.8	16.9	
Mo-98	97.6	100.0	35.0
	351.0	45.7	
	253.3	31.4	
Mo-100	180.7	100.0	10.9
	237.6	87.2	
	157.5	74.5	

Table 5.1: Table showing only the three most probable gammas resulting from thermal neutron capture for the isotopes contained within the GT.

5.6.5 Neutron capture - delayed radiation data

Decay data have been retrieved from NuDat 2.6 for many of the radioactive isotopes created by neutron capture. NuDat 2.6 is an online software which stores nuclear structure and decay data (National Nuclear Data Center 2015); it contains the energy and probability of each decay particle. Conveniently, NuDat 2.6 provides E^j_{CD}, equal to the product of each radiation energy and associated fractional probability per disintegration, in units of MeV/Bq s; these units are equivalent to the more-intuitive MeV/decay.

The data from NuDat 2.6 have been tabulated in Table 5.2 for the isotopes ${}^{A+1}_{Z}\mathrm{X}$ which are radioactive. The decay data of daughter nuclei for which data was missing for the prompt nuclei are not considered.

For each isotope considered, the data retrieved is that of decay from ground state, except ${}^{117}\mathrm{Cd}$ which doesnt decay from ground level. Some isotopes decay from the ground state by more than one mode and the NuDat 2.6 E^j_{CD} quantities include the probabilities of this process.

Not all decay particles have been considered for each isotope; those for which E^j_{CD} is multiple orders of magnitude smaller than the most-energy-intense particles have not been considered. Decay chains have not been investigated beyond the first decay of the isotope created by neutron capture, ${}^{A+1}_{Z}\mathrm{X}$.

NuDat 2.6 uses the mean β energy instead of end-point energy to calculate E^j_{CD}; one could use end-point energy instead in a very conservative estimation of β heating.

Since ${}^{18}\mathrm{O}$ is not included in the ENDF library, neither the prompt gammas resulting from ${}^{18}\mathrm{O}$ neutron capture, nor the decay of the resulting ${}^{19}\mathrm{O}$ are considered.

	Half Life	Decay Mechanism	Decay Intensity (MeV/ Bq s)					HALF LIFE	DECAY CONSTANT
			gamma	beta-	beta+	electron	TOTAL	(seconds)	(1/seconds)
Ni-59	7.60E+04 (years)	electron capture/beta+ emissio	2.315E-03		9.000E-09	4.304E-03	6.619E-03	2.397E+12	2.892E-13
Ni-63	101.2 (years)	beta- emission		1.743E-02			1.743E-02	3.191E+09	2.172E-10
Ni-65	2.51719 (hours)	beta- emission	5.584E-01	6.275E-01		1.096E-04	1.186E+00	9.062E+03	7.649E-05
Cr-51	27.701 (days)	electron capture/beta+ emissio	2.966E-03			3.651E-03	6.617E-03	2.393E+06	2.896E-07
Cr-55	3.497 (minutes)	beta- emission	6.719E-04	1.101E+00			1.101E+00	2.098E+02	3.304E-03
Fe-55	2.744 (years)	electron capture/beta+ emissio	1.623E-03			3.120E-03	4.743E-03	8.653E+07	8.010E-09
Fe-59	44.495 (days)	beta- emission	1.196E+00	1.171E-01			1.313E+00	3.844E+06	1.803E-07
Si-31	157.36 (minutes)	beta- emission	7.015E-04	5.956E-01			5.963E-01	9.442E+03	7.341E-05
Cu-64	12.701 (hours)	electron capture/beta+ emissio or beta- emission	1.811E-01	7.340E-02	4.900E-02	1.957E-03	3.054E-01	4.572E+04	1.516E-05
Cu-66	5.12 (minutes)	beta- emission	9.780E-02	1.067E+00		2.647E-05	1.165E+00	1.615E+08	4.293E-09
C-14	5700 (years)	beta- emission		4.950E-02			4.950E-02	1.798E+11	3.856E-12
Mn-56	2.5789 (hours)	beta- emission	1.683E+00	8.322E-01			2.515E+00	9.284E+03	7.466E-05
P-32	14.268 (days)	beta- emission		6.950E-01			6.950E-01	1.233E+06	5.623E-07
S-35	87.37 (days)	beta- emission		4.876E-02			4.876E-02	7.549E+06	9.182E-08
S-37	5.05 (minutes)	beta- emission	2.947E+00	7.999E-01			3.747E+00	3.030E+02	2.288E-03
Co-60	1925.28 (days)	beta- emission	2.504E+00	9.641E-02		3.631E-04	2.601E+00	1.663E+08	4.167E-09
Al-28	2.245 (minutes)	beta- emission	1.779E+00	1.242E+00			3.021E+00	1.347E+02	5.146E-03
Na-24	14.997 (hours)	beta- emission	4.121E+00	5.546E-01			4.676E+00	5.399E+04	1.284E-05
Ca-41	1.02E+05 (years)	electron capture/beta+ emissio	4.161E-04			2.274E-03	2.690E-03	3.217E+12	2.155E-13
Ca-45	162.61 (days)	beta- emission	1.143E-08	7.690E-02		1.630E-07	7.690E-02	1.405E+07	4.934E-08
Ca-47	4.536 (minutes)	beta- emission	9.481E-01	4.004E-01		6.270E-05	1.349E+00	3.919E+05	1.769E-06
Ca-49	8.718 (minutes)	beta- emission	3.179E+00	8.640E-01			4.043E+00	5.231E+02	1.325E-03
Mg-27	9.458 (years)	beta- emission	8.934E-01	7.020E-01			1.595E+00	5.675E+02	1.221E-03
Zr-93	1.61E+06 (days)	beta- emission	1.464E-01	2.020E-02		2.060E-02	1.872E-01	5.077E+13	1.365E-14
Zr-95	64.032 (hours)	beta- emission	7.328E-01	1.171E-01		2.656E-03	8.525E-01	5.532E+06	1.253E-07
Zr-97	16.749 (seconds)	beta- emission	8.156E+01	7.027E-01		1.384E-02	8.228E+01	6.030E+04	1.150E-05
B-12	0.0202 (hours)	beta- emission		6.353E+00			6.353E+00	2.020E-02	3.431E+01
Cd-107	6.5 (days)	electron capture/beta+ emissio	3.365E-02		2.840E-04	8.295E-02	1.169E-01	2.340E+04	2.962E-05
Cd-109	461.4 (days)	electron capture/beta+ emissio	2.663E-01			8.061E-02	3.469E-01	3.986E+07	1.739E-08
Cd-115	44.56 (hours)	beta- emission	3.312E-02	6.032E-01		7.480E-05	6.364E-01	3.850E+06	1.800E-07
Cd-117	3.36 (seconds)	beta- emission	2.035E+00	1.700E-01			2.205E+00	1.210E+04	5.730E-05
O-19	26.88 (years)	beta- emission	9.397E-01	1.775E+00			2.715E+00	2.688E+01	2.579E-02
Mo-93	4000 (hours)	electron capture/beta+ emissio	1.243E-02			2.983E-02	4.226E-02	1.261E+11	5.495E-12
Mo-99	65.976 (minutes)	beta- emission	1.436E-01	3.859E-01		2.760E-03	5.323E-01	2.375E+05	2.918E-06
Mo-101	14.6	beta- emission	1.424E+00	5.230E-01		2.556E-02	1.973E+00	8.760E+02	7.913E-04

Table 5.2: The energy per decay of each type of radiation emitted from most isotopes contained within the GT.

5.7 Regression analysis of the corrected signal

Once the SCK-CEN GT signal has been corrected for thermal delay and self-heating, useful information can be obtained from the resulting signal. The corrected/processed GT signal represents an experimental measurement of the term $H(\vec{r}_G, t)$ found in equations (4.59) and (4.60), where G is the GT inner body.

Figure 5.16(L) shows a stylized signal of the kind typically measured by the GT over a normal MNR operating day with constant neutron flux ϕ. This thesis assumes the change in $H(\vec{r}_G, t)$ with time is the result of increased gamma emissions by in-core fission-product and activated isotopes.

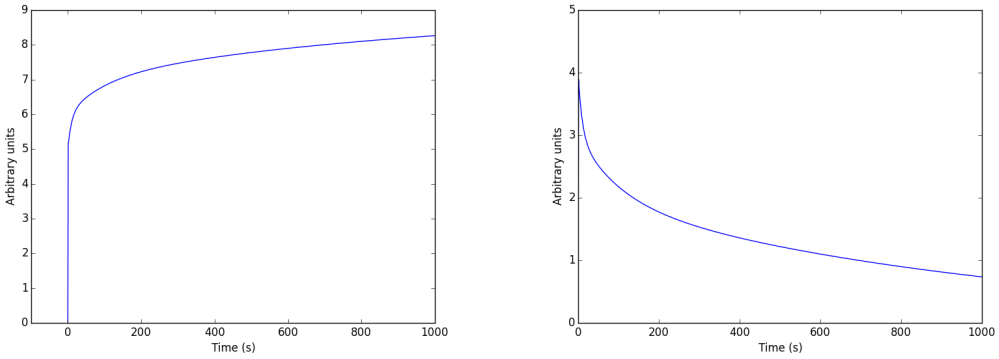

Figure 5.16: (L) form of function described by equation (5.41), (R) and by equation (5.42).

The signal of Figure 5.16(L) can be modelled by a function of the form:

$$H(\vec{r}_G, G, t) = a + \sum_{g=1}^{G} b_g \left[(1 - \mathrm{e}^{-\lambda_g t}) \right], \tag{5.41}$$

where a is the magnitude of the constant nuclear heating associated with the prompt gammas, b_g are the magnitudes of the G delayed heating groups with half lives of λ_g.

Following reactor shutdown the typically-observed GT signal of Figure 5.16(R) is best described by this function:

$$H(\vec{r}_G, G, t) = \sum_{g=1}^{G} b_g \mathrm{e}^{-\lambda_g t}. \tag{5.42}$$

Fitting equations (5.41) and (5.42) to the GT signal using a, b_g and λ_g as the fitting parameters results in a description of the aggregated delayed gamma groups from fission and neutron capture in the entire core, as detected at position $\vec{r}_G$. This fitting process requires a non-linear fitting algorithm since the λ_g terms are exponential. See section H for a discussion of the fitting methodology used within this thesis.

The GT signal has been collected in MNR in various locations and neutron fluxes. To make these results comparable, the coefficients in equation (5.41) must be normalized to an arbitrarily-defined reference of heating. Although the reference can be arbitrary, it is best to define this reference in a way which simplifies analysis, and to make sure the reference itself doesn't require a dedicated calculation or measurement.

Within this thesis the reference value of heating, $H_{\mathrm{ref}}(\vec{r}_G, G)$, is defined as the nuclear heating, in W/g, of the GT by the prompt gammas only of volume G at position $\vec{r}_G$. This value is equal to the coefficient a in equation (5.41), and is obtained experimentally. This definition of $H_{\mathrm{ref}}(\vec{r}_G, G)$

is thought have merit because the prompt gamma flux and heating is directly proportional to the reactor power for all $\vec{r}_G$. Since this definition is position dependent, the quantities of comparision between GT measurements will be the fractions $b_g/a = b_g/H_{\text{ref}}(\vec{r}_G, G)$.

Explicitly, this normalization is:

$$H(\vec{r}_G, G, t) = a + \sum_{g=1}^{G} b_g \left[(1 - \mathrm{e}^{-\lambda_g t})\right] \tag{5.43}$$

$$\frac{H(\vec{r}_G, G, t)}{H_{\text{ref}}(\vec{r}_G, G)} = \frac{a}{H_{\text{ref}}(\vec{r}_G, G)} + \frac{b_1}{H_{\text{ref}}(\vec{r}_G, G)}(1 - \mathrm{e}^{-\lambda_1 t}) + \frac{b_2}{H_{\text{ref}}(\vec{r}_G, G)}(1 - \mathrm{e}^{-\lambda_2 t}) \ldots \tag{5.44}$$

The same treatment applies to (5.42) even though there is no prompt gamma heating post-shutdown. The $H_{\text{ref}}(\vec{r}_G, G)$ measured post-startup at the same location $\vec{r}_G$ is normalized as:

$$\begin{aligned} H(\vec{r}_G, G, t) &= \sum_{g=1}^{G} b_g \mathrm{e}^{-\lambda_g t} \\ \frac{H(\vec{r}_G, G, t)}{H_{\text{ref}}(\vec{r}_G, G)} &= \frac{b_1}{H_{\text{ref}}(\vec{r}_G, G)} \mathrm{e}^{-\lambda_1 t} + \frac{b_2}{H_{\text{ref}}(\vec{r}_G, G)} \mathrm{e}^{-\lambda_2 t} \ldots \end{aligned} \tag{5.45}$$

Chapter 6

Measurements with the SCK-CEN GT in MNR and analysis

This chapter presents the results of the experimental use of the SCK-CEN GT and the associated analysis using the methods outlined in the previous chapter.

6.1 Experimental results

This section presents some of the SCK-CEN GT-20 experimental results; the data in this section has been processed with only the first 4 or 5 steps discussed in section 5.3.

These data sets have been collected with the GT in one of two grid locations: the graphite location 8F and the Be location 2A. These locations have been selected because the vertical center of 2A is likely to have the greatest neutron and gamma flux of any GT core location (other than the central irradiation facility at 5C), and because the use of 8F interferes the least with MNR daily operations.

For easy comparision between 8F and 2A, the GT was placed at vertical location G in both locations. This vertical location is close to the vertical center of the core.

6.1.1 Measurements in location 8F

MNR grid location 8F contains a graphite assembly. Pool water runs through the center of this assembly; the GT and instrument rig was placed within this water hole.

Figure 6.1 shows data collected over 5 calendar days, Monday October 19 to Friday October 23, inclusive; the data accumulated over the Monday and Friday do not show the entire operating day. The GT was placed into the core at 9:05 pm Monday and removed at 1:23 pm Friday.

The GT is clearly responsive to reactor startup and shutdown; Figure 6.1 shows 4 of the daily shutdown events and associated low overnight heating.

Figures 6.2 through 6.5 show in more detail the data of Tuesday, Wednesday, Thursday and Friday, respectively. At start-up on each day MNR was brought to a nominal reactor power of 2.5 MW. Figures 6.2, 6.3 and 6.4 show the reduction in reactor power to 2.0 MW during the last 2 operating hours of the day.

The post start-up data sets of Tuesday October 20 and Friday October 23 have been used for further processing. These data sets are detailed in Figures 6.2 and 6.5 and clearly show the smooth increase in nuclear heating, post-startup, which is attributed to the delayed gamma heating. The Lin N data recorder confirm only small control room changes were made to the neutron flux on these days. The post start-up data from the other days (Figures 6.3 and 6.4) are not useful because many

or large control room changes in the shim/safety rod position and power demand have obscured the delayed gamma heating.

Processing of the data sets of Tuesday October 20 and Friday October 23 with steps 5 through 8 discussed in section 5.3 results in the fit curves shown in Figures 6.6 and 6.7; the noisy recorded data is shown in these figures for comparison.

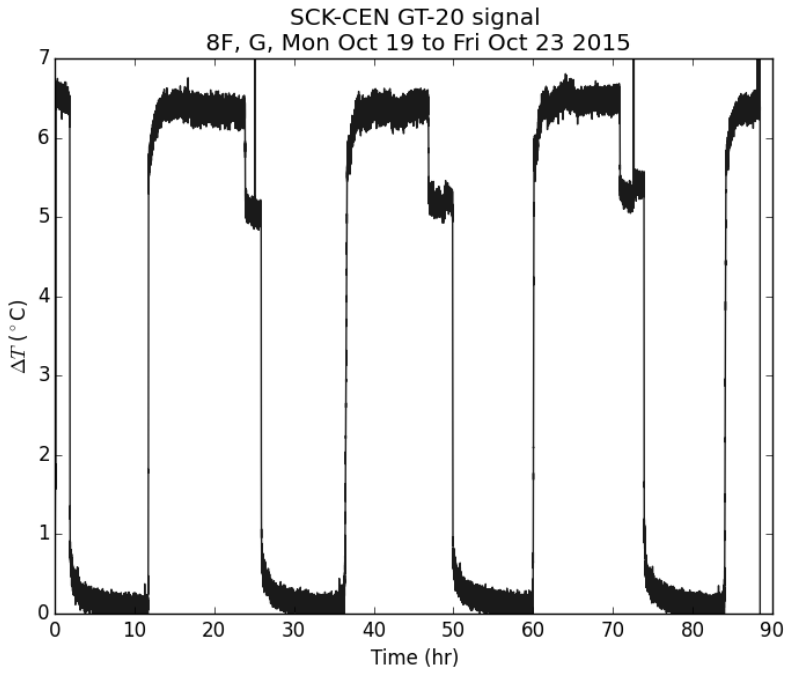

Figure 6.1: GT data collected between Monday Oct. 19 to Friday Oct. 23 in 8F/G.

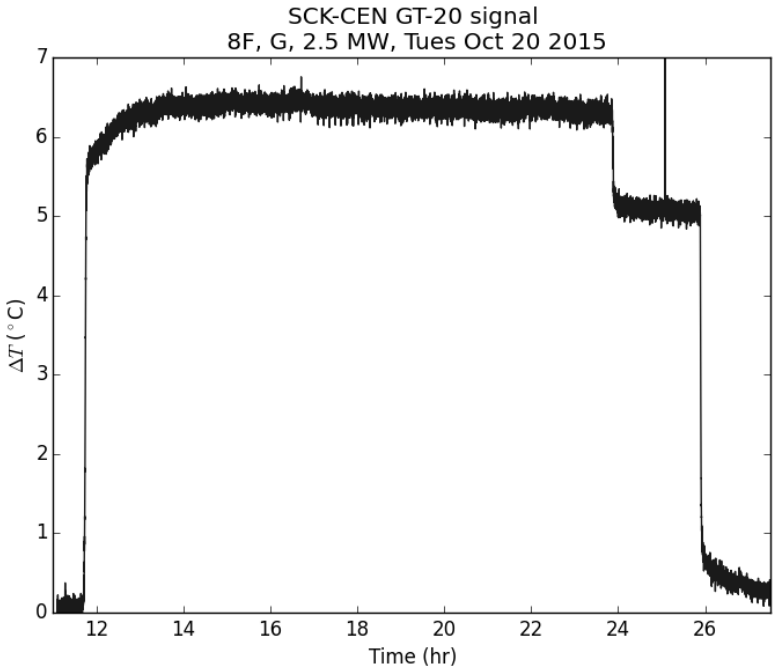

Figure 6.2: GT data from 8F/G showing the Tuesday Oct. 20 reactor operation. Time on bottom axis is relative to the start of data aquisition on 9:05 pm Monday Oct. 19.

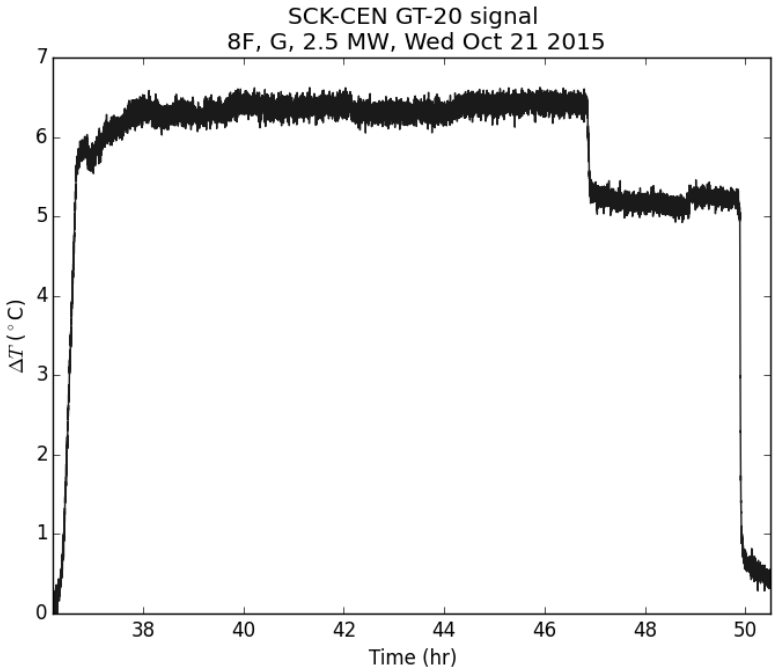

Figure 6.3: GT data from 8F/G showing the Wednesday Oct. 21 reactor operation. Time on bottom axis is relative to the start of data aquisition on 9:05 pm Monday Oct. 19.

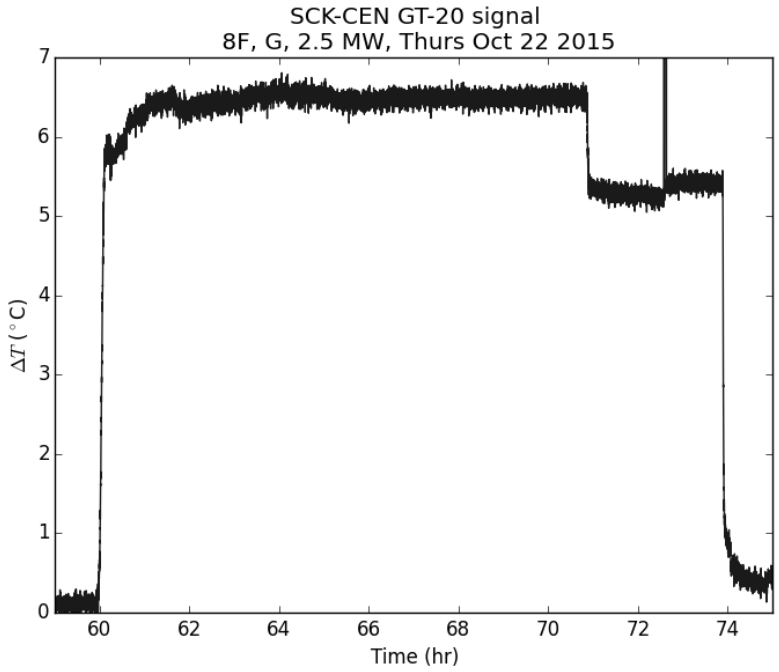

Figure 6.4: GT data from 8F/G showing the Thursday Oct. 22 reactor operation. Time on bottom axis is relative to the start of data aquisition on 9:05 pm Monday Oct. 19.

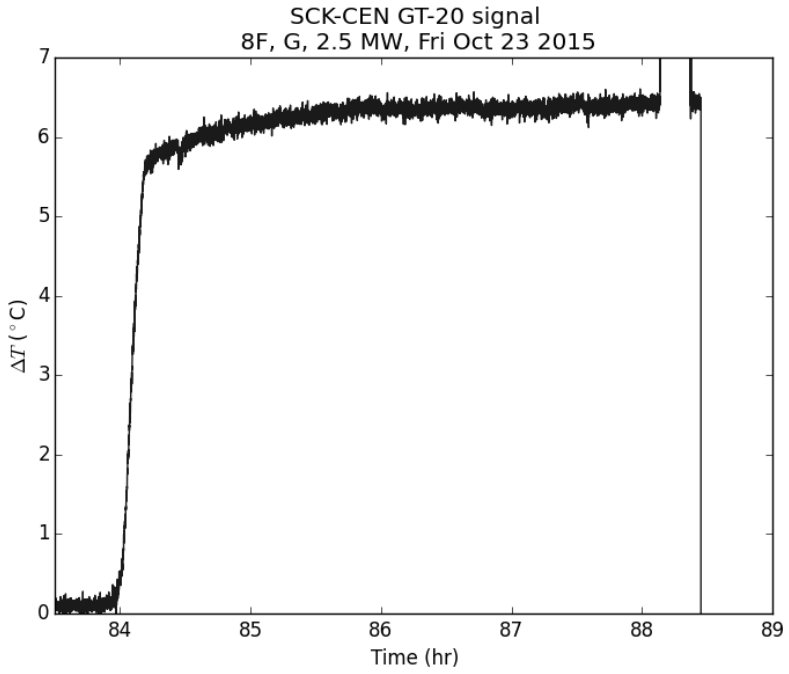

Figure 6.5: GT data from 8F/G showing the Friday Oct. 23 reactor operation. Time on bottom axis is relative to the start of data aquisition on 9:05 pm Monday Oct. 19.

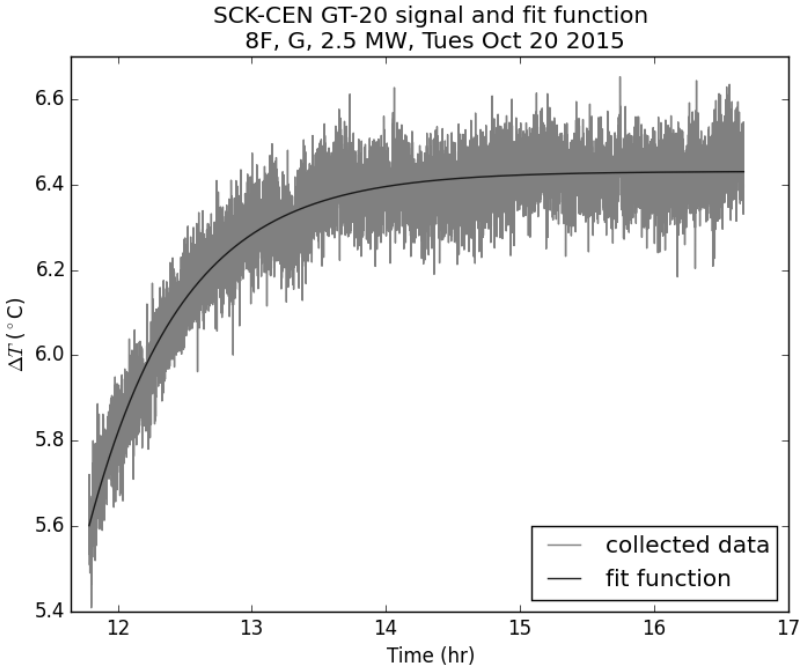

Figure 6.6: GT data from Tuesday Oct. 20 and the fit curve.

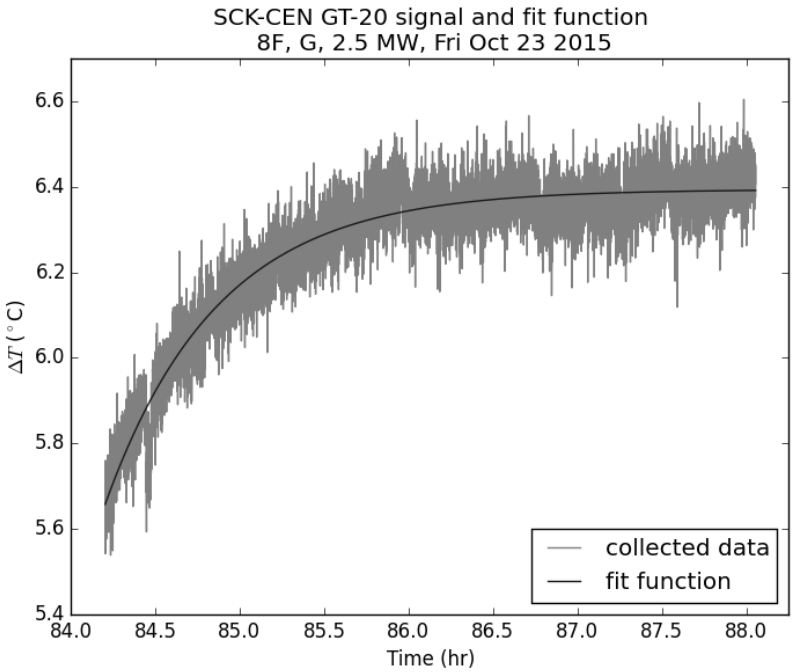

Figure 6.7: GT data from Friday Oct. 23 and the fit curve.

6.1.2 Measurements in location 2A

MNR grid location 2A contains a Be reflector assembly. Pool water runs through the center of this assembly; the GT and instrument rig was placed within this water hole.

Figure 6.8 shows data collected over 17 calendar days, Saturday October 24 to Monday November 9, inclusive; the data accumulated over the first Saturday and last Monday do not show the entire operating day. The GT was placed into the core at 10:53 pm Saturday October 24 and removed at 9:27 am Monday November 9. On start-up on each day MNR was brought to a nominal reactor power of 2.5 MW. On some days, the reactor's power was reduced to 2.0 MW during the last 2 operating hours of the day.

Figures 6.9 and 6.10 detail the data sets of Tuesday November 3 and Thursday November 5, respectively. These data sets have been used for further processing. Figures 6.11 and 6.12 show the curves fit to these data sets.

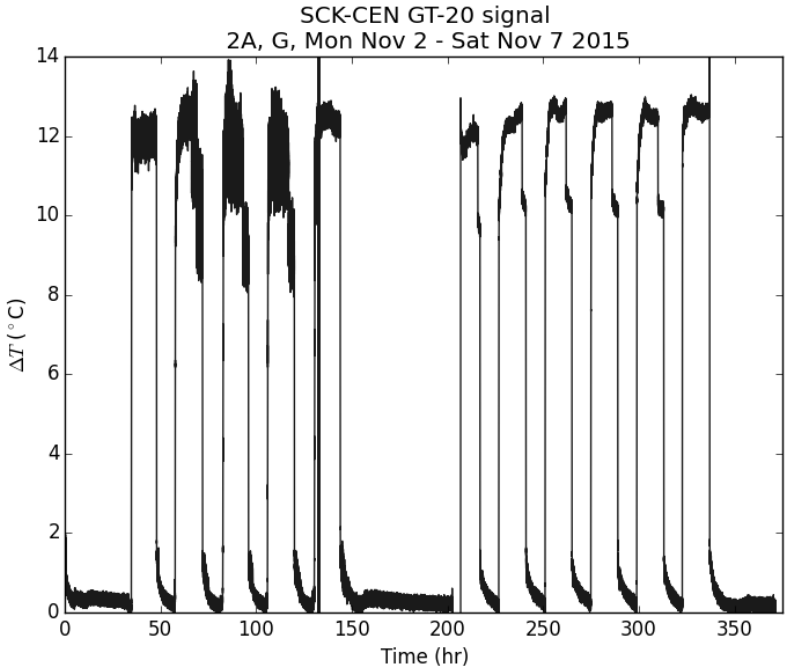

Figure 6.8: GT data collected between Saturday Oct. 24 to Monday Nov. 9 in 2A/G.

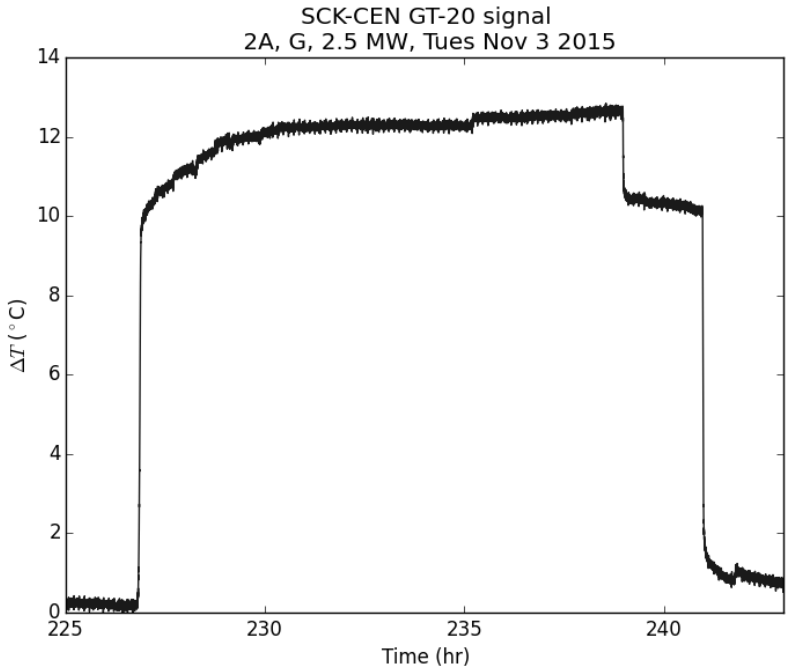

Figure 6.9: GT data from 2A/G showing the Tuesday Nov. 3 reactor operation. Time on bottom axis is relative to the start of data aquisition on 10:53 pm Saturday Oct. 24.

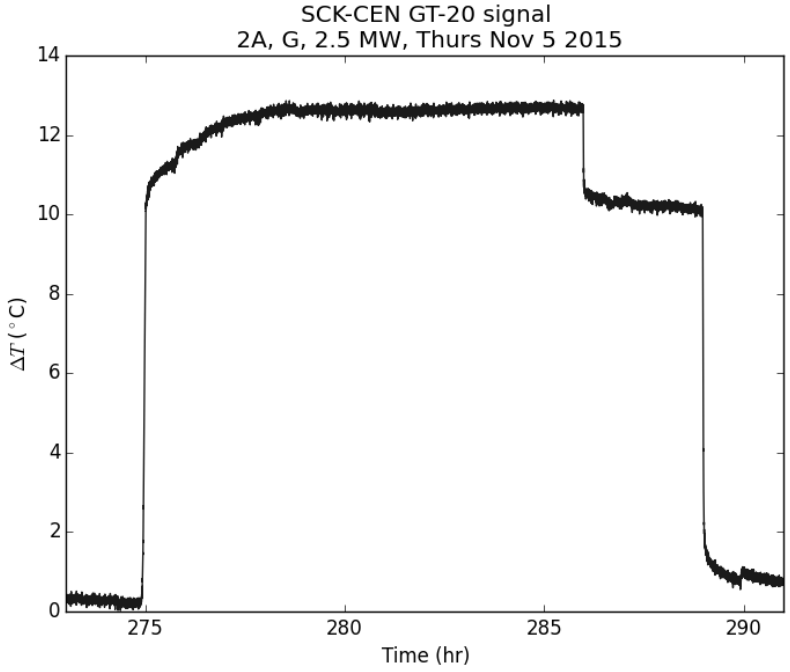

Figure 6.10: GT data from 2A/G showing the Tuesday Nov. 5 reactor operation. Time on bottom axis is relative to the start of data aquisition on 10:53 pm Saturday Oct. 24.

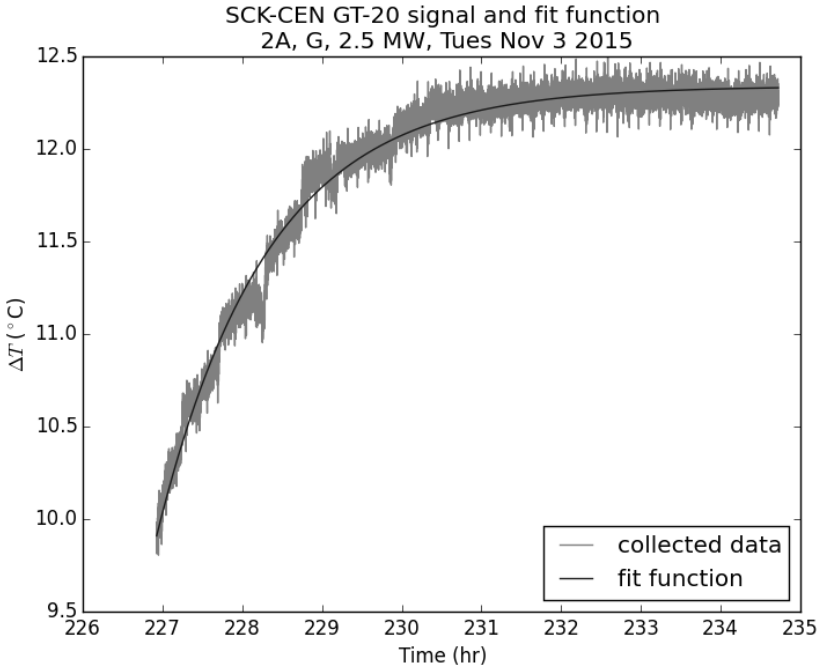

Figure 6.11: GT data from Tuesday Nov. 3 and the fit curve.

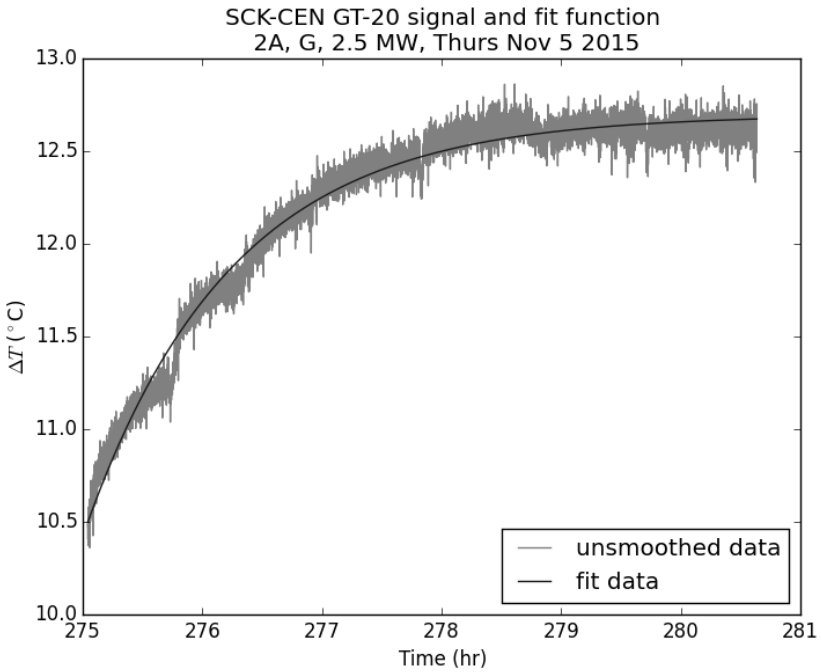

Figure 6.12: GT data from Thursday Nov. 5 and the fit curve.

6.2 Quantities calculated with the MCNP6 RC model

6.2.1 Neutron and prompt photon flux

Using the MCNP6 RC model, the neutron flux and prompt photon flux have been calculated at 6 potential GT in-core environments: 2 CIF (5C) locations (vertical centre and top), 2 graphite (8F) positions (vertical center and top) and 2 Be (2A) positions (vertical center and top). The center of 5C is likely to have neutron and photon fluxes higher than anywhere else in the RC core; the top of 8F is likely to have one of the lowest fluxes.

Figures 6.13 and 6.14 show the calculated neutron and photon spectra. These figures also present the energy-integrated neutron and photon flux at 3.0 MW, which were scaled using C in section B. The only uncertainties considered in Figures 6.13 and 6.14 are Monte Carlo errors.

As expected in a thermal reactor, there is a preponderance of thermal neutrons at all locations. The photon spectra show 8F contains a softer prompt photon spectra than the other locations.

	n flux divided by n flux in 5C vertical center	p flux divided by p flux in 5C vertical center
5C vertical center	1.00	1.00
5C top	0.37	0.42
8F vertical center	0.15	0.23
8F top	0.06	0.11
2A vertical center	0.36	0.36
2A top	0.15	0.17

Table 6.1: Neutron and photon scalar fluxes relative to the vertical center of 5C. Errors of all values are better than 1.7%.

Using the energy-integrated neutron and photon flux values from Figures 6.13 and 6.14, Table 6.1 presents the same quantities relative to the vertical center of 5C, which is the evaluated location with the greatest flux. This table shows the prompt photon flux varies less through the core than the neutron flux.

6.2.2 Neutron reaction rates

Figure 6.15, 6.16, 6.17, 6.18, 6.19, 6.20, 6.21 and 6.22 present the reaction tallies calculated using the MCNP6 FM tally multiplier card with the MCNP6 MNR Reference Core model - as outlined in section 5.6.3.

The reaction tallies were calculated at the following GT locations within the Reference Core: 5C core midplane, 5C top, 2A core midplane, 2A top, 8F core midplane and 8F top. Only the 2A core midplane, and 8F core midplane results are presented since they have been used in the GT self-heating calculations. The uncertainties in Figures 6.15 and 6.19 are Monte Carlo errors.

These tallies are not scaled to any specific reactor power, or atomic concentration and are FM_{product} quantitites; these tallies must be multiplied by the associated atomic concentration and the power scaling factor C from section B to obtain absolute reaction rates. Thus, an isotope with a large FM_{product} tally may play a minor role in GT self-heating if its associated atomic concentration is small.

Notice these figures show MT-102 (n,γ) reactions are dominant. The MT=103 (n,p), MT=107 (n,α) and MT=16 (n,2n) reactions are all relatively insignificant, therefore only (n,γ) reactions have been considered in self-heating studies of the SCK-CEN GT.

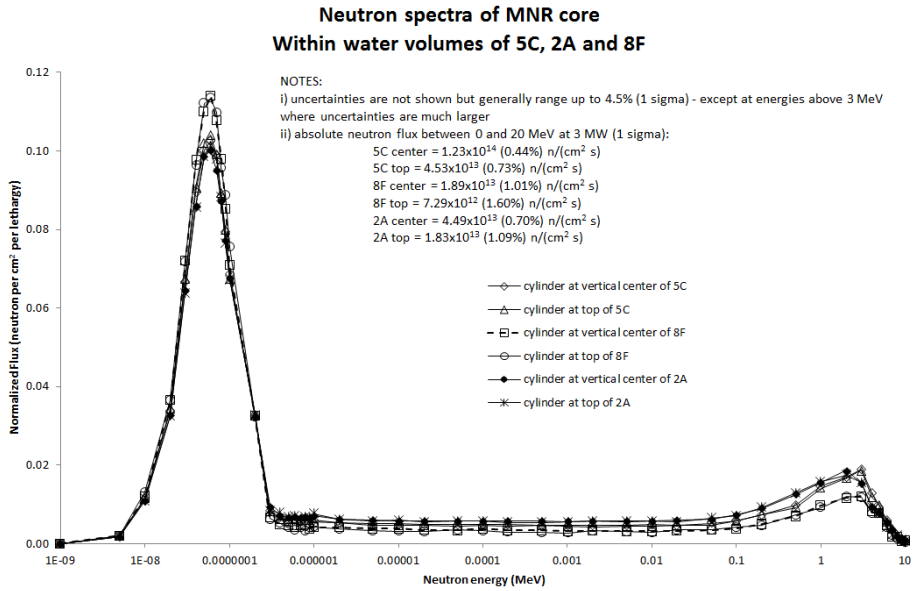

Figure 6.13: Neutron flux in the tallied volumes using the 50-group energy grid.

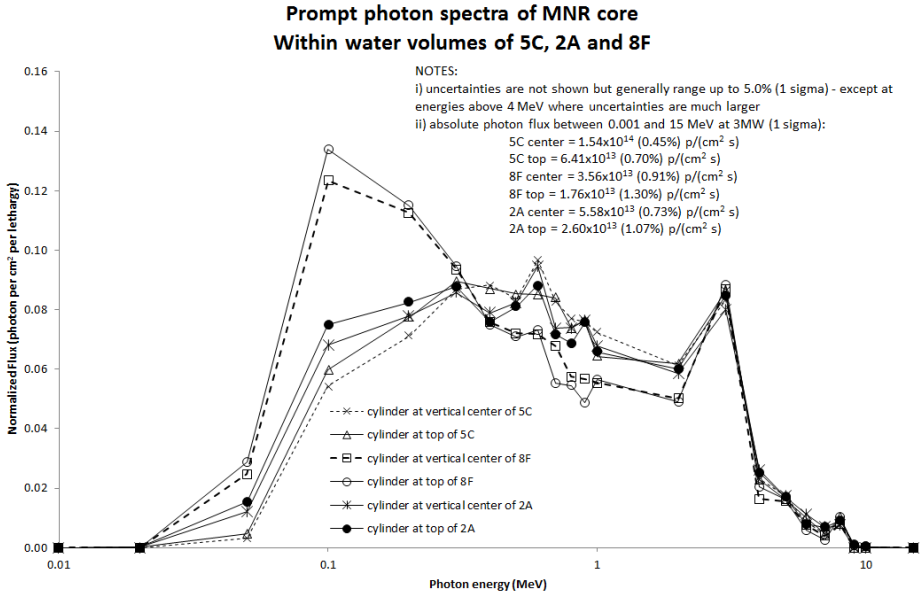

Figure 6.14: Photon flux in the tallied volumes using the 25-group energy grid.

The MT=102 reaction rates are dominanted by reactions in the thermal range for all isotopes - these results are not detailed in this thesis, but were observed in the energy bins of the MCNP6 output. This domination by thermal captures qualifies the use of the thermal neutron libraries CapGam and IAEA PGAA in the GT self-heating study.

Some isotopes do not have specified tallies because the MNCP6 libraries are missing the associated microscopic cross sections. All cross sections are defined for the MT-102 (n,γ) reactions which form the basis of the GT self-heating calculations.

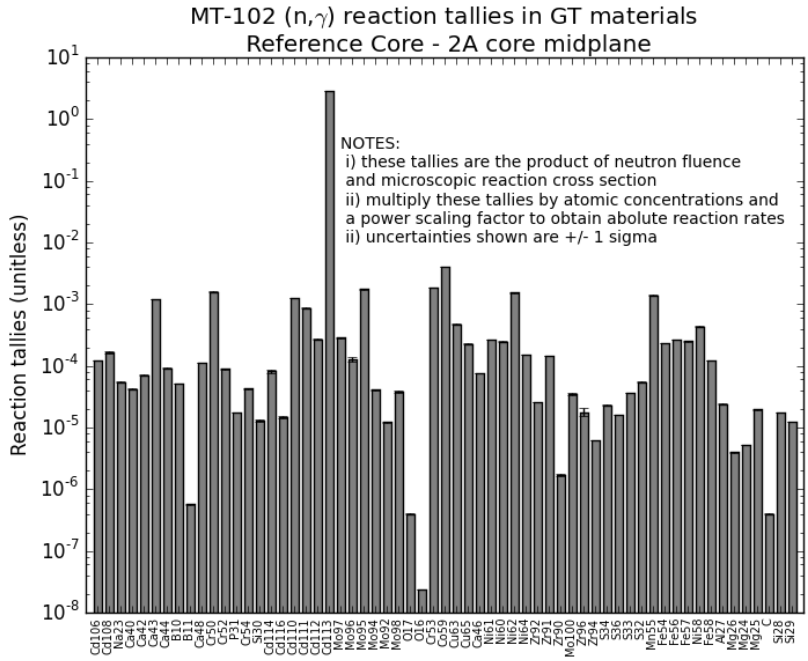

Figure 6.15: MT-102 reaction tallies at from the MCNP6 RC MNR model using the FM card; 2A core midplane.

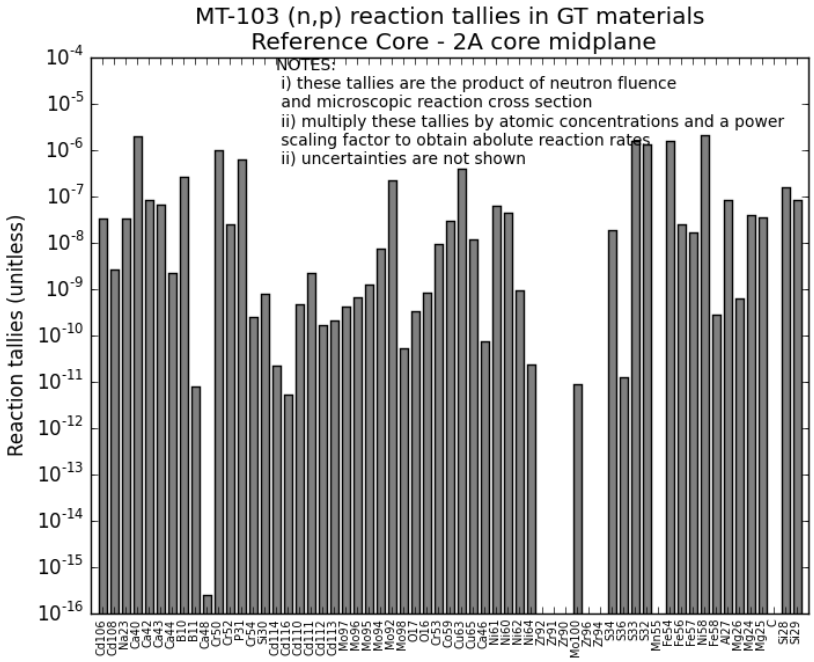

Figure 6.16: MT-103 reaction tallies at from the MCNP6 RC MNR model using the FM card; 2A core midplane.

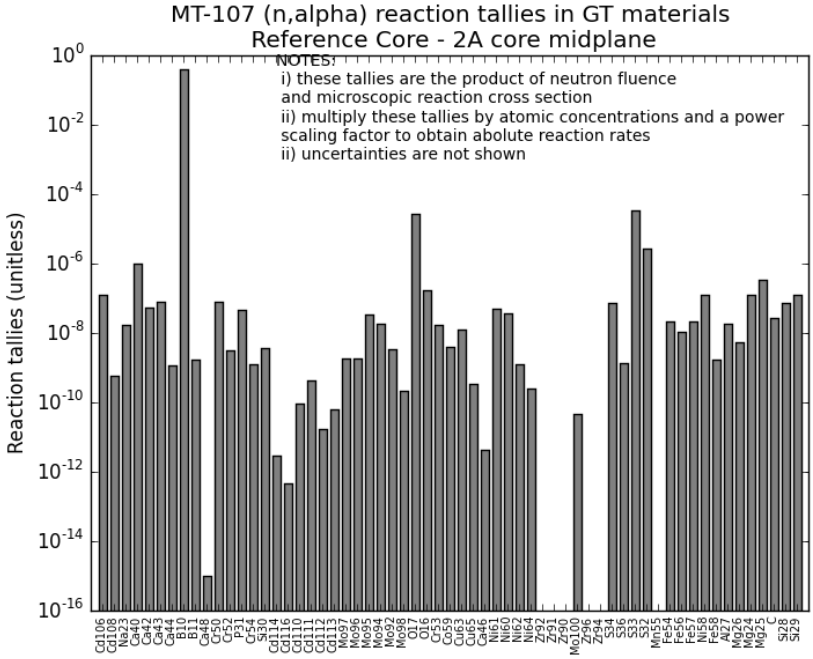

Figure 6.17: MT-107 reaction tallies at from the MCNP6 RC MNR model using the FM card; 2A core midplane.

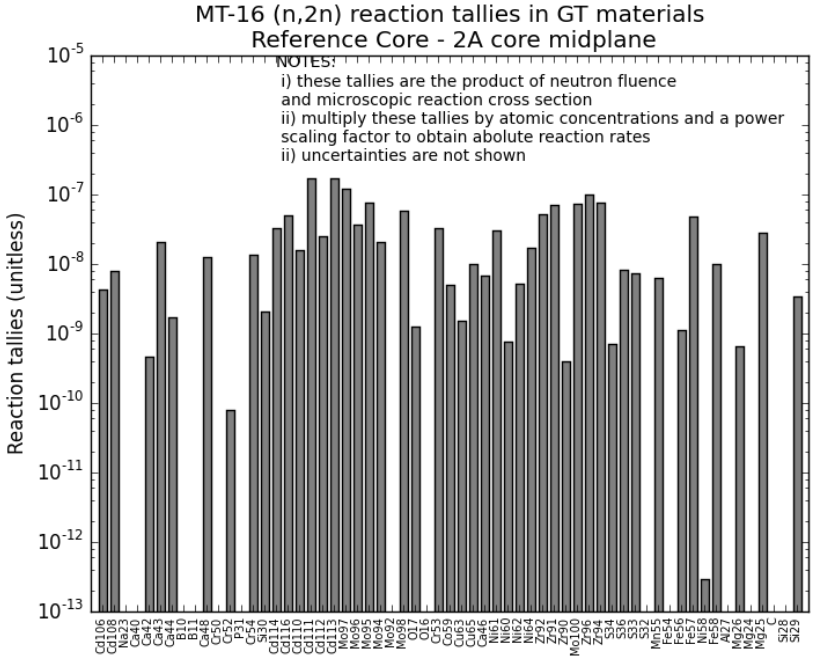

Figure 6.18: MT-16 reaction tallies at from the MCNP6 RC MNR model using the FM card; 2A core midplane.

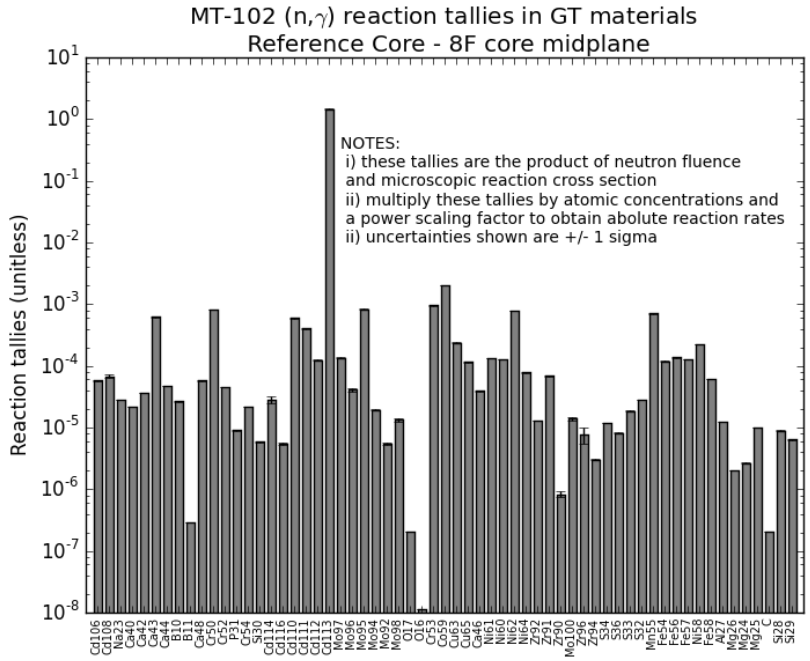

Figure 6.19: MT-102 reaction tallies at from the MCNP6 RC MNR model using the FM card; 8F core midplane.

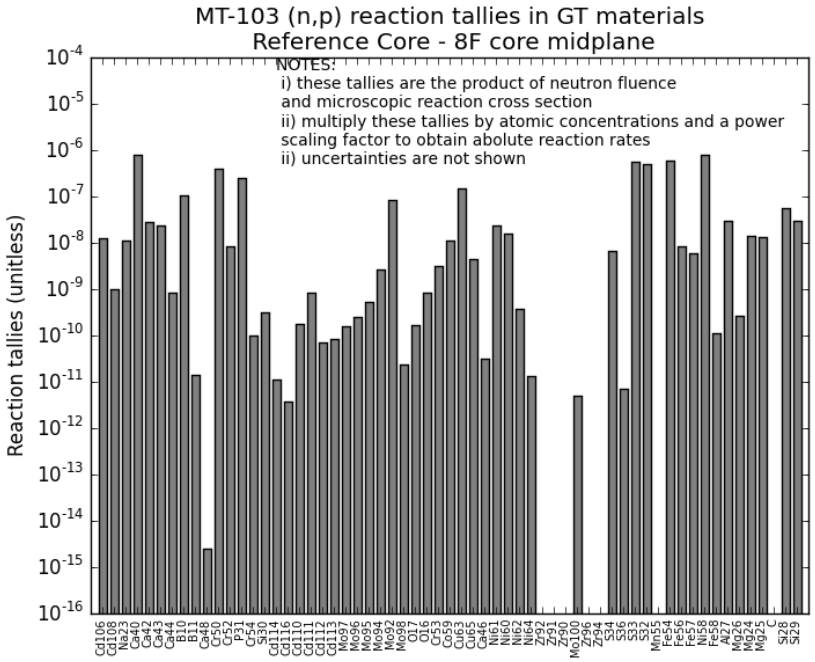

Figure 6.20: MT-103 reaction tallies at from the MCNP6 RC MNR model using the FM card; 8F core midplane.

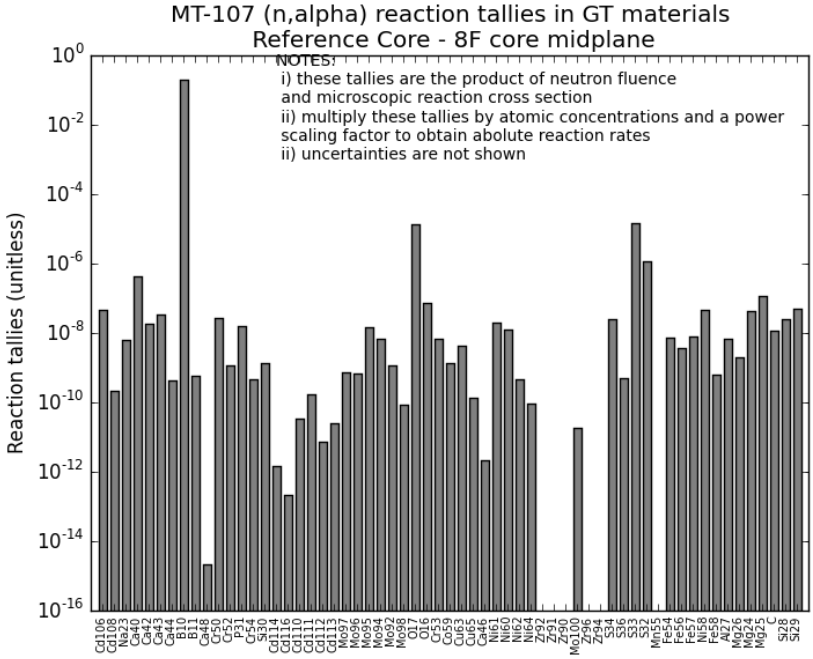

Figure 6.21: MT-107 reaction tallies at from the MCNP6 RC MNR model using the FM card; 8F core midplane.

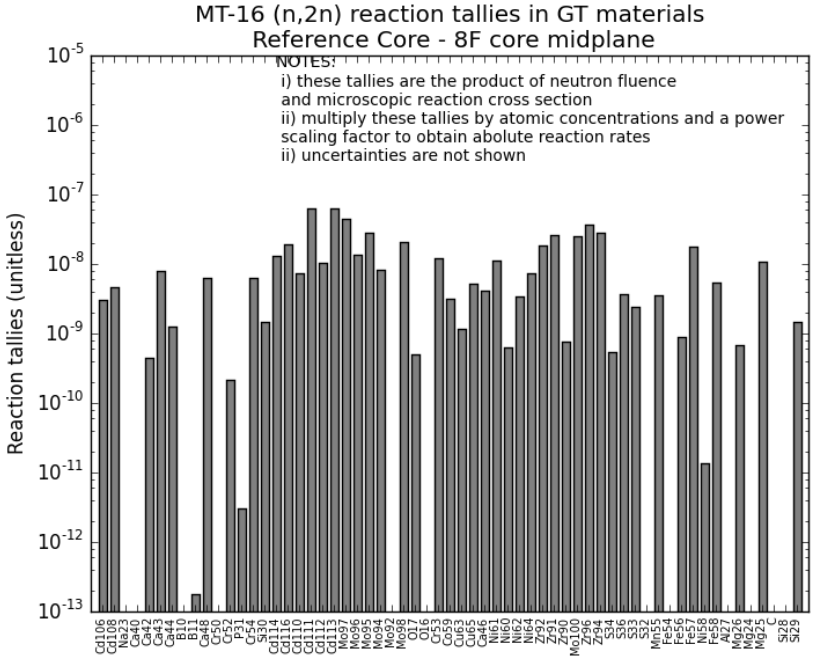

Figure 6.22: MT-16 reaction tallies at from the MCNP6 RC MNR model using the FM card; 8F core midplane.

6.2.3 Neutron and prompt-gamma heating of the SCK-CEN GT

The MCNP6 MNR Reference Core model, with the full SCK-CEN GT and instrument rig geometries, was used to calculate the neutron and prompt-gamma heating of the SCK-CEN GT inner body. Table 6.2 summarizes the results at various core locations at 2.5 MW using the constants listed in Appendix B. The uncertainties given in the table result from the Monte Carlo errors on the F6 energy deposition tallies and the uncertainty on the reactor power.

Notice the neutron heating, as expected, is significantly lower than the gamma heating.

Since MCNP6 doesn't have the capability to track the delayed gamma sources, the delayed gamma heating was not calculated.

Location	Power (MW)	Neutron heating (W/g)	Prompt photon heating (W/g)
8F/G	2.5 MW	$8.18 \times 10^{-04} \pm 11.0\%(1\sigma)$	$9.74 \times 10^{-02} \pm 7.8\%(1\sigma)$
2A/G	2.5 MW	$2.15 \times 10^{-03} \pm 8.8\%(1\sigma)$	$1.91 \times 10^{-01} \pm 7.6\%(1\sigma)$

Table 6.2: Heating of the SCK-CEN inner-body, as calculated with the MCNP6 Reference Core model.

Location	Power (MW)	Neutron scalar flux (1/s cm^2)	Prompt gamma scalar flux (1/s cm^2)
8F/G	2.5 MW	$1.57 \times 10^{13} \pm 7.4\%(1\sigma)$	$2.55 \times 10^{13} \pm 7.7\%(1\sigma)$
2A/G	2.5 MW	$3.47 \times 10^{13} \pm 7.2\%(1\sigma)$	$4.13 \times 10^{13} \pm 7.4\%(1\sigma)$

Table 6.3: Scalar flux in the SCK-CEN inner-body, as calculated with the MCNP6 Reference Core model.

6.3 MCNP6 analysis of gamma transport within the SCK-CEN GT

As discussed in section 5.6, 75 ${}^kE(|\vec{r}_G - \vec{r}|, E')$ terms are required to calculate the GT self heating. These terms were calculated with 75 dedicated MCNP6 photon-transport calculations of the full SCK-CEN GT body resulted; the resulting 75 mean transported energy terms are in Table 6.4.

Unsurprisingly, gammas originating in the 304L volumes (shown in Figure 5.15) deposit less energy, on average, in the GT's inner body than those originating in the 316L and alumina/TC volumes. This is the result of much more 304L material existing outside the GT inner body than 316L and alumina/TC volumes. Gammas originating in 304L material simply have a smaller chance of being deposited within the inner body than gammas originating in 316L or alumina/TC material.

Large numbers of histories were used to force the relative uncertainties to very small values. Since these uncertainties are so small compared to other uncertainties in the self-heating calculation, they were not propagated.

6.4 Self-heating of the SCK-CEN GT

A Python 2.7.10 code solving equation (5.36) has been written to calculate the prompt and delayed GT self-heating resulting from MT-102 (n,γ) reactions (Ref 2015). The program harvests prompt gamma data from CapGam and IAEA PGAA data stored in data files dedicated to individual isotopes; all these isotope files were created for this calculation.

The prompt MT-102 (n,γ) spectra of three of the most relevant isotopes within the SCK-CEN GT are shown in Figure 6.23; the spectrum of ^{16}O is also included because it has few prompt gammas and is useful as a check against tabulated data. No nuclear data uncertainties were considered in the calculation of the GT self-heating.

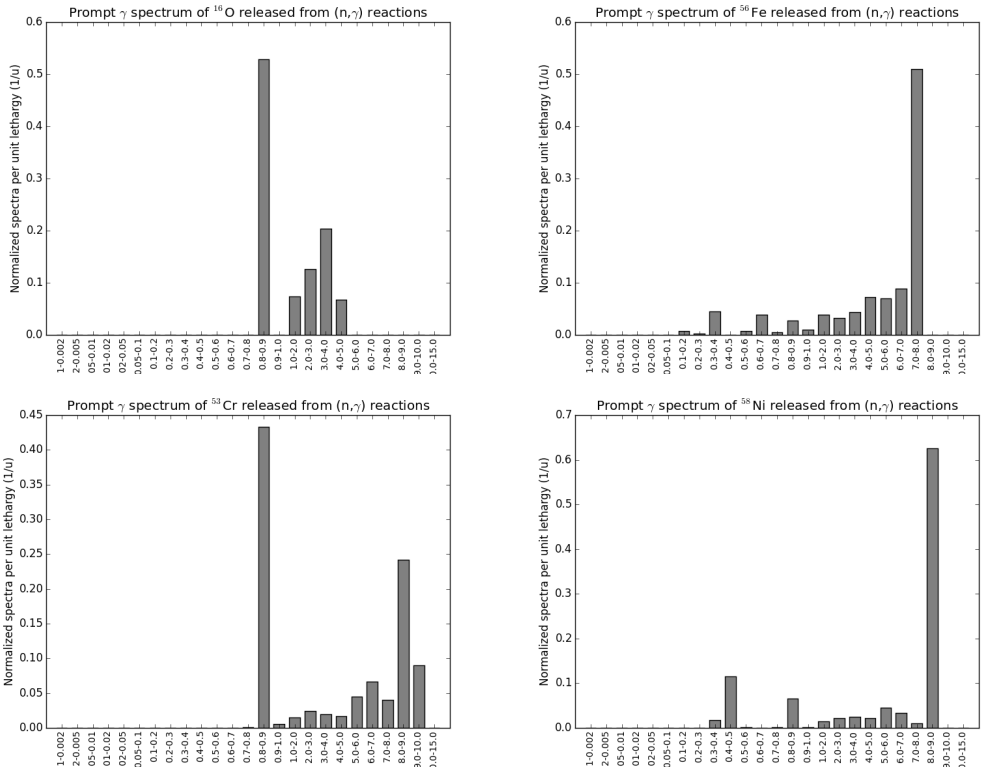

Figure 6.23: Prompt gamma spectra from (n,γ) reactions in some GT materials. All horizontal axes are in unites of MeV

Figure 6.24 shows there is a large amount of prompt gamma power emitted by (n,γ) reactions in the 304L material at 2.5 MW. The power of gamma radiation actually absorbed by the GT's inner body is shown in Figure 6.25; notice the energy absorption rate is a small fraction of the rate of energy emitted. The powers of absorbed prompt gammas, emitted by 316L and alumina/TC materials, are shown in Figure 6.26 and 6.27. The total prompt absorbed power, emitted by all isotopes in all materials, from (n,γ) reactions is shown in Figure 6.28; this is the sum of Figures 6.25, 6.26 and 6.27.

Figure 6.28 shows the sum of absorbed power, from all isotopes, in all GT material, at 2.5 MW, is $0.0285 \pm 3.7\%(1\sigma)$ W/g; the inner body mass of the SCK-CEN GT is 0.396 g so this heating corresponds to $0.0113 \pm 3.7\%(1\sigma)$ W. The uncertainties of all prompt emitted and absorbed powers have been obtained by propagating the Monte Carlo reaction rate uncertainties and the reactor power uncertainty.

The self-heating from delayed gammas and delayed charged particles have been calculated using delayed particle data harvested the NuDat 2.6 database. Figures 6.29 through 6.31 present the delayed heating by gammas by all isotopes in each GT material. Figure 6.32 presents the total delayed gamma heating by each isotope, from all materials.

Figures 6.33 through 6.35 present the delayed heating by charged particles by all isotopes, divided

Energy Bin Boundaries (MeV)		304L Material MeV per history	304L Material Relative Error	316L Material MeV per history	316L Material Relative Error	Alumina/TC Material MeV per history	Alumina/TC Material Relative Error
0.001	**0.002**	1.268E-04	0.0015	5.739E-04	0.0007	5.737E-04	0.0007
0.002	**0.005**	2.954E-04	0.0016	1.339E-03	0.0007	1.338E-03	0.0007
0.005	**0.01**	6.326E-04	0.0015	2.869E-03	0.0006	2.869E-03	0.0007
0.01	**0.02**	1.265E-03	0.0015	5.737E-03	0.0006	5.739E-03	0.0006
0.02	**0.05**	2.840E-03	0.0014	1.248E-02	0.0006	1.245E-02	0.0006
0.05	**0.1**	3.389E-03	0.0012	1.187E-02	0.0005	1.143E-02	0.0005
0.1	**0.2**	1.943E-03	0.0012	5.683E-03	0.0006	5.412E-03	0.0006
0.2	**0.3**	1.524E-03	0.0012	4.350E-03	0.0005	4.213E-03	0.0005
0.3	**0.4**	1.704E-03	0.0011	4.917E-03	0.0005	4.803E-03	0.0005
0.4	**0.5**	2.015E-03	0.0011	5.857E-03	0.0005	5.740E-03	0.0005
0.5	**0.6**	2.358E-03	0.0011	6.882E-03	0.0005	6.754E-03	0.0005
0.6	**0.7**	2.705E-03	0.0012	7.913E-03	0.0005	7.769E-03	0.0005
0.7	**0.8**	3.045E-03	0.0012	8.920E-03	0.0005	8.760E-03	0.0005
0.8	**0.9**	3.375E-03	0.0012	9.894E-03	0.0005	9.718E-03	0.0005
0.9	**1**	3.694E-03	0.0012	1.083E-02	0.0005	1.064E-02	0.0005
1	**2**	5.245E-03	0.0012	1.537E-02	0.0005	1.510E-02	0.0005
2	**3**	7.895E-03	0.0012	2.309E-02	0.0005	2.262E-02	0.0005
3	**4**	1.066E-02	0.0012	3.113E-02	0.0005	3.038E-02	0.0005
4	**5**	1.365E-02	0.0012	3.982E-02	0.0005	3.873E-02	0.0005
5	**6**	1.687E-02	0.0012	4.919E-02	0.0005	4.769E-02	0.0005
6	**7**	2.033E-02	0.0012	5.923E-02	0.0005	5.728E-02	0.0005
7	**8**	2.398E-02	0.0012	6.986E-02	0.0005	6.741E-02	0.0005
8	**9**	2.783E-02	0.0012	8.103E-02	0.0005	7.805E-02	0.0005
9	**10**	3.183E-02	0.0012	9.267E-02	0.0005	8.913E-02	0.0005
10	**15**	4.473E-02	0.0012	1.302E-01	0.0005	1.248E-01	0.0005

Table 6.4: Mean transported energy terms for gamma radiation originating in the 3 material regions of the GT.

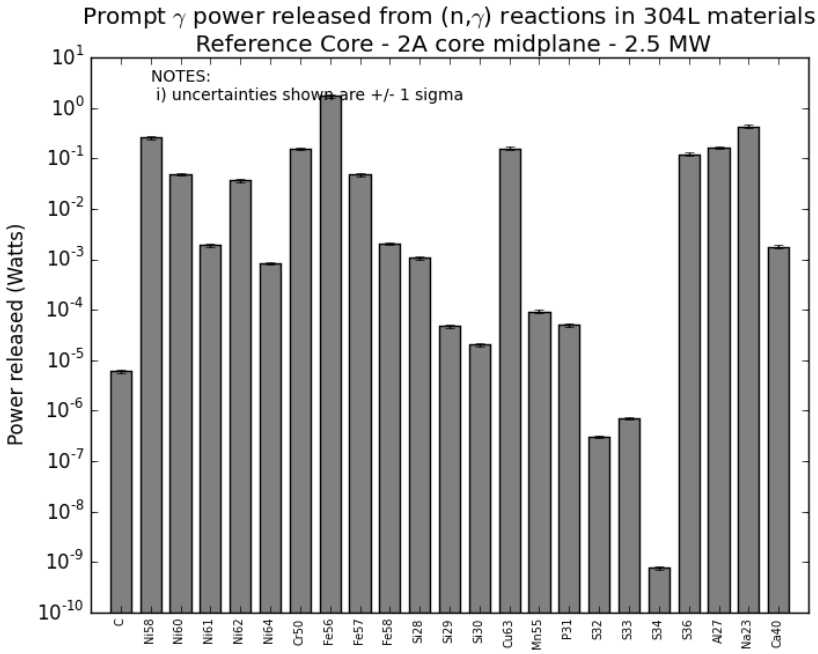

Figure 6.24: Prompt power of gammas released by MT-102 (n,γ) reactions in each isotope of the 304L material.

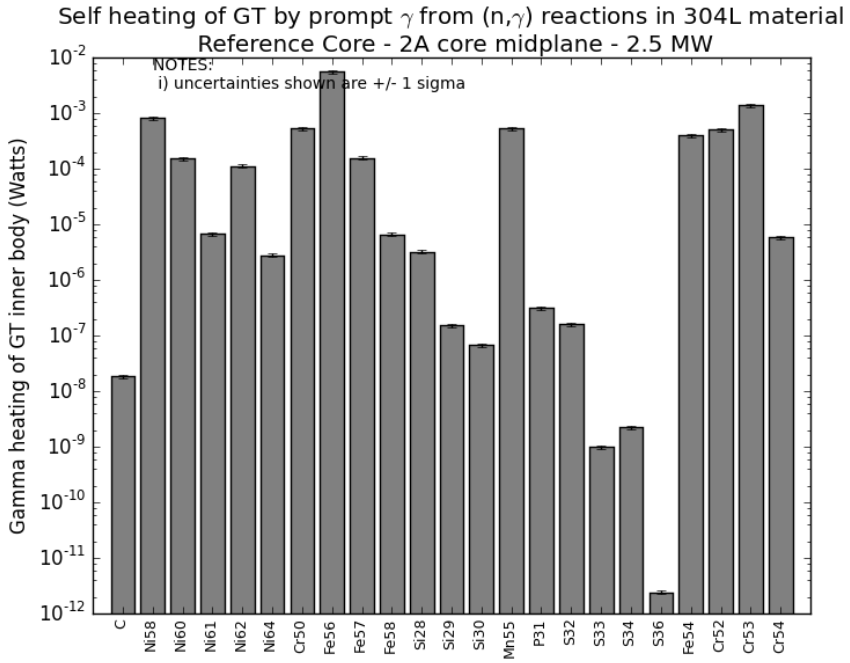

Figure 6.25: Prompt self-heating by gammas released by MT-102 (n,γ) reactions in each isotope of the 304L material.

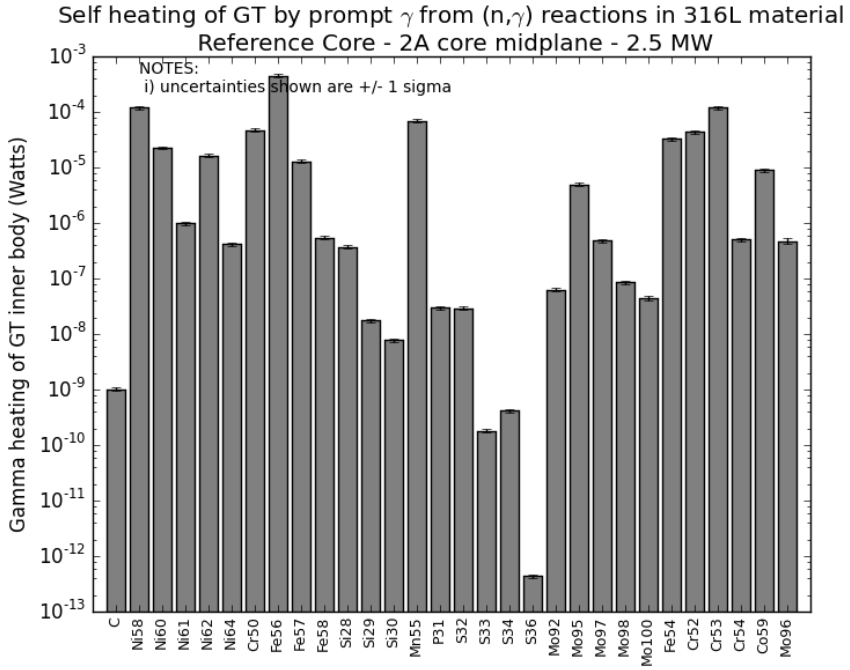

Figure 6.26: Prompt self-heating by gammas released by MT-102 (n,γ) reactions in each isotope of the 316L material.

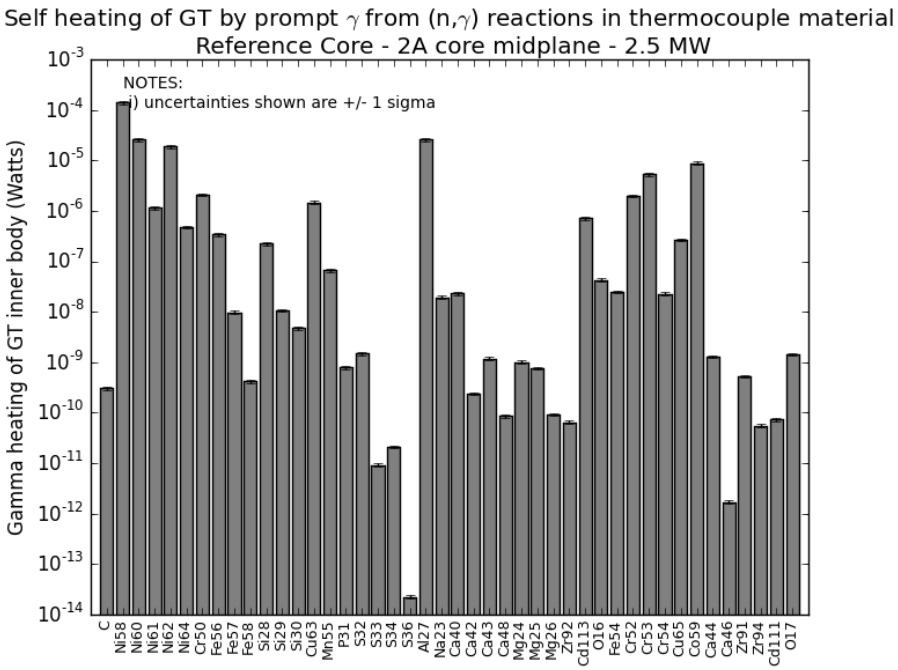

Figure 6.27: Prompt self-heating by gammas released by MT-102 (n,γ) reactions in each isotope of the alumina/TC materials.

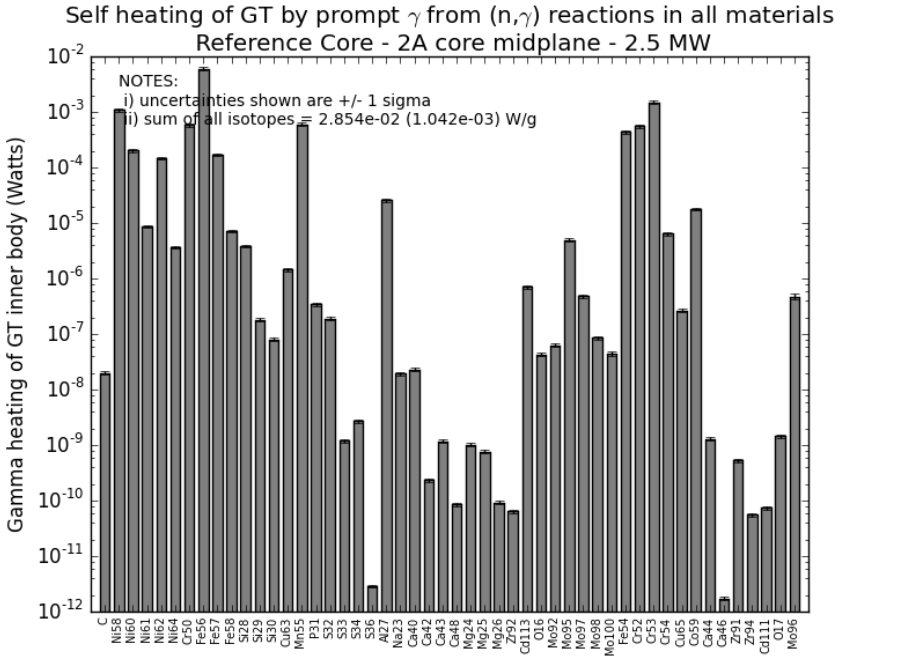

Figure 6.28: Total prompt self-heating of the SCK-CEN GT by gammas released by MT-102 (n,γ) reactions in each isotope of all materials.

by GT materials. These charged particles may be e^+ or e^- emitted through decay or the Auger effect.

Figure 6.36 presents the delayed heating by all particles from all isotopes in all GT materials. At 2.5 MW in the vertical center of core location 2A, after 24 hours the delayed self-heating component is $0.00546 \pm 5.0\%(1\sigma)$ W/g - significantly smaller than the $0.0285 \pm 3.7\%(1\sigma)$ W/g prompt heating.

The SCK-CEN also conducted a self-heating study of the GT. Little is known about this work, except that it considered only the delayed betas and three most probable gammas from only a few important isotopes (Vermeeren 2014); the SCK-CEN results concur with the much more extensive calculations conducted in this thesis.

The self-heating data has been used to correct the nuclear heating measured by the SCK-CEN GT. For example, the total prompt self-heating value from Figure 6.28 and the total delayed self-heating data from Figure 6.36, were subtracted from the measured total nuclear heating of the GT at core location 2A at 2.5 MW. Similar corrections at other locations and reactor powers have been completed.

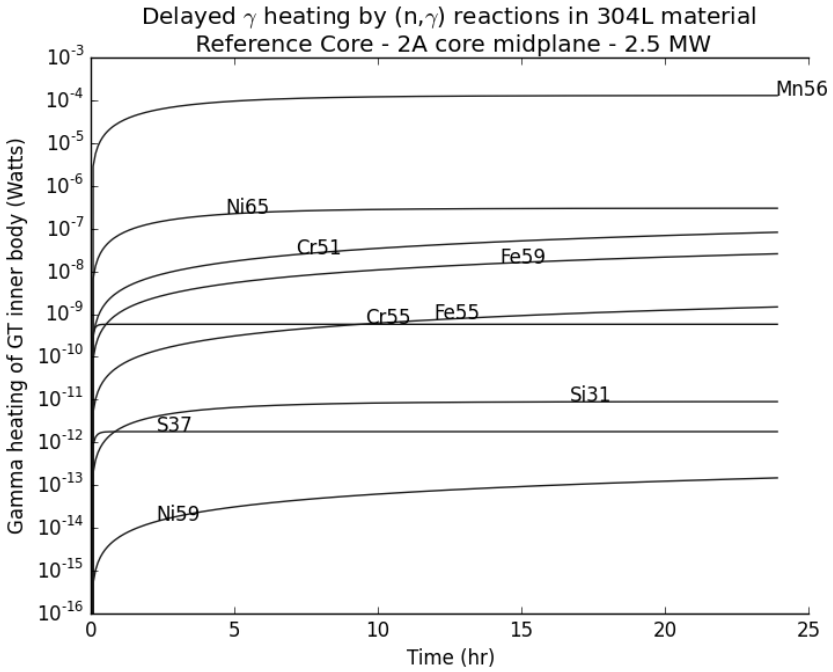

Figure 6.29: Delayed self-heating by gammas released by MT-102 (n,γ) reactions in each isotope of the 304L material.

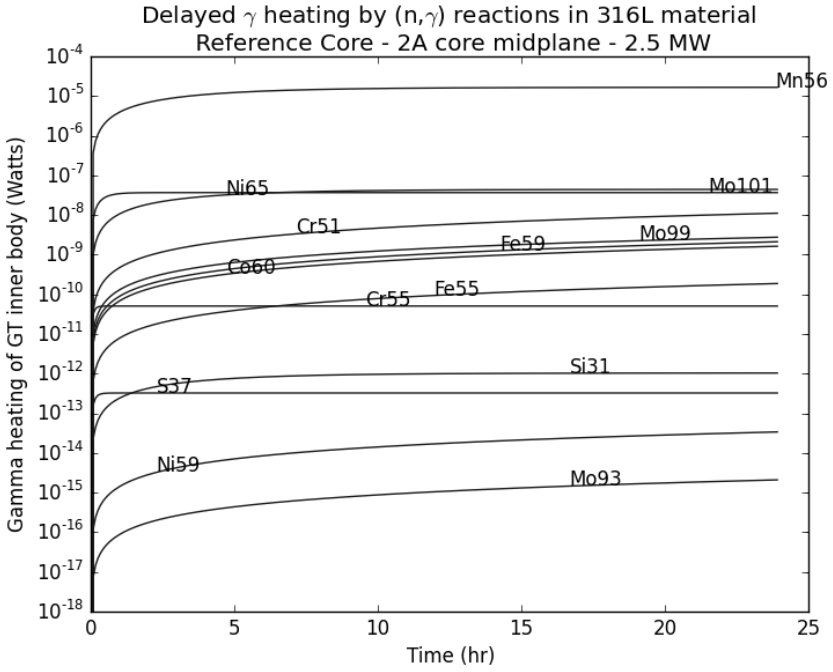

Figure 6.30: Delayed self-heating by gammas released by MT-102 (n,γ) reactions in each isotope of the 316L material.

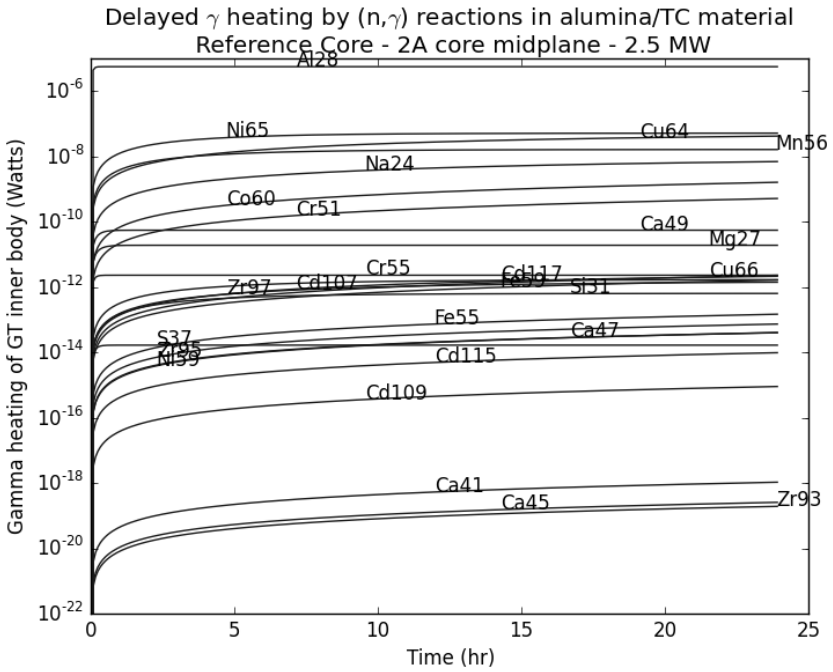

Figure 6.31: Delayed self-heating by gammas released by MT-102 (n,γ) reactions in each isotope of the alumina/TC materials.

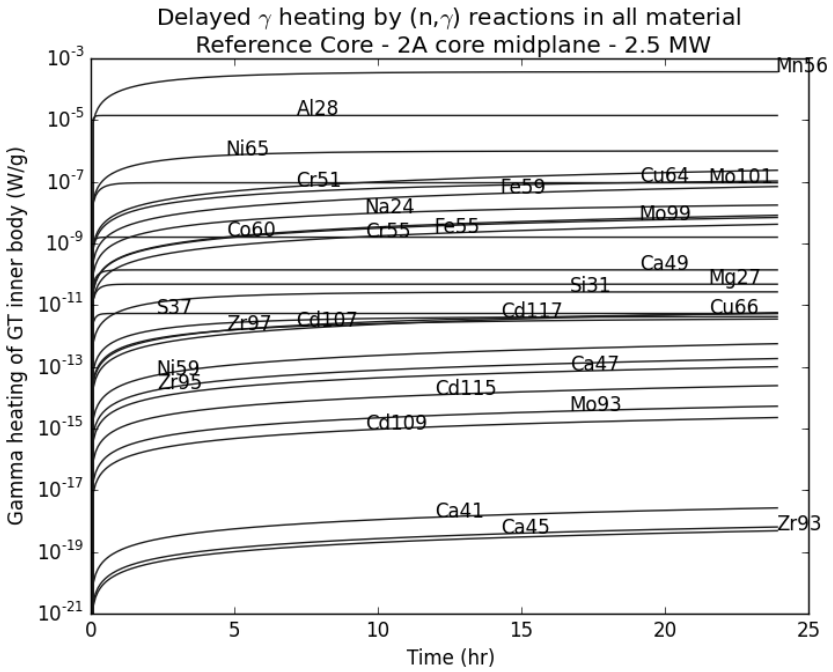

Figure 6.32: Delayed self-heating by gammas released by MT-102 (n,γ) reactions in each isotope of all materials.

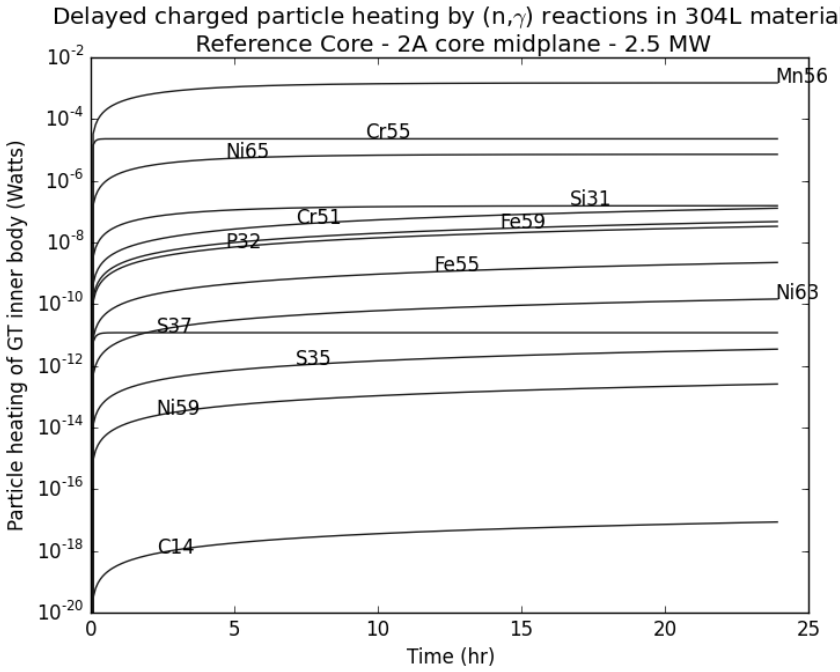

Figure 6.33: Delayed self-heating by charged particles released by MT-102 (n,γ) reactions in each isotope of 304L material.

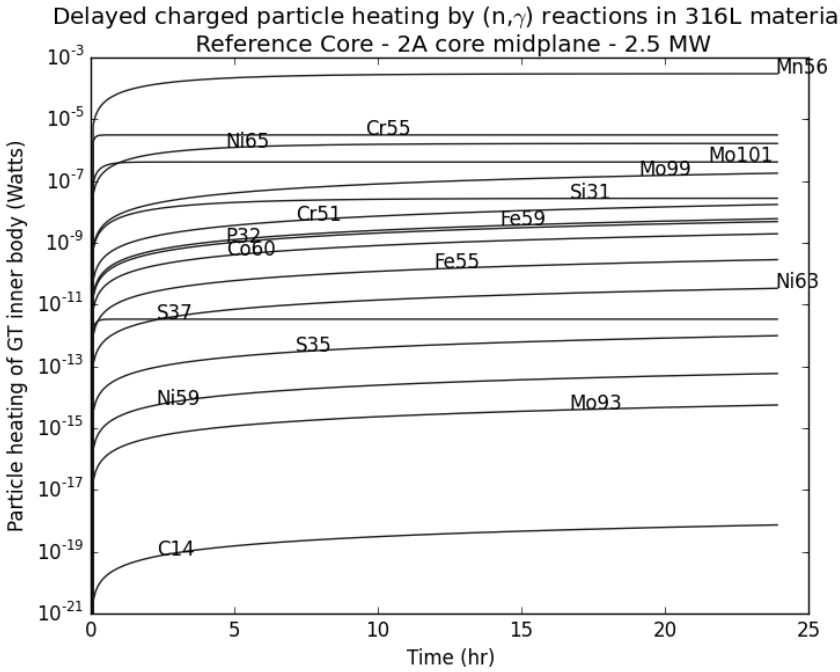

Figure 6.34: Delayed self-heating by charged particles released by MT-102 (n,γ) reactions in each isotope of 316L material.

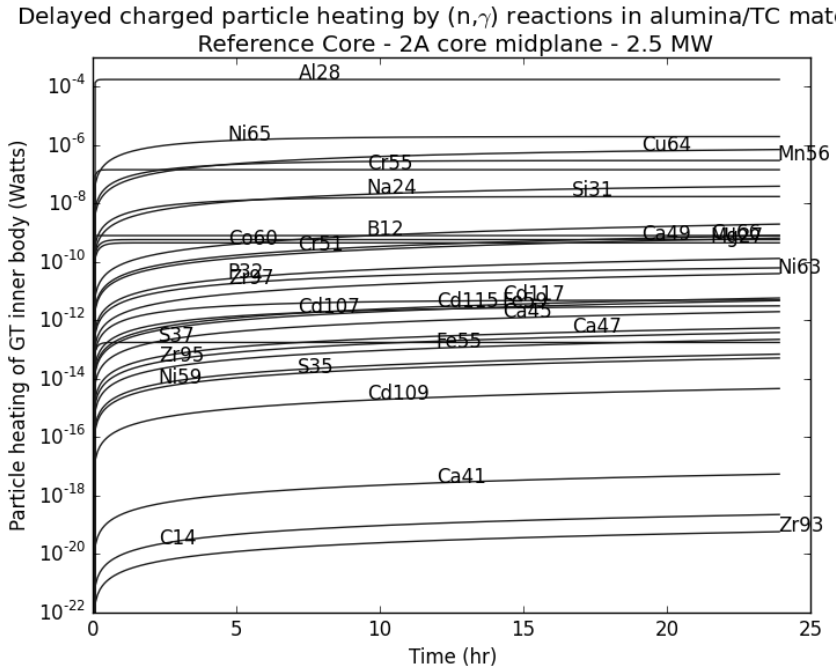

Figure 6.35: Delayed self-heating by charged particles released by MT-102 (n,γ) reactions in each isotope of alumina/TC materials.

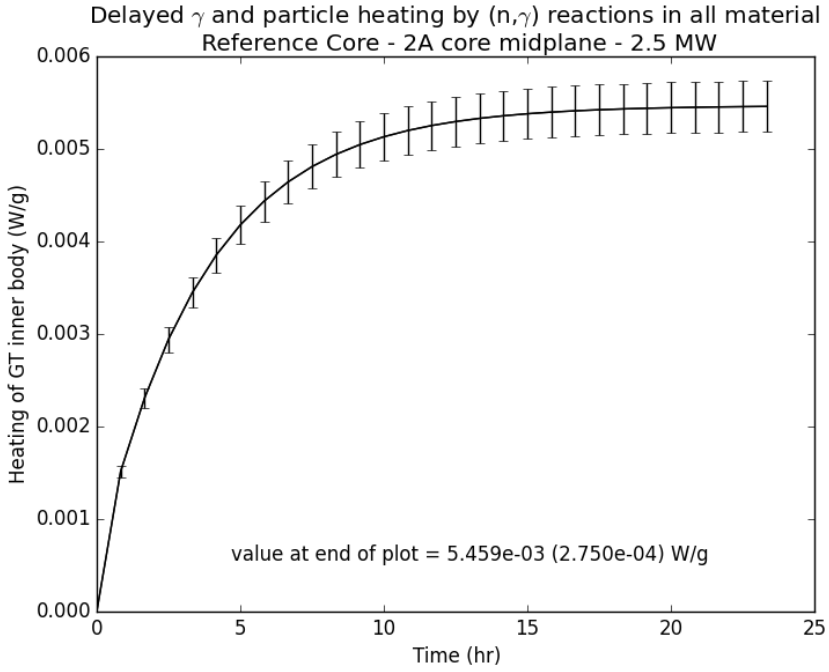

Figure 6.36: Delayed self-heating by gammas and charged particles released by MT-102 (n,γ) reactions in all isotopes in all SCK-CEN GT materials.

6.5 The SCK-CEN GT-20 bias

The SCK-CEN GT-20 has a constant "off-zero" bias; the cause of this deviation is not known and is assumed not to indicate a problem with the instrument. This error has been subtracted from the GT signal, as is common with such a bias (NIST 2015a).

This offset has been measured to average $\Delta T = 0.63 \pm 6.1\%\,^{\circ}\mathrm{C}$. This error was measured many-weeks after the GT-20 had been irradiated, which avoids any self-heating contribution from short-lived activated isotopes within the GT.

Another GT, SCK-CEN GT-22 which has never been irradiated, has a similar off-zero magnitude of $\Delta T = 0.71 \pm 2.4\%\,^{\circ}\mathrm{C}$.

6.6 Results of analysis of the SCK-CEN GT-20 signal

The uncertainties of A', C' and ΔT have been propagated into the uncertainty of $Q(t)/\rho$, σ_Q. The self-heating uncertainty is small in comparison, and therefore has not been considered in σ_Q.

6.6.1 Coefficients obtained by regression analysis of GT data

Figure 6.38 presents the nuclear heating $Q_{\mathrm{field}}(t)/\rho$ calculated from the SCK-CEN GT signal, using the steps outlined in section 5.3. The four time series shown are those which have been selected for futher processing, as discussed in section 6.1.

Table 6.6 presents the constants of the time series shown in Figure 6.38.

All this data was collected from core 59Jiv, shown in Figure 6.37.

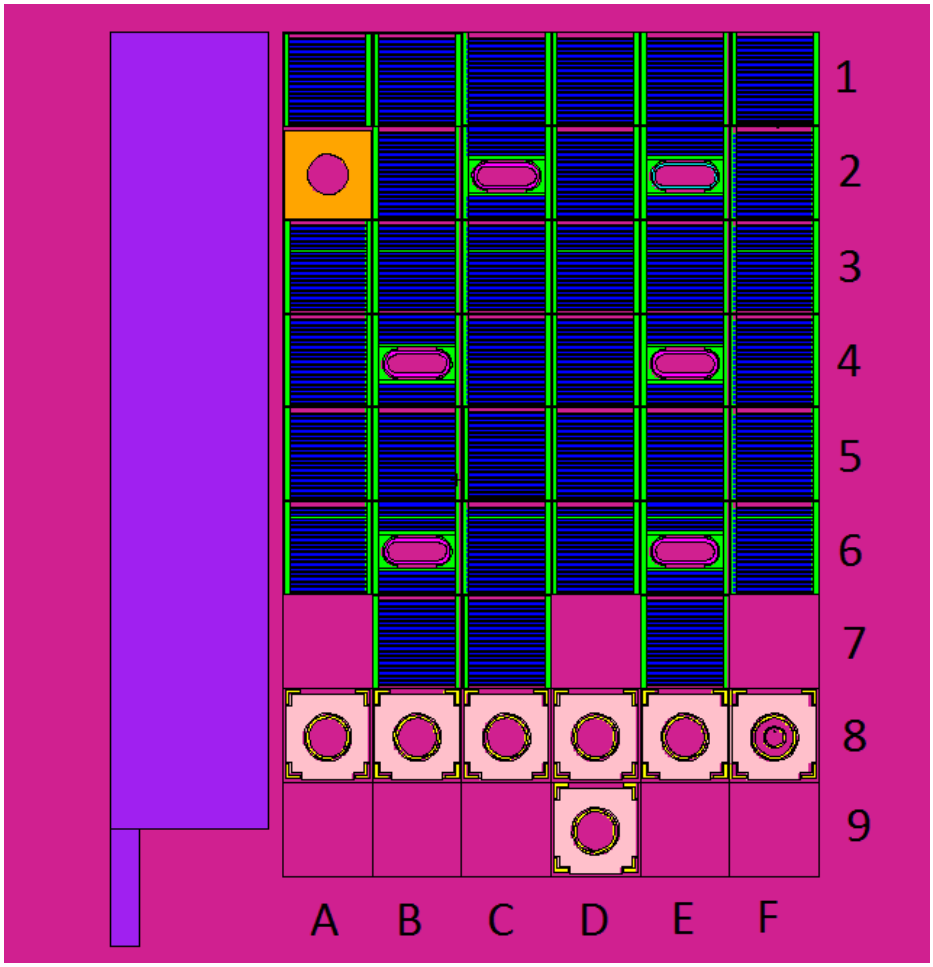

Figure 6.37: Map of core 59Jiv.

Case	Date	Nominal Power (MW)	Core	Location
1	Tues Oct 20, 2015	2.5	59Jiv	8F/G
2	Fri Oct 23, 2015	2.5	59Jiv	8F/G
3	Tues Nov 3, 2015	2.5	59Jv	2A/G
4	Thurs Nov 5, 2015	2.5	59Jv	2A/G

Table 6.5: Details of the data sets used for regression analysis.

Case	Prompt Heating	Delayed Heating	Delayed/Prompt	Decay Constant
1	$0.1112 \pm 1.2\%$ W/g	$0.01715 \pm 0.8\%$ W/g	$0.1542 \pm 1.4\%$	$0.000464 \pm 0.04\%$ 1/s
2	$0.1124 \pm 1.1\%$ W/g	$0.01507 \pm 0.6\%$ W/g	$0.1341 \pm 1.3\%$	$0.000452 \pm 1.8\%$ 1/s
3	$0.1936 \pm 1.0\%$ W/g	$0.05042 \pm 0.1\%$ W/g	$0.2604 \pm 1.0\%$	$0.000214 \pm 3.3\%$ 1/s
4	$0.2070 \pm 1.1\%$ W/g	$0.04543 \pm 0.3\%$ W/g	$0.2195 \pm 1.1\%$	$0.000237 \pm 2.4\%$ 1/s

Table 6.6: Results of regression analysis.

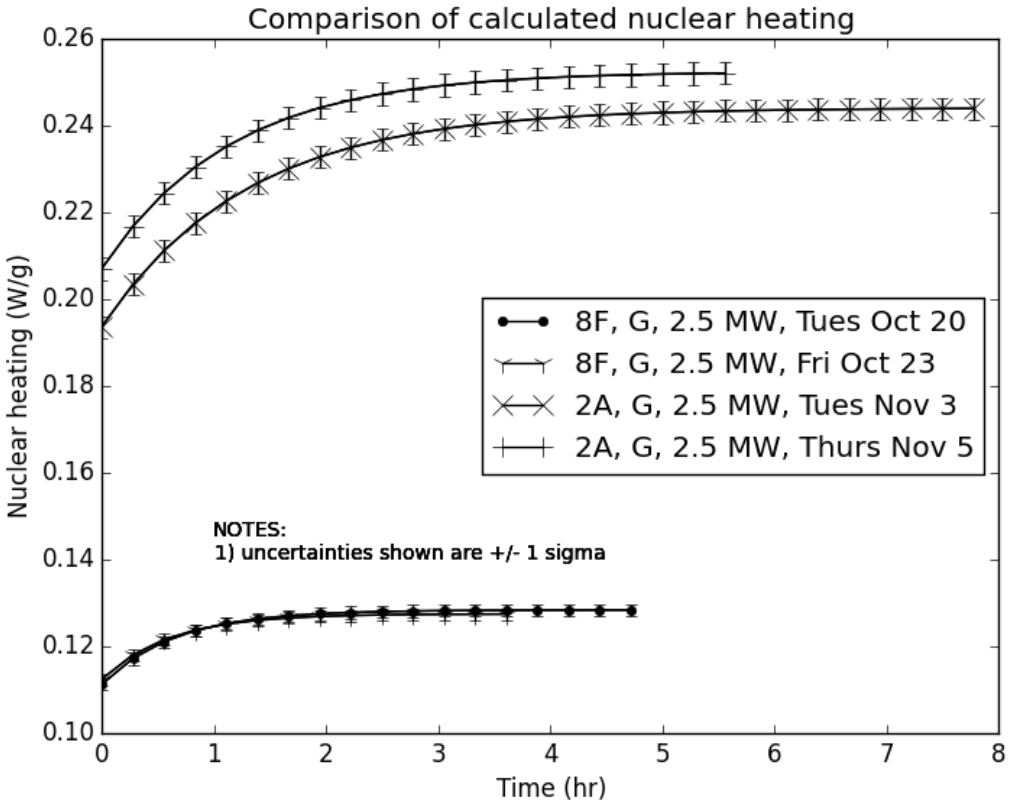

Figure 6.38: Calculated $Q_{\text{field}}(t)/\rho$ data sets used for curve fitting to determine the delayed-gamma heating constants.

6.7 Discussion of the results

When deriving the coupled neutron-gamma point kinetic equations (4.61), equations (4.35), (4.36) and (4.59) were assumed to be true; those equations are written again here for convenience:

$$\begin{aligned}\Phi(\vec{r},t) &= \upsilon_\gamma g(t)\kappa(\vec{r})\\ C_g(\vec{r},t) &= C_g(t)\kappa(\vec{r})\\ H(\vec{r}_G,G,t) &= \frac{\mu_{\text{effective}}(G,E^{\text{avg}})}{\rho}E^{\text{avg}}(\vec{r}_G)\upsilon_\gamma g(t)\kappa(\vec{r}).\end{aligned}$$

The above equations give value to the reactor's total gamma population $g(t)$ expressed by equations (4.56) and equations (4.61): $g(t)$ scales the local gamma spatial distribution $\kappa(\vec{r})$ in all locations of the core simultaneously. If equations (4.35) and (4.36) were true the local flux $\Phi(\vec{r},t)$, and by equation (4.59) the local nuclear heating $H(\vec{r}_G,G,t)$ plotted in Figure 6.38 would increase by the same fraction and with the same time constant at all $\vec{r}$. But this is not what Figure 6.38 and Table 6.6 demonstrate.

The constants of Table 6.6 suggest the magnitude and decay constant of the nuclear heating attributed to the delayed gammas are position dependent. The fraction of heating attributed to delayed gammas is smaller at location 8F compared to that measured at location 2A; the delayed-gamma heating at location 8F also has a larger decay constant (a shorter time constant).

This evidence suggests one (or more) factor of $H(\vec{r}_G,G,t)$ in equation (4.59) is a function of both t and $\vec{r}$. With no method to systematically study each factor, educated guesses must be made to determine which factor is suspect.

Since $g(t)$ was derived from first principles for equations (4.56) without large assumptions, the concept of $g(t)$ is probably correct. The factor most likely to blame is the gamma spatial distribution $\kappa(\vec{r})$ which was assumed to be time-independent in section 4.2.2 with no prior evidence this was true.

If κ is a function of both time and position equations (4.35) and (4.36) must be rewritten as:

$$\Phi(\vec{r},t) = \upsilon_\gamma g(t)\kappa(\vec{r},t) \tag{6.1}$$

$$C_g(\vec{r},t) = C_g(t)\kappa(\vec{r},t). \tag{6.2}$$

The following sections discuss two physical mechanisms which may explain why $\kappa(\vec{r},t)$ is dependent on both t and $\vec{r}$.

6.7.1 Mechanism 1: differences between prompt and delayed gamma spectra

To begin a discussion of κ it is best to refer back to the familiar and established neutron point kinetic equations (4.31). During the derivation of these equations the neutron transport and absorption processes have been considered with the inclusion of the property dictating neutron absorption, Σ_a, in equation (4.28). Equation (4.28) then yields expressions of both $n(t)$ and $\psi_1(\vec{r})$, after assuming equation (4.29) is true.

The assumption of equation (4.29) is very important because it states the spatial and temporal neutron flux components are separable: $\psi(\vec{r})$ is dependent on the variable $\vec{r}$ only and $n(t)$ is dependent on t only. This model of the neutron flux states that no matter when neutrons appear within the reactor geometry, either as prompt-fission neutrons or delayed neutrons, their spatial distribution will be described (relatively, rather than absolutely) according to the function $\psi(\vec{r})$.

Physically, the function $\psi(\vec{r})$ gives an indication of the ability of the neutrons to be transported from their source to $\vec{r}$. The distance neutrons can travel through a geometry depend upon the

material and the neutron energy. For any given critical assembly then, $\psi(\vec{r})$ will change with time if the neutron energy (at the source) changes with time.

Delayed neutrons have a softer spectrum than prompt-fission neutrons so one could define in any reactor: 1) $\psi_{\mathrm{P}(\vec{r})}$, to describe the spatial distribution of prompt neutrons, and 2) $\psi_{\mathrm{D}(\vec{r})}$, to describe the spatial distribution of delayed neutrons. However, the fraction of all neutrons which are delayed is usually less than 1% (Duderstadt and Hamilton 1976; 63). Therefore, when using the neutron point kinetic equations the entire neutron spatial distribution is approximated by a single function $\psi(\vec{r})$ which would be very close to $\psi_{\mathrm{P}(\vec{r})}$.

Measurements show the function κ is dependent on time, this may be because delayed gammas have a softer spectrum than prompt photons, but also because delayed gammas appear in significant quantities compared to prompt gammas.

There is no known measurement of the population yield of delayed gammas relative to prompt gammas, but Table 2.1 shows that when integrated over time, delayed gammas can be expected to carry approximately the same amount of fission energy as prompt fission gammas. Also, Table 3.1 showed the calculated heating resulting from delayed gammas in volumes in various critical assemblies was generally over 25%.

Figures 6.39 and 6.40 show the delayed photons have a softer spectrum than prompt photons and the delayed gamma spectrum becomes even softer with time following fission.

In a critical assembly, prompt fission gammas emitted from fuel material are absorbed as they move through the geometry; their distribution could be described by a function $\kappa_{\mathrm{P}}(\vec{r})$. The function $\kappa_{\mathrm{P}}(\vec{r})$ would be constant as reactor power changed and therefore constant in time. A function describing the delayed gamma distribution could be described by $\kappa_{\mathrm{D}}(\vec{r},t)$ which would change in time as the delayed gamma emission spectra changes. Therefore the total gamma distribution function $\kappa(\vec{r},t)$ would also be time dependent.

These differences in prompt and delayed gamma spectra may be strong enough to explain the results of Table 6.6.

In addition to the difference in spectra, the GT positions in 2A and 8F have different environments, the first is surrounded by Be and the second by C. Figure 6.41 shows the mass attenuation coefficients of these elements. These quantities are compared relatively in Figure 6.42 and show the C environment would certainly absorb more gammas below 0.1 MeV than Be.

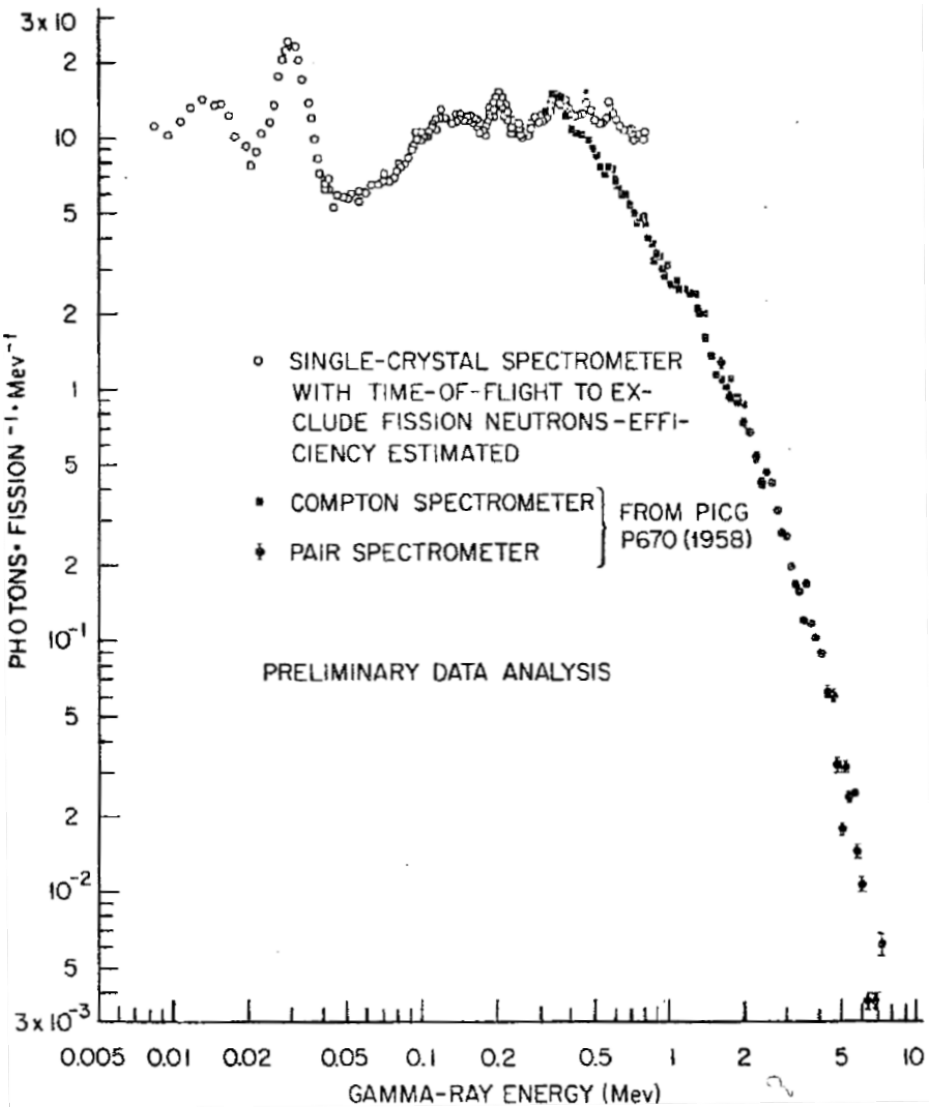

Figure 6.39: Prompt gamma spectrum emitted within 10^{-7} s after fission of ^{235}U (Keepin 1965; 66).

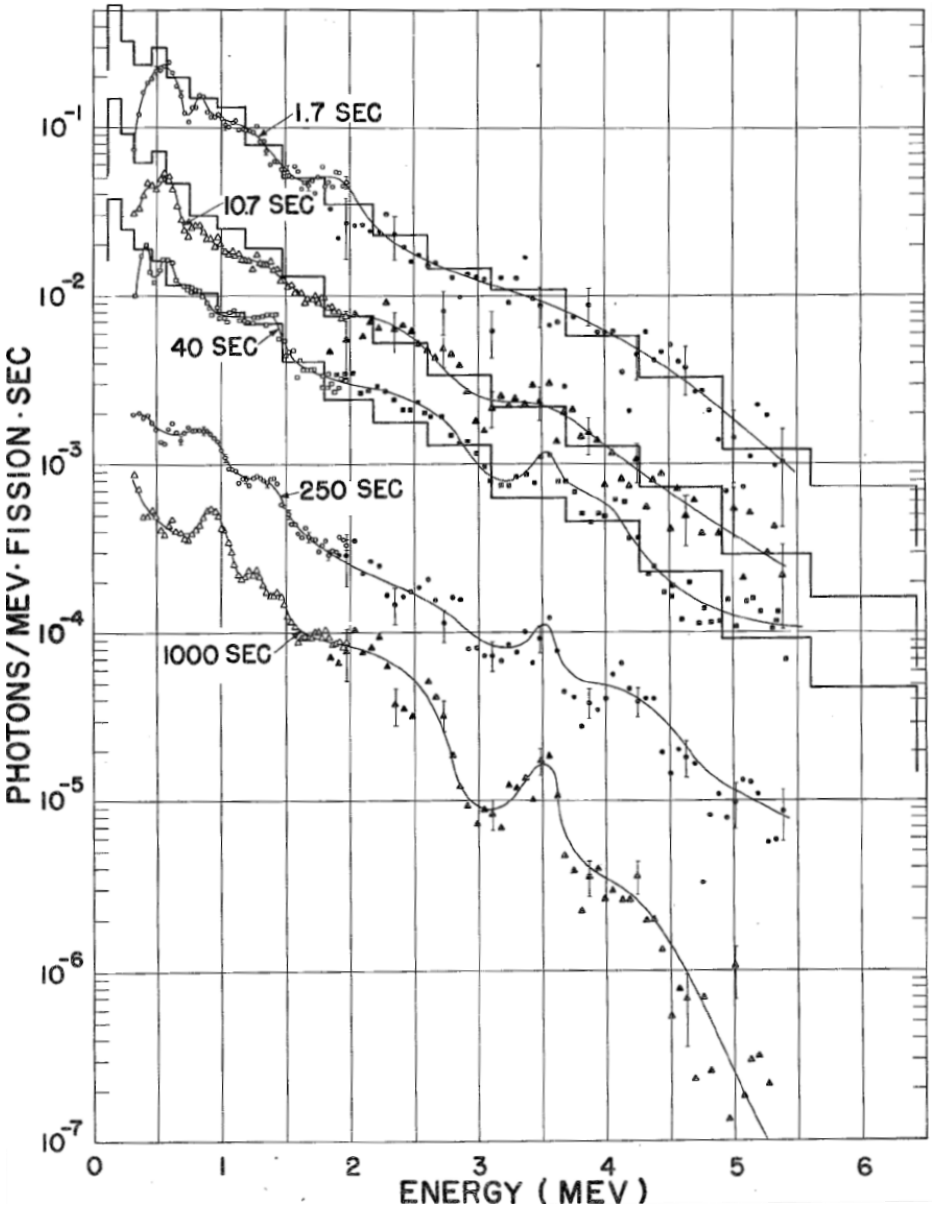

Figure 6.40: Delayed gamma spectra observed as a function of time after fission of ^{235}U (Keepin 1965; 132).

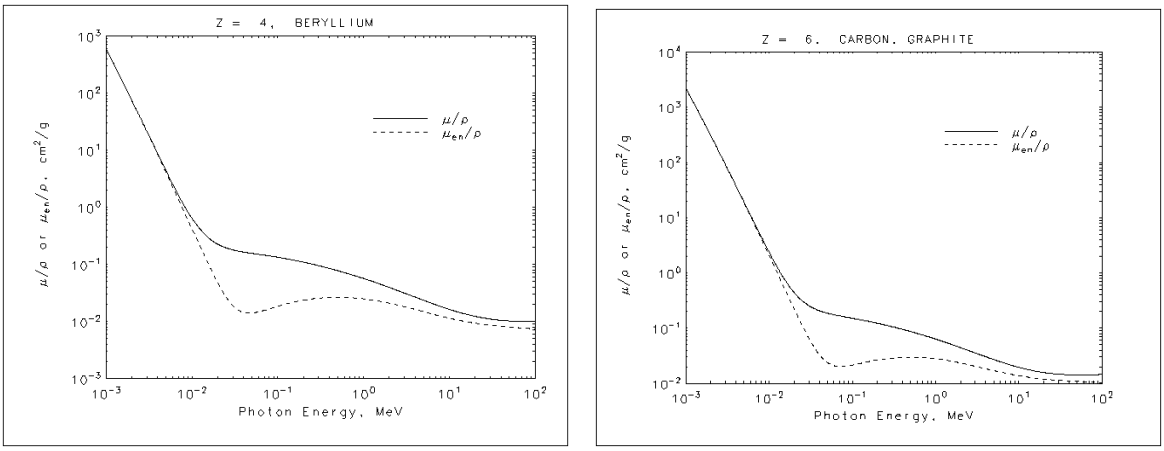

Figure 6.41: The mass attenuation coefficients (solid line) and mass energy-absorption coefficients (dotted line) for Be and C (Hubbell and Seltzer 2014).

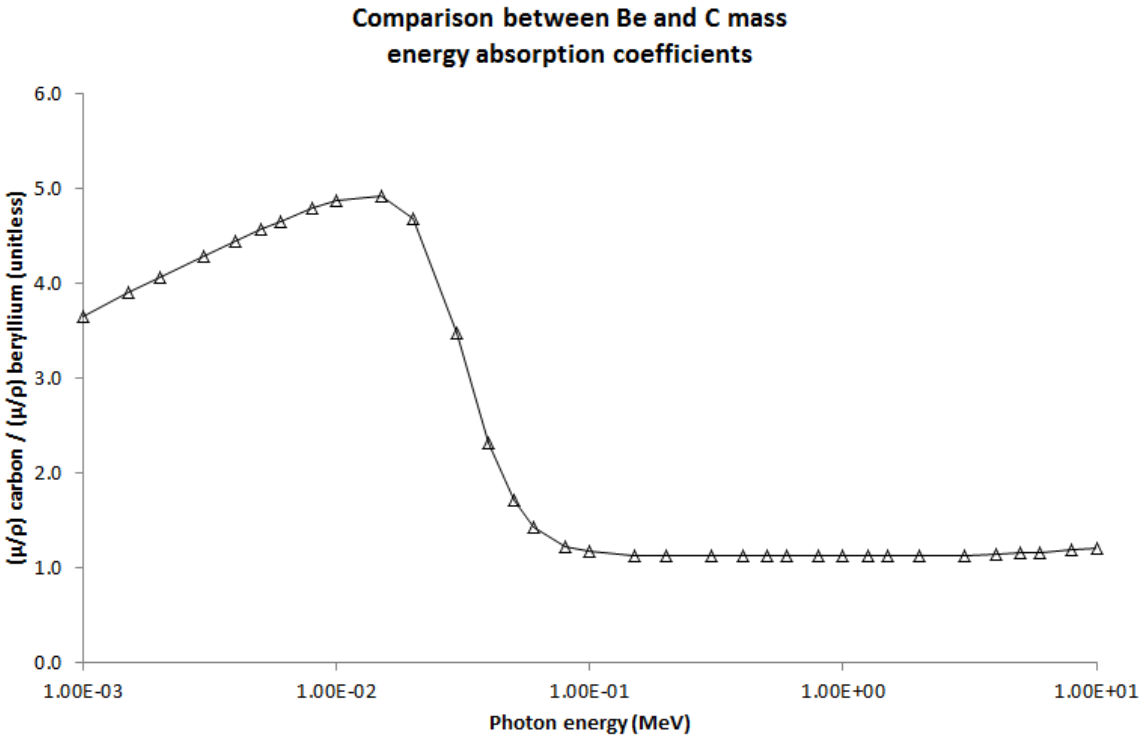

Figure 6.42: Plot showing the magnitude of the mass energy-absorption coefficient of C relative to that of Be.

6.7.2 Mechanism 2: dependency on control rod position changes

As detailed in section 5.2.3, it was assumed the large shim/safety rod position changes made in MNR throughout a normal operating day have a neglibible effect on the long-duration delayed-gamma heating trend sought in the GT signal. This assumption was made without a lot of supporting evidence so the validity of this assumption must now be reexamined as shim/safety rod movement may be a possible cause of the differing dynamics presented in Table 6.6.

Figure 6.43 shows the shim/safety rod positions as recorded by reactor operators on the days analyzed in Table 6.6. Time zero on this plot is the time the reactor reached full power, and corresponds to time zero on Figure 6.38. On all days examined, the plot shows shim/safety rods begin at nearly-withdrawn positions and are gradually inserted throughout the operating day.

If the shim/safety rod position strongly affects the data series $Q_{\text{field}}(t)/\rho$, the two 8F plots should have similar curves in Figure 6.43, as they do in Figure 6.38; the 2A plots would also. Figure 6.43 shows no such evidence. Qualitatively, the shim/safety rod position appears to be uncorrelated to the behavior of $Q_{\text{field}}(t)/\rho$ and the assumption in section 5.2.3 appears to be valid.

Thus, the shim/safety rod movement is unlikely to be the cause of $\kappa(\vec{r},t)$ being dependent on t and $\vec{r}$.

6.7.3 The coupled neutron and nuclear heating point kinetics (NHPK) model

The derivation of the coupled neutron-gamma point kinetic equations (4.61) depended on equations (4.35), (4.36) and (4.59) which all assumed $\kappa(\vec{r})$ to be independent of t; all these equations must now be rewritten.

Equations (4.35) and (4.36) have already been rewritten as equations (6.1) and (6.2).

Equation (4.59) expressed $H(\vec{r}_G,G,t)$ which can now be expressed instead with a sum of prompt and delayed gamma components:

$$H(\vec{r}_G,G,t) = H_{\text{P}}(\vec{r}_G,G,t) + H_{\text{D}}(\vec{r}_G,G,t) \tag{6.3}$$

$$\begin{aligned} H(\vec{r}_G,G,t) &= \frac{\mu_{\text{effective}}(G,E_{\text{P}}^{\text{avg}})}{\rho} E_{\text{P}}^{\text{avg}}(\vec{r}_G)\Phi_{\text{P}}(\vec{r}_G,t) \\ &+ \frac{\mu_{\text{effective}}(G,E_{\text{D}}^{\text{avg}})}{\rho} E_{\text{D}}^{\text{avg}}(\vec{r}_G,t)\Phi_{\text{D}}(\vec{r}_G,t), \end{aligned} \tag{6.4}$$

where:

$\Phi_{\text{P}}(\vec{r}_G,t)$ = prompt gamma scalar flux; $1/(\text{cm}^2 s)$

$\Phi_{\text{D}}(\vec{r}_G,t)$ = delayed gamma scalar flux

$E_{\text{P}}^{\text{avg}}(\vec{r}_G)$ = average prompt photon energy; MeV

$E_{\text{D}}^{\text{avg}}(\vec{r}_G,t)$ = average delayed photon energy

$\mu_{\text{effective}}(G,E_{\text{P}}^{\text{avg}})/\rho$ = effective mass energy-absorption coefficient of the prompt gammas; $1/\text{cm}\cdot\text{cm}^3/\text{g}$

$\mu_{\text{effective}}(G,E_{\text{D}}^{\text{avg}})/\rho$ = effective mass energy-absorption coefficient of the delayed gammas.

Notice $E_{\text{D}}^{\text{avg}}(\vec{r}_G,t)$ and thus $\mu_{\text{effective}}(G,E_{\text{D}}^{\text{avg}})$ are written as dependent on time and $E_{\text{P}}^{\text{avg}}(\vec{r}_G)$ is not.

The rewriting of equations (4.61) is more difficult because equation (4.60) has been invalidated by the discovery that $\kappa(\vec{r},t)$ is time-dependent; equation (4.60) was the tool to be used in the conversion of $g(t)/g_{\text{ref}}$ into heating. There is now no need for equations (4.61) to define $g(t)/g_{\text{ref}}$ since there is no manner to determine nuclear heating from $g(t)/g_{\text{ref}}$. Additionally, equations (4.61) need coefficients obtained with a GT and equation (4.60), which has been invalidated. So, equations (4.61) are of no use any longer.

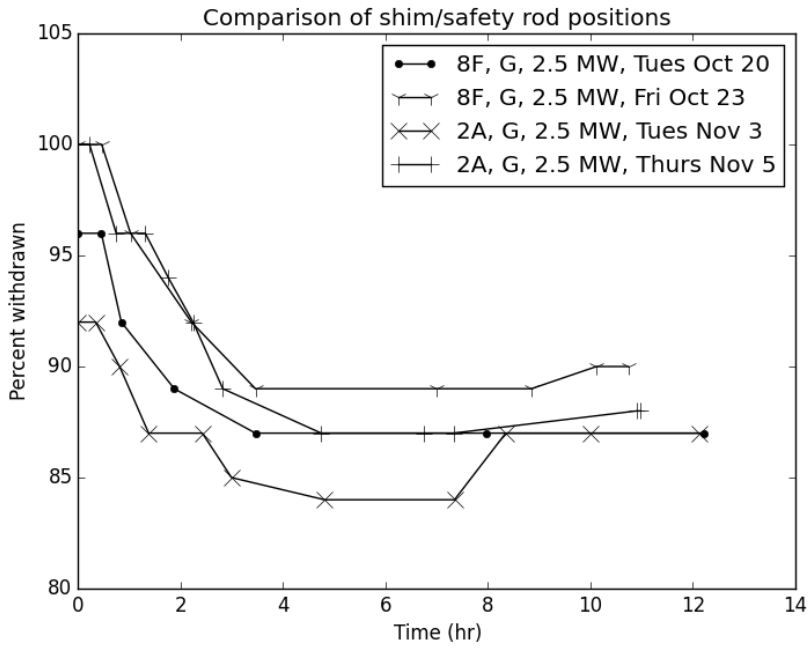

Figure 6.43: Control rod positions on the days the GT data sets were collected.

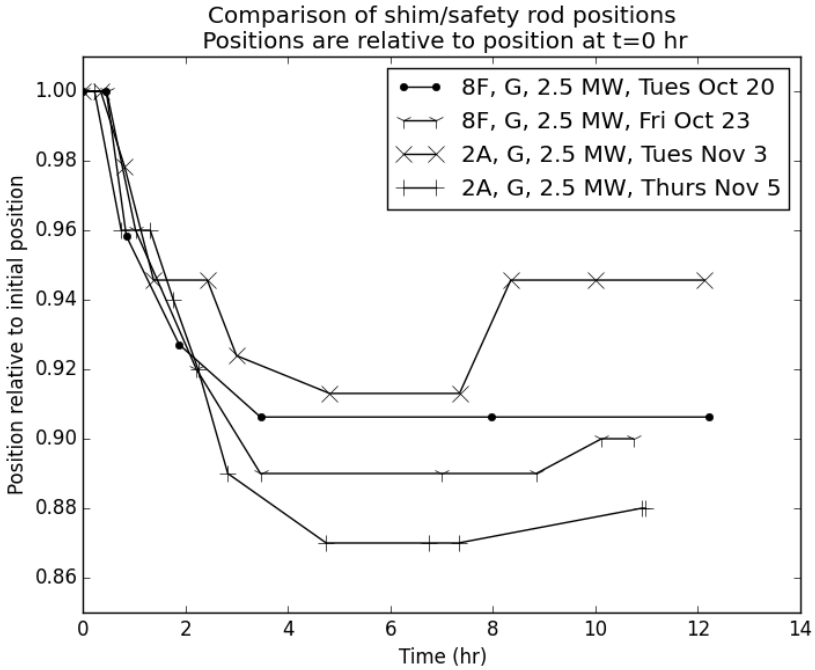

Figure 6.44: Control rod positions on the days the GT data sets were collected, relative to initial positions.

The coupled neutron-gamma equations (4.56) are still considered a valid expression of $g(t)$ since they have been derived from first principles and do not use coefficients which require a GT to define. But as discussed already, an equation solving for $g(t)/g_{\text{ref}}$ will only be of value once $\kappa(\vec{r},t)$ can also be defined.

The theory of coupled point kinetics models still has value though and can be written to use the experimental data of Table 6.6. Instead of coupling $g(t)/g_{\text{ref}}$ to $n(t)/n_{\text{ref}}$, the nuclear heating $H(\vec{r}_G,G,t)$ can be coupled to $n(t)/n_{\text{ref}}$. The equations would then predict nuclear heating in a specific volume G at positiion $\vec{r}_G$, provided a measurement of the dynamic gamma heating at this location has previously been made with the volume G. These nuclear heating point kinetic (NHPK) equations can be written as:

$$
\begin{aligned}
\frac{1}{n_{\text{ref}}}\frac{\mathrm{d}n(t)}{\mathrm{d}t} &= \left[\frac{\rho(t)-\beta}{\Lambda}\right]\frac{n(t)}{n_{\text{ref}}} + \sum_{n=1}^{6}\lambda_n C_n(t) \qquad (6.5)\\
\frac{\mathrm{d}C_n(t)}{\mathrm{d}t} &= \frac{\beta_n}{\Lambda}\frac{n(t)}{n_{\text{ref}}} - \lambda_n C_n(t) \qquad n=1,2...6.\\
\frac{\mathrm{d}H(\vec{r}_G,G,t)}{\mathrm{d}t} &= a(\vec{r}_G,G)\upsilon\Sigma\frac{n(t)}{n_{\text{ref}}} - L_h H(\vec{r}_G,G,t) + \sum_{h=1}\lambda_h(\vec{r}_G,G)C_h(t)\\
\frac{\mathrm{d}C_h(t)}{\mathrm{d}t} &= b_h(\vec{r}_G,G)\upsilon\Sigma\frac{n(t)}{n_{\text{ref}}} - \lambda_h(\vec{r}_G,G)C_h(t)\\
&\vdots\\
H &\quad \text{instances of this equation.}
\end{aligned}
$$

where:
$\frac{n(t)}{n_{\text{ref}}}$ = relative number of neutrons in the core at time t; unitless
n_{ref} = reference number of neutrons in the core; unitless
$a(\vec{r}_G,G)$ = prompt heating coefficient; W/g
$b_h(\vec{r}_G,G)$ = delayed heating coefficient of delayed heating group h; W/g
$\lambda_h(\vec{r}_G,G)$ = decay constant of delayed heating group h; 1/s
$C_h(t)$ = heating variable of group h; 1/cm^3
υ = core-averaged neutron speed; cm/s
Σ = core-averaged macroscopic cross section, for all relevant reactions and isotopes; 1/cm
H = the number of exponential groups required to describe the total heating
L_h = loss rate coefficient; 1/s .

In equations (4.61) Keepin's grouping and regression analysis was used to describe the dynamic behavior of $g(t)/g_{\text{ref}}$. The same analysis can be used with the GT data to define the constants $a(\vec{r}_G,G)$, $b_h(\vec{r}_G,G)$ and $\lambda_h(\vec{r}_G,G)$ in equations (6.5). These equations were written assuming the GT used to obtain these constants is able to determine absolute nuclear heating, thus allowing equations (6.5) to solve for the absolute nuclear heating $H(\vec{r}_G,G,t)$. If the GT is only capable of measuring relative heating these coefficients and the heating would also be expressed in relative terms.

Notice the constants $a(\vec{r}_G,G)$, $b_h(\vec{r}_G,G)$ and $\lambda_h(\vec{r}_G,G)$, and $H(\vec{r}_G,G,t)$ do not apply to the entire core but are specific to G, Z (the material of G) and $\vec{r}_G$.

Figure 6.46 shows equations (6.5) can duplicate the heating measured with the GT on Tuesday November 3 when $n(t)/n_{\text{ref}}$ is constant; the function fit to the November 3 data is re-plotted in Figure 6.45 for convenience. This solution was obtained by solving the coupled $\mathrm{d}H(\vec{r}_G,G,t)/\mathrm{d}t$ and $\mathrm{d}C_h(t)/\mathrm{d}t$ equations from (6.5) in MATLAB with the $ODE45$ solver with $a(\vec{r}_G,G) = 0.1936$ W/g, $b_h(\vec{r}_G,G) = 0.05042$ W/g and $\lambda_h(\vec{r}_G,G) = 0.000214$ 1/s, which are the Tuesday November 3 constants in Table 6.6 (The MathWorks 2004).

The use-value of the NHPK equations is illustrated by Figures 6.47 and 6.48: once the equations' coefficients have been determined experimentally, the nuclear heating can be predicted (Figure 6.48) for any given $n(t)/n_{\text{ref}}$ (Figure 6.47).

In all solutions, $n(t)/n_{\text{ref}} = 1.0$ when the reactor's thermal power (without delayed gammas) is equal to the nominal reactor power of the associated constants from Table 6.5.

All solutions of equations (6.5) have been obtained with preliminary estimates of the variable L_h and the product $\upsilon\Sigma$. The nature of these variables has been examined by solving for both in special conditions.

When t is very large and $n(t)/n_{\text{ref}}$ is constant $\mathrm{d}H(\vec{r}_G, G, t)/\mathrm{d}t = C_h(t)/\mathrm{d}t = 0$. Assuming a fictional reactor with no delayed gammas is under examination, then $b_h(\vec{r}_G, G) = 0$ and $\lambda_h(\vec{r}_G, G) = 0$ for all h. Also assume $n(t)/n_{\text{ref}}$ is a constant 1.0, then $H(\vec{r}_G, G, t) = a(\vec{r}_G, G)$ and the heating rate equation of (6.5) is:

$$\begin{aligned}
\frac{\mathrm{d}H(\vec{r}_G, G, t)}{\mathrm{d}t} &= a(\vec{r}_G, G)\upsilon\Sigma\frac{n(t)}{n_{\text{ref}}} - L_h H(\vec{r}_G, G, t) + \sum_{h=1} \lambda_h(\vec{r}_G, G)C_h(t) \\
0 &= a(\vec{r}_G, G)\upsilon\Sigma - L_h a(\vec{r}_G, G) \\
L_h &= \upsilon\Sigma.
\end{aligned}$$

In a reactor with one delayed gamma-heating group and constant $n(t)/n_{\text{ref}} = 1.0$, at large t the heating variable rate equation of (6.5) is:

$$\begin{aligned}
\frac{\mathrm{d}C_h(t)}{\mathrm{d}t} &= b_h(\vec{r}_G, G)\upsilon\Sigma\frac{n(t)}{n_{\text{ref}}} - \lambda_h(\vec{r}_G, G)C_h(t) \\
0 &= b_1(\vec{r}_G, G)\upsilon\Sigma - \lambda_1(\vec{r}_G, G)C_1(t) \\
C_1(t) &= \frac{b_1(\vec{r}_G, G)\upsilon\Sigma}{\lambda_1}.
\end{aligned}$$

Knowing $H(\vec{r}_G, G, t) = a(\vec{r}_G, G) + b_1(\vec{r}_G, G)$ at large t the corresponding heating rate equation of (6.5) is then used to solve for L_h:

$$\begin{aligned}
\frac{\mathrm{d}H(\vec{r}_G, G, t)}{\mathrm{d}t} &= a(\vec{r}_G, G)\upsilon\Sigma\frac{n(t)}{n_{\text{ref}}} - L_h H(\vec{r}_G, G, t) + \sum_{h=1} \lambda_h(\vec{r}_G, G)C_h(t) \\
0 &= a(\vec{r}_G, G)\upsilon\Sigma - L_h(a(\vec{r}_G, G) + b_1(\vec{r}_G, G)) + b_1(\vec{r}_G, G)\upsilon\Sigma \qquad (6.6) \\
0 &= (a(\vec{r}_G, G) + b_1(\vec{r}_G, G))\upsilon\Sigma - L_h(a(\vec{r}_G, G) + b_1(\vec{r}_G, G)) \qquad (6.7) \\
L_h &= \upsilon\Sigma. \qquad (6.8)
\end{aligned}$$

Thus in both cases of $H = 0$ and $H = 1$, $L_h = \upsilon\Sigma$; this definition of L_h results in the correct units.

To determine the value of the product $\upsilon\Sigma$ the MATLAB solution of equations (6.5) was run in two cases, where the value of the product in one case was 100 times that of the other. Both cases used the same dynamic $n(t)/n_{\text{ref}}$ of Figure 6.49. The perturbation reveals $\upsilon\Sigma$ affects only the rate $H(\vec{r}_G, G, t)$ approaches and departs steady state conditions. Figures 6.50 and 6.51 present the results of these two cases. This parametric study isn't capable of defining the true value of $\upsilon\Sigma$ but any value $\upsilon\Sigma \geq 1.0$ 1/s matches the experimentally-obtained exponential functions of Table 6.6; thus $\upsilon\Sigma = 1.0$ 1/s was used when solving equations (6.5) to obtain the data presented in Figure 6.48.

6.7.4 Summary

The total prompt and delayed gamma heating has been measured in two locations of the MNR core. The results in Figure 6.38 and Table 6.6 show the gamma distribution function κ is dependent on t and $\vec{r}$.

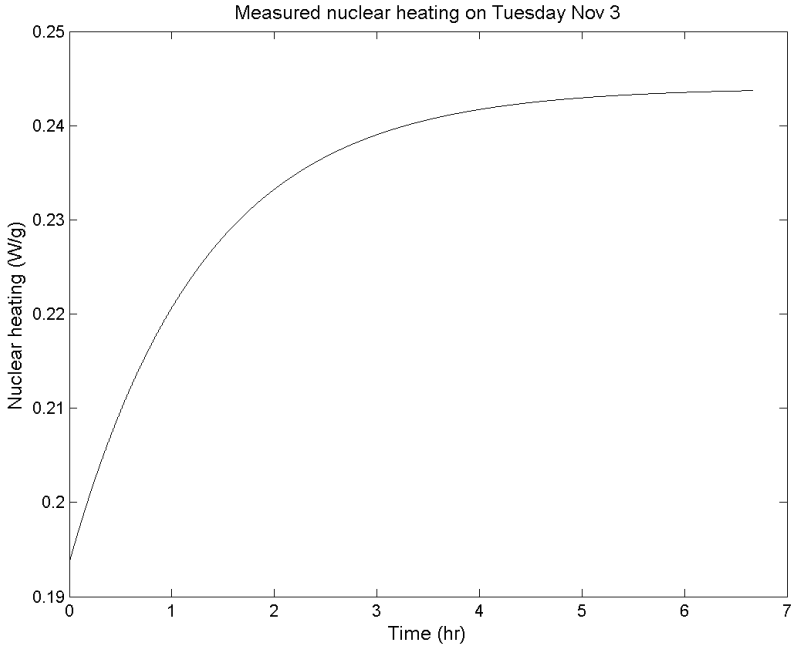

Figure 6.45: Exponential function plotted using the Tuesday November 3 constants in Table 6.6.

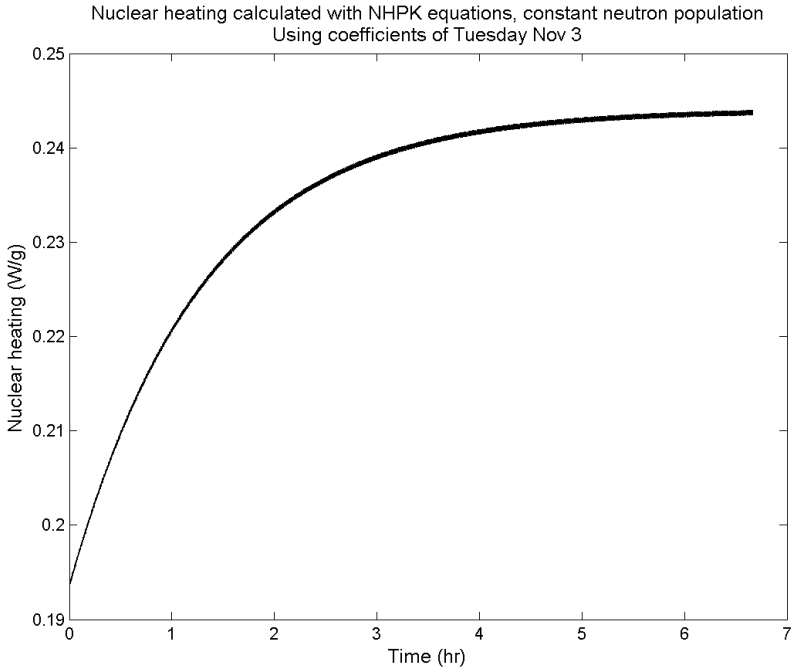

Figure 6.46: Heating calculated by equations (6.5) using a constant neutron flux, duplicating the experimental data of Figure 6.45.

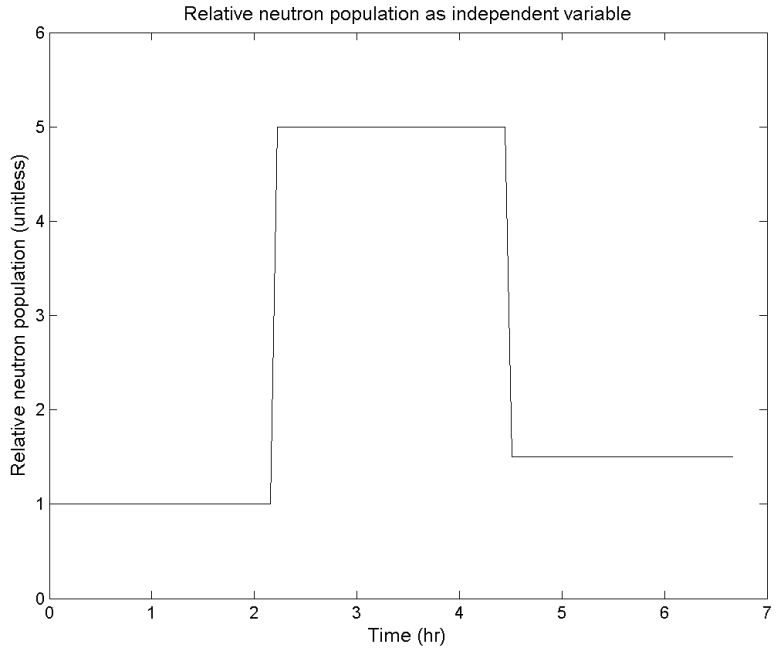

Figure 6.47: A time-dependent data series of normalized $n(t)$.

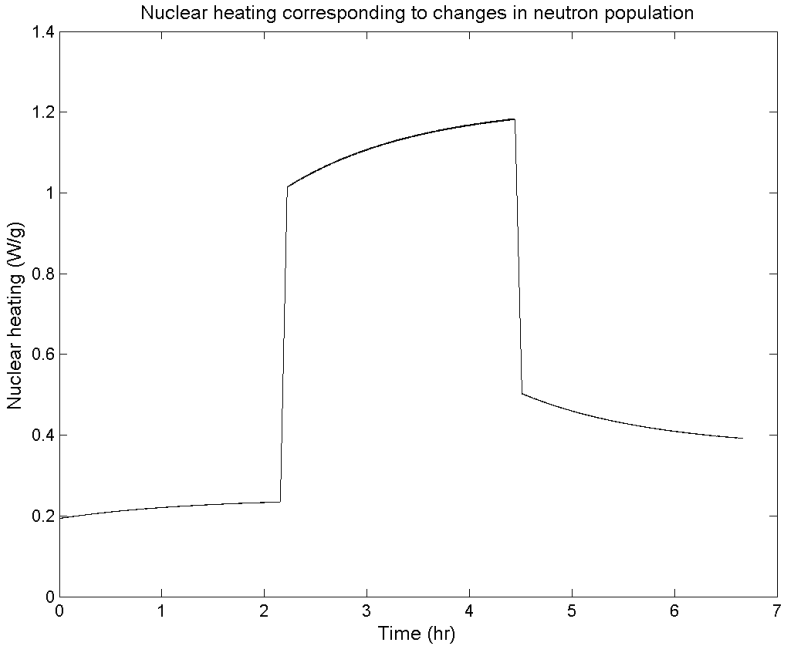

Figure 6.48: The nuclear heating predicted by the NHPK equations, corresponding to the changing neutron population of Figure 6.47.

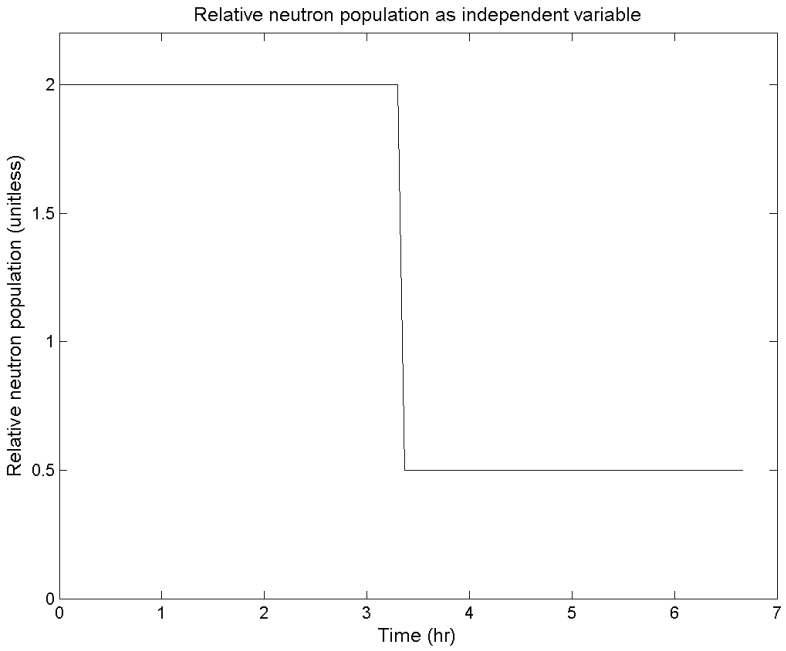

Figure 6.49: A time-dependent data series of normalized $n(t)$.

Given the dependency of κ on both t and $\vec{r}$, the previous assumption of dependency on $\vec{r}$ means equation (4.59) needs to be modified and there is no value in calculating $g(t)$ with the coupled neutron-photon point kinetics (PPK) equations (4.56) unless $\kappa(\vec{r}, t)$ can be calculated or measured.

The coupled neutron and nuclear heating point kinetics (NHPK) equations (6.5) can be used to couple the nuclear heating $H(\vec{r}_G, G, t)$ to the core's relative neutron population $n(t)/n_{\text{ref}}$, where $H(\vec{r}_G, G, t)$ is the nuclear heating in a specific volume G at position $\vec{r}_G$. In the case of the SCK-CEN GT, $H(\vec{r}_G, G, t)$ has been shown to be dominated by photon heating but the heating of another G volume or material may be dominated by neutrons as shown by the work in section E.4.1. The coefficients $a(\vec{r}_G, G)$, $b_h(\vec{r}_G, G)$ and $\lambda_h(\vec{r}_G, G)$ contained in these equations therefore must be obtained with a dynamic measurement of the heating of G in location $\vec{r}_G$.

After the coefficients of the NHPK equations have been determined experimentally, $H(\vec{r}_G, G, t)$ can be predicted as a function of the core's relative neutron population $n(t)/n_{\text{ref}}$ using an ODE solver.

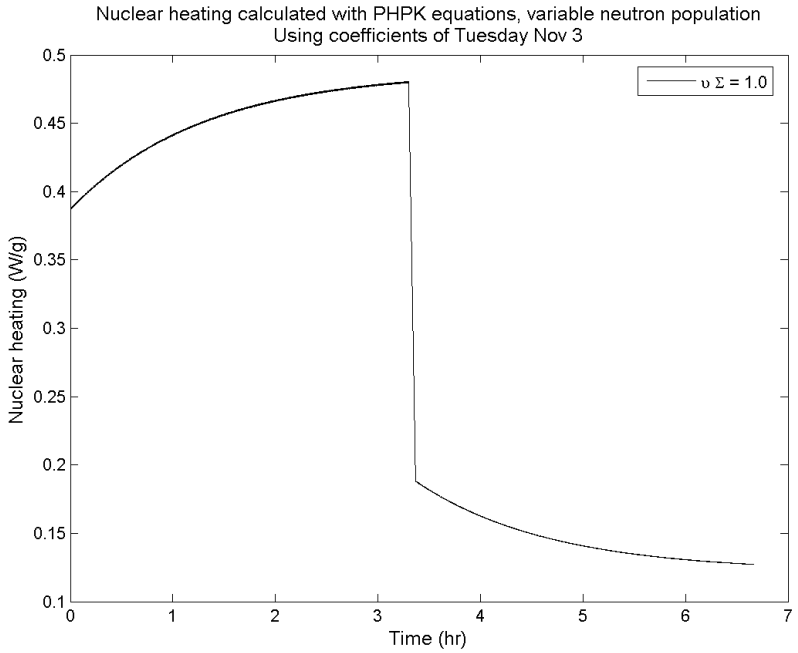

Figure 6.50: The nuclear heating predicted by the NHPK equations, corresponding to the changing neutron population of Figure 6.49; using $\upsilon\Sigma = 1.0$.

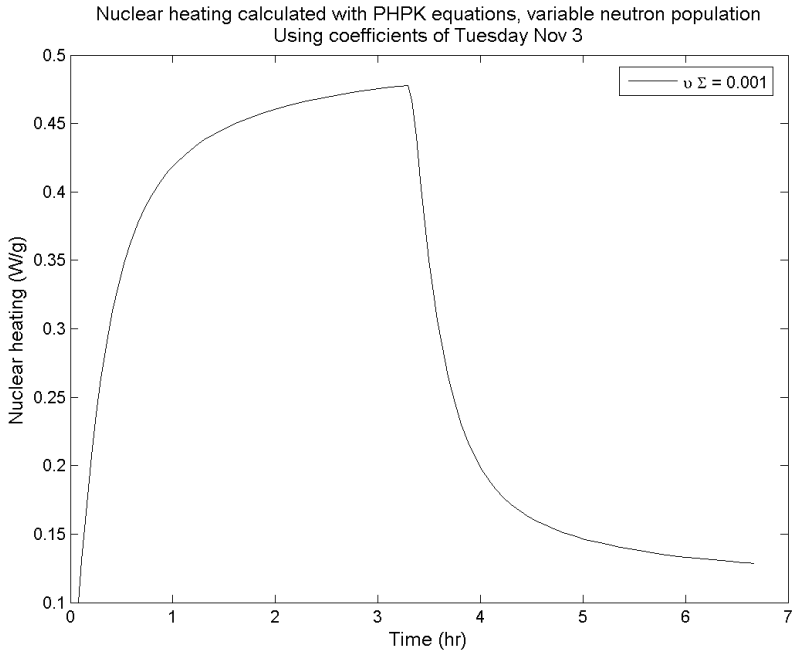

Figure 6.51: The nuclear heating predicted by the NHPK equations, corresponding to the changing neutron population of Figure 6.49; using $\upsilon\Sigma = 0.001$.

Chapter 7

Summary, conclusions and recommendations for future work

7.1 Summary of motivation and analysis

A literature review has revealed no existing descriptions of the in-core time dependent delayed-gamma heating of a MTR, or any other reactor. Many experimental programs have measured an integrated gamma dose, but no references could be found which describes the dynamics of the time-dependent heating. Experimental devices have incidentally recorded this time-dependent heating, but no quantitative descriptions or generalized models have been developed with these observations. Additionally, while some mature Monte Carlo codes have been shown capable of calculating in-core prompt-gamma heating, these codes lack the ability to describe the total (prompt and delayed) in-core time-dependent gamma heating.

Therefore, one objective of this study was to measure the total time-dependent nuclear heating within a materials testing reactor (MTR) core to isolate and describe the heating component caused by delayed gammas. To achieve these goals an SCK-CEN GT was commissioned in the McMaster Nuclear Reactor (MNR) and was used to measure the delayed-gamma component of nuclear heating in two core locations. Analysis of the GT's signal resulted in a dynamic description of the delayed-gamma heating of the GT.

This study also aimed to develop a new time-dependent nuclear heating model capable of predicting nuclear heating as a function of neutron flux, and which can reproduce the heating measured in MNR. Two new models which describe the time and position-dependent in-core prompt and delayed gamma heating were derived: the nuclear heating equation and the coupled neutron and nuclear heating point kinetics (NHPK) model.

The nuclear heating equation is a generalized equation describing the time-dependent nuclear heating in a volume of interest, within an arbitrary geometry. Such an equation is valuable to symbolically represent the relevant physical processes and abstract them from any specific geometry, reaction or material. This equation uses tallies/scores from Monte Carlo calculations as coefficients and uses the in-core neutron flux as an independent variable. The nuclear heating equation has been implemented in a study of the SCK-CEN GT self-heating.

The NHPK model is an extension of the neutron point-kinetics equations by coupling the core's neutron population to nuclear heating in a volume of interest. The NHPK model uses the constants obtained by the GT measurements in MNR as inputs; the reactivity or in-core neutron flux is an independent variable within the NHPK equations. This model will allow others to predict the nuclear heating of the GT as the reactor power changes.

The NHPK model has been implemented with an ODE solver to confirm it duplicates the exper-

imental data collected by the SCK-CEN GT and to demonstrate the equations' predicted nuclear heating as a function of a dynamic neutron flux input.

7.2 Summary of novelties

This thesis contains the following original work:

1. **Derivation of the nuclear heating equation** (4.21)**.** This equation symbolically represents all sources of radiation and the associated energy deposition of each source, to express the total nuclear heating a volume of interest. This equation has been used to calculate self-heating in the SCK-CEN GT.

2. **Derivation of the coupled neutron and nuclear heating point kinetics (NHPK) equations** (6.5)**.** Solving this equation predicts the nuclear heating in a volume of interest as a function of in-core neutron population or reactivity.

3. **Using Keepin's grouping method to describe the aggregated in-core delayed nuclear heating and gamma yields.** The SCK-CEN GT experimental data has been described with exponential functions. The delayed gamma yields have also been described with exponential functions, similar to the way Keepin has used exponential functions to describe delayed neutron yields; this method of describing gamma yields has been used in the derivation of equations (4.56).

4. **Derivation of the calibration equation** (5.26)**.** This equation allows the SCK-CEN GT signal to be converted into a W/g value, in static or transient conditions.

5. **Developed a Python program to calculate self-heating in the SCK-CEN GT by (n,γ) reactions using equation** (4.21)**.** This program uses prompt emission data from the CapGam (National Nuclear Data Center 2015) and IAEA Database of Prompt Gamma Rays from Slow Neutron Capture for Elemental Analysis (IAEA 2015); delayed emission data is from NuDat 2.6 (National Nuclear Data Center 2015).

6. **Commissioned an SCK-CEN GT in the McMaster Nuclear Reactor for the specific purpose of measuring the total time-dependent gamma heating within a MTR core.**

7. **Analysis of the SCK-CEN GT signal showing the photon spatial distribution $\kappa(\vec{r}, t)$ is time and position-dependent.**

7.3 Recommendations for future work

The following tasks are recommended to extend the analysis contained within this thesis:

1. **Plan GT irradiation experiments where the entire reactor operation is dedicated to obtaining a clean GT signal.** Within this thesis, the use of the GT in MNR was during normal MNR operation. While this makes the GT use relatively simple, the trends within the collected data describing the delayed gamma heating are usually obscured by small changes in MNR conditions; efforts should be made to minimize any changes in reactor power during GT irradiation.

2. **Complete further analysis on the assumptions made in the derivation of the NHPK equations.** Using the MCNP6 Reference Core model, the sensitivity of prompt gamma heating of the GT to changes in control rod position could be determined with the comparison of two cases, one with perturbed control rod positions. The sensitivity of nuclear heating in the GT to fission product inventory and burn-up could be completed with the same method.

3. **Incorporate an ODE solver into the Python code calculating the GT self-heating to allow for changes in neutron flux.** No analysis of the post-shutdown delayed gamma heating has been conducted in this thesis. The SCK-CEN GT clearly records this nuclear heating, however to calculate the GT self-heating following significant changes in neutron flux require the consideration of these changes in the self-heating calculations. The Python program developed in this thesis calculates self-heating while assuming a constant neutron flux.

4. **Change the GT lead wire to one with more shielding to see if the GT signal noise can be reduced.** As all instruments, the SCK-CEN GT's signal contains some noise. The GT itself cannot be modified since it is sealed from the manufacturer. But perhaps changing the lead wire with another having a better shielding would reduce the signal noise. This is the only component in the GT signal chain which is easily replaceable.

5. **Investigate the possibility of making the NHPK equations applicable to all core locations.** The NHPK equations describe nuclear heating at a single location. Using the known delayed gamma spectra, perhaps Monte Carlo investigations could relate nuclear heating at one location to other in-core locations.

6. **Compare the predictions of the NHPK equations to dynamic GT meansurements.** The SCK-CEN GT could be placed in MNR during a significant change in neutron flux. The predictions of the NHPK equations (using coefficients associated with this location) could then be compared to the measurements.

7.4 Conclusions

The nuclear heating equation can be used to describe the time-dependent nuclear heating in a volume of interest G, within any geometry. This equation uses tallies/scores from Monte Carlo calculations as inputs and uses the in-core neutron flux as an independent variable.

The coupled neutron and nuclear heating point kinetics (NHPK) equations (6.5) can be used to predict the nuclear heating $H(\vec{r}_G, G, t)$ in a specific volume G at a specific position $\vec{r}_G$ as a function of the core's relative neutron population, provided a dynamic measurement of nuclear heating in G at $\vec{r}_G$ has already been made; the coefficients $a(\vec{r}_G, G)$, $b_h(\vec{r}_G, G)$ and $\lambda_h(\vec{r}_G, G)$ contained in equations (6.5) are obtained with this measurement.

The fraction of nuclear heating caused by delayed gammas has been found to be position dependent, as was the time constant of this heating. This dependency is suspected to result from the delayed fission gammas having a softer spectra than prompt fission gammas, and progressively softening as decay progresses. The fraction of delayed gamma heating was observed to be larger in the Be in-core environment than in a C environment; these environments absorb the softer delayed gammas differently.

Appendix A

The Monte Carlo method and associated uncertainties

The statistical sampling technique called the Monte Carlo method, evolved into its modern form after seminal methods were developed by Manhatten Project mathematicians and physicists. Although the principles of statistical sampling techniques have been around for hundreds of years, it was the development of the first electronic computing machine ENIAC, in 1945, which made the method practical; before ENIAC was developed, the large number of relatively simple calculations required by the Monte Carlo method formed an obstacle to implementation.

Every event in a particle's life is a stochastic process: birth, direction of travel, absorption, scattering, secondary particle generation and fission. The Monte Carlo method simulates the lives of many individual particles moving within a subject geometry; the recorded events of one life is called a history and are simulated by sampling from the probability distribution of each lifetime event with random numbers.

After simulating many histories, the average particle behaviour is then statistically inferred; knowledge of some average quantity, such as the number of particles moving through a volume or energy deposited within a volume, is useful because it represents the expected behaviour of the real system. This average is called the tally in MCNP6 and the score in TRIPOLI4.

A.1 Monte Carlo uncertainties

To obtain an expression of uncertainty on the resulting tally, each history is considered a single sample x_i from a random variable X (X-5 Monte Carlo Team 2008; 2-109). The tally or score, is the mean of the samples, $\bar{x}$; this sample mean is considered an efficient unbiased estimator of the true population mean μ (Johnson *et al.* 2000; 223).

From theory, it is known that when n samples (histories) are taken from a population having a mean μ and variance σ^2, the sample mean is itself a random variable $\bar{X}$ whose distribution has the mean μ and a variance related to n by (Johnson *et al.* 2000; 205):

$$S_{\bar{X}}^2 = \frac{\sigma^2}{n}.$$

As with most populations though, the variance σ^2 is unknown, but it is considered acceptable for large n to approximate the population variance with the sample variance S^2 (Johnson *et al.* 2000; 212). The standard deviation of the tally is then (X-5 Monte Carlo Team 2008; 2-110):

$$S_{\bar{X}} = \frac{S}{\sqrt{n}}.$$

It must be noted that $S_{\bar{X}}$ expresses precision, and there is no parameter which expresses accuracy. To eliminate systematic errors, the user must make sure the geometry is appropriately modelled and the particle histories are sampled in a manner which reflects the real particle population (X-5 Monte Carlo Team 2008; 2-111).

By the central limit theorem, Z is a random variable whose distribution function approaches that of the standard normal distributions as $n \to \infty$ with a mean equal to μ (Johnson *et al.* 2000; 208):

$$Z = \frac{\bar{X} - \mu}{S/\sqrt{n}},$$

which allows one to construct confidence intervals about μ using the standard normal probability distribution (X-5 Monte Carlo Team 2008; 2-111).

A.2 Propagation of errors

The errors in this thesis are propagated using the ubiquitous formula (Taylor 1982; 73):

$$\sigma_f = \sqrt{\left(\frac{\partial f(A,B,...)}{\partial A}\right)^2 (\sigma_A)^2 + \left(\frac{\partial f(A,B,...)}{\partial B}\right)^2 (\sigma_B)^2 + ...},$$

which assumes all variables are normally distributed and mutually independent. The uncertainties σ_i are absolute, not relative errors.

Appendix B

Scaling of MCNP6 MNR reference core tallies

The reactor power scaling factor, C, is multiplied by all MCNP6 tallies to obtain a meaningful result because each tally is implicitly known to be "per starting particle" (X-5 Monte Carlo Team 2008; 2-81); in the case of a criticality MNCP6 simulation, the starting particles are the fission neutrons. C has units of 1/s and represents the number of fission neutrons created per second. It is calculated as:

$$C = \text{(number of fissions per second)(number of fission neutrons released per fission)}$$

$$C = \left(\frac{P_{\mathrm{TH}}}{Q_{\mathrm{F}} 1.6022 \times 10^{-13} \frac{\mathrm{J}}{\mathrm{MeV}}} \right) (\nu),$$

where:

P_{TH} = thermal reactor power; in units of W=J/s

Q_{F} = recoverable energy per fission, core averaged; in explicit units of MeV, implicitly MeV/fission

ν = number of fission neutrons released by fission, core averaged; explicitly unitless, implicitly 1/fission.

"Core averaged" means averaged over all fissionable isotopes (where applicable) and all neutron energies in all volumes of the core.

As an example, the following values have been assumed: $P_{\mathrm{TH}} = 3 \times 10^6$ W, $Q_{\mathrm{fission}}^{\mathrm{recoverable}}$=200 MeV and ν=2.418. Thus $C = 2.26 \times 10^{17}$ fission neutrons/s. An error of 7.0% has been assumed on the primary coolant flow guage in MNR which the operators use to determine reactor power, thus this uncertainty is carried to P_{TH} and C.

Appendix C

Scaling of JHR TRIPOLI4 scores

When normalizing the TRIPOI4 scores the energy per fission must be estimated. This value is assumed to be 193.7 MeV when the fresh core is considered, and 200 MeV when the equilibrium core is considered; the difference being that many fissionable isotopes, not just ^{235}U are present in the equilibrium core.

The following demonstrates some random examples of how TRIPOLI scores have been scaled to reactor power within this report (all decimal places provided by TRIPOLI4 have been spared truncation):
a) the number of fissions per second in a 70 MW start-up core:

$$R_{\mathrm{F}}^{\mathrm{total}} = \frac{70\mathrm{MW} \cdot 1.0 \times 10^{6} \frac{\mathrm{W}}{\mathrm{MW}} \cdot 1 \frac{\mathrm{J/s}}{\mathrm{W}}}{1.6022 \times 10^{-13} \frac{\mathrm{J}}{\mathrm{MeV}} \cdot 193.7 \frac{\mathrm{MeV}}{\mathrm{fission}}} = 2.25 \times 10^{18} \frac{\mathrm{fission}}{\mathrm{s}}$$

b) the normalized total core fission reaction rate scored by TRIPOLI4 over all fuel volumes in the start-up core is:

$$S_{\mathrm{F}}^{\mathrm{total}} = 4.250078 \times 10^{-1} \pm 0.0132\% \frac{\mathrm{fission}}{\mathrm{s}}$$

c) the fission reaction rate scored by TRIPOLI for one of the three innermost fuel plates of assembly EC101 is:

$$S_{\mathrm{F}}^{\mathrm{fp}} = 5.291205 \times 10^{-4} \pm 0.2255\% \frac{\mathrm{fission}}{\mathrm{s}}$$

so the predicted fission rate in the scored fuel plate is simply the appropriate fraction of the total fission rate:

$$R_{\mathrm{F}}^{\mathrm{fp}} = \frac{S_{\mathrm{F}}^{\mathrm{fp}}}{S_{\mathrm{F}}^{\mathrm{total}}} \cdot R_{\mathrm{F}}^{\mathrm{total}}$$

$$R_{\mathrm{F}}^{\mathrm{fp}} = \frac{5.291205 \times 10^{-4} \pm 0.2255\% \frac{\mathrm{fission}}{\mathrm{s}}}{4.250078 \times 10^{-1} \pm 0.0132\% \frac{\mathrm{fission}}{\mathrm{s}}} \cdot 2.25 \times 10^{18} \frac{\mathrm{fission}}{\mathrm{s}}$$

$$R_{\mathrm{F}}^{\mathrm{fp}} = 2.80 \times 10^{15} \frac{\mathrm{fission}}{\mathrm{s}}$$

d) the volume-averaged absolute neutron flux between 1 and 2 MeV in the target carbon cylinder at the center of assembly EC101 is:

$$S_{\mathrm{flux}}^{\mathrm{cyl}} = 6.722908 \times 10^{-5} \pm 0.8372\% \frac{\mathrm{neutron} \cdot \mathrm{cm}}{\mathrm{s} \cdot \mathrm{u}}$$

so the predicted neutron flux between 1 and 2 MeV in the target carbon cylinder is:

$$\phi = \frac{6.722908 \times 10^{-5} \frac{\text{neutron} \cdot \text{cm}}{\text{s} \cdot \text{u}}}{1.963\text{cm}^3} \cdot \frac{2.25 \times 10^{18} \frac{\text{fission}}{\text{s}}}{4.25 \times 10^{-1} \frac{\text{fission}}{\text{s}}} = 1.82 \times 10^{14} \frac{\text{neutron}}{\text{cm}^2 \cdot \text{s} \cdot \text{u}}$$

To calculate the flux without units of "per unit lethargy", the above formula is used by starting with the appropriate TRIPOLI4 score.
e) the electron surface current, of all energies, over a surface with an area of 15.7cm^2 is:

$$C_{\text{elec}} = 2.075846 \times 10^{-5} \pm 1.657956\% \frac{\text{electron}}{\text{s}}$$

so the predicted electron flux through the surface is:

$$\phi = \frac{2.075846 \times 10^{-5} \pm 1.657956\% \frac{\text{electron}}{\text{s}}}{15.7\text{cm}^2} \cdot \frac{2.25 \times 10^{18} \frac{\text{fission}}{\text{s}}}{4.250078 \times 10^{-1} \frac{\text{fission}}{\text{s}}}$$

$$\phi = 7.00 \times 10^{12} \pm 1.65 \frac{\text{electrons}}{\text{cm}^2 \cdot \text{s}}$$

f) the volume-averaged prompt photon energy deposition, by photons of all energies is:

$$S_{\text{ED}}^{\text{cyl}} = 7.22 \times 10^{-6} \frac{\text{MeV}}{\text{s}}$$

so the actual energy deposited in the cylinder (with a volume of 1.963 cm^3 and density of 2.26 g/cm^3) by these photons is then calculated as:

$$Q^{\text{cyl}} = \frac{7.22 \times 10^{-6} \frac{\text{MeV}}{\text{s}} \cdot 1.6022 \times 10^{-13} \frac{\text{J}}{\text{MeV}}}{1.963\text{cm}^3 \cdot 2.26 \frac{\text{g}}{\text{cm}^3}} \cdot \frac{2.25 \times 10^{18} \frac{\text{fission}}{\text{s}}}{4.250078 \times 10^{-1} \frac{\text{fission}}{\text{s}}}$$

$$Q^{\text{cyl}} = 1.38 \frac{\text{W}}{\text{g}}$$

Appendix D

Spectral considerations

D.1 Normalization of spectra

When a score or tally is divided into a grid of energy bins, usually the bins will be of varying widths. Since the tally of each bin increases or decreases with the width of the energy bin, the ability to compare bin tallies to each other is lost unless the tallies are made independent of energy bin width by dividing the tallies by some value representative of the bin width; spectral plots always require this treatment. The bin width itself could be used as a divisor and the units of flux, for example, within the bin would then be:

$$[S_{\text{flux}}] = \frac{\frac{\text{neutron}\cdot\text{cm}}{\text{s}}}{\text{eV}} = \frac{\text{neutron}\cdot\text{cm}}{\text{s}\cdot\text{eV}}.$$

However, some bins may have a width of 1.0×10^{-9} eV and others of 1.0×10^{6} eV, which would create great variance between the magnitude of the width-independent tallies and ultimately, indiscernible plots.

Alternatively the energy bin width could be described by units of lethargy (Bell and Glasstone 1970; 207):

$$u = \ln\left[\frac{E_{\text{upper}}}{E_{\text{lower}}}\right]$$

where the two energy terms are the upper and lower energy bin boundaries. The units of flux within such an energy bin divided by lethargy are:

$$[S_{\text{flux}}] = \frac{\text{neutron}\cdot\text{cm}}{\text{s}\cdot\text{u}}.$$

The resulting width-independent tally plot well on a linear scale once they have been normalized.

Absolute tallies of each energy bin are by definition not independent of energy bins and thus units of lethargy are not involved in their calculation.

D.2 Energy bins

Throughout this thesis energy bin structures are used. The following table presents the boundaries of the 3 structures which have been used for with MCNP6 for MNR analysis. These boundaries have been selected for their convenient numbers and their even span between maximum and minimum energies, except the lowest and highest neutron and photon boundary. The lowest photon boundary, 1.0 keV, is the limit for transported photons used throughout this thesis. The highest photon energy,

15 MeV, and highest neutron, 20 MeV, were selected knowing few particles exist above this energy in the core.

MCNP6 presents energy-divided tallies with the upper boundary of the associated energy bin; for example a tally result within the energy bin between 1 and 2 MeV is presented with a label of "2 MeV" in the output file; within this thesis, descriptions of MCNP6 tallies have adopted this naming convention in summaries of results such as plots and tables.

TRIPOLI4 tally results do the opposite and list the lower energy bin boundary, so TRIPOLI4 scores within this thesis use the lower boundary label. TRIPOLI4 neutron scores used a 51 group structure which is detailed in section E.3.

Bin Boundaries (MeV)

Lower	Upper	Lower	Upper	Lower	Upper
0	1.00E-09	0	5.00E-07	0.001	0.002
1.00E-09	5.00E-09	5.00E-07	1.00E-05	0.002	0.005
5.00E-09	1.00E-08	1.00E-05	1.00E-04	0.005	0.01
1.00E-08	2.00E-08	1.00E-04	1.00E-03	0.01	0.02
2.00E-08	3.00E-08	1.00E-03	1.00E-02	0.02	0.05
3.00E-08	4.00E-08	1.00E-02	1.00E-01	0.05	0.1
4.00E-08	5.00E-08	1.00E-01	1.00E+00	0.1	0.2
5.00E-08	6.00E-08	1.00E+00	20	0.2	0.3
6.00E-08	7.00E-08			0.3	0.4
7.00E-08	8.00E-08			0.4	0.5
8.00E-08	9.00E-08			0.5	0.6
9.00E-08	1.00E-07			0.6	0.7
1.00E-07	2.00E-07			0.7	0.8
2.00E-07	3.00E-07			0.8	0.9
3.00E-07	4.00E-07			0.9	1
4.00E-07	5.00E-07			1	2
5.00E-07	6.00E-07			2	3
6.00E-07	7.00E-07			3	4
7.00E-07	8.00E-07			4	5
8.00E-07	9.00E-07			5	6
9.00E-07	0.000001			6	7
0.000001	0.000002			7	8
0.000002	0.000005			8	9
0.000005	0.00001			9	10
0.00001	0.00002			10	15
0.00002	0.00005				
0.00005	0.0001				
0.0001	0.0002				
0.0002	0.0005				
0.0005	0.001				
0.001	0.002				
0.002	0.005				
0.005	0.01				
0.01	0.02				
0.02	0.05				
0.05	0.1				
0.1	0.2				
0.2	0.5				
0.5	1				
1	2				
2	3				
3	4				
4	5				
5	6				
6	7				
7	8				
8	9				
9	10				
10	15				
15	20				

Table D.1: (L) 50 group neutron bin structure; (C) 8 group neutron bin structure; (R) 25 group photon bin structure.

Appendix E

Gamma heating dependencies

This chapter searches for variables upon which in-core gamma heating may depend. Finding dependent variables is useful to understand the parameters which affect gamma heating; this exploration also indicates where efforts should be expended to further advance the understanding, or develop a simplified model of in-core gamma heating.

This chapter also calculates the absolute nuclear heating within a high-neutron-flux MTR, the Jules Horowitz Reactor (JHR). These calculations are important to demonstrate the magnitude of gamma and neutron heating which can be expected within a reactor core.

E.1 The Jules Horowitz Reactor

The French Jules Horowitz Reactor is a high-flux research reactor which is planned to commence operation in 2017.

The JHR is designed to host complex in-core experimental devices to answer questions regarding a) the material aging of Generation II and III reactor materials; b) fuel performance and safety margin improvements in Generation II and III reactors; c) the fuel and material designs of Generation IV reactors, and; d) to produce radioisotopes for the European market (Iracane 2005; 438).

E.2 JHR specifications

With a nominal power of 100 MW and small dimensions ($\varnothing$ = 740 mm and active fuel height of 600 mm), the JHR core will produce peak neutron fluxes of $5 \times 10^{15} \frac{\mathrm{n}}{\mathrm{cm^2 s}}$ (Iracane 2005; 438); these parameters will also result in a very large specific power (460 $\frac{\mathrm{kW}}{\mathrm{litre}}$) and induce large temperature gradients and intense photon fluxes (Blanchet *et al.* 2008; 731).

The JHR core is constructed with an aluminum block containing 37 cylindrical holes; each hole is approximately 10 cm in diameter (as shown in Figure E.1) and each will host either a fuel assembly or an in-core experimental devices. The core is to be surrounded by a beryllium reflector which will reduce neutron leakage and provide thermalized flux locations within the reflector; like the core, the reflector is designed to host experimental devices and irradiation sites - the reflector is shown in Figure E.2.

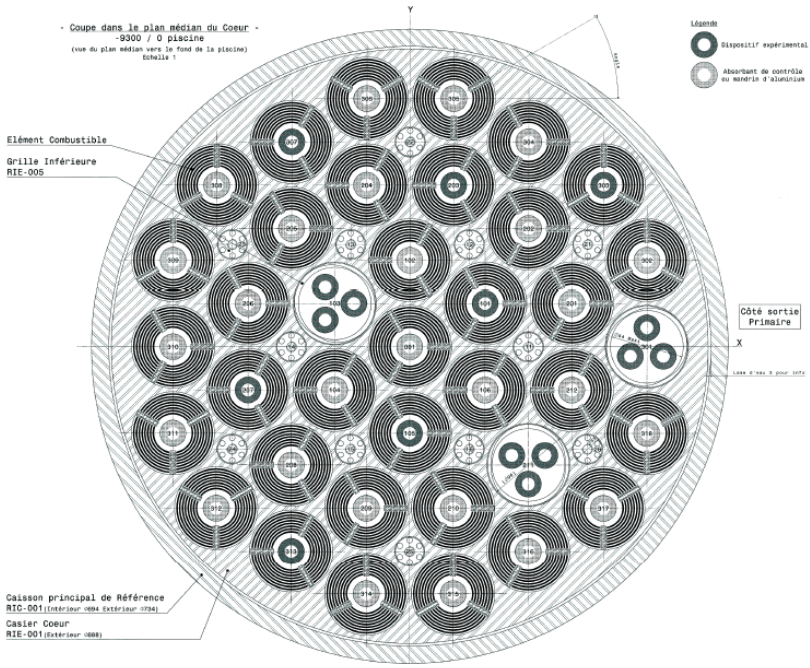

Figure E.1: The JHR core showing 37 cylindrical locations for either fuel assemblies or experimental devices (Blanchet 2006).

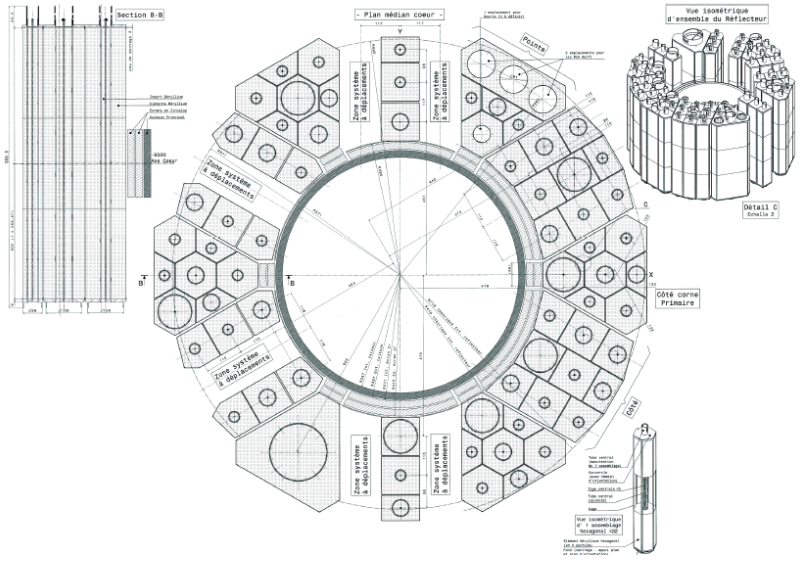

Figure E.2: The JHR reflector (Blanchet 2006).

E.3 Methods of analysis

E.3.1 Methods of calculation

All radiation transport calculations in this chapter were made with the Monte Carlo radiation transport code TRIPOLI4.9 (Diop *et al.* 2006).

The TRIPOLI4.9 model of the JHR core and reflector geometry used in this thesis was developped by the CEA/DEN/CAD/DER/SRJH Physics Analysis Group. The author of this thesis configured this existing JHR model as described throughout this thesis, to obtain the corresponding results. All calculations were run on CEA clusters.

The cross-sections used with TRIPOLI4 for this thesis are based upon the JEFF-3.1.1 nuclear data library and uses photo-atomic cross-sections from EPDL-97. The CEAV 5.1.2 library (an implementation of JEFF-3.1.1 and EPDL-97) was used with calculations conducted on the CEA Cadarache Mezel cluster. A few calculations used the CEAV 5.1.1 library before being upgraded to CEAV 5.1.2 on the CEA Bruyeres-le-Châtel Curie cluster; there is thought to be no significant differences between CEAV 5.1.1 and CEAV 5.1.2. All cross section data was processed at 21 C.

All TRIPOLI4 calculations have been conducted in CRITICITY mode, whereby the code calculates the multiplication factor k, plus all user-defined SCORES. TRIPOLI4 can be operated by tracking only neutrons, or coupled neutrons-photons, or coupled neutrons-photons-electrons-positrons.

All energy deposition quantities, for all particles, have been calculated using DEPOSITED_ENERGY scores, averaged over a volume of interest. All volume flux quantities have been calculated with FLUX scores averaged over a volume. All surface flux quantities have been calculated with COURANT scores averaged over a surface.

E.3.2 Labelling of JHR core components

Throughout this chapter, fuel assemblies (EC), inter-assembly mandrels (IA), pilot rods (AP), compensation rods (AC) and safety rods (ASA) will be discussed. Each of these core components is labelled with a number, designating its position; the map of labelled core components is shown in Figure E.3.

E.3.3 Start-up core configuration (zero burn-up)

The start-up core (with zero burn-up) is the first core the JHR will operate on. The TRIPOLI4 model of the start-up core and reflector has been modified to the following configuration for this report:

- 36 JHR fuel assemblies
- 1 false in-core device, made of aluminum, in the fuel assembly EC103 location
- 19.75% ^{235}U-enriched fuel - all assemblies with zero burn-up
- 8 Hf bars at locations IA12, IA13, IA14, IA15, IA16, IA21, IA23 and IA25
- 4 ASA bars at locations 001, 201, 205 and 209, in position +30 cm
- 4 AP bars at locations 206, 212, 304 and 315, in position 0 cm
- 8 AC bars at locations 102, 202, 208, 210, 305, 309, 310 and 318, in position -31 cm
- 11 AC bars at locations 104, 106, 204, 302, 306, 308, 311, 312, 314, 316 and 317, in position 30 cm
- all perhipheral (SI) locations are aluminium

It is assumed the start-up core is to be operated at 70 MW. The modelled JHR start-up core and reflector configuration is shown in Figure E.4.

E.3.4 Start-up core configuration (equilibrium burn-up)

After 9 fuel cycles the start-up core will reach equilibrium burn-up. This equilibrium core differs from the zero-burnup start-up core configuration only in its rod positions and substantial fission product inventory. The following is a configuration of the equilibrium burn-up core (CEA 2016):

- 36 JHR fuel assemblies
- 1 false in-core device, made of aluminum, in the fuel assembly EC103 location
- 19.75% ^{235}U-enriched fuel
- EC208, EC303, EC304, EC305, EC306, EC 308, EC309, E310, EC315 - with zero burn-up
- the other assemblies with burnup values as presented in Figure E.5
- all IA locations are aluminum
- 4 ASA bars at locations 001, 201, 205 and 209, in position +30 cm
- 4 AP bars at locatioins 206, 212, 304 and 315, in position 0 cm
- 8 AC bars at locations 102, 202, 208, 210, 305, 309, 310 and 318, in position -31 cm
- 11 AC bars at locations 104, 106, 204, 302, 306, 308, 311, 312, 314, 316 and 317, in position 30 cm
- all perhipheral (SI) locations are aluminium

Note that the 8 Hf rods in the zero-burn-up core, at the IA locations are not present in the equilibrium core.

It is assumed the start-up core is to be operated at 70 MW.

E.3.5 Summary of TRIPOLI4 parameters

The following is a list of important parameters of all TRIPOLI4 calculations contained within this report (unless noted otherwise in specific cases):

- TRIPOLI4 version number 4.9.0
- TRIPOLI4 models contain complete geometrical details and material descriptions of the core and reflector
- CEAV 5.1.2 nuclear data library used for nearly all calculations (the rest were completed with CEAV 5.1.1)
- all calculations have been made in CRITICITY (criticality) mode, which track neutrons as the primary particle; if photons, electrons and positrons are tracked, they appear as a result of neutron/material interactions; thus it is said that these particles are tracked in a "coupled" manner
- photons below the energy of 1 keV are not tracked
- electrons and positrons below 2.5 keV are not tracked

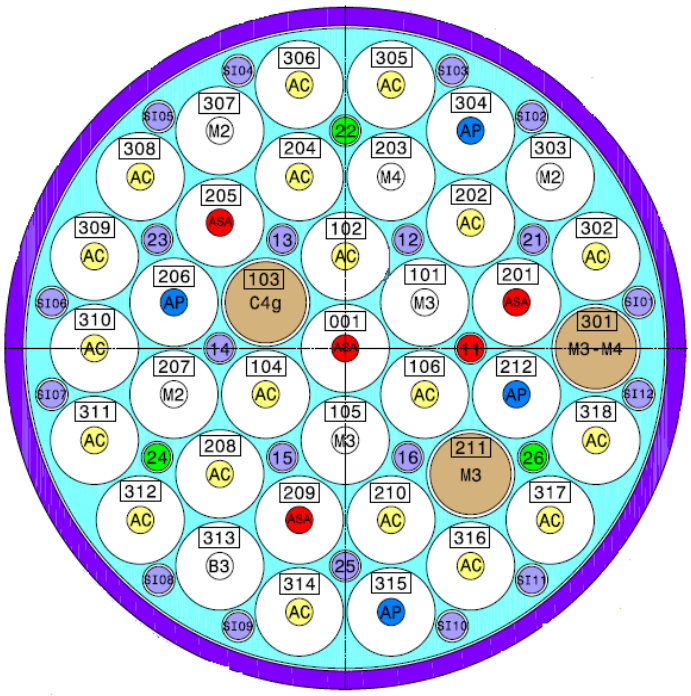

Figure E.3: JHR core showing the component labels (TA 2011). The 34 fuel-element configuration shown has not been analyzed in this thesis.

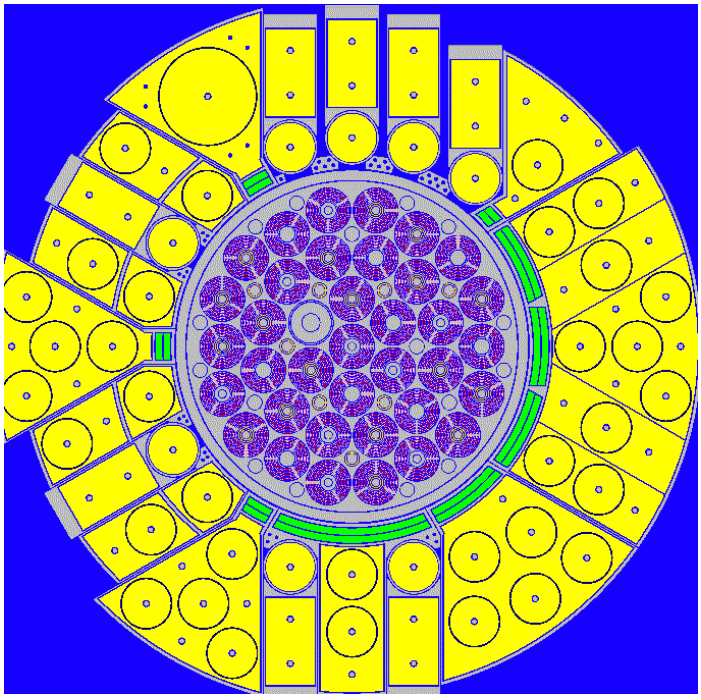

Figure E.4: A horizontal section at the vertical mid-plane of the TRIPOLI4 model of the JHR start-up core.

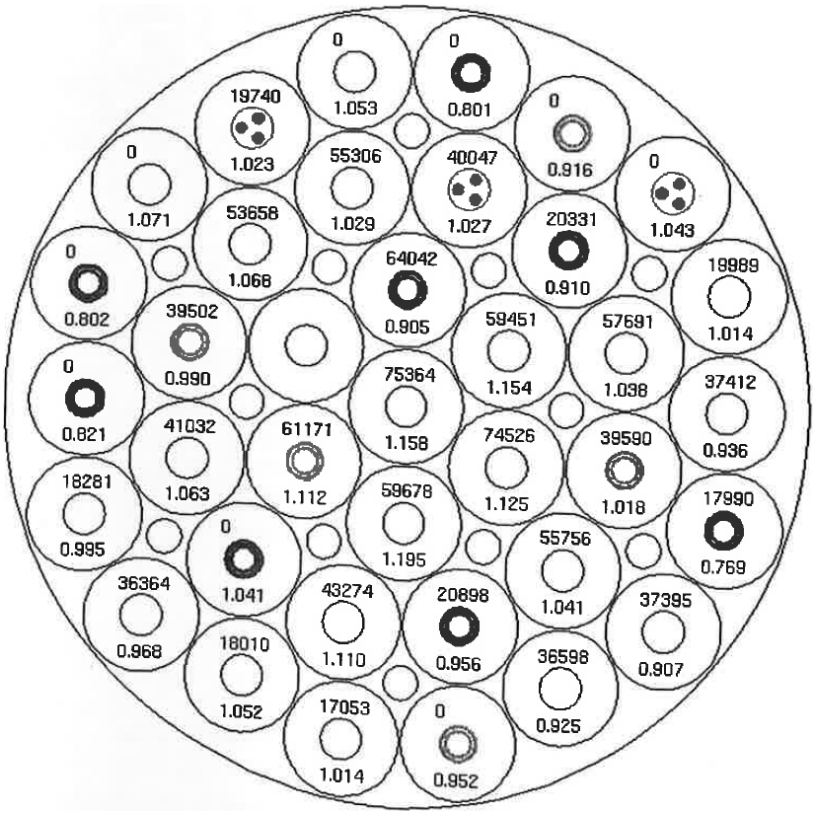

Figure E.5: Startup core configuration (equilibrium burn-up) showing the burn-up (top number, in units of MW days per tonne) of each fuel assembly.

Placing a low-energy cut-off on photon and electron/positron transport is an effort to save computing time. The low-energy thresholds of 1 kev and 2.5 keV are justified by the fact that the respective particles have an extremely small distance of travel at these energies and carry relatively small amounts of energy. These specific cut-off values are used in other CEA studies (Vaglio-Gaudard *et al.* 2014).

E.3.6 Calculation of delayed gamma heating

The energy deposition values calculated by TRIPOLI4 are the prompt sources only. SRJH has adopted the practice of scaling the prompt gamma dose by 1/0.7 to account for the delayed gammas. This value is based upon CEA studies of delayed gamma sources and is applied uniformly spatially (CEA 2016). Given the time-dependent nature of the delayed gammas, this is a simplistic way to calculate the delayed gamma heating (although it may be conservative). This method has been adopted within this report.

E.3.7 TRIPOLI4 biases

CEA studies have compared the biases of TRIPOLI4 to experimental nuclear heating data taken from critical assemblies. SRJH uses the results of Amharrak et al. who described TRIPOLI4 to be systematically low by a factor of 1.04, and to have an uncertainty of 3.5% (1 σ) (CEA 2016). These values have been adopted within this report to calculate total gamma heating.

E.3.8 Uncertainties

TRIPOLI presents scores and sigma values with many decimal places. Presenting all decimal places can't be justified, and selecting an appropriate number of decimal places in each instance would be logistically difficult. Thus a convention has been adopted whereby scores (and numbers which are a function of scores) are presented with two decimal places and uncertainties with a single decimal place. Unfortunately, this convention is responsible for absurd situations where two decimal places are presented on scores which have uncertainties orders-of-magnitude larger than the last decimal place.

E.4 Start-up core (no burn-up) calculations

E.4.1 Nuclear heating in common materials

TRIPOLI4 was used to calculate nuclear heating with two-particle (coupled neutrons-photons) calculations. Vertical sample cylinders of 5 mm ∅ (and 100 mm length) were placed within the JHR model at various locations. The neutron and photon energy deposition was calculated in each sample cylinder for a number of common materials.

Previous experimental CEA studies have used 5 mm ∅ material samples (CEA 2016); a length of 100 mm was selected because this is many times the diameter and is also short enough to receive a nearly-uniform irradiation when centered at the vertical mid-plane of the core where the vertical neutron flux distribution is nearly flat.

The samples were placed within the long aluminum cylinder (the mandrel) at the centre of fuel assembly EC101 and EC307, and within the aluminum cell at the EC103 location. Figure E.6 shows the stylized geometries.

Additionally, the photon energy deposition was recalculated after the density of the sample cylinders was changed to one-tenth and one-hundredth typical density. Neutron energy deposition was not calculated in the cases of the reduced density because the processing time required to obtain acceptable statistics in high Z material is excessive. The purpose of calculating the photon energy deposition in low-density material is to increase the S/M ratio without changing the sample cylinder dimensions. Table E.1 presents the S/M ratios for the sample cylinders in which the energy deposition was calculated.

Results

Figure E.7 shows the calculated energy deposition of both neutrons and gammas in EC101. All curves shown are either neutron-only or gamma-only energies - no curve is comprised of both neutron and gamma energy deposition.

The gamma energy deposition of Figure E.7 is plotted with three curves: a) one curve corresponding to a cylinder with material of a typical density, b) one curve for material of one-tenth of typical density, and c) one curve for material of one-hundredth of typical density.

Figure E.7 demonstrates energy deposition per gram increases with the ratio S/M in high Z material.

An increase in heating of Ni, Nb, Gd and Hf is observed (relative to neighboring elements of the same density); this is also demonstrated in samples of one-tenth and one-hundredth typical density. This indicates the increased heating of these elements is independent of the S/M ratio, and therefore independent of geometry and density; it seems the materials demonstrating increased gamma heating either have higher photon absorption cross-sections, or are large sources of photons.

The bottom curve in Figure E.7 shows the neutron energy deposition. Ni, Nb, Gd and Hf also have elevated values of deposited neutron energy as a result of their relatively large neutron absorption cross-sections. Figure E.8 plots the same neutron data in both linear and logarithmic scales; the logarithmic plot facilitates reading data close to zero.

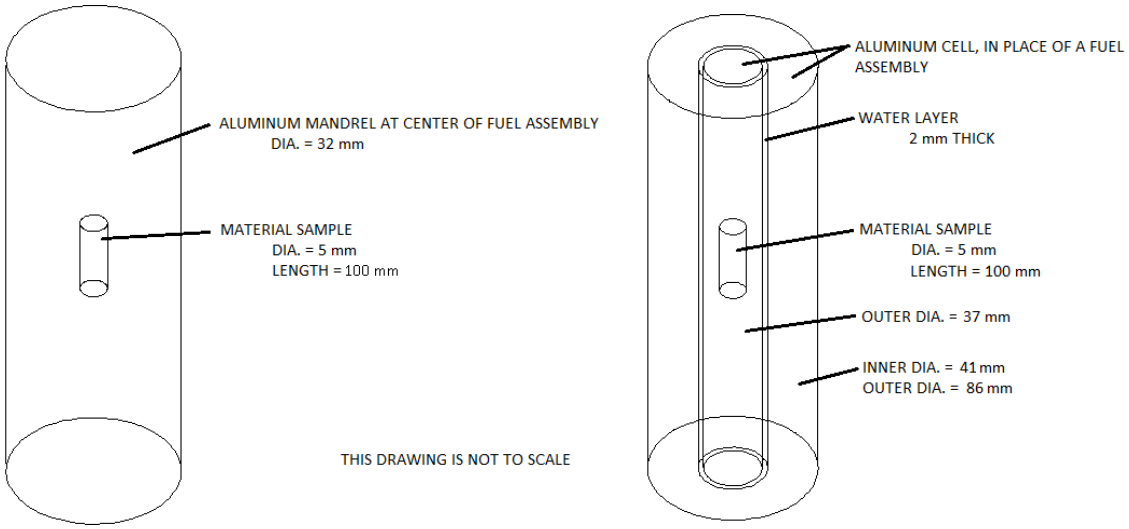

Figure E.6: (L) geometry placed at center of fuel assemblies EC101 and EC307, (R) geometry placed at the EC103 location. The material samples are centered about the core's vertical center.

	Typical Density			1/10 of Typical Density		1/100 of Typical Density	
	S (cm^2)	M (g)	S/M (cm^2/g)	M (g)	S/M (cm^2/g)	M (g)	S/M (cm^2/g)
Be	16.10	3.63	4.43	0.36	44.32	0.04	443.23
C	16.10	4.44	3.63	0.44	36.28	0.04	362.82
Al	16.10	5.30	3.04	0.53	30.37	0.05	303.69
Fe	16.10	15.45	1.04	1.55	10.42	0.15	104.19
Ni	16.10	17.48	0.92	1.75	9.21	0.17	92.13
Cu	16.10	17.59	0.92	1.76	9.15	0.18	91.51
Zr	16.10	12.78	1.26	1.28	12.60	0.13	125.95
Nb	16.10	16.83	0.96	1.68	9.57	0.17	95.68
Gd	16.10	15.51	1.04	1.55	10.38	0.16	103.79
Hf	16.10	26.13	0.62	2.61	6.16	0.26	61.61
W	16.10	37.80	0.43	3.78	4.26	0.38	42.60
Bi	16.10	19.14	0.84	1.91	8.41	0.19	84.10

Table E.1: S/M ratios for the sample cylinders of Figure E.6.

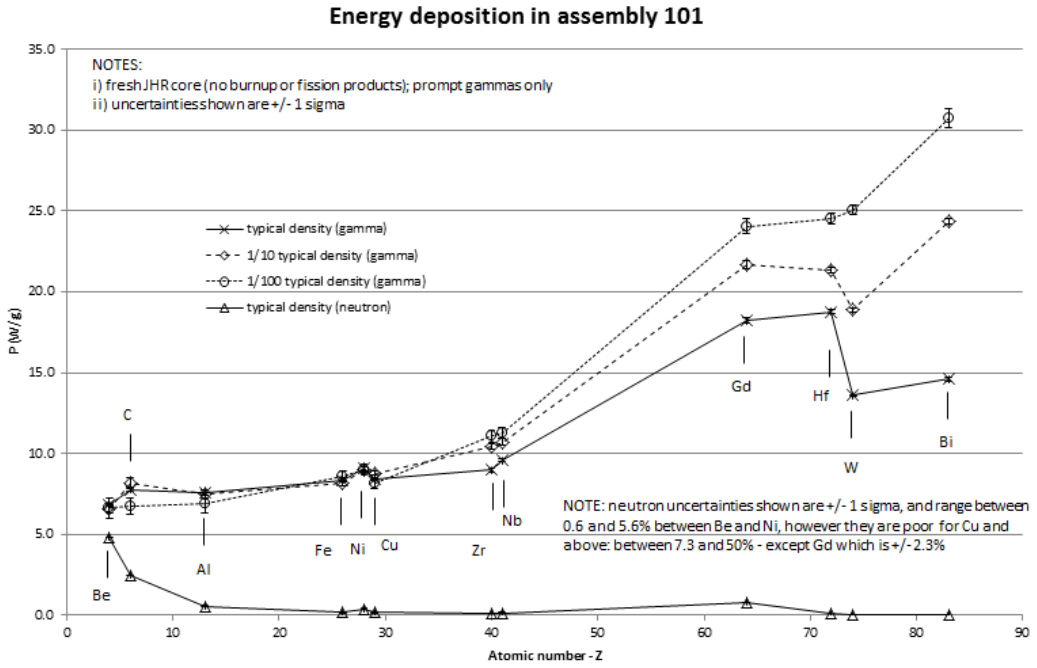

Figure E.7: Nuclear heating calculated for neutrons and gammas in the mandrel of fuel assembly EC101.

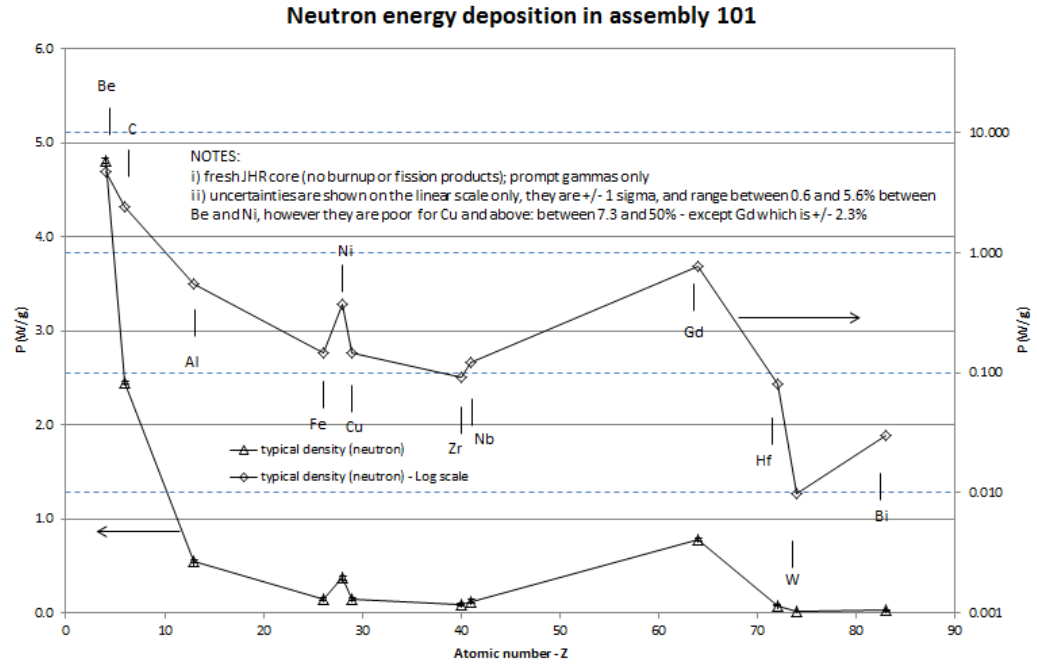

Figure E.8: Neutron heating of sample within the mandrel of EC101 in both linear and logarithmic scales.

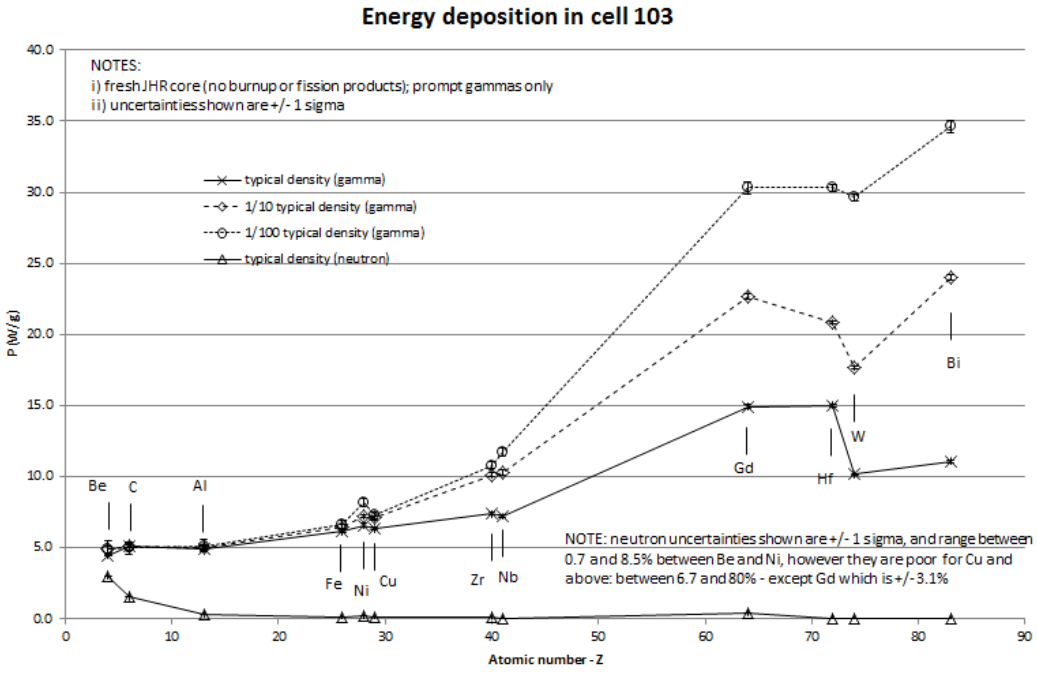

Figure E.9: Nuclear heating calculated for neutrons and gammas in non-fuelled location EC103.

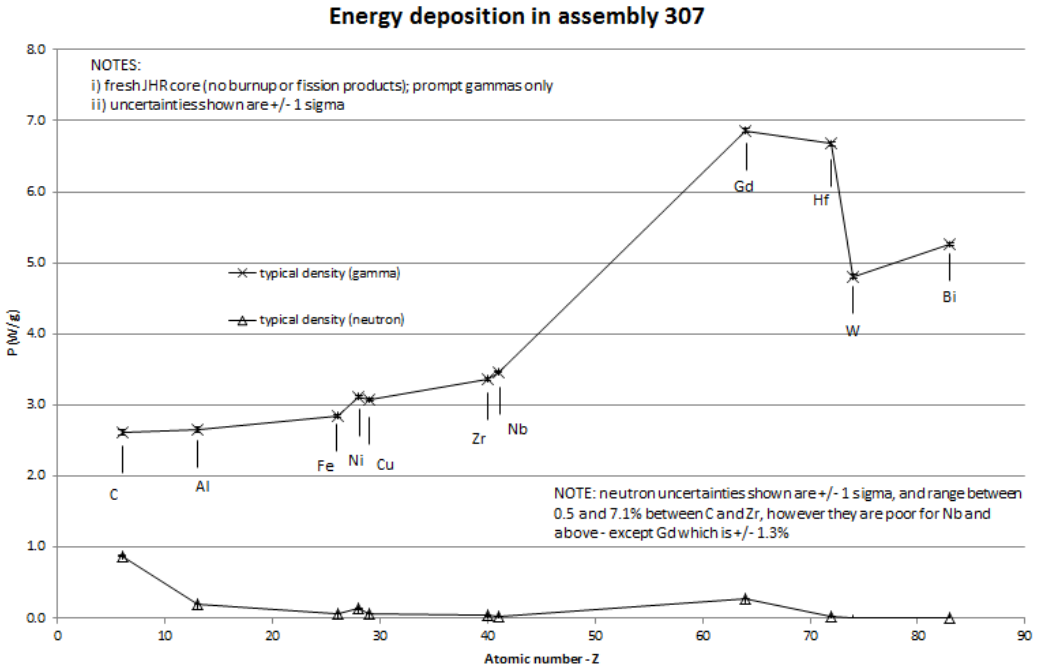

Figure E.10: Nuclear heating calculated for neutrons and gammas in the mandrel of fuel assembly EC307.

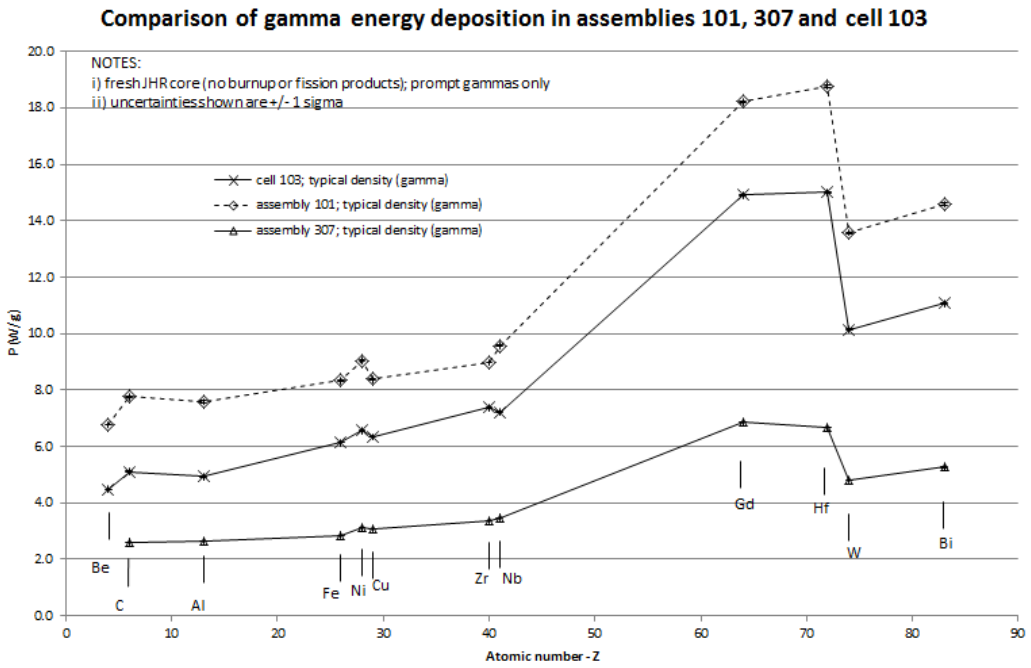

Figure E.11: Gamma heating calculated in the mandrel of fuel assembly EC101, EC103 and EC307.

Sample cylinder within assembly 307 - 70 MW							
		Typical sample cylinder density					
		Calculated prompt energy deposition				Total gamma heating plus nuclear data biases and additional 3.5% on sigma	
		PHOTONS		NEUTRONS			
ELEMENT	Z	W/g	sigma (%)	W/g	sigma (%)	W/g	sigma (%)
carbon	6	2.61	1.3	0.88	0.6	3.88	3.7
aluminum	13	2.65	1.2	0.19	1.4	3.94	3.7
iron	26	2.85	0.7	0.05	2.9	4.24	3.6
nickel	28	3.12	0.6	0.13	2.1	4.63	3.6
copper	29	3.07	0.7	0.05	4.1	4.57	3.6
zirconium	40	3.37	0.6	0.03	7.1	5.00	3.6
niobium	41	3.47	0.5	0.02	11.4	5.15	3.5
gadolinium	64	6.86	0.4	0.27	1.2	10.19	3.5
hafnium	72	6.68	0.4	0.03	9.6	9.93	3.5
tungsten	74	4.81	0.8	0.00	289.4	7.15	3.6
bismuth	83	5.26	0.5	0.01	0.0	7.82	3.5

Table E.2: Calculated absolute gamma and neutron energy deposition within the sample cylinder placed within the mandrel of fuel assembly EC307 mandrel, at 70 MW.

Sample cylinder within assembly 101 - 70 MW							
		Typical sample cylinder density					
		Calculated prompt energy deposition				Total gamma heating plus nuclear data biases and additional 3.5% on sigma	
		PHOTONS		NEUTRONS			
ELEMENT	Z	W/g	sigma (%)	W/g	sigma (%)	W/g	sigma (%)
beryllium	4	6.78	1.2	4.81	0.6	10.07	3.7
carbon	6	7.77	1.4	2.45	0.6	11.54	3.8
aluminum	13	7.59	2.2	0.54	2.7	11.27	4.1
iron	26	8.35	1.3	0.15	5.9	12.40	3.7
nickel	28	9.05	1.6	0.37	5.6	13.45	3.9
copper	29	8.40	1.2	0.15	7.2	12.48	3.7
zirconium	40	8.98	1.2	0.09	13.5	13.34	3.7
niobium	41	9.57	1.1	0.12	22.1	14.22	3.7
gadolinium	64	18.22	0.8	0.78	2.3	27.08	3.6
hafnium	72	18.78	0.7	0.08	13.6	27.90	3.6
tungsten	74	13.59	0.3	0.01	50.7	20.19	3.5
bismuth	83	14.60	0.8	0.03	23.9	21.69	3.6
water		8.69	2.1	19.34	0.6	12.91	4.1
		1/10 of typical density					
ELEMENT	Z	W/g	sigma (%)	W/g	sigma (%)	W/g	sigma (%)
beryllium	4	6.56	3.9	-	-	9.75	5.3
carbon	6	8.15	3.8	-	-	12.11	5.2
aluminum	13	7.50	3.6	-	-	11.14	5.0
iron	26	8.19	1.9	-	-	12.16	4.0
nickel	28	9.01	1.7	-	-	13.38	3.9
copper	29	8.78	1.8	-	-	13.05	3.9
zirconium	40	10.44	1.8	-	-	15.51	3.9
niobium	41	10.71	2.0	-	-	15.92	4.1
gadolinium	64	21.67	1.1	-	-	32.20	3.7
hafnium	72	21.38	0.8	-	-	31.77	3.6
tungsten	74	18.88	0.6	-	-	28.06	3.6
bismuth	83	24.36	0.8	-	-	36.19	3.6
		1/100 of typical density					
ELEMENT	Z	W/g	sigma (%)	W/g	sigma (%)	W/g	sigma (%)
beryllium	4	6.63	9.6	-	-	9.86	10.2
carbon	6	6.73	7.4	-	-	10.00	8.2
aluminum	13	6.87	7.7	-	-	10.21	8.4
iron	26	8.59	4.1	-	-	12.76	5.4
nickel	28	9.02	3.7	-	-	13.40	5.1
copper	29	8.13	3.7	-	-	12.08	5.1
zirconium	40	11.07	3.6	-	-	16.45	5.0
niobium	41	11.29	3.0	-	-	16.77	4.6
gadolinium	64	24.07	1.9	-	-	35.76	4.0
hafnium	72	24.55	1.3	-	-	36.47	3.7
tungsten	74	25.08	1.1	-	-	37.25	3.7
bismuth	83	30.74	1.9	-	-	45.68	4.0

Table E.3: Calculated absolute gamma and neutron energy deposition within the sample cylinder placed within the mandrel of fuel assembly EC101 mandrel, at 70 MW.

Sample cylinder within aluminum cell 103 - 70 MW							
		Typical sample cylinder density					
		Calculated prompt energy deposition				Total gamma heating plus nuclear data biases and additional 3.5% on sigma	
		PHOTONS		NEUTRONS			
ELEMENT	Z	W/g	sigma (%)	W/g	sigma (%)	W/g	sigma (%)
beryllium	4	4.48	1.5	2.99	0.7	6.65	3.8
carbon	6	5.12	1.6	1.53	0.7	7.60	3.9
aluminum	13	4.94	2.5	0.32	3.6	7.33	4.3
iron	26	6.14	1.4	0.09	7.1	9.13	3.8
nickel	28	6.58	1.7	0.18	8.5	9.77	3.9
copper	29	6.34	1.2	0.11	6.7	9.42	3.7
zirconium	40	7.38	1.2	0.07	11.2	10.97	3.7
niobium	41	7.21	1.1	0.03	36.5	10.72	3.7
gadolinium	64	14.92	0.9	0.42	3.0	22.17	3.6
hafnium	72	15.02	0.7	0.05	17.9	22.31	3.6
tungsten	74	10.14	0.3	0.00	79.9	15.07	3.5
bismuth	83	11.09	0.8	0.02	24.1	16.47	3.6
		1/10 of typical density					
ELEMENT	Z	W/g	sigma (%)	W/g	sigma (%)	W/g	sigma (%)
beryllium	4	4.88	4.8	-	-	7.25	6.0
carbon	6	5.08	4.7	-	-	7.55	5.9
aluminum	13	5.02	3.8	-	-	7.46	5.2
iron	26	6.48	1.9	-	-	9.63	4.0
nickel	28	7.21	1.7	-	-	10.71	3.9
copper	29	7.08	1.8	-	-	10.53	3.9
zirconium	40	10.13	1.5	-	-	15.05	3.8
niobium	41	10.28	1.7	-	-	15.27	3.9
gadolinium	64	22.68	0.9	-	-	33.70	3.6
hafnium	72	20.84	0.7	-	-	30.96	3.6
tungsten	74	17.68	0.5	-	-	26.27	3.5
bismuth	83	24.01	0.7	-	-	35.67	3.6
		1/100 of typical density					
ELEMENT	Z	W/g	sigma (%)	W/g	sigma (%)	W/g	sigma (%)
beryllium	4	4.94	10.9	-	-	7.34	11.4
carbon	6	5.00	8.6	-	-	7.43	9.3
aluminum	13	5.14	8.6	-	-	7.64	9.3
iron	26	6.63	4.2	-	-	9.86	5.4
nickel	28	8.21	3.5	-	-	12.20	5.0
copper	29	7.26	3.0	-	-	10.79	4.6
zirconium	40	10.80	2.4	-	-	16.05	4.3
niobium	41	11.71	2.4	-	-	17.39	4.2
gadolinium	64	30.30	1.3	-	-	45.01	3.7
hafnium	72	30.30	0.9	-	-	45.02	3.6
tungsten	74	29.65	0.8	-	-	44.05	3.6
bismuth	83	34.62	1.3	-	-	51.44	3.7

Table E.4: Calculated absolute gamma and neutron energy deposition within the sample cylinder placed within the aluminum cell at EC103 position, at 70 MW.

Based on Figure E.7 and E.8 it is speculated that the significantly increased gamma heating of Ni, Nb, Gd and Hf is the result of neutron energy deposition; many neutron-capture gammas, originating from within the sample cylinder, are absorbed within the same cylinder resulting in larger gamma heating rates than would be experienced if the neutron absorption cross-sections were smaller. If correct, this is an interesting finding which should induce those concerned with gamma heating to consider the neutron absorption cross-sections of their samples irradiated within a mixed neutron and gamma field.

Figure E.9 and Figure E.10 demonstrate the same Z dependency of gamma heating in cylindrical samples placed within the aluminium cell of EC103 and the fuel assembly EC307, respectively. Figure E.11 compares the gamma heating of all the typical-density curves from EC101, EC103 and EC307; gamma heating is clearly greater at central core locations.

Table E.3 through E.2 present the absolute gamma heating values of each energy deposition calculation in this section. The "calculated prompt energy deposition" values in these tables were used to produce Figure E.7 through E.10. The "total gamma plus nuclear data biases and additional 3.5% on sigma" include prompt and delayed gammas, plus the TRIPOLI4 biases; the prompt gamma heating is divided by 0.7 to account for the delayed gamma dose, 4% is added to the subsequent number to account for systematic biases resulting from nuclear data, and 3.5% is added quadratically to the standard deviation to account for model uncertainties.

Notice the large amount of energy deposited in water (with a density corresponding to 293 K) by neutrons in EC101 (Table E.3).

E.4.2 Changes in spectra in the presence of C

It is well known that neutron and photon spectra change as they interact with material, thus the spectrum of an incident radiation field will change within a sample target.

The JHR neutron and gamma spectra, averaged over the sample cylinder volume in EC101 was calculated when the cylinder was filled with C and compared to the same cylinder when empty. C was selected because of its history as a reference material.

Results

The results are shown in Figure E.12 and Figure E.13. The differences in photon and neutron spectra appear to be small. These small changes are likely a result of C being a relatively weak neutron and photon absorber, and the sample cylinder being relatively small in diameter. Presumably a larger diameter C cylinder would induce significant neutron moderation and soften the volume-averaged neutron spectrum.

These results induce further questions: a) how would the spectra change if the sample material were a stronger absorber? b) how would the spectra change if the sample were larger? c) how would the spectra change if the sample were both large and made of a strong absorber? d) what would be the magnitude of change in energy deposition with sample depth? These questions are addressed in subsequent sections.

E.4.3 Gamma absorption spectra

To determine which part of the photon spectra deposits the most energy, the geometry shown in Figure E.14 was placed in EC101. The environment surrounding the sample cylinder was made of the structural aluminum typically found in JHR (not pure Al).

Both the inner cylinder and outer layer of the sample cylinder were made of pure Al in one case, and Hf in another case. For both Al and Hf cylinders the photon energy deposition was scored on the inner and outer sample volumes. Most importantly, the photon energy deposition was scored spectrally and many histories were run, which resulted in an indication of the energy deposition

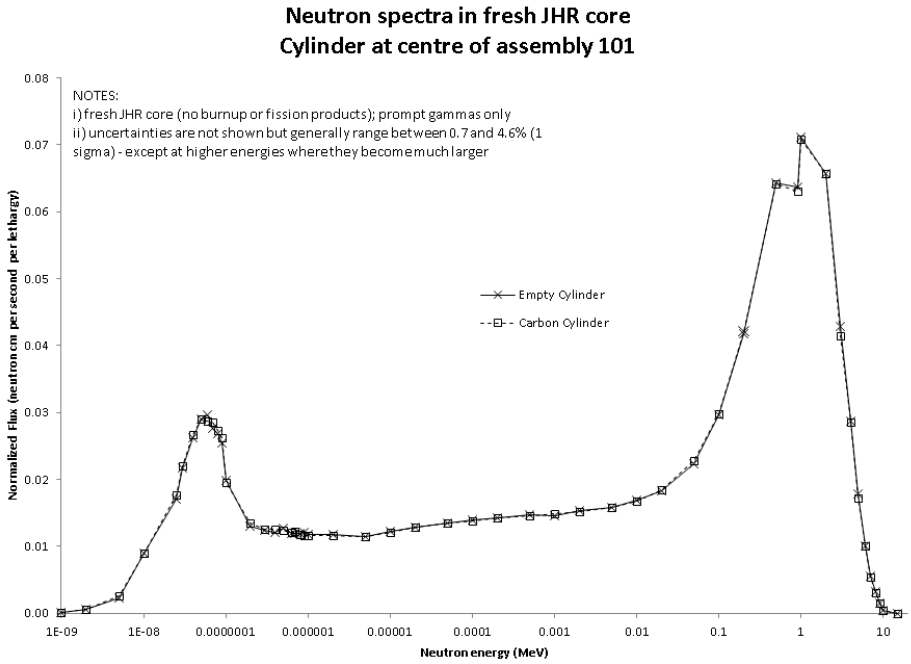

Figure E.12: Comparison between neutron spectra when cylinders (within the mandrel of fuel assembly EC101) are empty and filled with C. The geometry used is shown in Figure E.6.

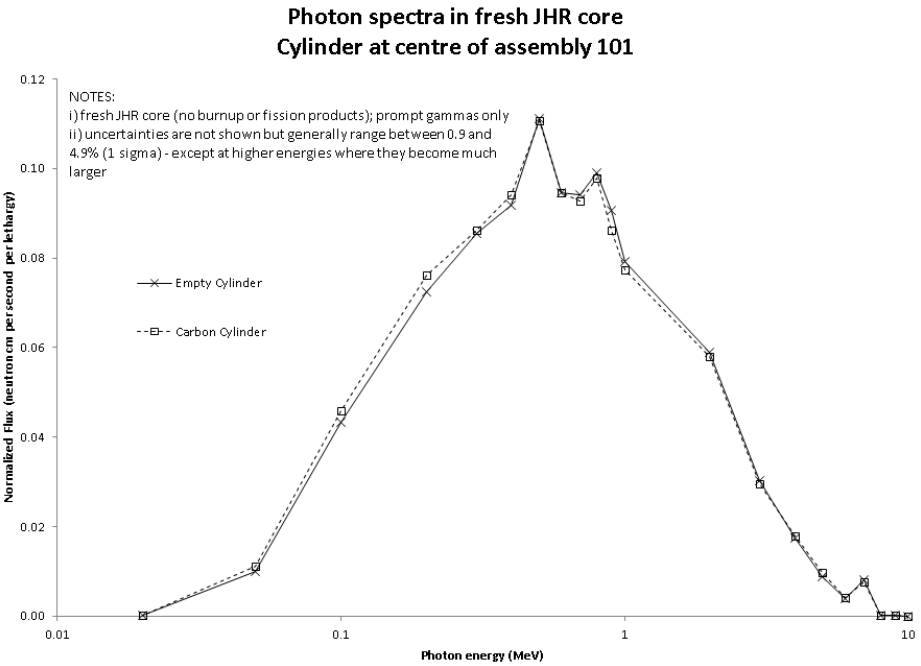

Figure E.13: Comparison between photon spectra when cylinders (within the mandrel of fuel assembly EC101) are empty and filled with C. The geometry used is shown in Figure E.6.

spectra with low uncertainties. This is valuable to show which energy bin is responsible for the deposition of the most amount of energy.

Results

Figure E.15 shows the photon energy deposition spectra, averaged over the central ∅ = 2.5 mm, L=97.5 mm Al and Hf cylinders placed in EC101. These curves imply that photons above 1 MeV deposit a significant amount of energy.

The typical spectrum in this core location (averaged over an empty and C cylinder of similar size) is shown in Figure E.13. It appears that the high energy photons deposit less energy only because there are less of them (the energy deposition curve at high energies reduces at roughly the same slope as the spectral curve of Figure E.13.

Low energy photons appear to deposit relatively-more energy in Hf than in Al.

E.4.4 Dependency of heating on sample depth

To examine how the JHR spectra and energy deposition change within various depths of a sample, sample geometries shown in Figure E.16 were placed within locations EC101, EC105 and the aluminum cell EC103. All three of these locations are within the 1st inner ring of JHR fuel assembly locations, thus they should have similar spectra (although EC103 is a non-fuelled location, unlike the other two).

The sample cylinders of ∅ = 5 mm, L=100 mm within EC101 and EC105 were made of 10 concentric layers, each 0.25 mm thick. The sample cylinder in EC101 was made of C, and the cylinder in EC105 of Bi; thus the two cylinders will serve as a comparison between identically sized cylinders, made of different material.

To examine the effect of a geometry change, the sample cylinder placed in EC103 was made 10 time larger: ∅ = 50 mm, L=100 mm. Each of the 10 concentric layers in EC103 were 2.5 mm thick. The cylinder was made of Bi, like the ∅ = 5 mm cylinder in EC105.

Four particles (neutrons, photons, electrons and positrons) were tracked in a coupled manner. Charged particle transport was allowed only in the sample cylinder and the surrounding 13.5 mm thick aluminium environment in each of EC101, EC105 and EC103.

The particle energy deposition was measured within each sample layer. The photon and neutron spectra was calculated within each layer. The electron flux was calculated over the outer surface of each cylinder layer.

Results

Figure E.17 shows the nuclear heating of the C cylinder within assembly EC101.

C shows significant neutron heating, because of the low Z of C, unlike Bi which has no significant neutron heating.

In four-particle transport, the photon energy is deposited mostly in the form of electron kinetic energy (the energy deposited by positrons and photons are insignificant) thus only electron energy deposition is presented. Figure E.18 shows the energy deposited by electrons is generally constant in each C layer of the ∅ = 5 mm cylinder; Figure E.19 shows the neutron energy deposition also changes very little with depth.

In contrast, Figure E.21 shows the Bi layers of the ∅ = 5 mm cylinder in EC105 absorb more electron energy in the outer layers than the inner layers, and much greater in the larger ∅ = 50 mm Bi cylinder of Figure E.23.

The reduced electron energy deposition in the inner layers of the sample cylinders is probably the result of a reduction in intensity of the photon spectrum with depth. Figure E.29 and Figure E.30 confirm significant photon flux depression within the inner layers of both Bi cylinders; Figure E.28

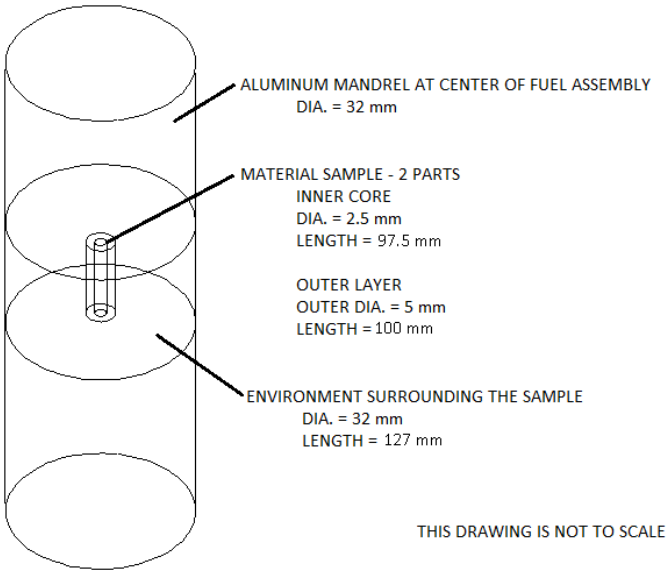

Figure E.14: The geometry used to calculate the effect of environmental material changes on nuclear heating, and gamma absorption spectra in the sample cylinder. The material sample is centered about the core's vertical center.

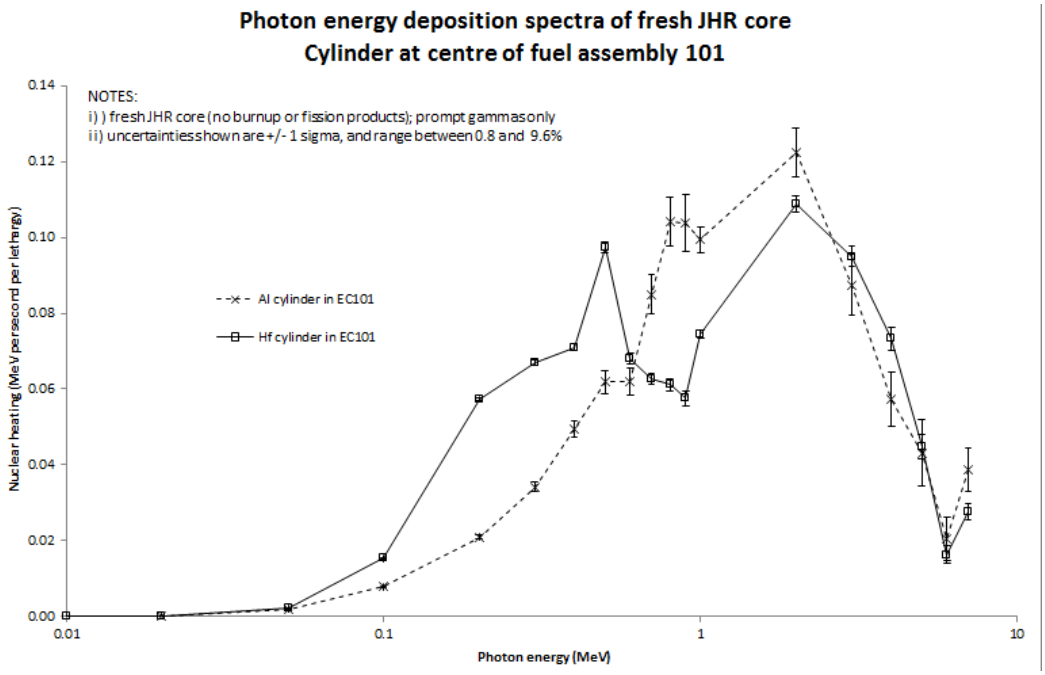

Figure E.15: Energy deposition calculated spectrally at core location EC101.

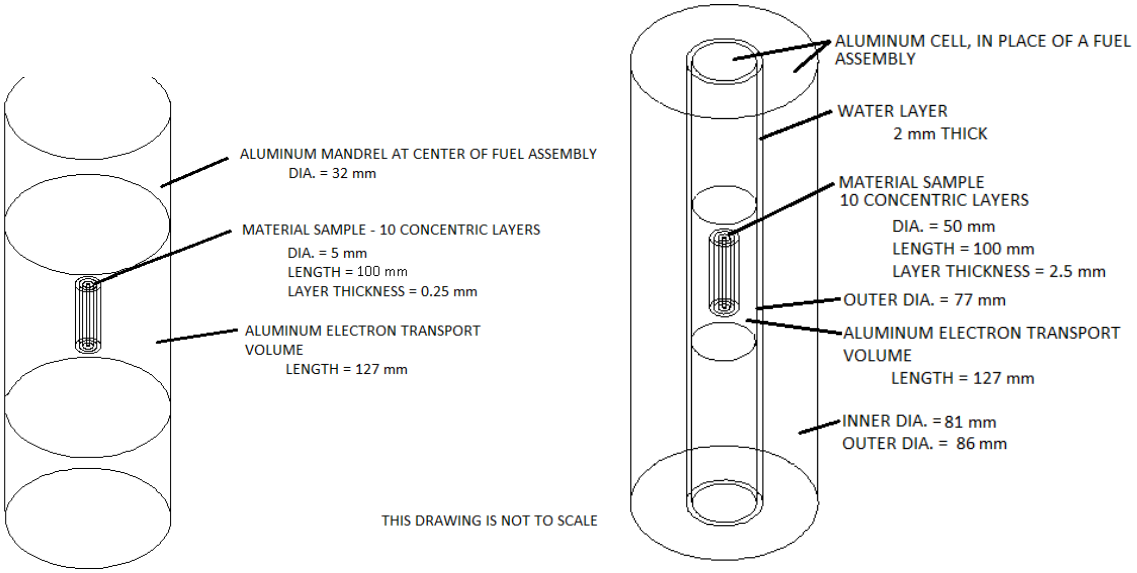

Figure E.16: The multi-layered material samples: (L) geometry used at center of fuel assemblies EC101 and EC105, (R) geometry used in non-fuelled assembly location EC103. The material samples are centered about the core's vertical center.

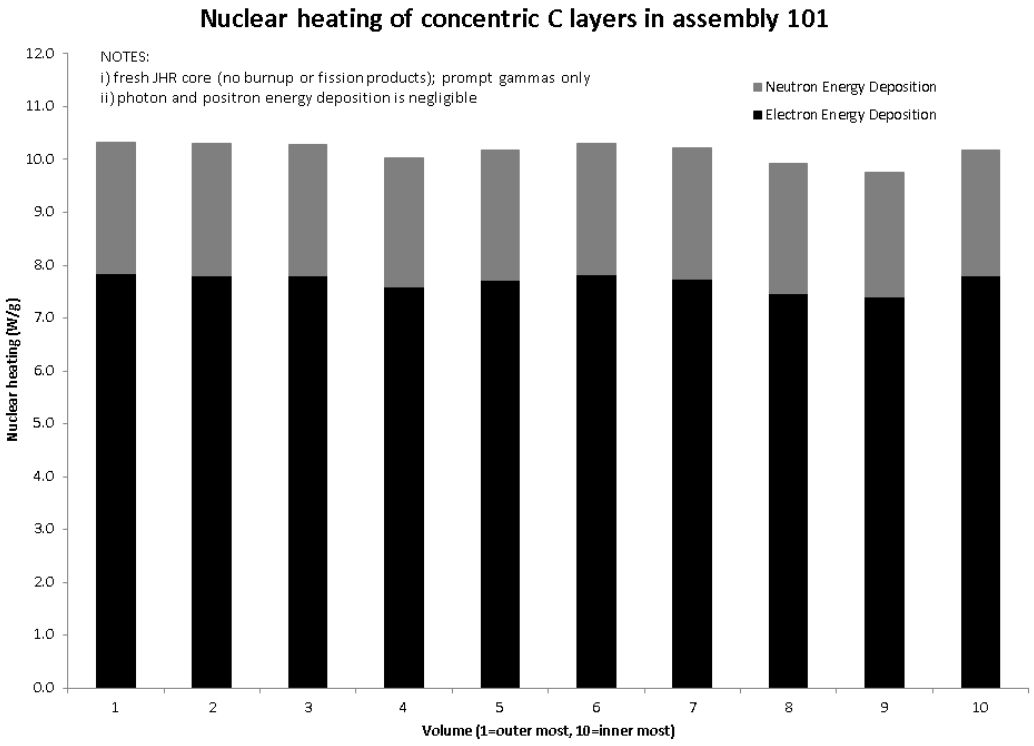

Figure E.17: Nuclear heating within the layers of the C sample cylinder placed within the mandrel of fuel assembly EC101.

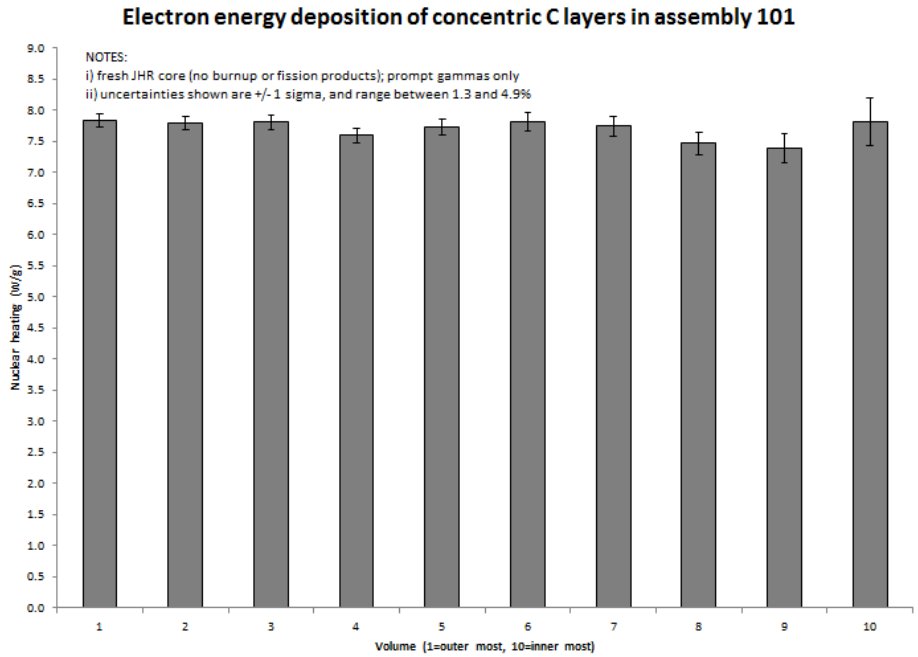

Figure E.18: Electron energy deposition within the layers of the C sample cylinder placed within the mandrel of fuel assembly EC101.

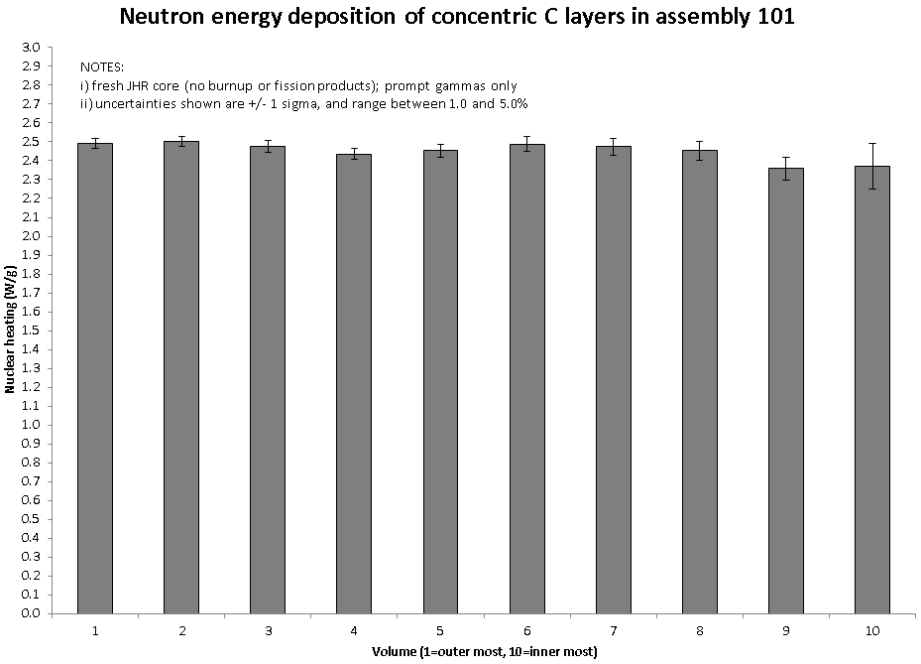

Figure E.19: Neutron energy deposition within the layers of the C sample cylinder placed within the mandrel of fuel assembly EC101.

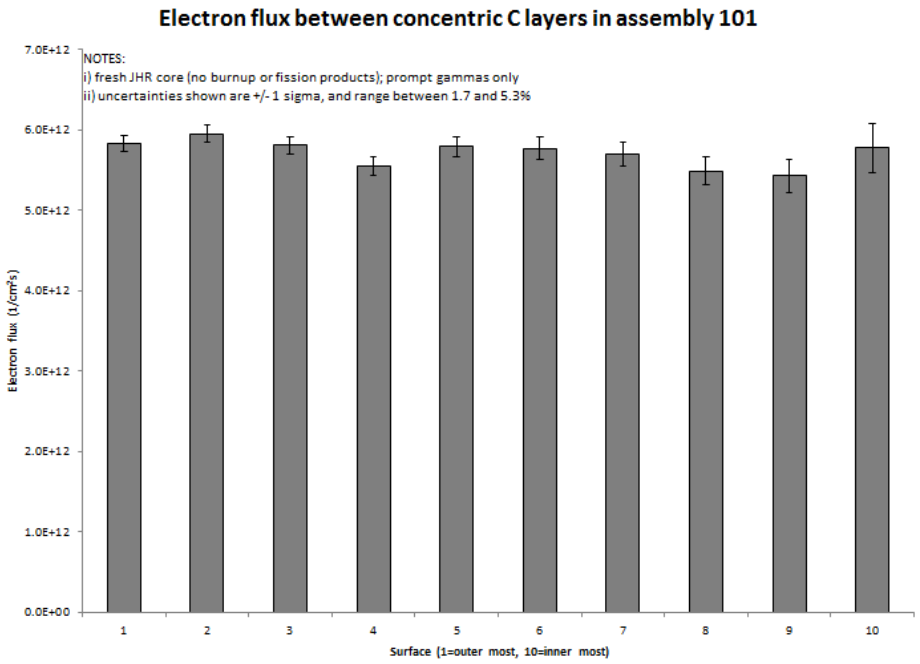

Figure E.20: Electron flux through the outer surface of each C layer of the cylinder placed within the mandrel of fuel assembly EC101.

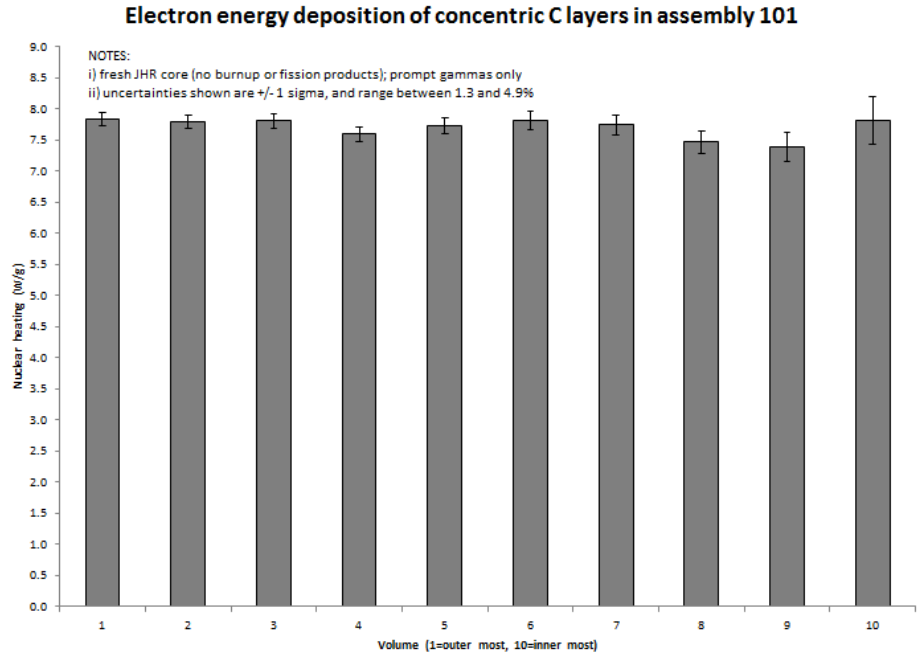

Figure E.21: Electron energy deposition within the layers of the Bi sample cylinder placed within the mandrel of fuel assembly EC105.

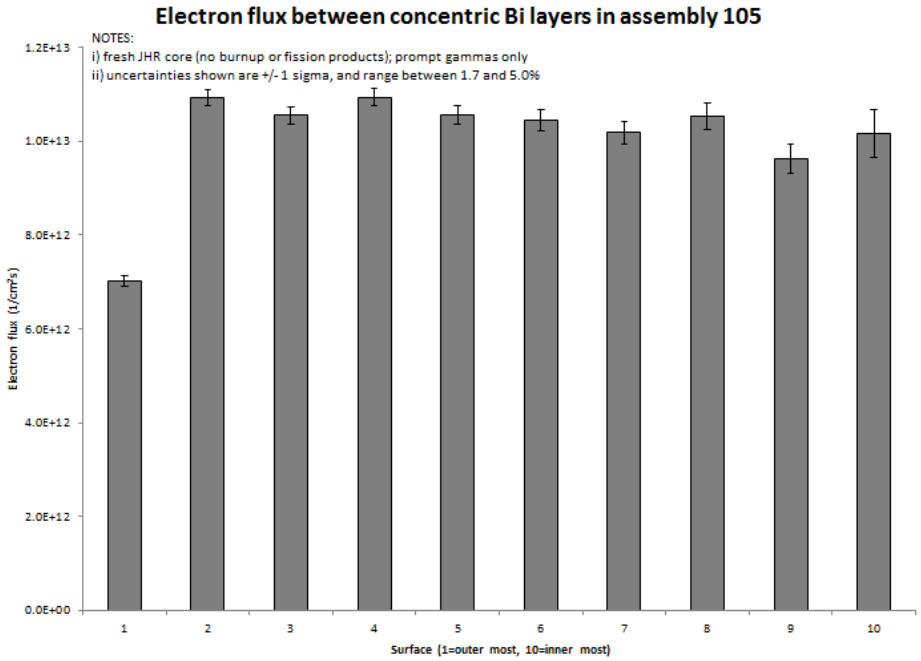

Figure E.22: Electron flux through the outer surface of each Bi layer of the cylinder placed within the mandrel of fuel assembly EC105.

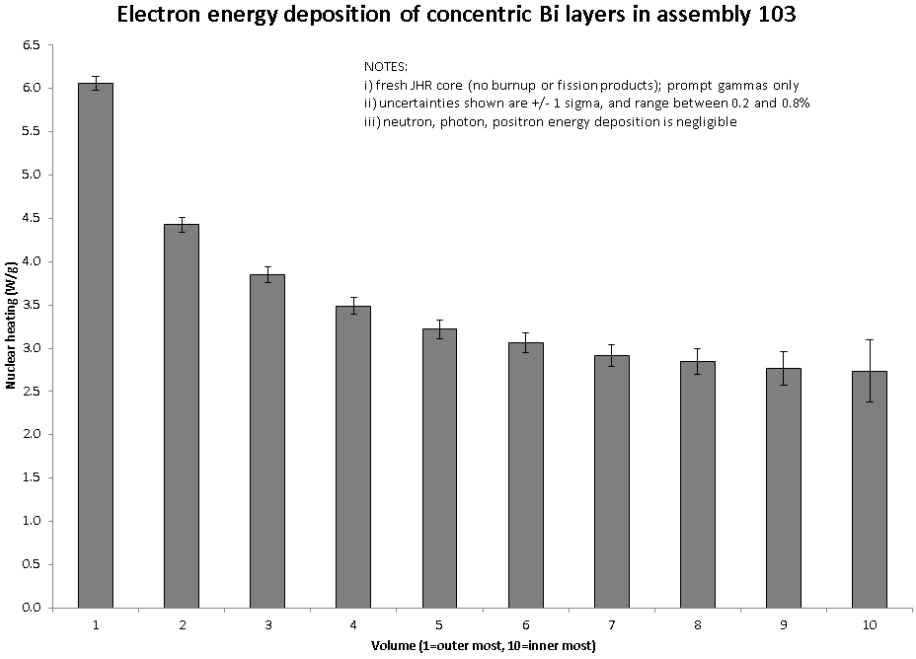

Figure E.23: Electron energy deposition within the layers of the Bi sample cylinder placed within the aluminum cell of position EC103.

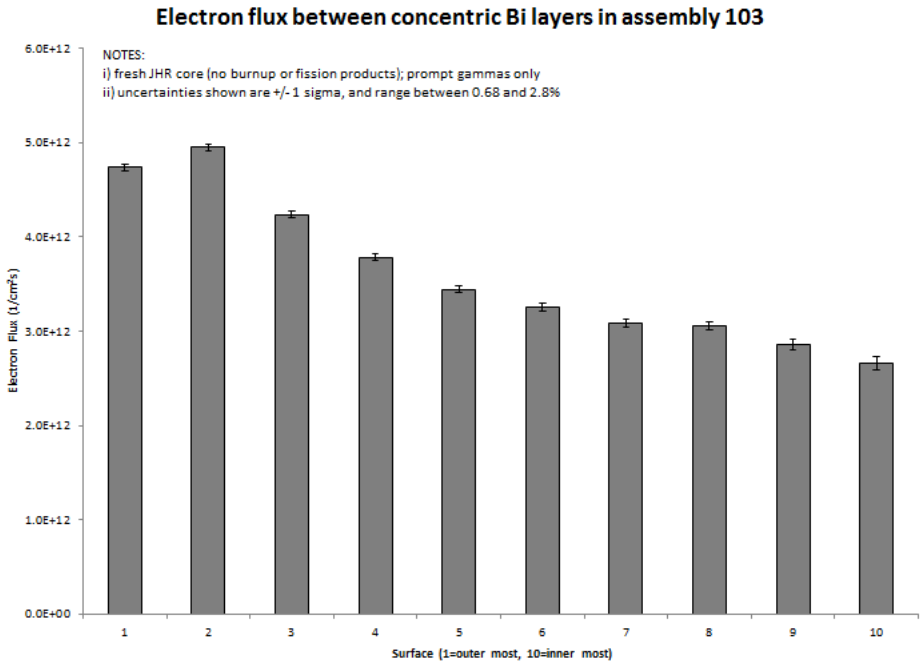

Figure E.24: Electron flux through the outer surface of each Bi layer of the cylinder cylinder placed within the aluminum cell of position EC103.

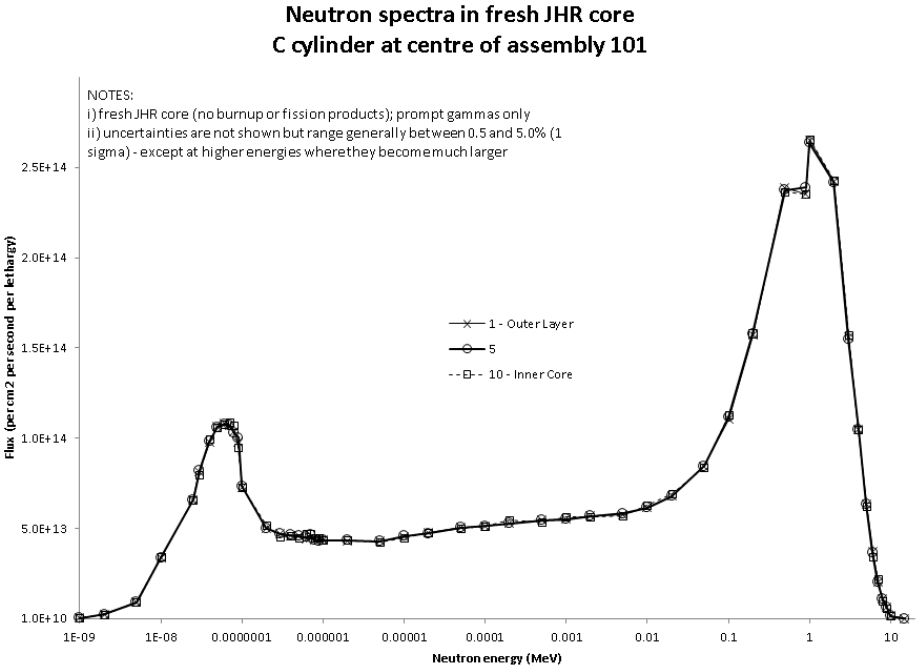

Figure E.25: Neutron spectra within the layers of the C cylinder within the mandrel of fuel assembly EC101.

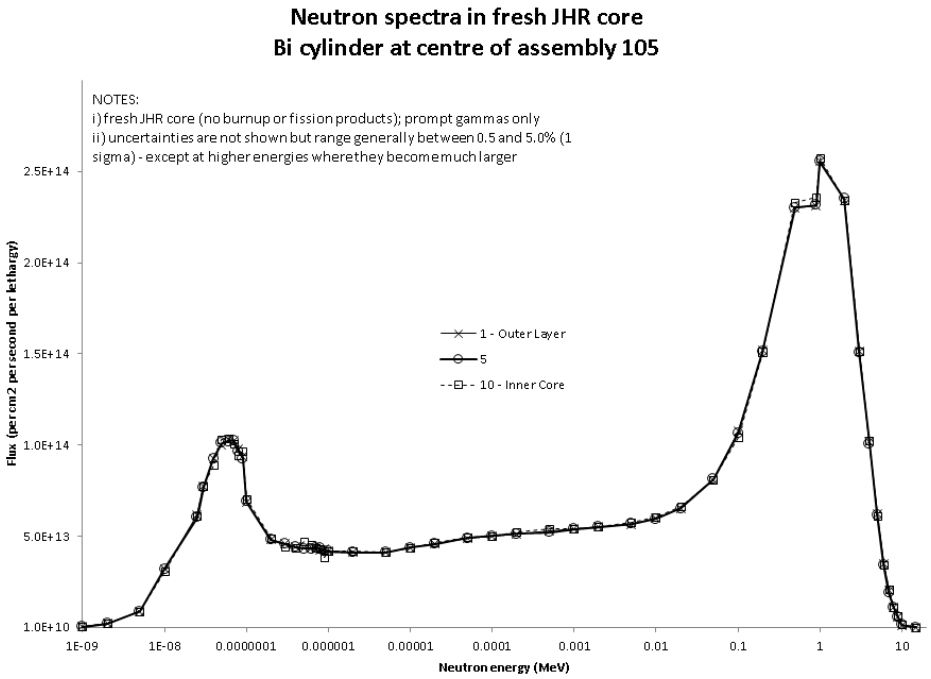

Figure E.26: Neutron spectra within the layers of the Bi cylinder within the mandrel of fuel assembly EC105.

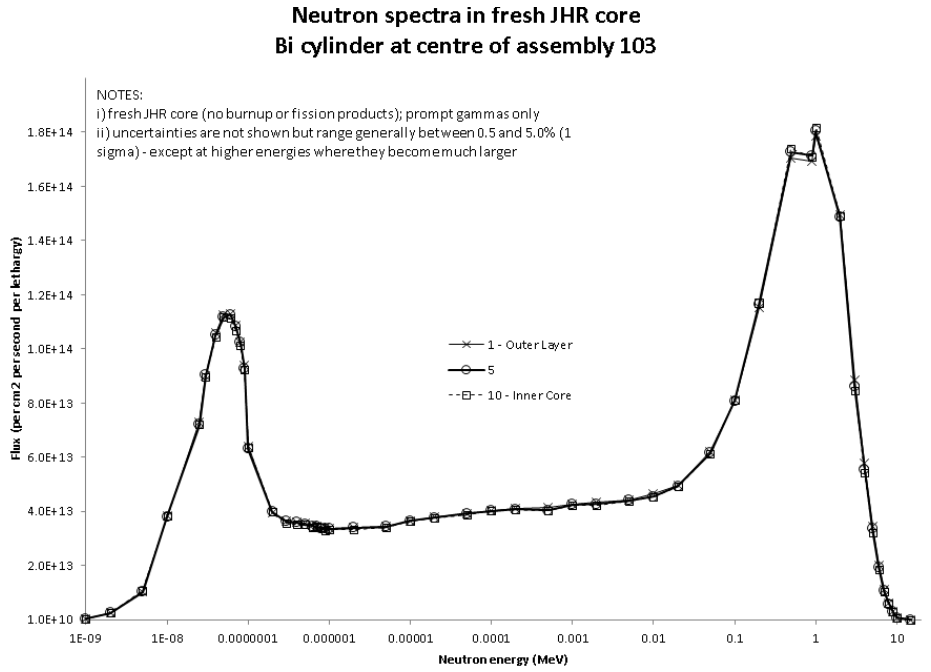

Figure E.27: Neutron spectra within the layers of the Bi cylinder within the aluminum cell of position EC103.

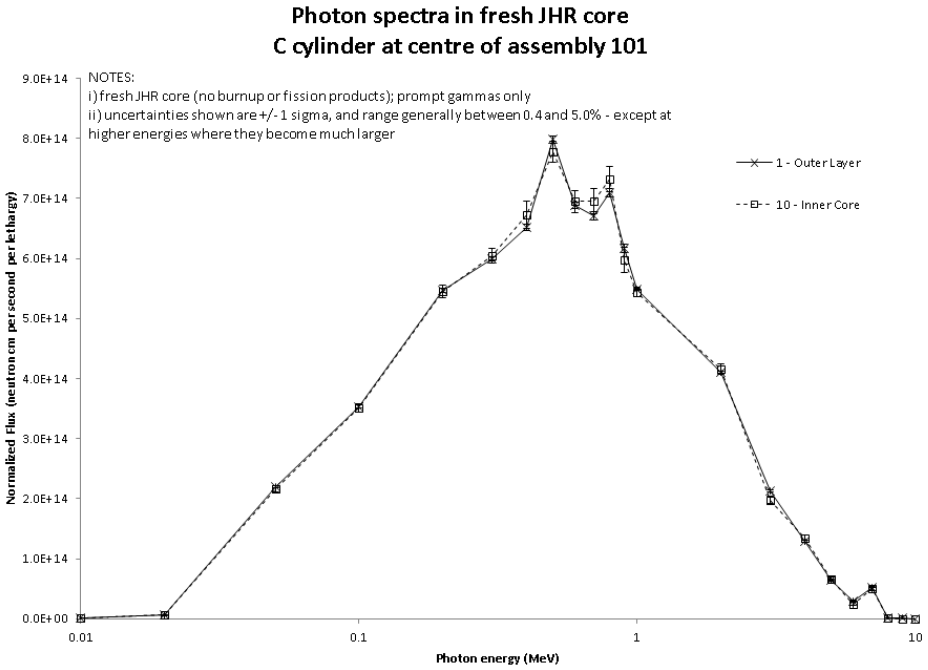

Figure E.28: Photon spectra within the layers of the C cylinder within the mandrel of fuel assembly EC101.

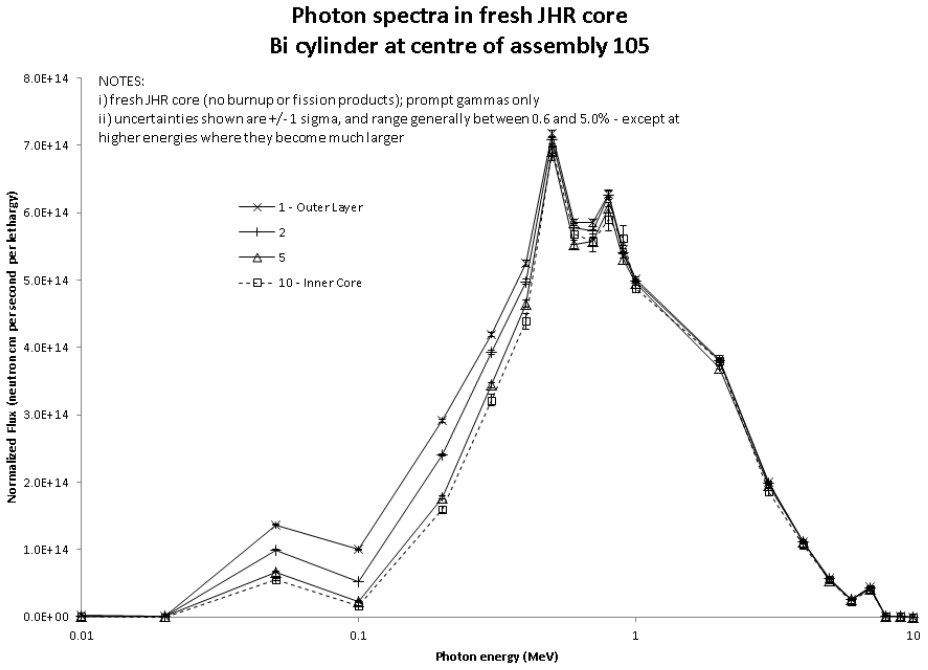

Figure E.29: Photon spectra within the layers of the Bi cylinder within the mandrel of fuel assembly EC105.

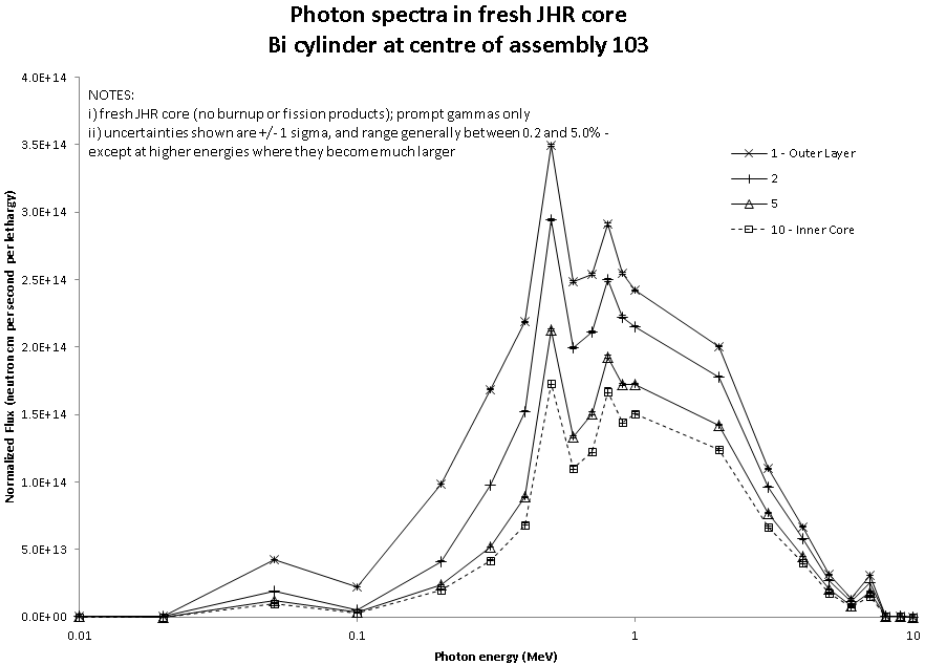

Figure E.30: Photon spectra within the layers of the Bi cylinder within the aluminum cell of position EC103.

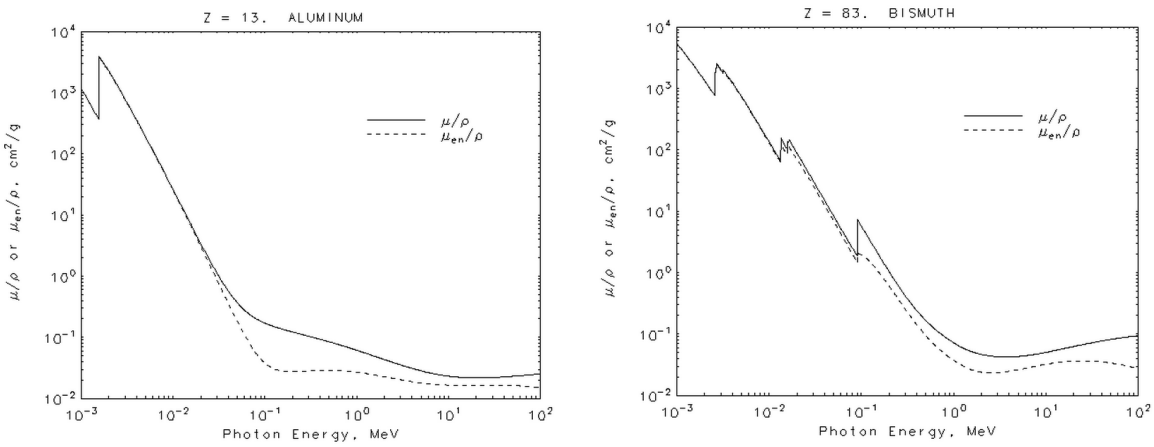

Figure E.31: The mass attenuation coefficients (solid line) and mass energy-absorption coefficients (dotted line) for Al and Bi (Hubbell and Seltzer 2014).

shows the C cylinder, which had little change in electron energy deposition with depth, also has little change in photon flux intensity with depth.

The neutron flux in all depths of all cylinders appears to change very little, as shown in Figure E.25, E.26 and E.27. Presumably if a strong neutron absorber was used as material for the sample cylinder, the neutron flux would reduce strongly with depth.

The electron flux crossing the outer surface of each cylindrical layer changes very little between outer surfaces of the C layers within assembly EC101 (see Figure E.20). This isn't surprising since photons are responsible for the generation of free electrons and Figure E.28 showed the photon flux changed little between layers of EC101.

In the small diameter Bi cylinder of EC105 the electron flux between layers seems to decrease a small amount as depth increases. The effect is easily visible in the large diameter Bi cylinder of EC103.

Fewer electrons cross the outer surface of the first Bi layer (as shown in Figure E.22 and Figure E.24) relative to the second-outermost surface. It is suspected that the electron flux crossing the second-outermost surface is greater because photons (coming from outside the sample cylinder) interact readily in the outermost Bi layer, producing a large number of free electrons which cross the second-outermost surface; in comparison, the electrons crossing the outermost surface are likely created by photon interaction in the surrounding Al volume, which produces fewer free electrons than does Bi. This explanation is supported by the examination of the mass energy-absorption coefficients.

Figure E.31 shows the mass energy-absorption coefficient for Al and Bi. When multiplied by the photon energy flux and density, this coefficient gives an energy quantity which is assumed absorbed by the material in question. This energy is nearly equal to the photon KERMA, so as a rough approximation this energy can be considered proportional to the number of free electrons created by photon/material interaction.

The integrated coefficient appears to be greater in Bi than Al over the range plotted in Figure E.31, but more importantly Bi also has a density approximately 3.6 times that of Al, thus is likely to create many more free electrons than Al, given the same photon irradiation.

The results of these TRIPOLI4 calculations demonstrate why the volume-averaged photon energy deposition (measured in W/g) increases as S/M increases - because the photon energy tends to be absorbed in the outer layers of the sample. One can imagine a cylinder with an extremely large diameter (and much larger length), as the diameter becomes arbitrarily large (creating a very small S/M ratio), photons coming from an external source would be absorbed nearly completely in the outer layers of the cylinder, depositing essentially no energy at the center of the cylinder. In this imaginary case the large volume, and thus large mass, would force the W/g to reduce to nearly zero.

These results also demonstrate the difficultly of dealing with the ratio W/g: in the case of an extremely large cylinder, or a smaller cylinder made of extremely absorbing material, the volume-averaged W/g may be small, despite the fact the total amount of energy deposited may be large in the outer surfaces.

Although the energy deposition has only been explored for cylindrical geometries, one can draw some conclusions for other geometries:

- thick geometries irradiated by a photon field will have depressed photon fluxes in their centers and experience significant gamma heating at shallow depths, despite the fact the W/g averaged over the entire volume may be small
- the above would also apply to medium-sized geometries made of high Z material
- thin geometries will have nearly-uniform fluxes at depth, and large heating measured in W/g
- the above would also apply to medium-sized geometries made of low Z material

E.4.5 Dependency of heating on surrounding material

Since nuclear heating (by neutrons and photons) is dependent upon the particle flux and spectrum, which both change as they move from the source through materials, one wonders how energy deposition would change within a sample with changes of the surrounding material. Additionally, one wonders if some sample materials are more sensitive to environmental changes than others.

To investigate, the geometry of Figure E.14 was placed within assembly EC101. The sample cylinder consisted of an inner core of $\varnothing = 2.5$ mm, L=97.5 mm and a surrounding outer layer $\varnothing = 5$ mm, L=100 mm. The material of both sample-cylinder volumes were simultaneously changed to various materials. The energy deposition was calculated in both the inner and outer sample volumes.

To determine the effects of environmental changes the mandrel surrounding the sample cylinder, which had a $\varnothing = 32$ mm, was sectioned into a length of 127 mm. This 127 mm segment (called the environment) surrounded the sample cylinder with 13.5 mm of material, and was changed to various common reactor materials: Al (structural aluminum found throughout the core, not pure Al), NaK, 316L stainless steel, C, Zr and H_2O.

The energy deposition within both volumes of the sample cylinder was calculated using DEPOSITED_ENERGY scores while the TRIPOLI4 calculations tracked four particles (neutrons, photons, electrons and positrons) in a coupled manner in CRITICITY mode. Charged particle transport was allowed only in the sample cylinder and the 13.5 mm thick environment.

Additionally, the energy deposition was recalculated while tracking only two particles (neutrons and photons) in the same geometry.

Two-particle Monte Carlo simulations are usually conducted at SRJH to calculate neutron and photon energy deposition because they require less processing than four-particle simulations. It is assumed within SRJH that calculating photon energy deposition with a two-particle simulation with a DEPOSITED_ENERGY score is an accurate estimation of photon energy deposition. In reality, the electrons and positrons which are created when photons interact with materials may transport the photon energy away from the volume of interest.

Scoring energy deposition in both the two and four particle simulations, using identical geometry in both cases, allows one to measure the accuracy of the two-particle photon DEPOSITED_ENERGY score because the four-particle case should be a more accurate description of where the energy of fission is ultimately deposited.

Results

The results of the four-particle calculations are shown in Figure E.32 and E.33. These figures show the energy deposited by electrons only, which carry most of the energy originally carried by photons. Neutron energy deposition is not included these figures.

The plotted data is the electron energy deposition in W/g, divided by the electron heating of the same volume when it is surrounded by C in W/g. Figure E.32 is of the inner volume of the sample cylinder, Figure E.33 of the outer volume.

These figures clearly show that changing the environmental material induces a significant change of energy deposited by electrons within the volumes of the sample cylinder.

Furthermore, it appears that the outer layer of the sample cylinder is affected more by environmental changes than the inner core when the sample is made of a material with a higher Z.

The Zr environment seems to shield the sample cylinder the most, presumably because Zr has the highest Z (compared to all other environmental materials tested) and thus is most likely to absorb photon energy.

It appears an environment of NaK allows for the most gamma heating - although the single datum point of an H_2O environment (using an Al target cylinder) suggests H_2O allows greater energy deposition than a NaK environment. Presumably H_2O and NaK are poor photon shields

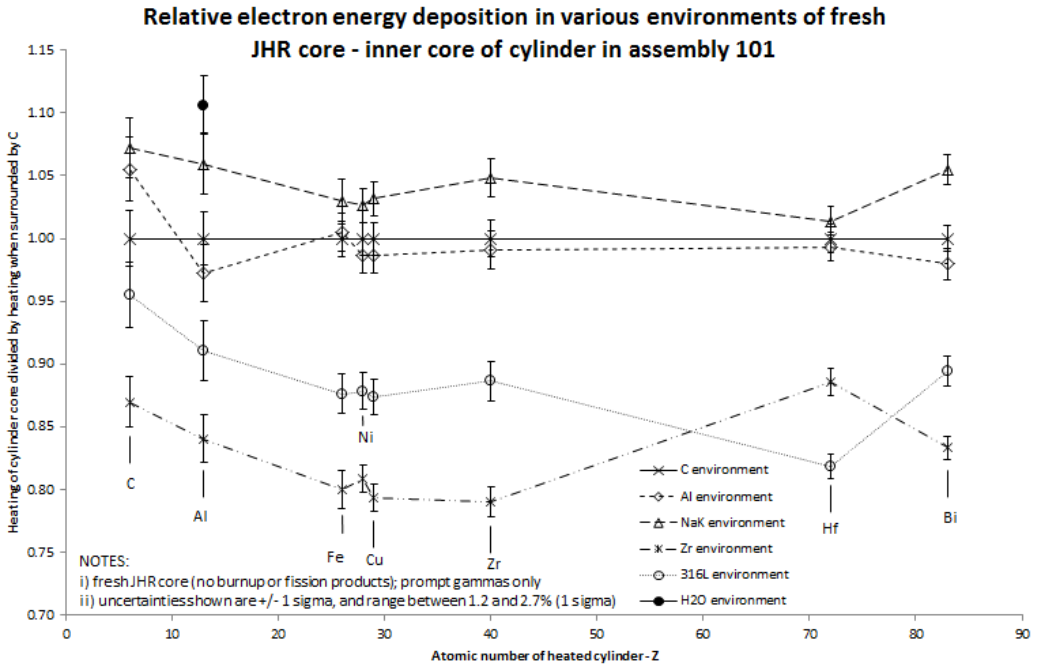

Figure E.32: Electron heating of inner core of sample cylinder (shown in Figure E.14) as the environment changes, relative to electron energy deposition in the same volume when surrounded by a C environment.

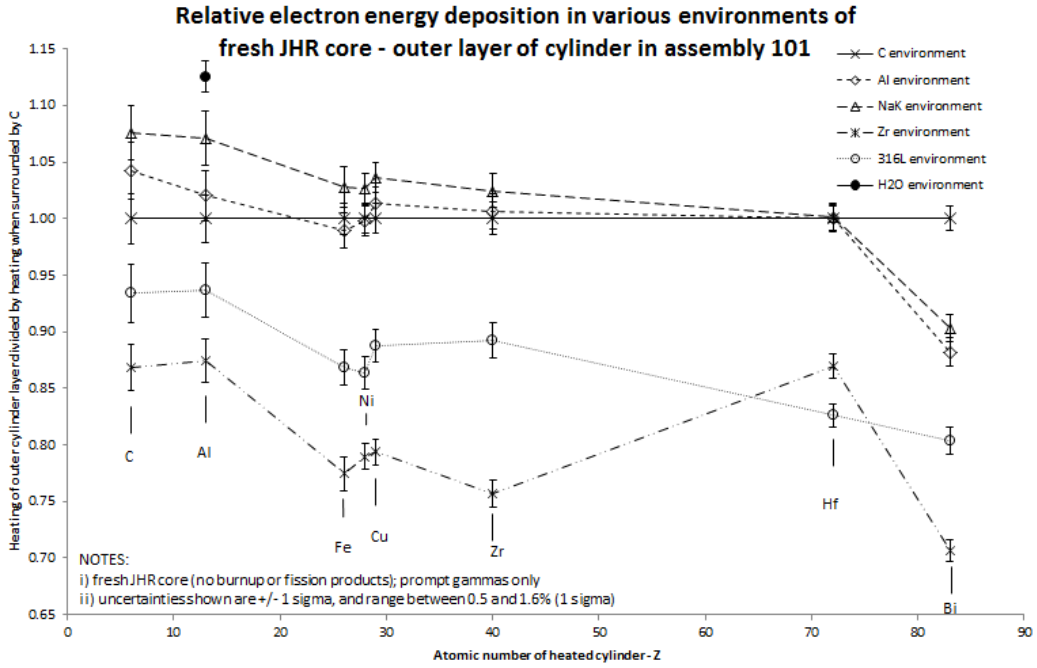

Figure E.33: Electron heating of outer layer of sample cylinder (shown in Figure E.14) as the environment changes, relative to electron energy deposition in the same volume when surrounded by a C environment.

		Electron energy deposition divided by photon KERMA				Total electron, positron, photon energy deposition divided by photon KERMA			
C Environment		**INNER CYLINDER**		**OUTER LAYER**		**INNER CYLINDER**		**OUTER LAYER**	
ELEMENT	**Z**		sigma (%)		sigma (%)		sigma (%)		sigma (%)
aluminum	13	1.02	2.8	0.97	1.6	1.04	1.5	0.98	0.9
zirconium	40	0.95	1.5	0.95	0.8	1.01	1.0	1.02	0.5
hafnium	72	0.88	1.2	0.85	0.6	0.98	0.8	0.96	0.4
bizmuth	83	0.90	1.2	0.83	0.6	1.03	0.7	0.97	0.3
Al Environment		**INNER CYLINDER**		**OUTER LAYER**		**INNER CYLINDER**		**OUTER LAYER**	
ELEMENT	**Z**		sigma (%)		sigma (%)		sigma (%)		sigma (%)
aluminum	13	0.96	2.9	1.00	1.6	0.97	1.7	1.01	1.0
zirconium	40	0.93	1.7	0.96	1.0	1.00	1.1	1.03	0.6
hafnium	72	0.89	1.2	0.86	0.6	1.00	0.8	0.97	0.4
bizmuth	83	0.86	1.4	0.83	0.7	0.99	1.0	0.97	0.5
NaK Environment		**INNER CYLINDER**		**OUTER LAYER**		**INNER CYLINDER**		**OUTER LAYER**	
ELEMENT	**Z**		sigma (%)		sigma (%)		sigma (%)		sigma (%)
aluminum	13	1.01	2.9	0.97	1.6	1.02	1.7	0.99	1.0
zirconium	40	0.96	1.5	0.96	0.9	1.02	1.0	1.03	0.5
hafnium	72	0.87	1.2	0.85	0.6	0.97	0.8	0.95	0.4
bizmuth	83	0.86	1.4	0.84	0.7	0.99	0.8	0.97	0.4
Zr Environment		**INNER CYLINDER**		**OUTER LAYER**		**INNER CYLINDER**		**OUTER LAYER**	
ELEMENT	**Z**		sigma (%)		sigma (%)		sigma (%)		sigma (%)
aluminum	13	1.01	2.8	1.04	1.6	1.04	1.6	1.07	1.0
zirconium	40	0.97	1.7	0.94	1.0	1.02	1.1	1.00	0.6
hafnium	72	0.87	1.2	0.86	0.7	0.98	0.8	0.96	0.4
bizmuth	83	0.89	1.2	0.85	0.6	1.01	0.7	0.85	0.5
316L Environment		**INNER CYLINDER**		**OUTER LAYER**		**INNER CYLINDER**		**OUTER LAYER**	
ELEMENT	**Z**		sigma (%)		sigma (%)		sigma (%)		sigma (%)
aluminum	13	1.05	3.0	1.04	1.8	1.09	2.1	1.08	1.3
zirconium	40	0.88	1.9	0.89	1.1	0.96	1.4	0.96	0.8
hafnium	72	0.87	1.3	0.83	0.7	0.99	0.8	0.94	0.4
bizmuth	83	0.85	1.4	0.81	0.7	0.98	1.0	0.96	0.5

Table E.5: Comparison between photon KERMA and energy deposited by electrons, photons and positrons (prompt gammas only).

		Positron energy deposition divided by the electron energy deposition				Photon energy deposition divided by the electron energy deposition			
C Environment		**INNER CYLINDER**		**OUTER LAYER**		**INNER CYLINDER**		**OUTER LAYER**	
ELEMENT	**Z**		sigma (%)		sigma (%)	%	sigma (%)	%	sigma (%)
carbon	6	0.01	16.2	0.01	10.6	0.00	9.6	0.00	5.9
aluminum	13	0.01	13.2	0.01	7.7	0.00	6.3	0.00	3.0
iron	26	0.03	6.2	0.02	3.8	0.01	2.1	0.01	1.3
nickel	28	0.04	4.7	0.03	2.8	0.01	2.1	0.01	1.1
copper	29	0.04	5.1	0.03	3.1	0.01	2.0	0.02	1.1
zirconium	40	0.03	5.7	0.03	3.7	0.03	1.8	0.05	0.9
hafnium	72	0.06	3.6	0.05	2.2	0.06	1.7	0.08	0.8
bizmuth	83	0.05	3.7	0.04	2.3	0.09	1.4	0.13	0.6

Al Environment		**INNER CYLINDER**		**OUTER LAYER**		**INNER CYLINDER**		**OUTER LAYER**	
ELEMENT	**Z**		sigma (%)		sigma (%)		sigma (%)		sigma (%)
carbon	6	0.01	17.7	0.01	10.1	0.00	13.0	0.00	7.2
aluminum	13	0.01	15.6	0.02	7.9	0.00	6.0	0.00	3.9
iron	26	0.03	7.5	0.03	4.0	0.01	2.4	0.01	1.5
nickel	28	0.04	5.3	0.03	3.2	0.01	2.2	0.01	1.2
copper	29	0.03	5.7	0.03	3.5	0.01	2.3	0.02	1.2
zirconium	40	0.04	6.4	0.03	4.0	0.03	2.2	0.04	1.1
hafnium	72	0.06	3.5	0.05	2.2	0.06	1.8	0.08	0.8
bizmuth	83	0.05	4.9	0.04	3.0	0.09	2.0	0.13	0.9

NaK Environment		**INNER CYLINDER**		**OUTER LAYER**		**INNER CYLINDER**		**OUTER LAYER**	
ELEMENT	**Z**		sigma (%)		sigma (%)		sigma (%)		sigma (%)
carbon	6	0.01	13.5	0.01	8.1	0.00	10.4	0.00	6.5
aluminum	13	0.02	13.0	0.02	8.3	0.00	6.9	0.00	4.9
iron	26	0.03	10.1	0.03	4.8	0.01	3.1	0.01	1.8
nickel	28	0.04	4.4	0.03	2.9	0.01	2.5	0.01	1.5
copper	29	0.03	5.2	0.03	3.0	0.01	2.1	0.01	1.1
zirconium	40	0.03	5.7	0.03	3.4	0.03	2.2	0.04	1.0
hafnium	72	0.06	3.6	0.05	2.1	0.06	1.7	0.07	0.9
bizmuth	83	0.05	4.1	0.04	2.4	0.09	1.7	0.12	0.8

Zr Environment		**INNER CYLINDER**		**OUTER LAYER**		**INNER CYLINDER**		**OUTER LAYER**	
ELEMENT	**Z**		sigma (%)		sigma (%)		sigma (%)		sigma (%)
carbon	6	0.02	12.9	0.02	7.4	0.00	10.3	0.00	5.8
aluminum	13	0.02	11.0	0.02	6.2	0.00	6.6	0.00	5.8
iron	26	0.03	9.4	0.03	5.3	0.01	4.2	0.33	1.8
nickel	28	0.04	4.8	0.04	2.9	0.01	3.3	0.01	1.9
copper	29	0.04	5.2	0.04	3.0	0.01	3.3	0.01	1.9
zirconium	40	0.03	6.3	0.04	3.7	0.02	2.8	0.02	1.8
hafnium	72	0.06	3.7	0.05	2.3	0.06	1.8	0.07	0.9
bizmuth	83	0.05	4.1	0.04	2.4	0.09	1.6	0.10	0.8

316L Environment		**INNER CYLINDER**		**OUTER LAYER**		**INNER CYLINDER**		**OUTER LAYER**	
ELEMENT	**Z**		sigma (%)		sigma (%)		sigma (%)		sigma (%)
carbon	6	0.04	10.9	0.03	6.9	0.00	13.2	0.00	8.3
aluminum	13	0.04	10.5	0.04	6.4	0.00	8.6	0.00	5.3
iron	26	0.05	6.9	0.05	4.1	0.01	3.5	0.01	2.9
nickel	28	0.05	6.1	0.05	3.6	0.01	3.1	0.01	1.9
copper	29	0.05	6.7	0.05	3.8	0.01	3.1	0.01	1.8
zirconium	40	0.06	6.6	0.05	3.8	0.03	2.8	0.03	1.5
hafnium	72	0.07	3.5	0.06	2.1	0.06	1.8	0.08	0.9
bizmuth	83	0.07	4.5	0.06	2.7	0.10	2.0	0.12	1.0

Table E.6: Positron and photon energy deposition compared to the energy deposited by electrons (prompt gammas only).

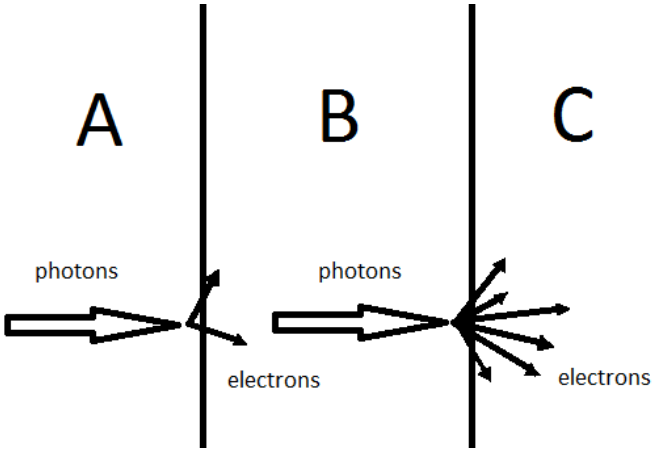

Figure E.34: Electronic inequality of high-density, high-Z material of region B, when region A is made of low-density, low-Z material.

because they have lower mass energy-absorption coefficients and/or densities than Zr and 316L stainless steel.

Table E.5 presents a comparison between a coupled two-particle TRIPOLI4 calculation of photon energy deposition, which calculated photon KERMA, and a coupled four-particle TRIPOLI4 calculation, which calculated the energy deposited by positrons, electrons and photons separately. This table does not include delayed gammas or delayed gamma energy in any way; only the prompt photons as calculated in TRIPOLI4 have been included.

Table E.5 shows the fraction "Electron energy deposition [calculated during four-particle transport] divided by photon KERMA [calculated during the two-particle transport]." This fraction is always above 0.5, indicating that electrons deposit the majority of the energy transferred from photons to charged particles. The remainder of the photon KERMA is ultimately deposited by positrons and photons, as shown by the fraction "Total electron, positron, photon energy deposition [calculated during four-particle transport] divided by photon KERMA [calculated during two-particle transport]."

Table E.6 compares the energy deposited by photons and positrons to the energy deposited by electrons, from four-particle TRIPOLI4 calculations. This table demonstrates electrons carry much more of the photon energy than positrons.

Within Table E.5, the inner-cylinder fractions are generally closer to unity than the outer-layer fractions. The "Electron energy deposition divided by photon KERMA" outer-layer fraction drops significantly below unity for high-Z sample materials.

The "Total electron, positron, photon energy deposition divided by photon KERMA" fraction is generally equal to unity in all cases for the inner cylinder, but still less than unity for the outer layer.

These small outer-layer fractions are probably caused by the outer layer being directly adjacent to the surrounding environment; Figure E.34 illustrates this effect.

Figure E.34 shows why sample material B may have a small "Electron energy deposition divided by photon KERMA" fraction. Assuming free electrons don't travel far in any material before depositing their energy, a few electrons (originating very close to the material boundary) pass over the A-B material interface into B and deposit their energy in region B - resulting in an actual energy deposition in A which is lower than the photon KERMA of region A.

If material A is low-density, low-Z material and material B is high-density, high-Z material, photon/material interactions in B will create many more free electrons than in A. Thus many more electrons may cross the B-C boundary and deposit their energy in C - resulting in an actual energy

deposition in B which is much lower than is indicated by photon KERMA in B.

Thus, the reason why the Table E.5 fractions are smaller in large Z targets than low-Z targets, for any given environment, is because photons are more likely to transfer energy to charged particles in high-Z material, and many of these electrons manage to escape, while the surrounding low-Z material does not contribute many electrons.

When the environment and outer layer are both made of Al the outer-layer "Electron energy deposition divided by photon KERMA" fraction is equal to unity, indicating there is a balance between the number of electrons entering the outer-layer and the number leaving. This is the state of electronic equilibrium which is considered in cavity theory.

The fraction "Total electron, positron, photon energy deposition divided by photon KERMA" in Table E.5 gives an important lesson: this fraction is usually close to or less than unity. Thus if one wanted to know the photon heating in a volume and assumed it was equal to the photon KERMA of a two-particle TRIPOLI4 calculation, it would be an acceptable (or conservative) approximation to the actual "photon energy deposition" which is correctly calculated by summing the energy deposition of photons, electrons and positrons after a more expensive four-particle calculation.

E.4.6 Dependency of heating on control rod position

Since control rod movements strongly distort the local neutron flux, it was speculated that perhaps changes in control rod position may also affect gamma heating. Control rods in JHR are to be inserted within fuel assemblies. Assemblies which host control rods cannot also host irradiation samples. Thus in these calculations, the vertical height of a control rod in EC102 is changed, while the gamma heating is calculated in the centre of another fuel assembly EC101.

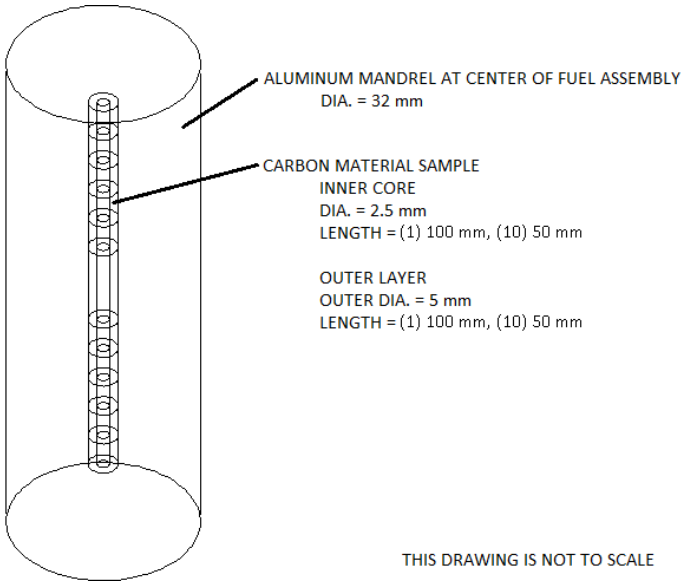

Figure E.35: The geometry used to calculate the effect of control rod position changes on nuclear heating. The material samples are centered about the core's vertical center.

To examine the nuclear heating with changes in control rod position, the geometry shown in Figure E.35 was placed within the mandrel at the centre of fuel assembly EC101. The sample geometry consists of 11 stacked sample cylinders, each with an inner cylindrical core of $\varnothing = 2.5$ mm and outer layer with an outer diameter of 5 mm, all made of C. The central (vertically) cylinder was located where the neutron flux changes little with vertical displacement, has a length of 100 mm;

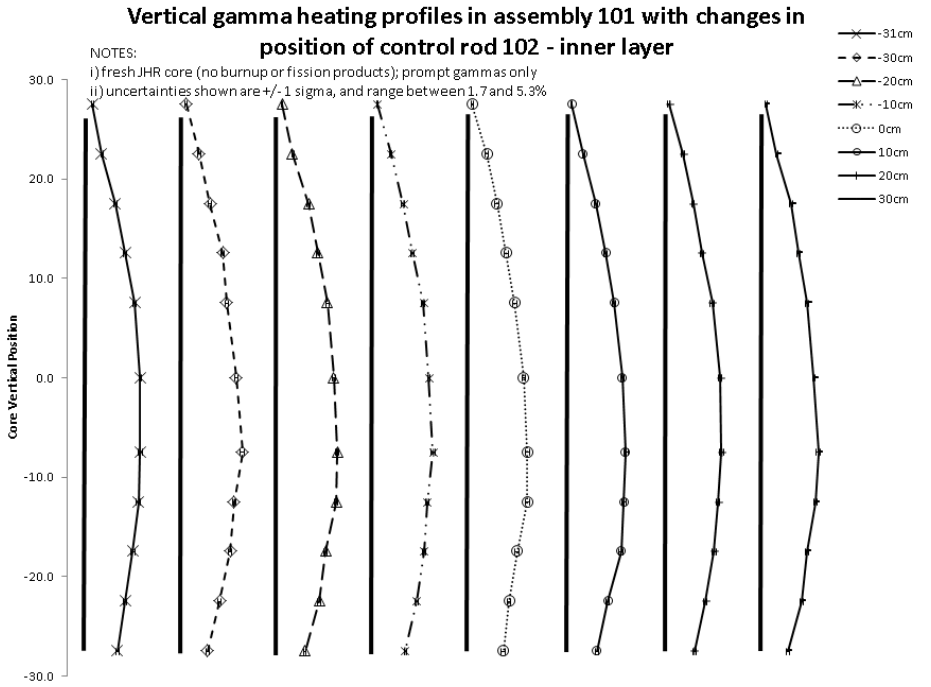

Figure E.36: Gamma heating profiles of the inner cores of the carbon samples located within assembly 101.

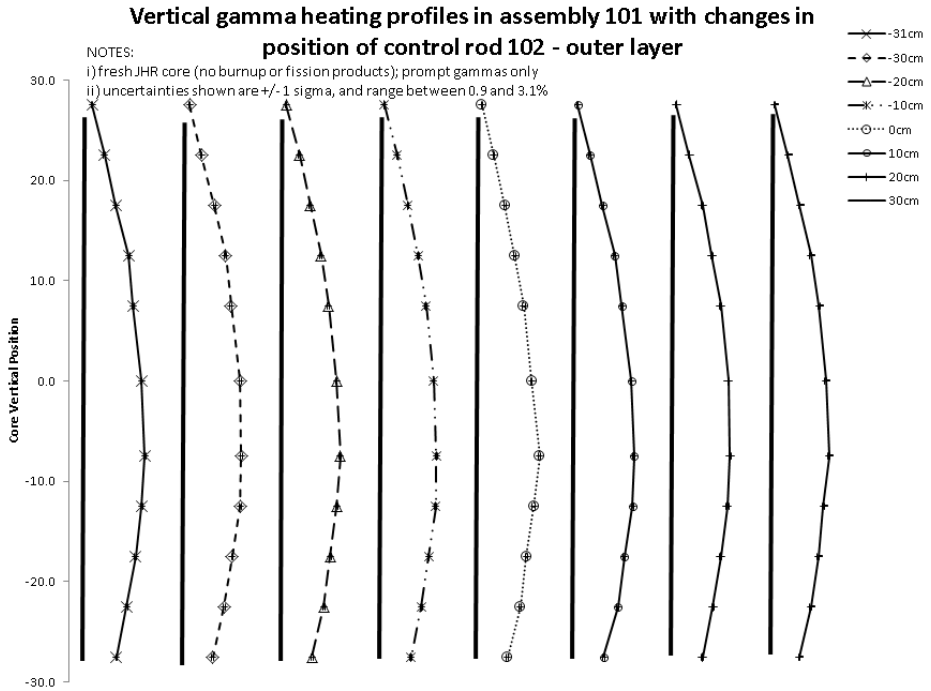

Figure E.37: Gamma heating profiles of the outer layers of the carbon samples located within assembly 101.

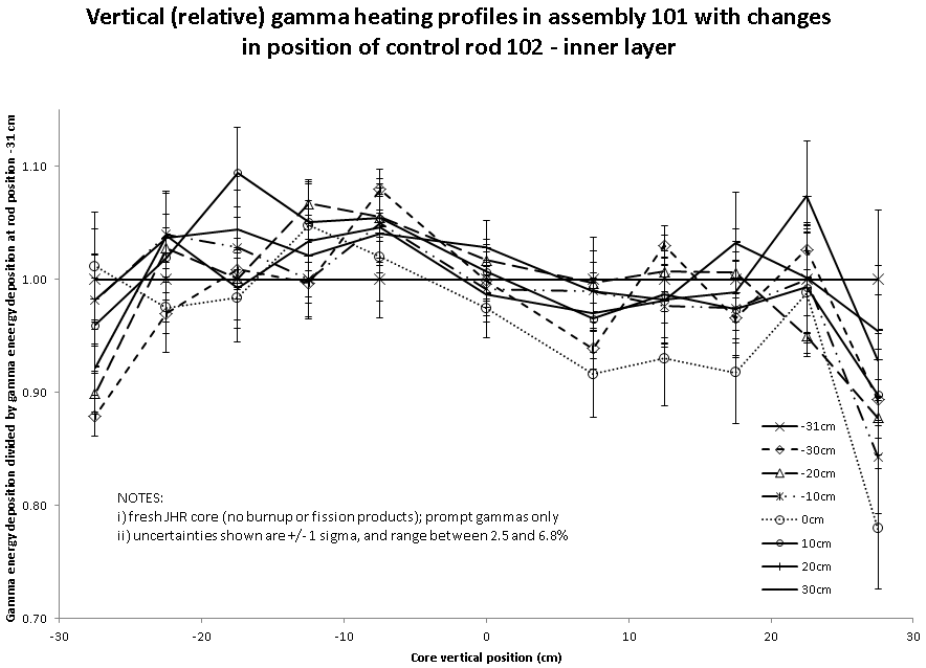

Figure E.38: Relative gamma heating profiles of the inner cores of the carbon samples located within assembly 101.

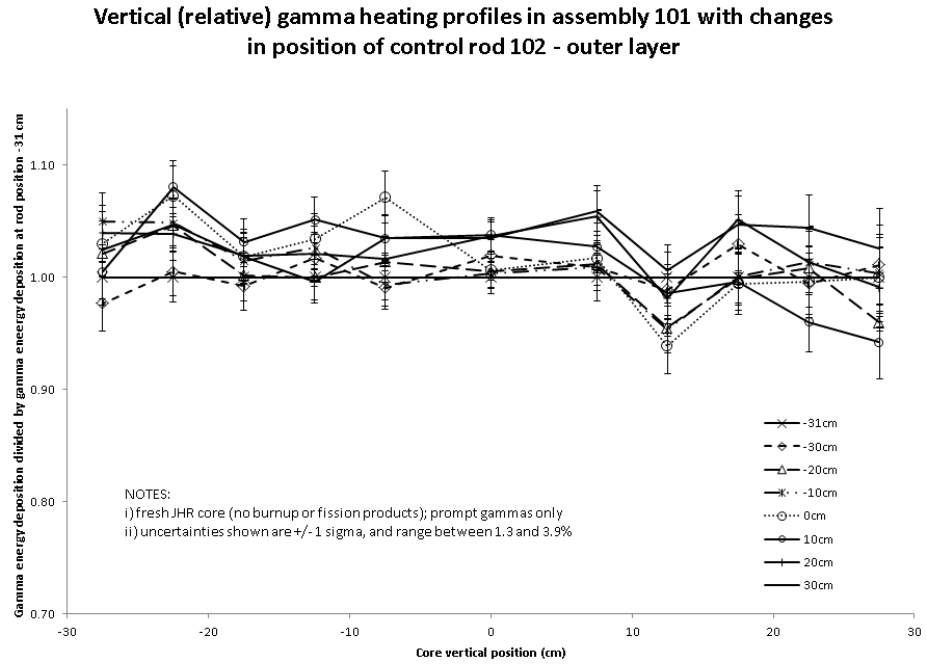

Figure E.39: Relative gamma heating profiles of the outer layers of the carbon samples located within assembly 101.

the rest are located where the neutron flux changes a lot vertically, thus they have a shorter height of 50 mm.

The energy deposition was calculated using DEPOSITED_ENERGY scores on each volume while the TRIPOLI4 calculations tracked two particles (neutrons, photons) in a coupled manner in CRITICITY mode. The photon energy deposition was measured within each sample volume as the control rod within fuel assembly EC102 moved from a position of -31 cm to 30 cm.

Results

Figure E.36 and E.37 show the vertical gamma heating profiles of the inner and outer sample layers are unchanged for each control rod position; the dark vertical lines have been added for visual reference. These unchanged profiles imply that changes in the EC102 control rod position make no significant difference on the nuclear heating in central locations of assembly EC101.

A relative inspection of the same data is presented in Figure E.38 and E.39. The data is presented as gamma heating at various rod positions, divided by the gamma heating in the same volume when the original rod position was at -31 cm. Error bar of 1 sigma are plotted on each point. None of the data points differ from a ratio of 1.0 by more than 2 sigma.

E.5 Equilibrium core calculations

All previous calculations in this report have been conducted with a TRIPOLI4 model of JHR with no fission product inventory. In this section the equilibrium core with fission products (as described in section E.3.4) was used to calculate neutron and photon spectra for comparison to the zero-burn-up core. This comparison should demonstrate if the presence of a significant fission product inventory and absence of absorber rods make a significant difference in the spectra.

TRIPOLI4 tracked neutrons and photons in a coupled manner for these calculations. TRIPOLI4 cannot track the decay of fission products or activation products, so although the fission product inventory has been extensively described in the TRIPOLI4 model, no delayed gammas have been considered at all in this section.

The geometry shown in Figure E.14 was placed within EC101 and EC307. The environment surrounding the sample cylinder was made of the structural aluminum typically found in JHR (not pure Al). Both the inner cylinder and outer layer of the sample cylinder were made of pure C.

E.5.1 Results

Figure E.40 shows the normalized neutron spectra averaged over the central $\varnothing$ = 2.5 mm, L=97.5 mm C cylinder placed in EC101 of the equilibrium core. For comparison, Figure E.40 also shows the neutron spectra calculated in the $\varnothing$ = 5 mm, L=100 mm C cylinder placed in EC101 of the fresh core (zero burnup) as previously shown in Figure E.12. Notice the cylinders over which the spectra have been averaged differ in size; this is thought to be acceptable given the insignificant change in neutron flux demonstrated between C layers in Figure E.25. The normalized neutron flux appears to change little at EC101 between the zero burn-up and equilibrium core.

The calculated neutron spectra averaged over the central $\varnothing$ = 2.5 mm, L=97.5 mm C cylinder placed in EC307 of the equilibrium core is also plotted in Figure E.40.

Figure E.41 shows the normalized (prompt-only) photon spectra averaged over the central $\varnothing$ = 2.5 mm, L=97.5 mm C cylinder placed in EC101 of the equilibrium core. For comparison, Figure E.41 also shows the neutron spectra calculated in the $\varnothing$ = 5 mm, L=100 mm C cylinder placed in EC101 of the fresh core (zero burn-up) as previously shown in Figure E.13. Notice the cylinders over which the spectra have been averaged differ in size; this is thought to be acceptable given the insignificant change in photon flux demonstrated between C layers in Figure E.28. The normalized photon flux appears to change little at EC101 between the zero burn-up and equilibrium core.

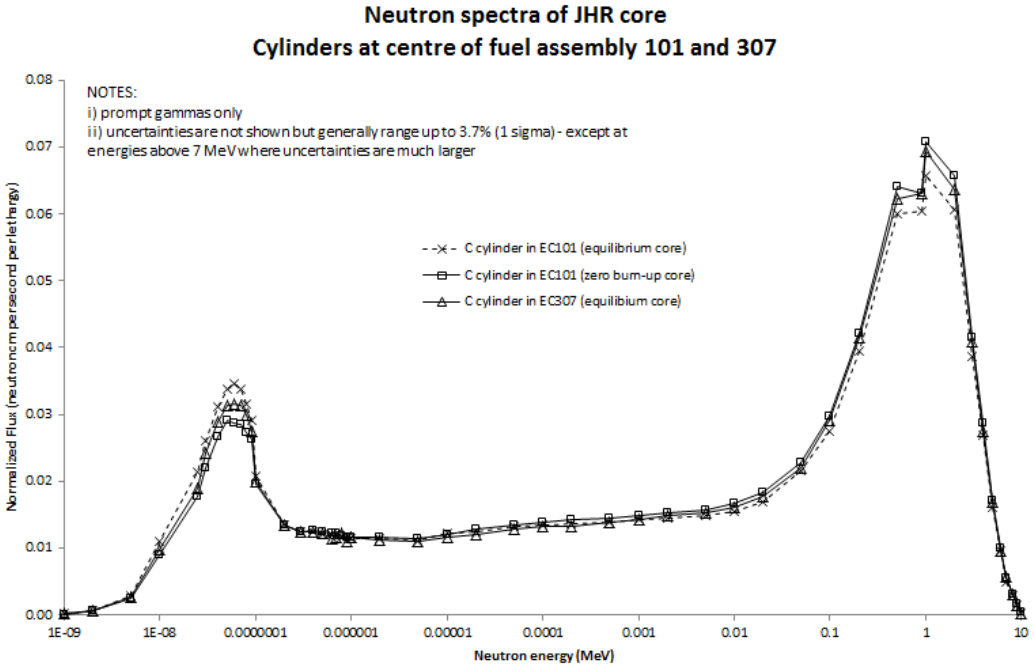

Figure E.40: Comparison between normalized neutron spectra of zero burn-up and equilibrium core at EC101.

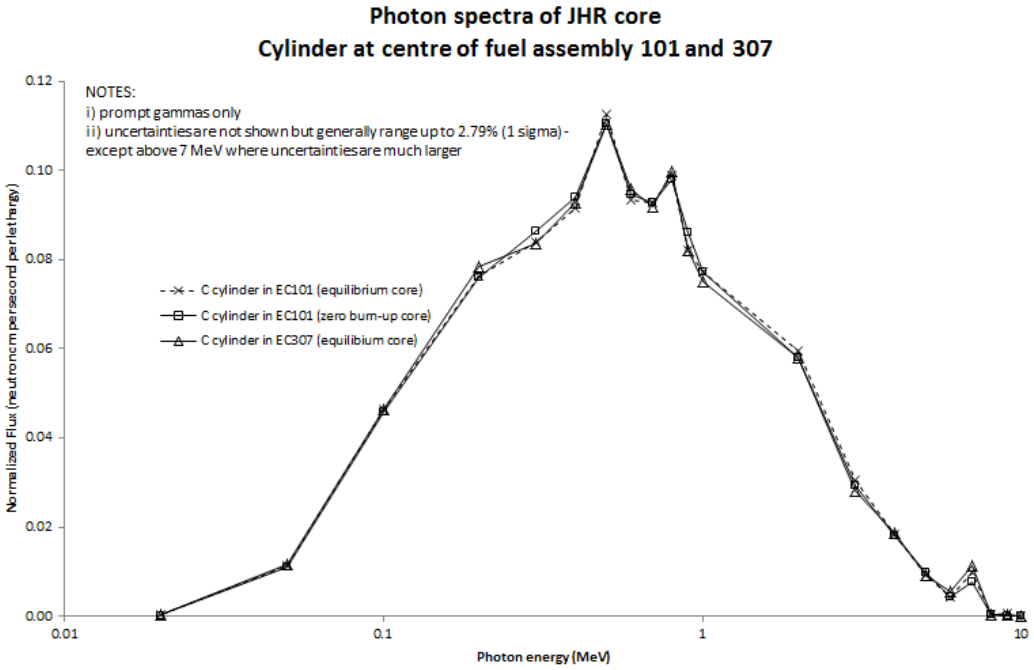

Figure E.41: Comparison between normalized photon spectra of zero burn-up and equilibrium core at EC101.

The calculated prompt photon spectra averaged over the central ∅ = 2.5 mm, L=97.5 mm C cylinder placed in EC307 of the equilibrium core is also plotted in Figure E.41.

E.6 Conclusions

E.6.1 General observations

These calculations predict that prompt gamma heating, in units of W/g, increases as the dimensions of a sample decrease. This results from self-shielding, and has been observed experimentally by others (Reilly and Peters 1971).

These studies have demonstrated gamma heating is dependent upon geometry of the sample, material of the sample, environment of the sample and spatial location of the sample. It would be useful if one could develop a single factor to predict in-core gamma heating of an in-core material sample, knowing only the reactor power; however, this report shows such a factor would be dependent upon all the variables listed above, and therefore require many parametric studies to develop.

E.6.2 Gamma heating in strong neutron absorbers

It appears strong neutron absorbers are likely to have significantly higher gamma heating in a mixed neutron/gamma radiation field, compared to non-neutron absorbers of a similar Z. This is suspected to result from the additional absorption of neutrons which release neutron-capture gamma radiation, which causes greater gamma heating. Figures E.7, E.9 and E.10 illustrate the heightened gamma heating of Ni, Nb, Gd and Hf.

E.6.3 Comparison of two and four-particle TRIPOLI4 calculations

Table E.5 shows one can calculate the photon KERMA in a volume with a two-particle TRIPOLI4 calculation, and it would likely be a conservative approximation to the actual photon energy deposition. This conclusion was obtained by comparing the results to four-particle TRIPOLI4 calculations.

E.6.4 Further analysis

Any opportunity for improvement in modelling of in-core gamma heating must begin where current methods either fail, don't agree with fundamental physics, or are simplistic. Within this chapter, no calculations revealed results which are obviously erroneous or non-physical. However, a very simplistic model was employed to calculate the delayed-gamma heating and could be improved further.

Appendix F

Thermocouples in the SCK-CEN GT

F.1 Thermocouples

Thermocouples are ubiquitous in industrial settings for measuring temperatures. Their operation depends upon the Seebeck effect, or the Seebeck electromotive force (EMF). This is the EMF which results over any length of metal wire, when one end is heated relative to the other end. For any metal, the ratio of the net change of Seebeck EMF, $\mathrm{d}E$, which results from a very small change of temperature, $\mathrm{d}T$, to that temperature increment is called the Seebeck coefficient (ASTM Committee E20 on Temperature Measurement 1993; 7):

$$\sigma(T) = \frac{\mathrm{d}E}{\mathrm{d}T}.$$

The Seebeck coefficient is temperature dependent and may be either positive or negative in magnitude. Over a small temperature difference, it might be assumed that the Seebeck coefficient is constant; in this case, the EMF generated over a wire with ends at different temperatures would simply be (ASTM Committee E20 on Temperature Measurement 1993; 10):

$$E \simeq \sigma \cdot (T_2 - T_1).$$

In the general case, where the Seebeck coefficient is temperature dependent, the total EMF generated is determined with an infinite sum of EMFs generated over an infinite number of infinitely small temperature changes (i.e. an integration). For a wire with one end at T_1 and the other at a higher temperature T_2 (ASTM Committee E20 on Temperature Measurement 1993; 9):

$$E = \int_{T_1}^{T_2} \sigma(T)\,\mathrm{d}T. \tag{F.1}$$

Simple thermocouples are made by joining one end of two metal wires at a heated junction with temperature T_2. Each wire responds by generating its own absolute EMF. The net EMF is the sum of the EMFs created by each wire, and is measured by a voltmeter across the opposite wire ends - Figure F.1 shows such a thermocouple. Each branch, or thermoelement, of the thermocouple must be made of a different material or the net measured voltage would always be zero.

An electrical schematic can be drawn for thermocouple analysis; each metal conductor exposed to a temperature gradient is represented as a resistor, R, and a voltage source, E; isothermal conductors would generate no EMF and would be represented simply as a resistance. The polarity of the two sources shown in Figure F.1 have been drawn to oppose each other, which may or may not be the

case in any given thermocouple - the polarity depends upon the sign of $\sigma(T)$ of each wire. Also note the resistance values of the thermoelements do not matter, since a potential is being measured, not an electrical current.

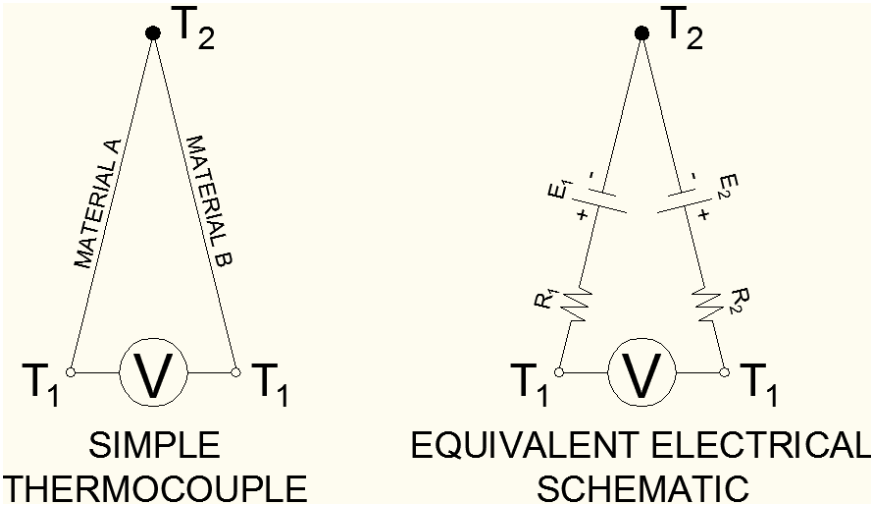

Figure F.1: A simple single-junction thermocouple.

Manufacturers characterise thermocouples by measuring the net EMF corresponding to a junction temperature, for many different temperatures (using the ITS-90 standard). A polynomial equation is developed by fitting to the resulting experimental plot. This equation allows thermocouple users to determine the junction temperature from a measured net EMF signal, and is usually of the form (ASTM Committee E20 on Temperature Measurement 1993; 165):

$$T = c_0 + c_1 E + c_2 E^2 + c_3 E^3 ... + c_n E^n, \tag{F.2}$$

where the coefficients c_i are supplied by the manufacturer, T is the temperature in °C and E is the measured net thermocouple EMF in mV. The EMF-temperature relationship described by the polynomial is based upon a simple thermocouple arrangement, as shown in Figure F.1, where the reference junction $T_1 = 0\,°\text{C}$.

In an industrial setting though, thermocouples do not have their thermoelements held at 0 °C. Furthermore the typical reference junction temperature is not constant but varies with the plant environment, thus the polynomial cannot be employed directly to determine the monitored temperature. Most electronic thermocouple readers have cold junction compensators (CJC) tuned specifically for the thermocouple type and correct for the EMF deviation which results from having $T_1 \neq 0\,°\text{C}$ (ASTM Committee E20 on Temperature Measurement 1993; 136). The compensator is placed in electrical series with the thermocouple and results in a measured net EMF as if the reference junction temperature were held at 0 °C, making the polynomial applicable.

F.2 The SCK-CEN GT differential thermocouple

The the SCK-CEN GT contains a K-type differential thermocouple manufactured by Thermocoax (SCK-CEN 2009; Tab 4). Differential thermocouples have two junctions, referred to as hot, T_H, and cold, T_C. The hot junction is embedded within the tip of the GT inner body, while the cold junction is within the metal-sheathed signal lead a few centimeters away from the instrument. Figure F.2

shows the spatial layout of the differential thermocouple as it is incorporated into the GT[1].

T_C is meant to provide a reference temperature - the pool water temperature. Since the GT's small lead wire is constantly in contact with the reactor pool water, has a very small mass per unit length and a high conductivity, the cold junction contained inside is unlikely to be heated above the pool temperature by radiation; all anlysis within this thesis assumes the cold junction temperature is equal to the reactor pool water temperature. The signal from a differential thermocouple indicates the difference $T_H - T_C$.

The thermocouple spans three regions of temperature: the reactor building, the reactor pool, T_C, and the tip of the inner body, T_H. While the GT is being irradiated in-core, the pool is warmer than the building and the inner body is warmer than the pool. Given this temperature distribution, an absolute voltage E for each conductor spanning a temperature gradient is shown in the electrical schematic of Figure F.2. Electrical resistances are of no consequence to thermocouples since thermocouples carry no current during normal operation.

The thermoelements of K-type thermocouples are nickel-chromium alloy, and nickel-aluminum alloy (ASTM Committee E20 on Temperature Measurement 1993). The positive thermoelement, KP, is an alloy that contains 89 to 90% nickel, 9 to 9.5% chromium plus smaller amounts of other constituents such as silicon, iron, carbon, manganese, cobalt and niobium. The negative thermoelement, KN, is typically composed of about 95 to 96% nickel, 1 to 1.5% silicon, 1 to 2.3% aluminum plus manganese, cobalt, iron copper and lead (ASTM E230/E230M-12 2013).

The total EMF V generated by the circuit in Figure F.2 is obtained with a sum of equation (F.1) terms, corresponding to the EMF generated in each wire:

$$
\begin{aligned}
V &= E_1 - E_2 - E_3 \\
V &= \left(\int_0^{T_R} \sigma_A(T)\,\mathrm{d}T + \int_{T_R}^{T_H} \sigma_A(T)\,\mathrm{d}T\right) - \left(\int_{T_C}^{T_H} \sigma_B(T)\,\mathrm{d}T\right) - \left(\int_{T_R}^{T_C} \sigma_A(T)\,\mathrm{d}T + \int_0^{T_R} \sigma_A(T)\,\mathrm{d}T\right) \\
V &= \int_{T_R}^{T_H} \sigma_A(T)\,\mathrm{d}T - \int_{T_C}^{T_H} \sigma_B(T)\,\mathrm{d}T - \int_{T_R}^{T_C} \sigma_A(T)\,\mathrm{d}T \qquad \text{(F.3)}
\end{aligned}
$$

where T_R is the temperature of the reactor building air. The terms integrated between 0 and T_R on the second line of the above equation are the additional EMFs which would be generated if the ends of the material A wires were 0 °C; notice in a differential thermocouple these terms are unimportant when measuring V because they cancel.

F.2.1 Calculating the EMF generated by an ideal differential thermocouple

Equation (F.3) is not practical for the calculating V in Figure F.2 since $\sigma_A(T)$ and $\sigma_B(T)$ are continuously variable with T. A practical polynomial can be derived to express V since the differential thermocouple of Figure F.2 is actually equivalent to the circuit in Figure F.3, which is expressed as:

[1]The polarity of the voltage sources drawn in the figure is not known, each has been drawn with the negative pole towards the hotter conductor end. The polarity depends upon the sign of the temperature-dependent Seebeck coefficient.

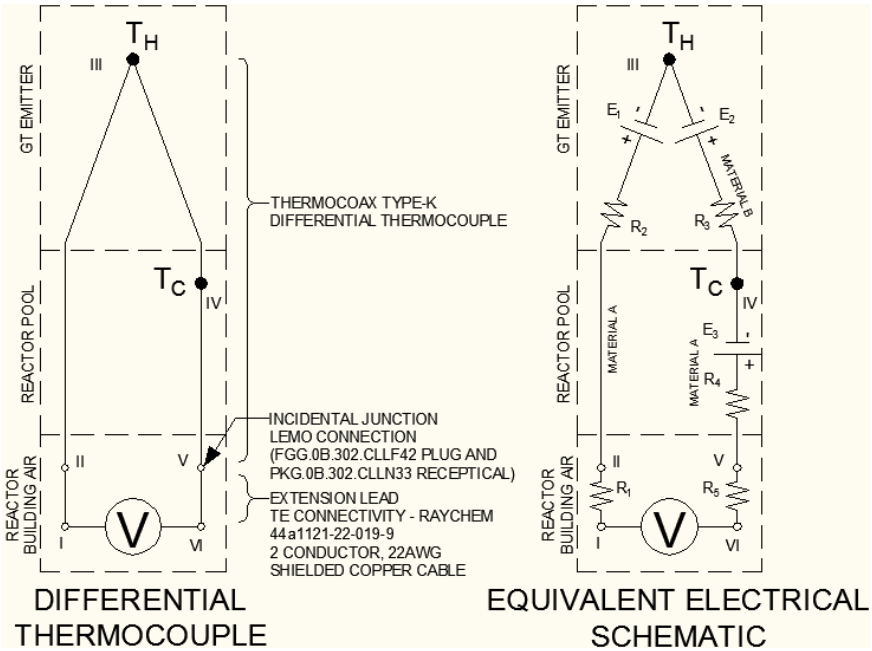

Figure F.2: The differential thermocouple used to measure the temperature difference between T_H and T_C of the SCK-CEN gamma thermometer.

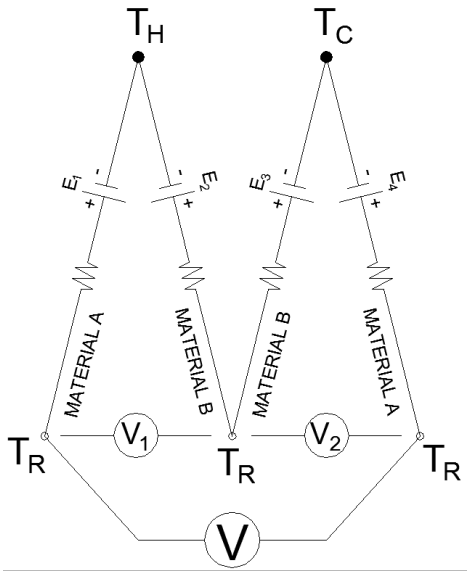

Figure F.3: A differential thermocouple made with two typical thermocouples wired in series, with reversed polarity, which is effectively identical to the circuit shown in Figure F.2.

$$
\begin{aligned}
V &= V_1 - V_2 \\
V &= (E_1 - E_2) - (E_4 - E_3) \\
V &= E_1 - E_2 + E_3 - E_4 \\
V &= \left(\int_0^{T_R} \sigma_A(T)\,\mathrm{d}T + \int_{T_R}^{T_H} \sigma_A(T)\,\mathrm{d}T\right) - \left(\int_0^{T_R} \sigma_B(T)\,\mathrm{d}T + \int_{T_R}^{T_H} \sigma_B(T)\,\mathrm{d}T\right) + \\
&\quad \left(\int_0^{T_R} \sigma_B(T)\,\mathrm{d}T + \int_{T_R}^{T_C} \sigma_B(T)\,\mathrm{d}T\right) - \left(\int_0^{T_R} \sigma_A(T)\,\mathrm{d}T + \int_{T_R}^{T_C} \sigma_A(T)\,\mathrm{d}T\right) \\
V &= \int_{T_R}^{T_H} \sigma_A(T)\,\mathrm{d}T - \int_{T_R}^{T_H} \sigma_B(T)\,\mathrm{d}T + \int_{T_R}^{T_C} \sigma_B(T)\,\mathrm{d}T - \int_{T_R}^{T_C} \sigma_A(T)\,\mathrm{d}T \\
V &= \int_{T_R}^{T_H} \sigma_A(T)\,\mathrm{d}T - \int_{T_C}^{T_H} \sigma_B(T)\,\mathrm{d}T - \int_{T_R}^{T_C} \sigma_A(T)\,\mathrm{d}T,
\end{aligned}
$$

which is the equation (F.3).

V_1 and V_2 from Figure F.3 can be each determined for known T_H and T_C temperatures with a temperature-to-voltage polynomial for K-type thermocouples; the coefficients for temperature-to-voltage polynomials are found in (ASTM E230/E230M-12 2013; Table 7). Since Figure F.3 is two identical thermocouples wired in series with reversed polarity, $V = V_1 - V_2 = V(T_H) - V(T_C)$ where $V(T_H)$ and $V(T_C)$ indicate the voltage calculated with the temperature-to-voltage polynomials. From the derivation above we know this EMF is also equivalent to V of Figure F.2, thus providing a practical polynomial for the SCK-CEN GT thermocouple.

F.2.2 CJC settings

The NI-9211 contains a CJC which is controlled by the associated virtual instrument within the LabVIEW program (Instruments 2015). No matter the CJC setting, it is assumed the CJC adds the following EMF to the measured V to compensate the circuit shown in Figure F.1:

$$EMF_{\text{correction}} = \int_0^{T_1} \sigma_A(T)\,\mathrm{d}T - \int_0^{T_1} \sigma_B(T)\,\mathrm{d}T. \tag{F.4}$$

With the "built-in" LabVIEW virtual thermocouple setting, T_1 is allowed to vary to always equal the ambient room temperature as measured by a thermistor within the NI-9211.

The EMF generated by the circuit of Figure F.2 was shown equal to $V = V_1 - V_2 = V(T_H) - V(T_C)$ where $V(T_H)$ and $V(T_C)$ indicate the voltage calculated with the temperature-to-voltage polynomials. The derivation of equation (F.3) assumed $T_R = 0\,^\circ\text{C}$. In reality $T_R \approx 22\,^\circ\text{C}$ (room temperature) and the derivation of equation (F.3) showed no cold junction compensation is desired to measure $T_H - T_C$. Therefore, to make $EMF_{\text{correction}} = 0\text{V}$ the "constant value" setting on the LabVIEW virtual thermocouple was used while defining $T_1 = 0\,^\circ\text{C}$; this is the prefered CJC setting for GT operation.

F.2.3 Conversion of GT data collected with "built-in" CJC setting

Some measurements were taken with the NI-9211 thermocouple input module set on "built-in." To utilize these data they need to be converted as if they were aquired in "constant value" mode:

1. convert the temperature read by LabVIEW to voltage V using the temperature-to-voltage polynomial of a normal K-type thermocouple

2. assume the reactor building temperature is always $T_R = 22\,^{\circ}\mathrm{C}$ (as confirmed by numerous measurements); this is a reasonable assumption since the building is climate controlled

3. calculate $EMF_{\text{correction}}$ for a normal K-type thermocouple with equation (F.4), which is simply equal to $V(22\,^{\circ}\mathrm{C})$ for a K-type thermocouple

4. reverse the correction the CJC made to the voltage in "built-in" mode with $V_{\text{corrected}} = V - EMF_{\text{correction}}$

This algorithm was confirmed by converting "built-in" data, and then comparing to "constant value" data collected while measuring the same physical quantity. All GT data collected in "built-in" mode was converted using this algorithm.

F.2.4 Systematic error

Unfortunately, the NI-9211 thermocouple input module is controlled by the LabVIEW DAQ program which uses a voltage-to-temperature polynomial for normal K-type thermocouples as shown in Figure F.1 (the coefficients of this polynomial are found in (ASTM E230/E230M-12 2013; Table 46)). Since a differential thermocouple was employed, not a normal thermocouple, a systematic error is introduced into the resulting measurements.

This error can be calculated. Figure F.4 shows the error $(\Delta T_{\text{approx}} - \Delta T)/\Delta T$ in percent for expected ranges of T_H and T_C, where $\Delta T = T_H - T_C$ and ΔT_{approx} is the value calculated by LabVIEW using equation (F.2). Note the error is always positive when $T_H > T_C$.

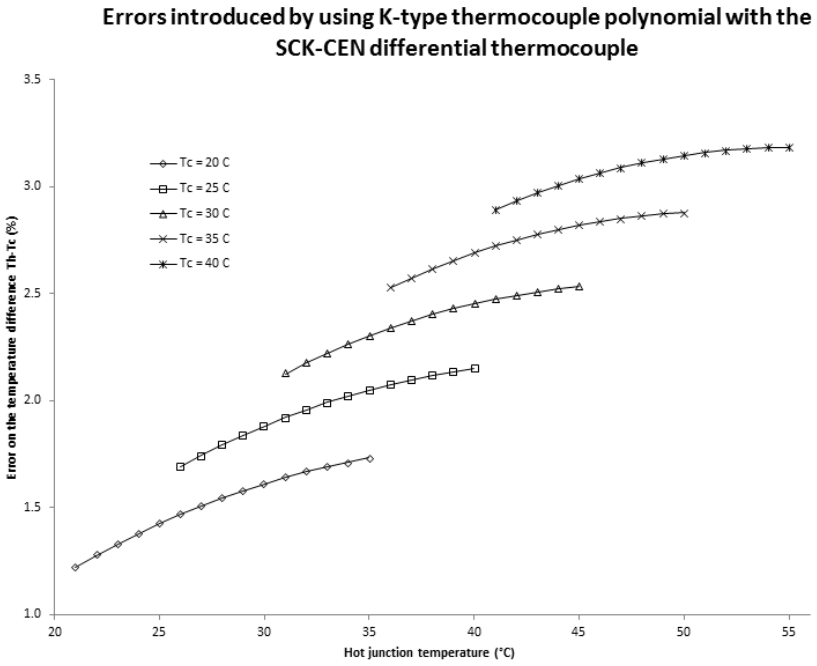

Figure F.4: Calculation of the systematic error introduced by use a regular K-type thermocouple polynomial to describe the voltage from the differential thermocouple contained within the SCK-CEN GT.

The signal ΔT_{approx} can be converted to ΔT with the following algorithm:

1. convert the temperature read by LabVIEW to voltage V using the temperature-to-voltage polynomial of a normal K-type thermocouple
2. assume the T_C is equal to the measured pool temperature; in reality T_C is probably slightly warmer since it is subjected to nuclear heating in the proximity of the GT's cold junction, as opposed to where the pool temperature is measured, approximately 2 m above the core
3. $V(T_C)$ is then calculated using T_C
4. $V(T_H)$ is obtained $V(T_H) = V + V(T_C)$
5. T_H is obtained with the voltage-to-temperature polynomial of a normal K-type thermocouple
6. the true ΔT is then calculated with $T_H - T_C$.

All GT data has been converted in this manner.

Appendix G

GT signal processing

Analysis of the recorded GT signal is meant to decompose the signal into two components: trends and noise. This section reviews the methods used to distinguish between the two components.

The voltage signal from the GT's thermocouple is classified as a non-periodic power signal in communications theory (Haykin 1989; 4). Although thermocouples provide a continuous signal, the thermocouple's output is recorded as a sequence of samples, creating a discrete time signal. All GT signals were recorded with a sample period T_s=1 s corresponding to a sampling rate of $f_s = 1/T_s$= 1 Hz (Haykin 1989; 67).

G.1 Discrete fourier transform

By the Fourier theorem, periodic signals can be constructed with a sum of an infinite number of sine waves. A periodic function in the time domain, $g(t)$, can be expressed as a function in the frequency domain, $G(f)$; both $g(t)$ and $G(f)$ contain the same information, but $G(f)$ expresses this information with the frequencies of the constituent functions, which collectively are called the spectrum of $G(f)$; $G(f)$ reveals the frequencies of the constituent functions even when they are obscured within $g(t)$.

Fourier transforms are often employed in signal processing to obtain $G(f)$ from $g(t)$ for the purpose of searching for periodic signals hidden within $g(t)$; since the GT signal satisfies Dirichlet's conditions, which indicates it to be Fourier transformable, this method has been applied to the GT signal (Haykin 1989; 22).

Discrete-time signals are receptive to treatment with a discrete Fourier transform (DFT). In most cases the fast Fourier transform (FFT) is employed, which is an algorithm allowing n number of sample points to be processed with practical speed, when n is large (MathWorks 2015c). A MatLab program has been written to process the GT signal with a FFT. Using a GT data set spanning 11.7 hrs, n=42,223, recorded on Friday July 26, 2013. This time span was selected for its apparent smoothness, aside from the usual noise, and very small shim/safety rod perturbations resulting from normal operations to maintain reactor power.

The n data points were loaded into a MatLab vector with elements x_j, indexed by $0 \leq j \leq n-1$. The DFT creates an associated vector with elements y_p made of complex numbers, indexed by $0 \leq p \leq n-1$. Each complex number y_p is calculated with an equation which is a trapezoidal-rule approximation to the Fourier transform integral (Haykin 1989; 71). The DFT equation employed in MatLab is (MathWorks 2015b):

$$y_{p+1} = \sum_{j=0}^{n-1} \omega^{jp} x_{j+1}$$

where w is:

$$\omega = \mathrm{e}^{-2\pi \mathrm{i}/n},$$

i is the imaginary unit.

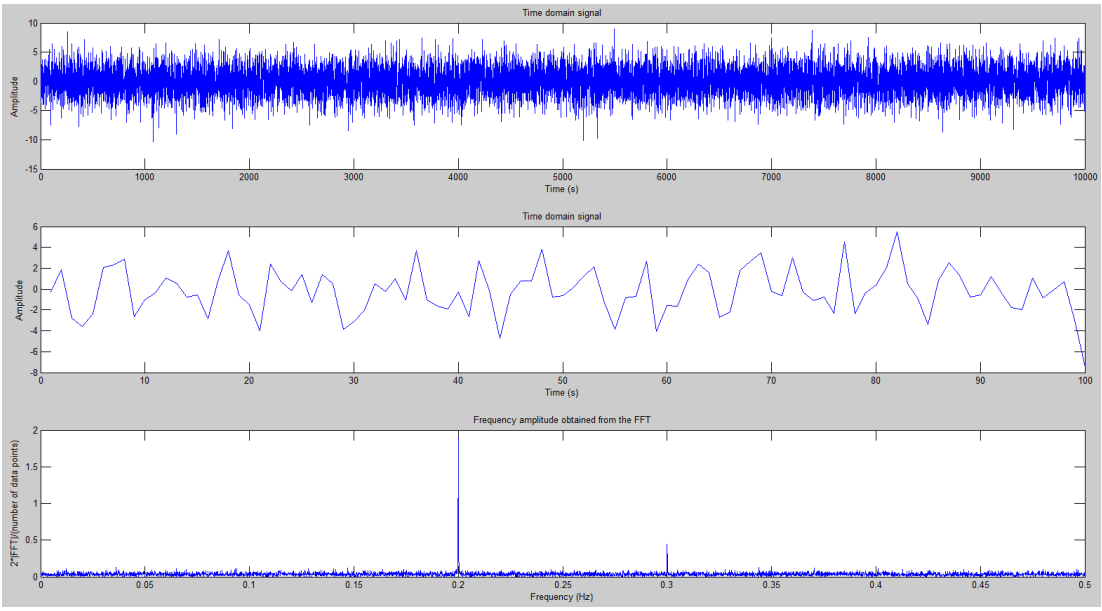

Figure G.1: Time domain signal of $y = 2\sin(2\pi 0.2t) + 0.5(2\pi 0.3t)$ + random noise and the corresponding amplitude spectrum.

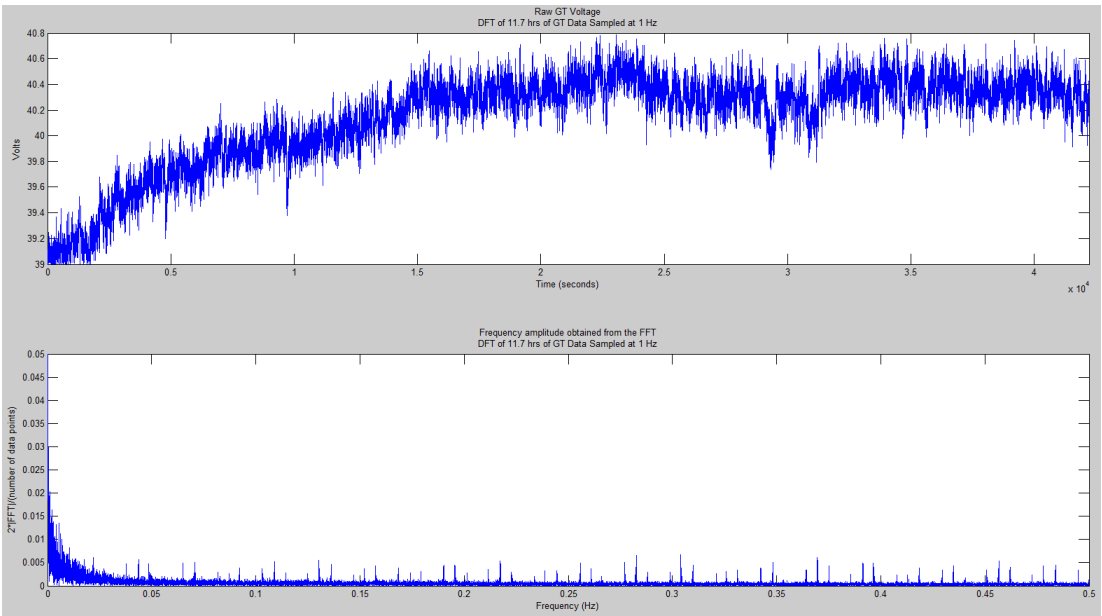

Figure G.2: The raw GT signal and the corresponding amplitude spectrum.

Each complex value y_p measures the amount of the frequency $f = p*(f_s/n)$ present in the sample

data (MathWorks 2015b). For example, the point y_p when $p = (42223 + 1)/2 = 21112$ is a measure of the frequency $\approx f_s/2$. By the sampling theorm, the 1 Hz sampling frequency is not capable of detecting component frequencies in x_j greater than 0.5 Hz so the DFT values $y_{p>21112}$ need not be examined (Haykin 1989; 70); for real x_j values, the series y_p is symmetric about y_{21112}, called the Nyquist point.

To visualize the DFT, the amplitude spectrum $|y_p|$ of the signal x_j is plotted against the frequency f (Haykin 1989; 24). Figure G.1 shows an example case using MatLab's FFT function, where the original signal $y = 2\sin(2.0\pi 0.2t) + 0.5(2\pi 0.3t) +$ random noise is plotted on the top two frames over different time spans to show the structure of the raw signal. The amplitude spectrum is shown in the bottom frame; the vertical axis values are equal to $2 * |y_p| /n$ (MathWorks 2015a). The amplitudes of the basis functions are clearly visible, although their amplitudes are not equal to exactly 2.0 and 0.5 because of the noise added to the system. The value y_0, corresponds to $f = 0$, and is omitted because it is equal to the sum of the values x_j.

Figure G.2 presents the GT signal's amplitude spectrum which does not show evidence of a periodic function hidden within the raw GT signal. The relatively flat region $0.05 \leq f \leq 0.5$ is considered white noise, likely resulting from random electron motion within the GT's electrical circuit (Smith 1998; 172); this noise is often called thermal noise (Haykin 1989; 604). The low frequency peaks over the range $f < 0.05$ results from the $1/f$ noise found in most measured signals (Smith 1998; 172).

G.2 Smoothing the raw GT signal

Valuable information within the GT signal data may be obscured by noise, so the GT signal must be processed to reveal the underlying features for enhanced presentation. The GT signal itself is a univariate time-series, a data set recording a single variable with time, univariate because all the data were collected at a constant frequency of 1 Hz.

Time series are often made of three superimposed components, i) a trend, ii) a "seasonal" component, and iii) a random effect (Kendall 1973; 16). The physical first principles of in-core gamma heating don't imply a seasonal or periodic component is likely to be observed in the presence of constant neutron flux; the same principles foreshadow the GT signal should contain a trend, therefore all processing of the GT signal must carefully reduce the random component to reveal the trend of interest (P.J. Brockwell 2002; 23).

Smoothing methods are often used to make trends more conspicuous and often involve the least squares fitting of a polynomial, or employing a simple moving average. Simple moving averages are easily calculated but weigh past observations with the same weight as the current observation, which can obscure the onset of a trend. Another method, exponential smoothing, weighs past observations with exponentially decreasing weights to give more significance to the most recent observations which highlights trends better than uniform weights (NIST 2015b).

A few smoothing techniques were tested on a noisy GT data set representative of typical raw GT data. This noise was superimposed on a GT response to a step change in heating corresponding to a 15 °C drop, as modelled by equation (5.19) with $\tau = 18.4$ s; this is thought to be a close representation of the most drastic change the GT signal can make. Figure G.3 shows the raw signal and single exponential smoothing (NIST 2015c):

$$S_t = \alpha y_{t-1} = (1 - \alpha)S_{t-1} \qquad 0 < \alpha \leq 1 \qquad t \geq 3,$$

where t is the time index, y_t the original GT data, S_t the smoothed value and α the smoothing constant. Figure G.3 (L) shows the 12 s time delay introduced by the smoothing, which is shown in detail in Figure G.3 (R). The smoothing and the delay reduce with increased α values; little optimization of α has been investigated.

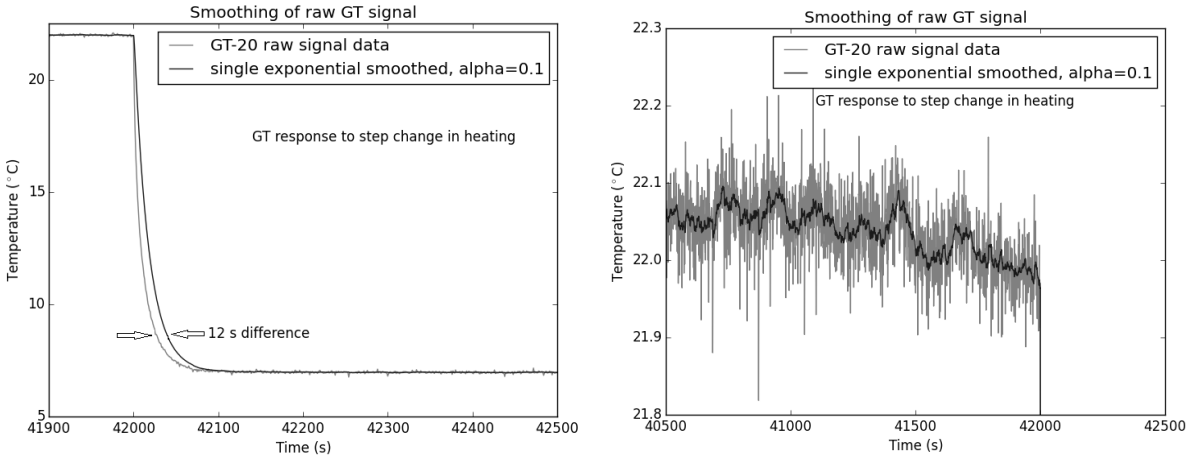

Figure G.3: (L) signal smoothing of a step change in GT nuclear heating; (R) a detail of the step change "cliff edge."

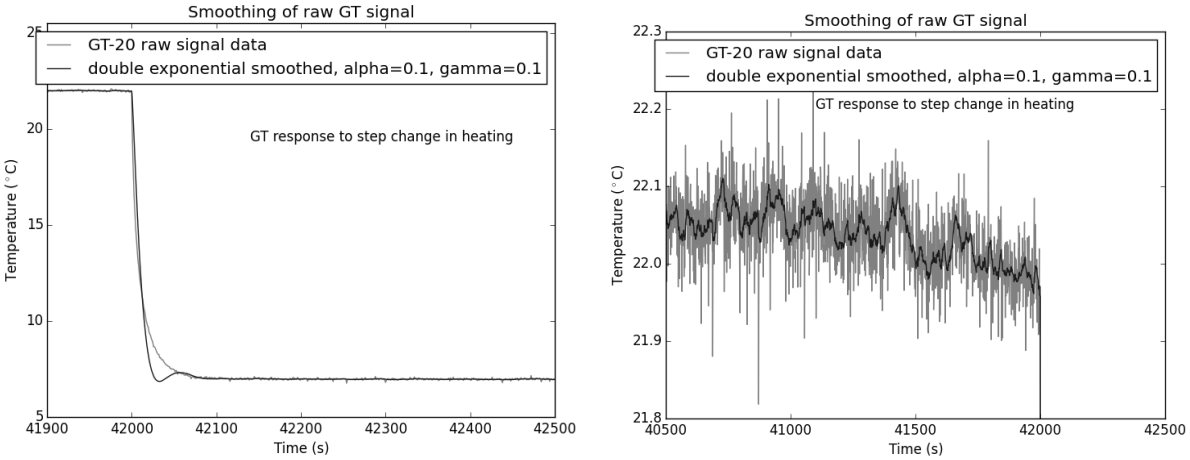

Figure G.4: (L) signal smoothing of a step change in GT nuclear heating; (R) a detail of the step change "cliff edge."

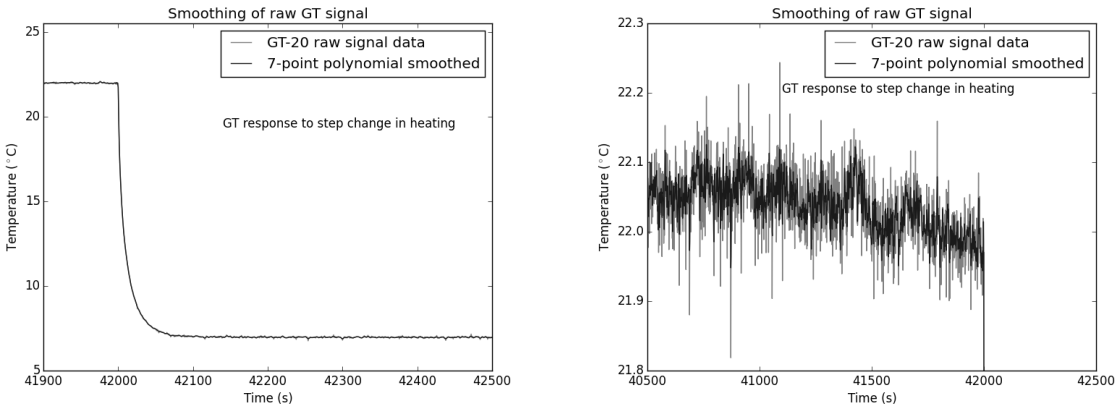

Figure G.5: (L) signal smoothing of a step change in GT nuclear heating; (R) a detail of the step change "cliff edge."

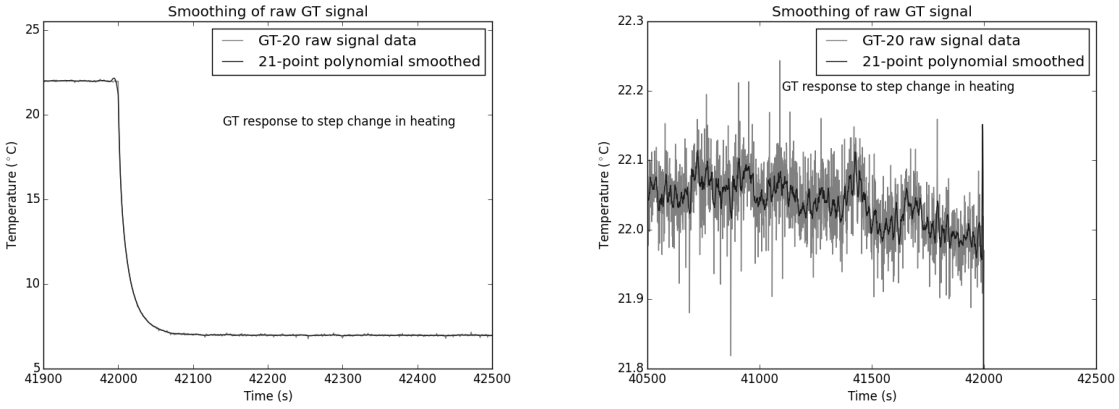

Figure G.6: (L) signal smoothing of a step change in GT nuclear heating; (R) a detail of the step change "cliff edge."

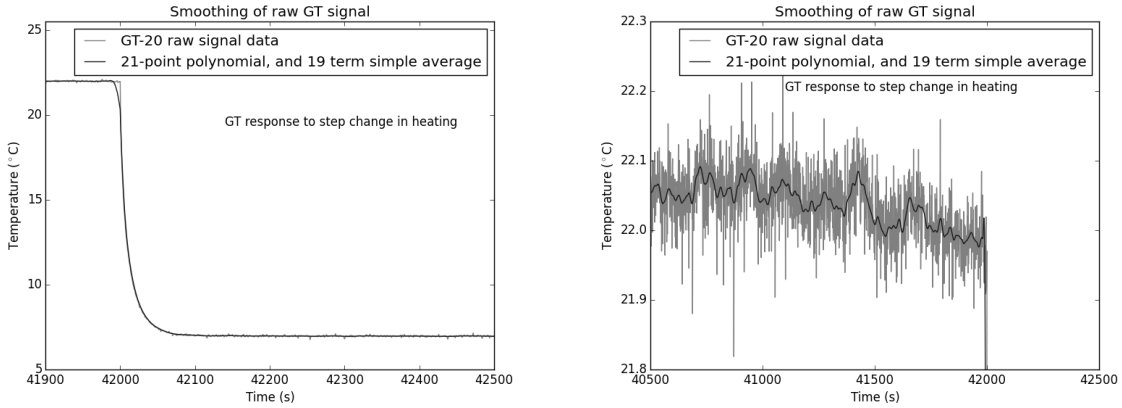

Figure G.7: (L) signal smoothing of a step change in GT nuclear heating; (R) a detail of the step change "cliff edge."

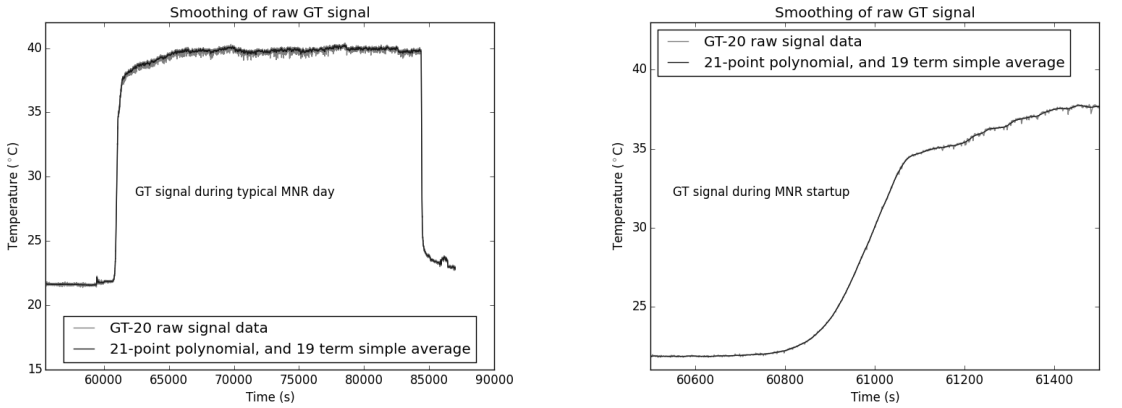

Figure G.8: (L) signal smoothing of data from a typical MNR day; (R) a detail of the MNR start-up.

Double exponential smoothing employs two equations with two smoothing constants, α and γ (NIST 2015d):

$$S_t = \alpha y_t + (1-\alpha)(S_{t-1} + b_{t-1}) \qquad 0 < \alpha \leq 1$$
$$b_t = \gamma(S_t - S_{t-1}) + (1-\gamma)b_{t-1} \qquad 0 < \gamma \leq 1,$$

where the initial values for $t = 1$ are:

$$S_1 = y_1$$
$$b_1 = \frac{1}{3}((y_2 - y_1) + (y_3 - y_2) + (y_4 - y_3))$$

With damping of $\alpha = 0.1$ and $\gamma = 0.1$ double exponential smoothing isn't as good as single, and over-shoots step changes, but has far less lag, as shown in Figure G.4.

A 7 point smoothing polynomial (using the element being smoothed and 3 elements on each side) was found to smooth as well as the double exponential, with none of the lag, see Figure G.5. Better yet at smoothing, is a 21 point smoothing polynomial in Figure G.6 (Kendall 1973; 31):

$$S_t = \frac{1}{3059}[-171y_{t-10} - 76y_{t-9} + 9y_{t-8} + 84y_{t-7} + 149y_{t-6} + 204y_{t-5} + 249y_{t-4} + 284y_{t-3} +$$
$$309y_{t-2} + 324y_{t-1} + 329y_t + 324y_{t+1} + 309y_{t+2} + 284y_{t+3} + 249y_{t+4} +$$
$$204y_{t+5} + 149y_{t+6} + 84y_{t+7} + 9y_{t+8} - 76y_{t+9} - 171y_{t+10}]$$

Simple moving averages replace the experimental data y_t with an averaged value S_t (P.J. Brockwell 2002; 25):

$$S_t = (2q+1)^{-1} \sum_{j=-q}^{q} y_{t-j} \qquad q+1 \leq t \leq n-q.$$

With small q averaging was found to provide very good response to trends (without lag or overshoot) but little smoothing. Increasing q increased the smoothing effect but rounded the "cliff edge" of a sharp change in signal.

To obtain the most amount of smoothing without introducing significant delay or over-shoot, experimenting showed using the 21 point smoothing polynomial on the raw data, and then a simple moving average, worked best. Given $\tau = 18.4$ s, a simple 18 s span (q=9) moving average was employed. The simple average's "cliff edge" rounding is thought to be acceptable since the long-term trends are of the most interest to this study; Figure G.7 presents the smoothing resulting over the GT step change, and Figure G.8 the smoothing of a typical MNR day and start-up. This scheme is employed with all GT data in this thesis.

G.3 GT signal noise and error

Every transducer produces noise of some kind. The signal-to-noise ratio y_t/s is used to quantify the noise.

Like most experimental data the true variance σ^2 of the GT data is unknown and must be approximated with the sample variance s^2. To calculate the sample variance the true value of the signal must be estimated. However, the usual method of approximating the true value of the signal with the sample mean cannot be used since the data is a time-series with a trend; the experimental

data are not multiple samples of a single variable y, but a collection of single samples of the dependent variable $y(t_i)$ at multiple time steps, t_i, each with a different true value.

In such a situation a function is fit to the experimental data to estimate the true value at t_i (Taylor 1982; 157). Once a function $f(t_i)$ with m fit paremters has been fit (see the methods in section H) to approximate the true value of the signal of N points, the true variance is approximated with (Taylor 1982; 120):

$$\sigma^2 \cong s^2 = \frac{1}{N-m} \sum_i \left[y_i - f(t_i) \right]^2 .$$

Within this thesis, all cases satisfied $N >> m$ so the above equation is simply equal to the root-mean-square (RMS) error.

Appendix H

Curve fitting methodology

Curve fitting in this thesis was accomplished with the software package gnuplot which uses the nonlinear least-squares (NLLS) Marquardt-Levenberg algorithm to fit a user-defined function to a data set (Williams and Kelley 2015; 62). This section discusses the details of the fitting process.

H.1 Curve fitting with gnuplot

The gnuplot package was selected because it gives the user the ability to dictate the function to be fit to the data; other software packages require the user to select from a fixed set of formulae.

The following practical steps were used to obtain quality solutions:

Non-smooth data was smoothed before fitting. See the smoothing methods detailed in section G.2.

As few exponential terms as possible were used. All fitting processes started with an equation of a single exponential term; more were added when it was clear at least one more exponential term was required.

First estimates of fit parameters were obtained by inspection of a data plot. Reasonable estimates of all fitting parameters are required before the program will converge to an acceptable solution without fatal errors, or without becoming stuck in local minimums; estimates of magnitudes and decay constants were obtained by visual inspections.

Used a very small convergence criterion. Fitting optimization ceased when the difference between sum of squared residuals of successive iterations was smaller than $fit\_limit = 1.0 \times 10^{-7}$; this definition is two orders of magnitude smaller than the default (Williams and Kelley 2015; 73).

Always checked the fit with an additional exponential term. Once an equation appeared to fit visually and with good statistics, one more exponential term was added to check that the resulting statistics didn't improve.

All residuals were plotted. Plotting this data is a very good visual quality check; it also aids in determining where most of the "sum of squares of residuals" variable is accumulated for possible improvement in the fit.

Final fits were closely examined for fit. The final fits were checked visually and statistically.

The data files given to gnuplot were always formatted with 3 columns: time, data and absolute data error.

H.2 Statistical evaluation of fit

Gnuplot uses a reduced χ^2 evaluation of the fit function (Williams and Kelley 2015; 73). Testing with χ^2 involves a comparison between the value of the fit fuction $f(x_i)$ and the corresponding datum point y_i, for all i. The basic formula of reduced χ^2 is (Taylor 1982; 229):

$$\tilde{\chi}^2 = \frac{1}{d}\chi^2 = \frac{1}{d}\sum_{i=1}^{n}\left(\frac{y_i - f(x_i)}{\sigma_i}\right)^2 \tag{H.1}$$

where n is the number of data points and d is the degrees of freedom, equal to the number of data points less the number of parameters being fitted (Williams and Kelley 2015; 66).

The collected datum y_i is one sample of a population normally distributed on the position x_i, with a distribution described by σ_i. χ^2 is simply a sum of terms comparing the devation between y_i and $f(x_i)$ and the standard deviation σ_i. The difference $y_i - f(x_i)$ will be large for a poor fit at position x_i, and small for a good fit; for a relative evaluation of this difference, the difference is compared to σ_i. For a "good fit" χ^2 should be close to d, thus $\tilde{\chi}^2$ should be close to 1.0 (Taylor 1982; 229)

Following fitting, gnuplot produces a report of the evaluation of the fit, which presents: the sum of squares of the residuals, RMS of the residuals, the $\tilde{\chi}^2$ value (named the "variance of the residuals"), uncertainties associated with the fit parameters, and a correlation matrix of the fit parameters filled with correlation coefficients.

Within this thesis the $\tilde{\chi}^2$ of all fits were orders of magnitude lower than 1.0. The RMS of the residuals were usually on the order of the standard deviation of the data being fit.

The correlation matrix gives an indication of the indepdendence of the fit parameters to each other. When an additional exponential term in the fit equation proves to be unnecessary, its associated fit parameters have often been found to be perfectly correlated (as indicated by a correlation value of 1.0 or -1.0) with other parameters within the equation, providing further proof the additional fit parameters are superfluous. Therefore, the correlation matrix was watched in all cases for 1.0 or -1.0 values. All fit parameters were found to be correlated to some degree.

The relative uncertainties associated with the fit parameters were found to be very small when both the RMS of the residuals and the $\tilde{\chi}^2$ were small.

H.3 Determining the uncertainties of the fitting parameters

Following the fitting of a function, gnuplot presents the uncertainties of the fit parameters but no references could be found which describes how they are calculated. To test gnuplot and the curve fitting methods, test data sets were made over the domain [0,50000] seconds with the following signal:

$$f(t) = a_1 + a_2(1 - \mathrm{e}^{\lambda_2 t}) + a_3(1 - \mathrm{e}^{\lambda_3 t}) + a_4(1 - \mathrm{e}^{\lambda_4 t}), \tag{H.2}$$

where all constants were defined to make $f(t)$ comparable in magnitude and shape to a GT signal observed during MNR daily operation.

Two test data sets were created with equation (H.2), both made of the smooth data as dictated by equation (H.2), but in one case the associated data uncertainty σ_i supplied to gnuplot is double the other. Fitting with gnuplot to both cases revealed: 1) both cases resulted in convergence to the correct fit parameters, 2) the $\tilde{\chi}^2$ was smaller in the case with larger uncertainty, as predicted by equation (H.1), and 3) the uncertainties associated with the fit parameters were unchanged between cases, thus gnuplot calculates fit parameter uncertainties with the data itself rather than the uncertainty σ_i provided in the data file. This experimentation shows the σ_i value is used in gnuplot only in the evaluation of $\tilde{\chi}^2$ to evaluate the fit, not in the calculation of the fit parameter uncertainties.

Another two test data sets were created with equation (H.2), both with random noise superimposed on the smooth $f(t)$ signal; the random noise of one data set (and the associated σ_i) was quadruple the other. The fit parameter uncertainties associated with the noisy data set were significantly larger. Thus, the smoothing processes discussed in section G.2 reduces the fit parameter uncertainties. This is problematic because fitting to smoothed data results in fit parameter uncertainties smaller than would result with the unsmoothed data, even if σ_i is representative of the unsmoothed data.

Gnuplot's predictions of fit parameter uncertainties have also been found to be unreasonably large with noisy signals.

Thus, for multiple reasons gnuplot's fit parameter uncertainties cannot be used and another method of calculating these uncertainties is required.

One tested method examines the variation of χ^2 with changes in a single fitting parameter (P.R. Bevington 1992; 147). If all fitting parameters except one, a_j, are assumed constant, χ^2 is then a function of a_j alone and a parabola can be fit to a plot of $\chi^2(a_j)$ using three values of a_j: a_{j1}, a_{j2} and a_{j3} and their three corresponding values of χ^2, $\chi^2_1 = \chi^2(a_{j1})$, $\chi^2_2 = \chi^2(a_{j2})$ and $\chi^2_3 = \chi^2(a_{j3})$; each χ^2 value is separated by Δa_j. An optimum parameter value of a_j can be calculated with:

$$a'_j = a_{j3} - \Delta a_j \left[\frac{\chi^2_3 - \chi^2_2}{\chi^2_1 - 2\chi^2_2 + \chi^2_3} + \frac{1}{2} \right]. \tag{H.3}$$

The above equation provides estimates of a'_j which concur with those of gnuplot. The values of a'_j obtained with the gnuplot fit have had their uncertainties calculated with (P.R. Bevington 1992; 146):

$$\sigma_j = \sqrt{2 \left(\frac{\partial^2 \chi^2}{\partial a_j^2} \right)^{-1}}, \tag{H.4}$$

where the second derivative term has been estimated with the finite difference approximation centered on a'_j (Cheney and Kincaid 1999; 180):

$$\frac{\partial^2 \chi^2}{\partial a_j^2} = \frac{1}{(\Delta a_j)^2} [\chi^2(a'_j + \Delta a_j) - 2\chi^2(a'_j) + \chi^2(a'_j - \Delta a_j)].$$

A definition of $\Delta a_j = 0.05(a'_j)$ has been used; all the above equations have shown not to vary with a doubling of the size of Δa_j. However tests showed predictions of σ_j are unreasonably small given the size of σ_i. Therefore this "variation of χ^2" method has not been used.

Instead the uncertainties presented in Table 6.6 have been obtained by a two-step fitting method: first to y_i to obtain estimates of a, b and λ, then to $y_i - \sigma_i$ to see the resulting difference in a, b and λ. This difference is the uncertainty presented in Table 6.6.

H.3.1 Tests of method

Two cases were created with the test data set by equation (H.2): one with the smooth $f(t)$ signal, another with superimposed random noise. The random noise had a standard deviation of 0.1 °C, which is a magnitude roughly equivalent to the GT signal noise.

Curve fitting with the smooth test signal, using the known fit parameters a_i and λ_i as first guesses, showed gnuplot agreed with the first guesses. With the noisy test signal, using the known fit parameters a_i and λ_i as first guesses, gnuplot suggested fit parameters which differed from the "true" initial guesses by only hundreths of a percent.

H.3.2 The problem of multiple sets of fit parameters

Fitting to the noisy test data set revealed the existance of sets of constants a_i and λ_i which differ from the "true" set but which provided as good a statistical fit. This is a problem: curve fitting to two noisy data sets with identical and unknown underlying trends may result in two different sets, leading to an observer concluding the underlying trends differ, or identical noisy data sets in the possession of two researchers may not be able to reproduce each other's fit parameters.

To avoid these problems these parameters must be determined methodically; the following sections discuss two methods.

Group stripping of data

Exponential functions with a single term, of the form:

$$F(t) = b_1 \mathrm{e}^{-\lambda_1 t},$$

appear linear when their natural log is plotted, where their slope is equal to the negative decay constant:

$$\begin{aligned} m &= \frac{y_2 - y_1}{x_2 - x_1} = \frac{Y_2 - Y_1}{X_2 - X_1} \\ m &= \frac{\ln(b_1 * \mathrm{e}^{-\lambda_1 t_2}) - \ln(b_1 * \mathrm{e}^{-\lambda_1 t_1})}{t_2 - t_1} \\ m &= \frac{\ln(b_1) + \ln(\mathrm{e}^{-\lambda_1 t_2}) - \ln(b_1) - \ln(\mathrm{e}^{-\lambda_1 t_1})}{t_2 - t_1} \\ m &= \frac{-\lambda_1 t_2 + \lambda_1 t_1}{t_2 - t_1} = \frac{-\lambda_1 (t_2 - t_1)}{t_2 - t_1} = -\lambda_1. \end{aligned}$$

where $X_i = t_i$ and $Y_i = \ln(F(t_i)) = \ln(b_1 * \mathrm{e}^{-\lambda_1 t_i})$.

Plotting exponential functions with multiple terms of the following form:

$$F(t) = b_1 \mathrm{e}^{-\lambda_1 t} + b_2 \mathrm{e}^{-\lambda_2 t} + ...,$$

on a X, Y plane appear non-linear unless one of the terms dominates, which usually happens when t is large. Knowing this behavior, Y of the GT heating data (post-shutdown) can be plotted to obtain first estimates of the group parameters λ_i and b_i.

At large t one exponential term will dominate as the others reduce in magnitude; with a single dominant term the function will appear linear with a slope equal to the negative of the dominant group's decay constant λ_i and a Y intercept equal to the natural log of the dominant group's coefficient $\ln(b_i)$ according to the following formula which is similar in form to $y = mx + b$:

$$\ln(F(t)) = \ln(b_1 \mathrm{e}^{-\lambda_1 t}) = -\lambda_1 t + \ln(b_1).$$

The exponential term (associated with one delayed gamma precursor group) can be subtracted or "stripped" from the GT data, and the process repeated with the resulting data to produce another estimate of another group's parameters (Valente 1963; 249).

The group parameters λ_i and b_i which result from this "stripping" process can be used as first estimates of the fit parameters, and make obtaining first estimates methodological; such a preliminary graphical analysis was also used by Keepin for the same purpose (Keepin *et al.* 1957; 7).

The *xrange* variable in gnuplot allows the user to curve fit to the data within specified sections of data. This feature was used to fit to sections of a data series with unique local features before fitting to the entire data set.

Fitting to smooth data

Experimenting with smooth data sets created with functions of known coefficients has demonstrated gnuplot's Marquardt-Levenberg algorithm converges to the correct coefficients, independent of the coefficients' initial guesses. Since this method is simpler than the stripping method, all coefficients presented in this thesis have been obtained by fitting to smooth data sets.

Appendix I

Instrument rig design

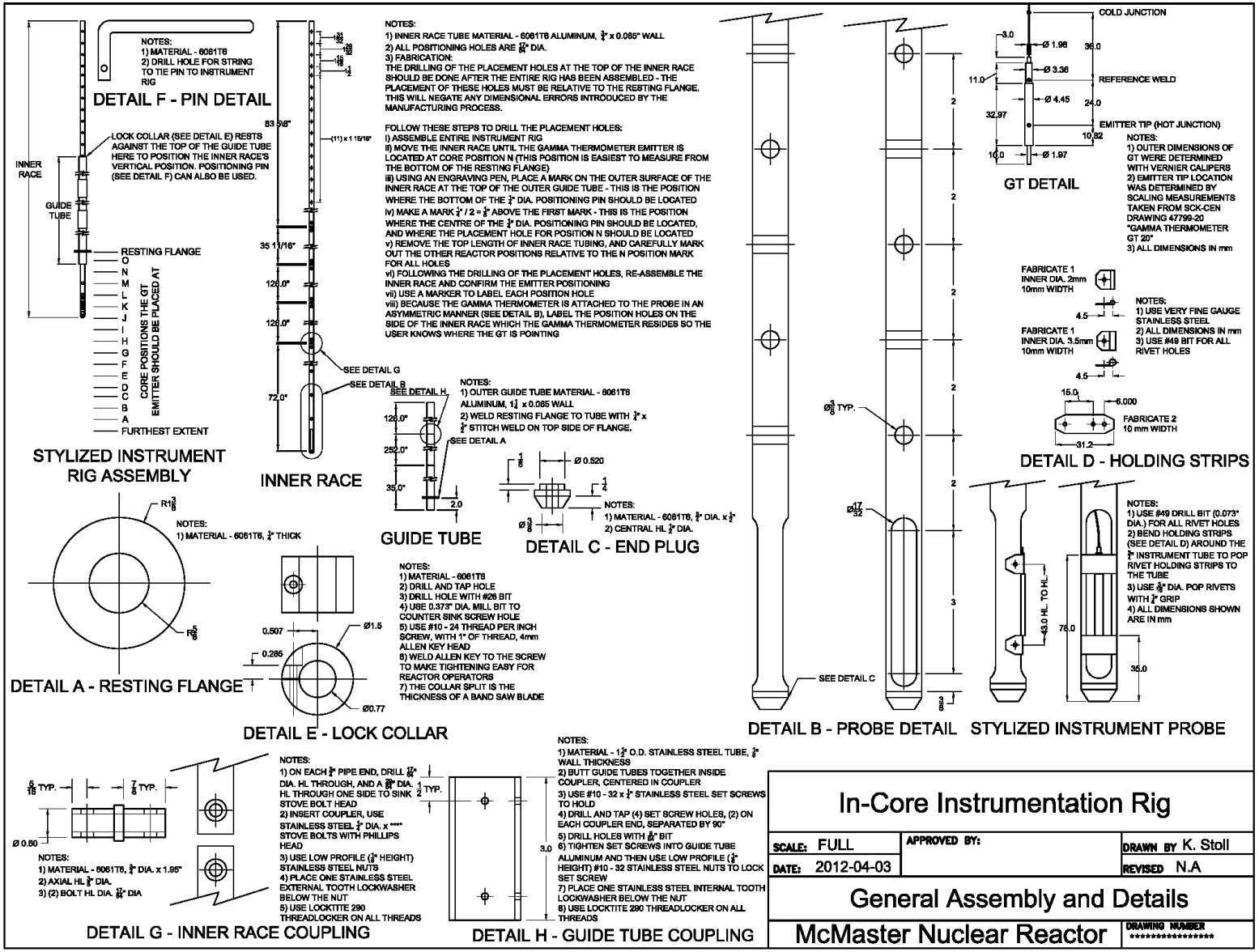

Figure I.1: Production drawing of the intrument rig.

Bibliography

(2015). Python 2.7.10. Technical report, Python Software Foundation.

Aarrestad, O. (1993). OECD Halden Reactor Project: Instrumentation Capabilities at Halden. Technical Report HWR-351, Institutt for Energiteknikk, Halden.

Amharrak, H., DiSalvo, J., Thiollay, N., Roche, A., Lyoussi, A., Bignan, G., and Reynard, C. (2010). Thermoluminescent detectors measurements in critical mock-up: Monte-Carlo calculations of cavity phenomena. In *2009 1st International Conference on Advancements in Nuclear Instrumentation, Measurement Methods and their Applications (ANIMMA)*, Piscataway, NJ, USA. IEEE.

Amharrak, H., DiSalvo, J., Lyoussi, A., Roche, A., Masson-Fauchier, M., Bosq, J., and Carette, M. (2011). Analysis and recent advances in gamma heating measurements in minerve facility by using tld and osld techniques. In *Proceedings of International Conference ANIMMA*.

Amharrak, H., DiSalvo, J., Lyoussi, A., Roche, A., Masson-Fauchier, M., Bosq, J., and Carette, M. (2012). Analysis of gamma-ray dosimetry experiments in the zero power MINERVE facility. *Journal of ASTM International*, **9**(3).

Amharrak, H., DiSalvo, J., Lyoussi, A., Carette, M., and Reynard-Carette, C. (2014). State of the art on nuclear heating in a mixed neutron-gamma field in research reactors. *Nuclear Inst.and Methods in Physics Research, A*, **749**(57-67).

Armstrong, A. (2013). private communication.

ASTM Committee E20 on Temperature Measurement (1993). Manual on the Use of Thermocouples in Temperature Measurement. Technical report, Philadelphia.

ASTM E230/E230M-12 (2013). Standard Specification and Temperature-Electromotive Force (emf) Tables for Standardized Thermocouples. Technical Report Volume 14.03, ASTM Int., Philadelphia.

Avelar, J. (2013). private communication.

Batistoni, P., Angelone, M., Petrizzi, L., and Pillon, M. (2004). Neutronics benchmark experiment on tungsten. In *Proceedings of the 11th Conference on Fusion Research, December 7, 2003 - December 12*, volume 329-333, Kyoto, Japan. Elsevier.

Beiser, A. (1995). *Concepts of Modern Physics*. McGraw-Hill, New York, 5th edition.

Bell, G. I. and Glasstone, S. (1970). *Nuclear Reactor Theory*. Litton Educational Publishing, New York.

Bernnat, W. and Siegel, K. (1987). Determination of local power in a PWR core based on measured gamma thermometer signals. *Kerntechnik*, **51**(1).

Blanchet, D. (2006). *Développements méthodologiques et qualification de schémas de calcul pour la modalisation des échauffements photoniques dans les dispositifs expérimentaux du futur réacteur d'irradiation technologique Jules Horowitz (RJH).* Ph.D. thesis, Université Blaise Pascal.

Blanchet, D., Blaise, P., D'Aletto, C., Salvo, J. D., and et al. (2005). Analysis of gamma-ray dosimetry experiments for the validation of the JHR nuclear heating calculation. In *Proc. Mathematics and Computation, Supercomputing, Reactor Physics and Nuclear and Biological Applications; American Nuclear Society.*

Blanchet, D., Huot, N., Sireta, P., Serviere, H., Boyard, M., Antony, M., Laval, V., and Henrard, P. (2008). Qualification of a gamma-ray heating calculation scheme for the future Jules Horowitz material testing reactor (RJH). *Annals of Nuclear Energy*, **35**(4).

Cacuci, D. (2010). *Handbook of Nuclear Engineering.* Springer, New York, USA.

Carcreff, H., Salmon, L., and Courtaux, C. (2013). First in-core measurement results obtained with the innovative mobile calorimeter CALMOS inside the OSIRIS material testing reactor. *IEEE Transactions on Nuclear Science.*

CEA (2013). `http://www.cad.cea.fr/rjh/Add-On/osiris\_gb.pdf`.

CEA (2016). Technical Report Internal CEA Report.

Chadwick, M. B., Herman, M., Oblozinsky, P., Dunn, M. E., Danon, Y., and Kahler, A. C. (2001). ENDF/B-VII.1 Nuclear Data for Science and Technology: Cross Sections, Covariances, Fission Product Yields and Decay Data. Technical Report LA-UR 11-05121, Los Alamos National Laboratory.

Cheney, W. and Kincaid, D. (1999). *Numerical Mathematics and Computing.* Brooks/Cole Publishing Company, Pacific Grove, 4th edition.

Day, S. (2001). MNR reference core for SAR. Technical Report MNR Technical Note 010705, McMaster Nuclear Reactor.

Day, S. (2002). Power-Peaking Factors in MNR. Technical Report MNR Technical Note 1999-07, McMaster Nuclear Reactor.

Demaziere, C., Pazit, I., Andersson, T., Severinsson, B., and Ranman, T. (2003). Analysis of an MTC noise measurement performed in Ringhals-2 using gamma-thermometers and in-core neutron detectors. *Progress in Nuclear Energy*, **43**(1-4).

Diop, C. M., Petit, O., Dumonteil, E., Hugot, F. X., Lee, Y. K., Mazzolo, A., and Trama, J. C. (2006). TRIPOLI-4: A 3D continuous-energy Monte Carlo transport code. In *2006 Winter Meeting of the American Nuclear Society*, volume 95, Albuquerque, NM, United states. American Nuclear Society.

Duderstadt, J. and Hamilton, L. (1976). *Nuclear Reactor Analysis.* John Wiley Sons, USA.

Durkee, J., James, M., McKinney, G., Waters, L., and Goorley, J. (2012). The MCNP6 delayed-particle feature. Technical Report LA-UR-12-00283, Los Alamos National Laboratory.

Evans, R. (1955). *The Atomic Nucleus.* McGraw-Hill, New York, USA.

Fourmentel, D., Reynard-Carette, C., Lyoussi, A., Villard, J., Malo, J., Carette, M., Brun, J., Guimbal, P., and Zerega, Y. (2013). Nuclear heating measurements in material testing reactor: a comparison between a differential calorimeter and a gamma thermometer. *IEEE Transactions on Nuclear Science*, **60**(1).

Gilmore, G. and Hemingway, J. (1995). *Practical Gamma-Ray Spectrometry*. John-Wiley Sons, Chichester, UK.

Glascock, M. (1996). Tables for Neutron Activation Analysis. Technical report, University of Missouri.

Goorley, T., James, M., Booth, T., Brown, F., and Bull, J. (2012). Initial MCNP6 release overview. *Nuclear Technology*, **180**.

Haaland, A., Devold, H., and Tosi, V. (1991). In-pile performance of miniaturised gamma thermometers. Technical Report HWR-313, OECD Halden Reactor Project.

Harris, R. (1999). *Nonclassical Physics : Beyond Newton's View*. Addison Wesley Longman, Menlo Park, USA.

Haykin, S. (1989). *An Introduction To Analog and Digital Communications*. John Wiley Sons, USA.

Herman, M. (2014). Sigma: Evaluated Nuclear Data File (ENDF) Retrieval Plotting. `http://www.nndc.bnl.gov/sigma/`, NNDC Brookhaven National Laboratory.

Herman, M. and Trkov, A. (2009). ENDF-6 Formats Manual: Data Formats and Procedures for the Evaluated Nuclear Data File ENDF/B-VI and ENDF/B-VII. Technical Report BNL-90365-2009, Cross Sections Evaluation Working Group.

Herminghuysen, K. and Blue, T. (1994). Development and evaluation of a neutron-gamma mixed-field dosimetry system based on a single thermoluminescence dosimeter. In *Eighth Symposium on Radiation Measurements and Applications*, volume 353, Netherlands.

Hill, I. and Luxat, J. (2006). *Application of Best Estimate Methods and Analysis of Uncertainity Methods to CANDU Channel Power*. Master's thesis, McMaster University.

Hubbell, J. and Seltzer, S. (2014). Tables of X-Ray Mass Attenuation Coefficients and Mass Energy-Absorption Coefficients. `http://www.nist.gov/pml/data/xraycoef/`, National Institute of Standards and Technology.

Hurst, G. S. and Turner, J. E. (1970). *Elementary Radiation Physics*. John Wiley Sons, Inc., New York.

IAEA (2007). Database of Prompt Gamma Rays from Slow Neutron Capture for Elemental Analysis. Technical report.

IAEA (2015). PGAA: Prompt Gamma-ray Neutron Activation Analysis. `https://www-nds.iaea.org/pgaa/pgaa7/index.html`. Accessed: Feb, 2015.

Instruments, N. (2015). NI 9211 Datasheet. `http://www.ni.com/datasheet/pdf/en/ds-197`.

Iracane, D. (2005). The JHR, A New Material Testing Reactor in Europe. *Nuclear Engineering and Technology*, **38**(5).

Ji, B. L., Byong, W. L., and Byung, C. L. (1995). Radiation streaming analysis in the radial and tangential beam tubes of a TRIGA research reactor using MCNP and comparison with measurement. *Nuclear Science and Engineering*, **121**(2).

Johnson, J. and Burns, T. (1981). Theoretical characterization of a dual-purpose gamma thermometer. In *American Nuclear Society 1981 Annual Meeting*.

Johnson, R., Miller, I., and Freund, J. (2000). *Probability and Statistics for Engineers*. Prentice Hall, New Jersey, 6th edition.

Keepin, G. R. (1965). *Physics of Nuclear Kinetics*. Addison-Wesley, USA.

Keepin, G. R., Wimett, T. F., and Zeigler, R. K. (1957). Delayed neutrons from fissionable isotopes of uranium, plutonium and thorium. *Journal of Nuclear Energy*, **6**.

Kendall, M. (1973). *Time-Series*. Griffiin London, London.

Kim, S. (1994). Monte Carlo evaluation of ATRC gamma heating measurements. In *1994 Annual Meeting of American Nuclear Society (papers in summary form only received)*, volume 70, USA.

Kizhakkekara, J., Katrik, P., and Bock, H. (1998). Development and test of a miniature gamma thermometer to determine the gamma dose rate inside a reactor core. In *Proceedings of International Conference on Nuclear Energy in Central Europe '98*, Ljubljana, Slovenia. Nucl. Soc. Slovenia.

Klein, J., Thiollay, N., Di-Salvo, J., Bosq, J., Wieryszkow, J., and et al. (2009). AMMON: An experimental program in the EOLE critical facility for the validation of the Jules Horowitz Reactor neutron and photon HORUS3D calculation scheme. In *In Proceedings of the IGORR (International Group on Research Reactors) 2009 Conference*.

Knoll, G. (2010). *Radiation Detection and Measurement*. John Wiley Sons, Inc., Hoboken, USA, 4rd edition.

Kreith, F. and Bohn, M. (2001). *Principles of Heat Transfer*. Brooks/Cole, Pacific Grove, CA, 6th edition.

Lamarsh, J. and Baratta, A. (2001). *Introduction to Nuclear Engineering*. Prentice Hall, Upper Saddle River, USA, 3rd edition.

LANL (2012). Document LAUR-10-07256 on http://mcnpx.lanl.gov/.

Lee, Y., David, J., and Carcreff, H. (2001). A gamma heating calculation methodology for research reactor application. European Nuclear Society.

Liu, M. N. (1994). Characteristics of Gamma Thermometers. Technical Report HWR-416, OECD Halden Reactor Project, Halden.

Lüthi, A. (1998). *Development and validation of gamma heating calculational methods for plutonium-burning fast reactors*. Ph.D. thesis, École Polytechnique Fédérale de Lausanne.

Lüthi, A., Chawla, R., and Rimpault, G. (2001). Improved gamma-heating calculationalmethods for fast reactors and their validation for plutonium-burning configurations. *Nuclear Science and Engineering*, **138**.

Malouch, F. (2012). Development and Experimental Validation of a Calculation Scheme for Nuclear Heating Evaluation in the Core of the OSIRIS Material Testing Reactor. *Journal of ASTM International*, **9**(4).

MathWorks (2015a). Discrete Fourier Transform. `http://www.mathworks.com/help/signal/ug/discrete-fourier-transform.html`. Accessed: Jan, 2015.

MathWorks (2015b). Discrete Fourier Transform (DFT). `http://www.mathworks.com/help/matlab/math/discrete-fourier-transform-dft.html`. Accessed: Jan, 2015.

MathWorks (2015c). Fast Fourier Transform (FFT). `http://www.mathworks.com/help/matlab/math/fast-fourier-transform-fft.html`. Accessed: Jan, 2015.

McMaster Nuclear Reactor (2002). McMaster Nuclear Reactor Safety Analysis Report. Technical report.

National Nuclear Data Center (2015). CapGam: Thermal Neutron Capture Gammas. `http://www.nndc.bnl.gov/capgam/`. Accessed: June, 2015.

Nieuwenhove, R. V. and Vermeeren, L. (2002). On-line gamma flux measurements by means of a self powered gamma detector. In *2001 IEEE Nuclear Science Symposium Conference Record*, volume 2, Piscataway, USA. IEEE.

NIST (2015a). NIST Engineering Statistics Handbook. `www.itl.nist.gov/div898/handbook/mpc/section5/mpc5332.htm#exprobe`. Accessed: Feb, 2015.

NIST (2015b). NIST Engineering Statistics Handbook. `http://www.itl.nist.gov/div898/handbook/pmc/section4/pmc4.htm`. Accessed: Feb, 2015.

NIST (2015c). NIST Engineering Statistics Handbook. `http://www.itl.nist.gov/div898/handbook/pmc/section4/pmc431.htm`. Accessed: Feb, 2015.

NIST (2015d). NIST Engineering Statistics Handbook. `http://www.itl.nist.gov/div898/handbook/pmc/section4/pmc433.htm`. Accessed: Feb, 2015.

OECD-NEA (2012). http://www.oecd-nea.org/tools/abstract/detail/NEA-1339/.

ORNL (2011a). Scale: A Comprehensive Modeling and Simulation Suite for Nuclear Safety Analysis and Design. Technical report.

ORNL (2011b). Scale: A Comprehensive Modeling and Simulation Suite for Nuclear Safety Analysis and Design. Technical Report ORNL/TM-2005/39, Oak Ridge National Laboratory. Available from Radiation Safety Information Computational Center at Oak Ridge National Laboratory as CCC-785.

ORNL (2012). https://rsicc.ornl.gov/codes/ccc/ccc7/ccc-755.html.

Pelowitz, D. P. (2013). MCNP6 Users Manual. Technical Report LA-CP-13-00634, Rev. 0, Los Alamos National Laboratory.

P.J. Brockwell, R. D. (2002). *Introduction to Time-Series and Forecasting*. Spring, London, 2nd edition.

Podgorsak, E. B. (2005). *Radiation Oncology Physics: A Handbook for Teachers and Students*. International Atomic Energy Agency, Vienna.

P.R. Bevington, D. R. (1992). *Data reduction and error analysis for the physical sciences*. McGraw-Hill, Inc., New York, 2nd edition.

Ravaux, S. (2013). *Qualification du Calcul de lÉchauffement Photonique dans les Réacteurs Nucléaires*. Ph.D. thesis, L'Université de Grenoble.

Reilly, H. and Peters, L. (1971). Calorimetric determination of relative gamma heating in materials of various thickness and atomic numbers. *Nuclear Technology*, **11**(1).

Rimpault, G., Bernard, D., Blanchet, D., Vaglio-Gaudard, C., Ravaux, S., and Santamarina, A. (2012). Needs of Accurate Prompt and Delayed Gamma-Spectrum and Multiplicity for Nuclear Reactor Designs. *Physics Procedia*, **31**(3-12).

Santos, J., Marques, J., Fernandes, A., and Osvay, M. (2007). Photon and fast neutron dosimetry using aluminium oxide thermoluminescence dosemeters in a pool-type research reactor. *Nuclear Inst. and Methods in Physics Research, A*, **580**(1).

SCK-CEN (2009). SCK-CEN Gamma Thermometer for McMaster Nuclear Reactor - A Product Information. Technical report, Reactor Technology Design, Mol.

Senn, R. and Mixon, W. (1971). Experimental measurement of gamma heat in the high flux isotope reactor. *Nuclear Technology*, **12**.

Silva, H. (1992). Determination of absorbed gamma doses in a pool research reactor. *Kerntechnik*, **57**(5).

Smith, S. W. (1998). The Scientist and Engineer's Guide to Digital Signal Processing. `http://www.dspguide.com/`. Accessed: Feb, 2015.

TA, A. (2011). RJH - Configuration de Référence. Technical Report TA-617165.

Tanaka, S. and Sasamoto, N. (1985). Gamma-ray absorbed dose measurements in media with plural thermoluminescent dosimeters having different atomic numbers. *Journal of Nuclear Science and Technology*, **22**(2).

Taylor, J. R. (1982). *An introduction to error analysis*. Oxford University Press, Mill Valley, CA.

Team, X.-. M. C. (2008). MCNP - A general Monte Carlo N-particle Transport Code, Version 5; Volume I: Overview and theory. Technical Report LA-UR-03-1987, Los Alamos National Laboratory.

The MathWorks, I. (2004). MATLAB 7.0.1.

Torkzadeh, F., Manouchehri, F., Nejad, F. Y., and Mohammadzadeh, A. H. (2007). In-core thermal high-neutron fluence measurement by TLD-activation method. *Nuclear Inst.and Methods in Physics Research, A*, **580**(3).

Tosi, V., Haaland, A., and Blazquez, J. (1995). The use of gamma thermometer as a multipurpose sensor. In *NEA, SMORN-VII, 7th Symposium on Reactor Surveillance and Diagnostics*.

Turner, J. (2008). *Atoms, Radiation, and Radiation Protection*. Wiley-VCH, Hoboken, USA, 3rd edition.

Vaglio-Gaudard, C., Leray, O., Colombier, A., D'Aletto, C., Gaubert, L., Gueton, O., Hudelot, J., Valentini, M., Sireta, P., Salvo, J. D., Gruel, A., Klein, J., Roche, A., Beretz, D., and Girard, J. (2012). Monte Carlo interpretation of the AMMON/REF experiment in EOLE for the JHR reactor calculations. In *International Conference on the Physics of Reactors 2012: Advances in Reactor Physics, PHYSOR 2012, April 15-20*, volume 2, Knoxville, USA. American Nuclear Society.

Vaglio-Gaudard, C., Stoll, K., Ravaux, S., Lemaire, M., and et al. (2014). Monte Carlo interpretation of the photon heating measurements in the integral AMMON/REF experiment in the EOLE facility. *IEEE Transactions on Nuclear Science*, **61**(1).

Valente, F. (1963). *A manual of experiments in reactor physics*. The Macmillan Company, New York.

Van Nieuwenhove, R. (1996). Gamma Thermometers for BR2. Technical Report NT.50/A007020/04/FM/RvN/hq, SCK-CEN.

Varvayanni, M., Catsaros, N., and Antonopoulos-Domis, M. (2008). A point kernel model for the energy deposited on samples from gamma radiation in a research reactor core. *Annals of Nuclear Energy*, **35**(12).

Vermeeren, L. (2014). private communication.

Vértes, A., Nagy, S., Klencsár, Z., and Lovas, R. (2003). *Handbook of Nuclear Chemistry*, volume 3. Kluwer Academic, Dordrecht.

Waring, J. and Smith, R. (1983). Recent reactor testing and experience with gamma thermometers. *IEEE Transactions on Nuclear Science*, **NS-30**(1).

Williams, T. and Kelley, C. (2015). gnuplot 5.0: An Interactive Plotting Program.

X-5 Monte Carlo Team (2008). MCNP - A General Monte Carlo N-Particle Transport Code, Version 5 - Volume I: Overview and Theory. Technical Report LA-UR-03-1987, Los Alamos National Laboratory.

Yamaguchi, S., Maekawa, H., Kosaka, K., Nakamura, T., and Porges, K. (1988). Measurements of gamma-ray heating in lithium-oxide, graphite and iron slab assemblies bombarded by D-T neutrons. In *Proceedings of the First International Symposium on Fusion Nuclear Technology (3 vols)*, Tokyo, Japan. Publ by Elsevier Science Publ BV (North-Holland).

Zill, D. G. and Cullen, M. R. (2000). *Advanced Engineering Mathematics*. Jones and Bartlett Publishers, Sudbury, MA, 2nd edition.

Zisis, T., Varvayanni, M., Savva, P., and Catsaros, N. (2010). Methods and instruments for assessing the in-core gamma heating of materials. *IEEE Transactions on Nuclear Science*, **57**(2).